

Technical Report 03-11

Grimsel Test Site
Investigation Phase V

GAM – Gas Migration Experiments in a Heterogeneous Shear Zone of the Grimsel Test Site

December 2006

P. Marschall and I. Lunati (editors)

**National Cooperative
for the Disposal of
Radioactive Waste**

Hardstrasse 73
CH-5430 Wettingen
Switzerland
Tel. +41 56 437 11 11

www.nagra.ch

Technical Report 03-11

Grimsel Test Site
Investigation Phase V

GAM – Gas Migration Experiments in a Heterogeneous Shear Zone of the Grimsel Test Site

December 2006

P. Marschall and I. Lunati (editors)

with contributions by:

S. Attinger, N. S. Brodsky, M. de Combarieu, J. Carrera,
T. Fierz, J. T. Fredrich, M. Garcia, J. Jodar, I. Lunati,
K. Kennedy, W. Kinzelbach, J.C. Major, P. Meier,
H. Ramajo, J. C. Stormont and T. Trick

**National Cooperative
for the Disposal of
Radioactive Waste**

Hardstrasse 73
CH-5430 Wettingen
Switzerland
Tel. +41 56 437 11 11

www.nagra.ch

This report was prepared on behalf of Nagra. The viewpoints presented and conclusions reached are those of the author(s) and do not necessarily represent those of Nagra.

ISSN 1015-2636

"Copyright © 2006 by Nagra, Wettingen (Switzerland) / All rights reserved.

All parts of this work are protected by copyright. Any utilisation outwith the remit of the copyright law is unlawful and liable to prosecution. This applies in particular to translations, storage and processing in electronic systems and programs, microfilms, reproductions, etc."

GTS Phase V



	NAGRA	National Cooperative for the Disposal of Radioactive Waste
	ANDRA	Agence nationale pour la gestion des déchets radioactifs
	BMWi	Bundesministerium für Wirtschaft und Technologie
	BGR	Bundesanstalt für Geowissenschaften und Rohstoffe
	FZK/INE	Forschungszentrum Karlsruhe, Institut für Nukleare Entsorgungstechnik
	GRS	Gesellschaft für Anlagen- und Reaktorsicherheit
	DOE/CAO	Department of Energy, Carlsbad Area Office
	SNL	Sandia National Laboratories
	ENRESA	Empresa Nacional de Residuos Radioactivos
	ERL/ITRI	Energy and Resources Laboratories / Industrial Technology Research Institute
	JNC	Japan Nuclear Cycle Development Institute
	Obayashi	Obayashi Corporation
	RWMC	Radioactive Waste Management Center
	RAWRA	Radioactive Waste Repository Authority
	SKB	Svensk Kärnbränslehantering AB
	EC	European Community

Foreword

Concepts for the disposal of radioactive waste in geological formations depend crucially on a thorough knowledge of relevant processes in the host rock and on an understanding of the whole repository system, comprising both engineered and geological barriers. The Grimsel Test Site (GTS) is a first-generation underground rock laboratory which is used to investigate many of these processes in hard, fractured rocks. It has been operated since 1984 by the Swiss National Cooperative for the Disposal of Radioactive Waste (NAGRA).

The laboratory is located in the crystalline rock of the Central Aar Massif, 450 m below the eastern flank of the Juchlistock at an altitude of 1730 m. It is reached via a 1200 m horizontal access tunnel, operated by the hydropower plant KWO. The layout of the tunnels that comprise the GTS allowed the establishment of a radiation controlled zone (IAEA type B/C) in 1990 in which experiments with radioactive tracers are carried out. With increasing experience in the implementation of in-situ experiments, improved process understanding and more advanced repository concepts, the experimental programmes at the GTS have gradually become more complex and more directly related to open questions defined by performance assessors or by regulatory bodies. Demonstration of disposal concepts by performing large- or full-scale, long-term experiments has also become a key aspect of investigations in the rock laboratory.

The investigation phase V of the Grimsel Rock Laboratory was initiated in 1997 in close co-operation with international partner organisations. Seven experimental programmes and projects are included in this Phase, covering a broad spectrum of investigations.

This report documents both the experimental and modelling results of the project **Gas Migration in Shear Zones (GAM)**, performed under the leadership of Nagra from 1998 – 2001.

The objective of the GAM project was to investigate the transport of solutes and gases in heterogeneous shear zones. The emphasis was on (i) the visualisation of channelling phenomena on the lab and field scale, (ii) the development of upscaling procedures and effective parameters for two-phase flow processes in fractured media and (iii) the development of consistent models for (single phase) solute and gas transport.

The project was initiated in 1998 on the basis of a collaboration agreement between Nagra, ENRESA (Spain) and the US-DoE (United States of America). ANDRA (France) participated in the project from 1999.

GTS Phase V



	NAGRA	National Cooperative for the Disposal of Radioactive Waste
	ANDRA	Agence nationale pour la gestion des déchets radioactifs
	BMWi	Bundesministerium für Wirtschaft und Technologie
	BGR	Bundesanstalt für Geowissenschaften und Rohstoffe
	FZK/INE	Forschungszentrum Karlsruhe, Institut für Nukleare Entsorgungstechnik
	GRS	Gesellschaft für Anlagen- und Reaktorsicherheit
	DOE/CAO	Department of Energy, Carlsbad Area Office
	SNL	Sandia National Laboratories
	ENRESA	Empresa Nacional de Residuos Radioactivos
	ERL/ITRI	Energy and Resources Laboratories / Industrial Technology Research Institute
	JNC	Japan Nuclear Cycle Development Institute
	Obayashi	Obayashi Corporation
	RWMC	Radioactive Waste Management Center
	RAWRA	Radioactive Waste Repository Authority
	SKB	Svensk Kärnbränslehantering AB
	EC	European Community

Vorwort

Bei der Entsorgung radioaktiver Abfälle wird aus Sicherheitsüberlegungen die Endlagerung in geologischen Formationen vorgesehen. Dafür sind Kenntnis über das Wirtgestein sowie ein vertieftes Verständnis der technischen Sicherheitsbarrieren von entscheidender Bedeutung.

Seit 1984 betreibt die Nagra (Nationale Genossenschaft für die Lagerung radioaktiver Abfälle) ein standortunabhängiges Felslabor im Grimselgebiet (FLG), in den granitischen Gesteinen des Zentralen Aar Massivs.

Das FLG liegt 450 m unter der Ostflanke des Juchlistocks auf einer Höhe von 1730 m ü.M. und kann durch einen 1200 m langen horizontalen Zugangstollen der Kraftwerke Oberhasli AG (KWO) erreicht werden. Im Jahr 1990 wurde in einem der Stollenabschnitte des FLG's eine kontrollierte Zone (IAEA Typ B/C) für Versuche mit radioaktiven Tracern eingerichtet.

Mit zunehmender Erfahrung in der Durchführung von Feldversuchen, verbessertem Systemverständnis der geologischen und technischen Barrieren sowie der weiterentwickelten Lagerkonzepte, verlagerten sich die Programm-Schwerpunkte zu komplexen, direkt auf die Anforderungen der Sicherheitsanalyse ausgerichteten Versuche. Langzeitdemonstrationsversuche gewannen in den letzten Jahren immer mehr an Bedeutung.

Die Untersuchungsphase V des FLG wurde 1997 in enger Zusammenarbeit mit den Partnerorganisationen geplant. Sie beteiligen sich wesentlich bei der Durchführung der insgesamt 7 Versuchsprogramme, die ein breites Spektrum wissenschaftlicher und technischer Fragestellungen abdecken.

Das Projekt **Gas Migration in Shear Zones (GAM)** wurde von 1998 bis 2001 unter der Leitung der Nagra durchgeführt. Der vorliegende Bericht fasst die Ergebnisse der Felduntersuchungen sowie der Interpretationsarbeiten zusammen.

Ziel des GAM-Projekts war es, die komplexen Transportvorgänge von gelösten und gasförmigen Stoffen in den wasserführenden Systemen einer heterogenen Scherzone zu untersuchen. Schwerpunkte des Untersuchungsprogramms waren (i) die phänomenologische Beschreibung solcher Transportvorgänge im Labor- und im Feldmassstab unter Verwendung von neuartigen Visualisierungstechniken, (ii) die Entwicklung von Modellkonzepten zur Herleitung von effektiven Zweiphasenflussparametern in geklüfteten Medien und (iii) die Entwicklung von numerischen Modellen, die den Transport von gelösten Stoffen sowie den Gastransport in konsistenter Weise beschreiben.

Auf der Basis eines Zusammenarbeitsvertrages zwischen Nagra, ENRESA (Spanien) und US-DoE (USA) wurde das Projekt 1998 ins Leben gerufen. ANDRA (France) beteiligte sich ab 1999 an diesem Projekt.

GTS Phase V



NAGRA National Cooperative for the Disposal of Radioactive Waste



ANDRA Agence nationale pour la gestion des déchets radioactifs



BMWi Bundesministerium für Wirtschaft und Technologie

BGR Bundesanstalt für Geowissenschaften und Rohstoffe

FZK/INE Forschungszentrum Karlsruhe, Institut für Nukleare Entsorgungstechnik

GRS Gesellschaft für Anlagen- und Reaktorsicherheit



DOE/CAO Department of Energy, Carlsbad Area Office

SNL Sandia National Laboratories



ENRESA Empresa Nacional de Residuos Radioactivos



ERL/ITRI Energy and Resources Laboratories / Industrial Technology Research Institute



JNC Japan Nuclear Cycle Development Institute

Obayashi Obayashi Corporation

RWMC Radioactive Waste Management Center



RAWRA Radioactive Waste Repository Authority



SKB Svensk Kärnbränslehantering AB



EC European Community

Préface

Le stockage définitif des déchets radioactifs est prévu, pour des questions de sûreté, dans des formations géologiques. La connaissance détaillée des roches d'accueil et une compréhension approfondie des processus se déroulant dans la roche et dans les barrières techniques de sûreté sont d'une importance décisive.

Le laboratoire souterrain du Grimsel (LSG) est un laboratoire de première génération en fonction depuis 1984, exploité par la Société coopérative nationale pour l'entreposage de déchets radioactifs (NAGRA).

Le laboratoire est situé à une altitude de 1730 m dans les roches granitiques du Massif Central de l'Aar, à 450 m de profondeur sous le flanc est du Juchlistock. On l'atteint par un tunnel d'accès horizontal exploité par la centrale électrique Oberhasli AG de la société KWO. En 1990, on a aménagé dans le LSG une zone de radiation contrôlée (type B/C de l'AIEA) pour des essais avec traceurs radioactifs.

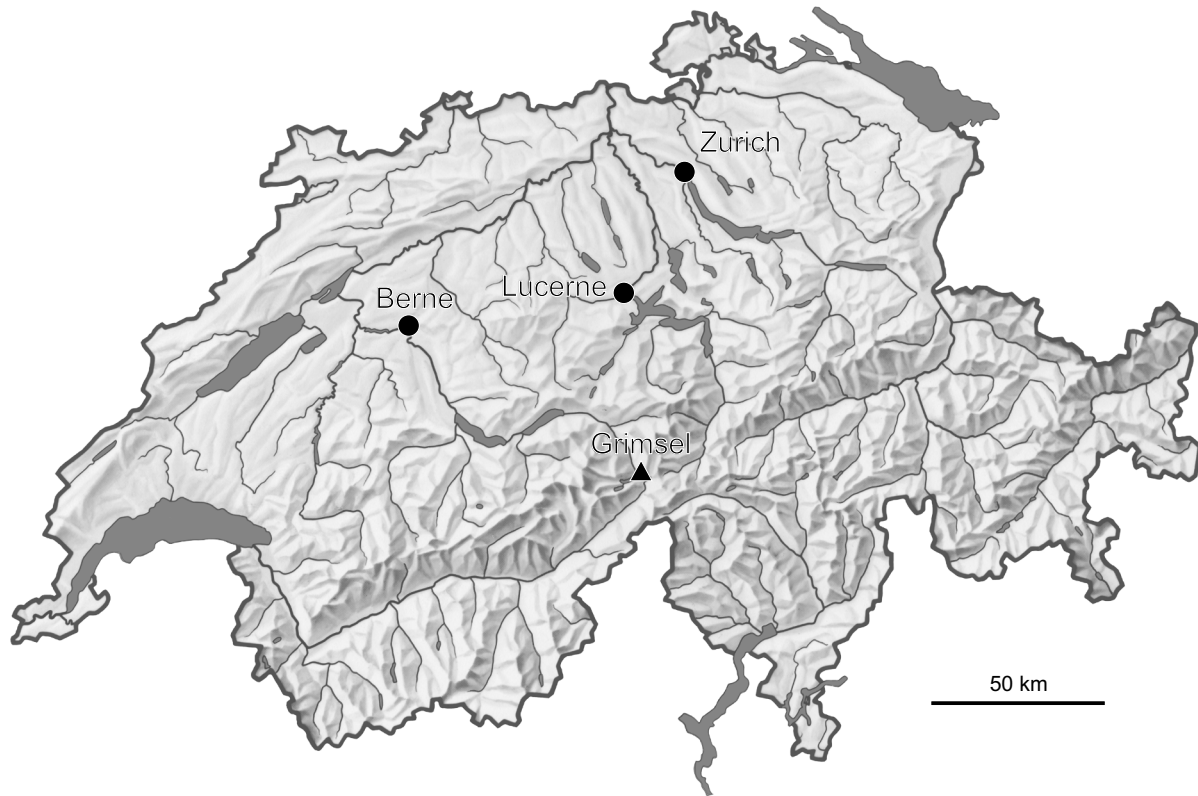
Avec l'expérience croissante dans la conduite d'essais in-situ, une meilleure compréhension des barrières géologiques et techniques, le programme de recherche s'est orienté vers des essais toujours plus complexes liés aux exigences des analyses de sûreté. La démonstration de faisabilité de concepts de dépôt à grande échelle et sur de longues durées est devenue l'un des points forts des recherches dans le laboratoire souterrain.

La phase de recherche actuelle du LSG, qui a débuté en 1997, a été planifiée en concertation étroite avec les partenaires internationaux. Elle comprend sept projets et programmes d'essais couvrant un large spectre de questions scientifiques et techniques.

Le projet «**Gas Migration in Shear Zones**» (GAM) a été réalisé entre 1998 et 2001 sous la direction de la Nagra. Le présent rapport résume les résultats des expériences sur le terrain ainsi que l'interprétation qui en a été faite.

L'objectif de ce projet était d'étudier les processus de transport complexes subis par des substances dissoutes ou gazeuses dans les systèmes aquifères d'une zone de cisaillement hétérogène. Les points focaux du programme de recherche étaient: (i) décrire la phénoménologie de ces processus de transport, en laboratoire et à l'échelle réelle, en recourant à de nouvelles techniques de visualisation, (ii) développer des modèles pour déduire les paramètres effectifs de l'écoulement diphasique en milieu faillé et (iii) mettre au point des modèles numériques décrivant de façon cohérente le transport des substances dissoutes et des gaz.

Ce projet a été lancé en 1998, sur la base d'un contrat de coopération passé entre la Nagra, l'ENRESA (Espagne) et le US-DOE (États-Unis). L'ANDRA (France) a rejoint le projet en 1999.



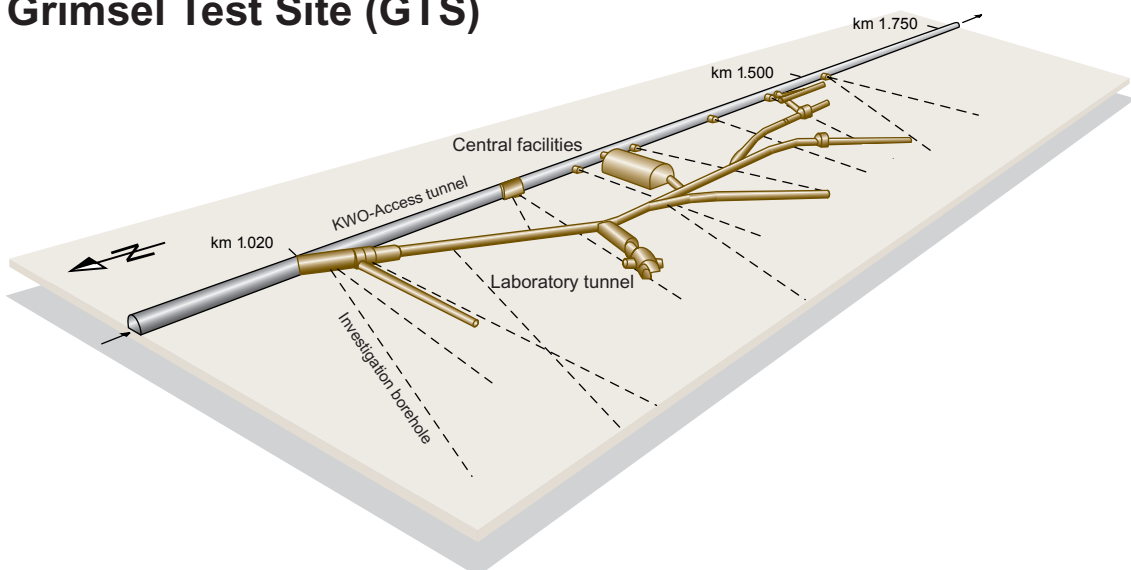
Location of Nagra's underground test facility at the Grimsel Pass in the Central Alps (Bernese Alps) of Switzerland

Grimsel area (view to the west)



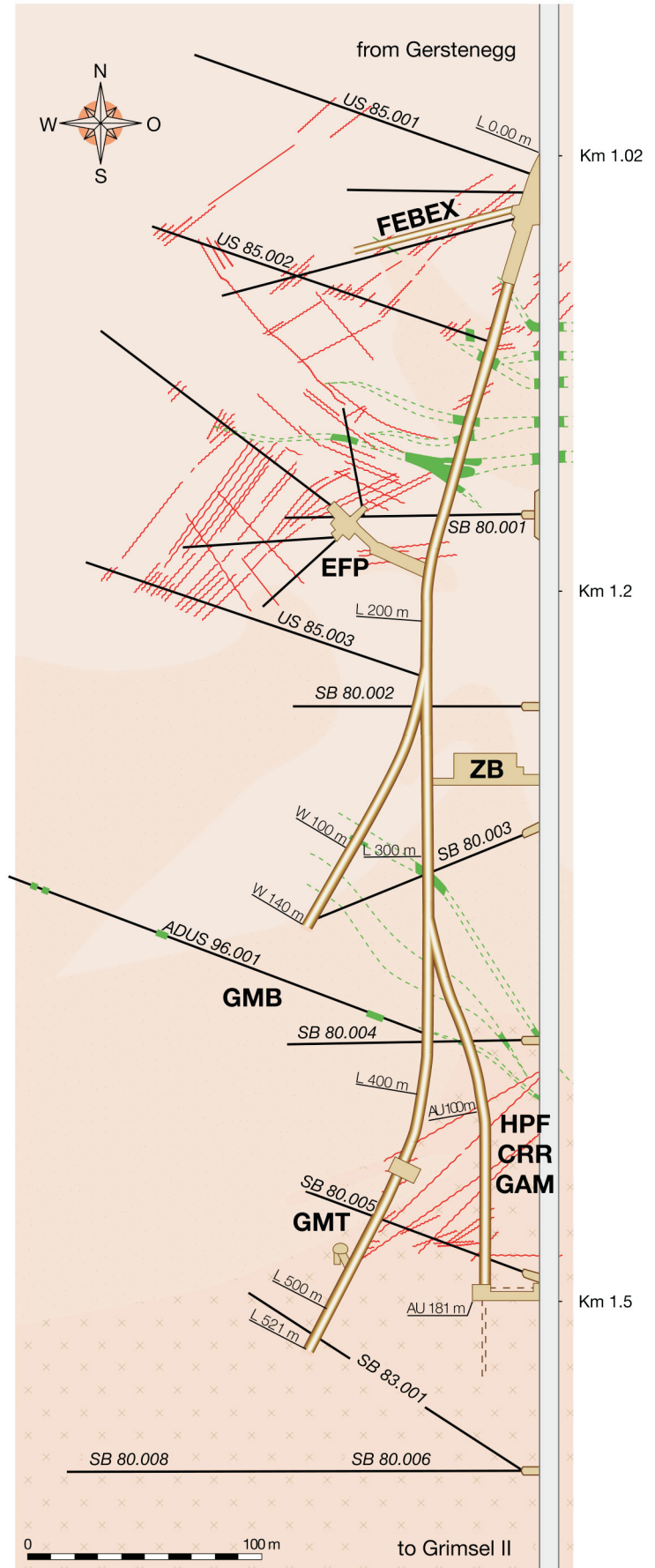
1 Gimsel Test Site 2 Lake Raeterichsboden 3 Lake Grimsel 4 Juchlistock

Grimsel Test Site (GTS)



Grimsel Test Site GTS

-  KWO-Access tunnel
-  Laboratory tunnel
-  Central Aaregranite (CAGR)
High biotite content CAGR
-  Grimsel-Granodiorite
-  Shear zone
-  Lamprophyre
-  Investigation borehole
- ZB** Central facilities
- GTS Phase V 1997-2002**
- HPF** Hyperalkaline Plume
- CRR** Colloid and Radionuclide Retardation
- GAM** Gastransport in the Geosphere
- FEBEX** 1:1 EBS – Demonstration (HLW)
- GMT** Gas Migration Test in the EBS
- GMB** Geophysical Methods in Boreholes
- EFP** Effective Parameters



Abstract

This report documents the scientific investigations carried out as part of the GAM project between June 1997 and April 2001 at the Grimsel Test Site (GTS) within the framework of Investigation Phase V (1997 – 2001). Four radioactive waste management organisations participated in the GAM experiment, namely ANDRA, ENRESA, NAGRA and Sandia National Laboratories (SNL) for the US Department of Energy (DOE). The experiment team consisted of the delegates of the participating organisations, research groups from the Swiss Federal Institute of Technology / Zurich and from the Technical University of Catalonia / Barcelona and, last but not least, several contractor teams.

Essential aims of the GAM investigation programme were the development and testing of **laboratory and field equipment for tracer experiments**. Innovative laboratory technologies were applied, such as Laser Scanning Confocal Microscopy and X-ray tomography, flow visualisation in artificial fractures, nuclear magnetic resonance measurements and neutron radiography. Furthermore, a new technique was tested for the recovery of well preserved core samples from the GAM shear zone. Novelities in field testing comprised the use of an on-line counter for the particle tracer tests and a georadar survey of gas and brine injection tests with a high frequency borehole antenna.

The development of **upscaling methodologies** and the derivation of **effective parameters** for single- and two-phase flow models was another issue of interest. The investigations comprised theoretical studies on solute transport in non-uniform flow fields and assessment of the impact of the microstructure on solute and gas transport. Closely related to these theoretical studies was the numerical interpretation of the combined solute and gas tracer tests, which revealed the great potential of such data sets with regard to model discrimination.

As a final step in the synthesis task of the GAM project, a **model abstraction process** was established, aimed at integrating the descriptive studies on various scales with the hydraulic investigations to produce a consistent conceptual model of flow and transport processes in the heterogeneous shear zone.

Zusammenfassung

Der vorliegende Bericht dokumentiert die wissenschaftlichen Arbeiten die im Rahmen des Projekts GAM zwischen Juni 1997 und April 2001 im Felslabor Grimsel (Internationales Forschungsprogramm – FLG / Phase V) durchgeführt wurden. Vier internationale Organisationen für die Entsorgung radioaktiver Abfälle nahmen am GAM Experiment teil, nämlich ANDRA, ENRESA, Nagra und Sandia National Laboratories im Auftrag des US Department of Energy (DOE). The Projektteam setzte sich zusammen aus Mitgliedern der teilnehmenden Organisationen, aus Forschungsgruppen der ETH Zürich und der Technischen Universität Barcelona sowie mehreren Kontraktorengruppen.

Wichtige Zielsetzungen des GAM Projekts waren die **Entwicklung und Erprobung von Labor- und Feldmethoden für Tracerexperimente**. Innovative Labortechniken wurden angewendet – hierzu gehören die sogenannte „Laser Scanning Confocal Microscopy“, die Röntgentomographie, die Visualisierung von Transportvorgängen in künstlichen Scherzonen, NMR Messungen an Kernproben und die Neutronenradiografie. Weiterhin wurde eine neue Methode zur Gewinnung von ungestörten Kernproben aus der GAM Scherzone entwickelt. Zu den Neuerungen im Bereich der Felduntersuchungen zählen die Erprobung einer Messeinheit zur in-situ Detektion von Partikeltracern sowie Georadarmessungen mit einer Hochfrequenz-Bohrlochsonde, die im Rahmen von Gas- und Salzwasserinjektionsversuchen durchgeführt wurden.

Die Entwicklung von sogenannten „**Upscaling**“ Methoden und die Herleitung **effektiver Parameter** für Transport- und Zweiphasenflussprozesse war ein weiterer Schwerpunkt des Untersuchungsprogramms. Die Arbeiten umfassten theoretische Studien zum Transport gelöster Stoffe in heterogenen Fliessfeldern sowie eine Untersuchung zum Einfluss der Mikrostruktur der Scherzone auf den Transport von gelösten und gasförmigen Stoffen. In enger Abstimmung mit diesen theoretischen Arbeiten wurden die verschiedenen Tracertests (gelöste Stoffe, Gas-tracer) mit Hilfe numerischer Modellierungen ausgewertet. Hierbei konnte aufgezeigt werden, dass die gemeinsame Interpretation von konventionellen Tracertests und Gastracertests zu einer verbesserten Modelldiskriminierung führt.

Als letzter Schritt in den Synthesearbeiten zum GAM Projekt wurde ein Verfahren zur **Modellabstraktion** erarbeitet. Zweck dieser Arbeiten war es, strukturgeologische Informationen auf verschiedenen Beobachtungsskalen mit den verfügbaren hydraulischen Daten zu einem konzeptuellen Modell zusammenzuführen, mit dem es möglich ist, Fliess- und Transportvorgänge in heterogenen Scherzonen mit konsistenten Parametermodellen zu beschreiben.

Résumé

Le présent rapport porte sur les travaux scientifiques réalisés dans le cadre du projet GAM entre juin 1997 et avril 2001 au Laboratoire souterrain du Grimsel (Programme de recherche international – LSG / Phase V). Les organisations nationales de quatre pays chargées de l'évacuation des déchets radioactifs ont participé à l'expérience GAM, à savoir l'ANDRA, l'ENRESA, la Nagra et Sandia National Laboratories sur mandat du Department of Energy (DOE). L'équipe de projet était composée de membres des organisations partenaires, de groupes de recherche de l'EPF Zurich et de l'Université technique de Barcelone ainsi que de plusieurs mandataires.

L'objectif premier du projet GAM consistait à **mettre au point et à tester des méthodes en laboratoire et in situ pour des expériences avec traceur**. On a recouru à des techniques de laboratoire innovatrices, dont la "Laser Scanning Confocal Microscopy", la radiotomographie, la visualisation de processus de transport dans des zones de cisaillement artificielles, des mesures RMN sur des carottes et la radiographie neutronique. Une nouvelle méthode a en outre été développée pour extraire des carottes non perturbées de la zone faillée du GAM. Au nombre des innovations dans le domaine des essais sur le terrain, il y a l'expérimentation avec une unité de mesure permettant de détecter in situ des particules traceuses ou encore les mesures par géoradar au moyen d'une sonde haute fréquence introduite dans les trous de forage; celles-ci ont été réalisées dans le cadre d'essais d'injection de gaz et de solutions salines.

Autre point fort de ce projet de recherche: les méthodes dites de "**upscaling**" et la déduction de **paramètres effectifs** pour connaître les processus de transport et d'écoulement diphasique. Les travaux ont englobé des études théoriques sur le transport de substances dissoutes dans des zones d'écoulement hétérogènes ainsi qu'une étude sur l'influence de la microstructure de la zone de cisaillement sur le transport des substances dissoutes ou gazeuses. En s'appuyant de près sur ces travaux théoriques, divers tests de traceurs (substances dissoutes, traceurs gazeux) ont ensuite été évalués au moyen de modèles numériques. Ce faisant, il a été possible de démontrer que l'interprétation conjointe de tests de traceurs conventionnels et de tests de traceurs gazeux permet une meilleure discrimination entre modèles.

La dernière partie des travaux de synthèse dans le cadre du projet GAM a consisté à élaborer un processus pour l'**abstraction de modèles**. Le but était de réunir les informations sur la structure géologique à diverses échelles d'observation et les données hydrauliques à disposition afin d'obtenir un modèle conceptuel permettant de décrire les processus d'écoulement et de transport dans les zones de cisaillement hétérogènes avec des modèles à paramètres cohérents.

Contents

Abstract	I
Zusammenfassung.....	II
Résumé	III
Contents	IV
List of Tables.....	VI
List of Figures	VI
1 Introduction	1
1.2 Expectations of the agencies.....	2
1.3 Report outline and authors.....	4
2 The GAM experiment – concept and experiment programme.....	7
2.1 Aims and concept	7
2.2 The GAM experimental site	9
2.3 Instrumentation of the site	13
2.4 GAM investigation programme.....	14
3 Laboratory investigations of core samples	15
3.1 Development of core recovery techniques.....	15
3.1.1 Core drilling campaigns in the GAM shear zone	15
3.1.2 Recovery of CoGAM98-001 and CoGAM98-002	15
3.1.3 Laboratory specimen preparation	16
3.1.4 Application of the improved core recovery technique.....	19
3.2 Determination of material parameters	19
3.2.1 Experimental set-up.....	20
3.2.2 Experimental methods	21
3.2.3 Results – testing of core matrix	23
3.2.4 Results – testing of shear zone.....	27
3.2.5 Summary and interpretation of property tests.....	32
3.3 Visualisation of pore space distribution.....	33
3.3.1 Scope and relevance	33
3.3.2 Experimental methods and results	33
3.3.3 Interpretation and conclusions.....	37
3.4 Visualisation of transport and two-phase phenomena	37
3.4.1 Scope and relevance	37
3.4.1 Experiments in artificial fractures	37
3.4.2 Non-destructive measurements on Grimsel cores by NMR and Neutron Tomography	42
4 Hydraulic characterisation of the shear zone.....	49
4.1 Field testing	49
4.1.1 Test equipment and experimental procedure.....	49

4.1.2	Overview of the hydraulic test campaigns.....	52
4.2	Diagnostic analysis	54
4.2.1	Fundamentals.....	54
4.2.2	Results	58
4.2.3	Interpretation of the results.....	62
4.3	Geostatistical inversion of hydraulic tests	63
4.3.1	Methodology.....	63
4.3.2	Results	65
5	Solute and particle tracer tests	67
5.1	Rationale, concepts and restrictions	67
5.2	The field experiments	69
5.2.1	Experimental set-up and procedure	69
5.2.2	Overview of tests and their configurations	71
5.2.3	Tests results	72
5.3	Modeling of tracer tests including a-priori hydraulic information	77
5.4	Theoretical study of solute tracer tests	81
5.4.1	Upscaling of solute transport in a non-uniform flow field	81
5.4.2	Effects of pore volume-transmissivity correlation.....	83
5.5	Summary of achievements.....	87
6	Gas tracer tests.....	89
6.1	Aims and concept	89
6.2	The field investigations.....	90
6.2.1	Overview of gas tracer experiments	90
6.2.2	Experimental set-up.....	93
6.2.3	Experimental procedure.....	94
6.2.4	Test results and preliminary interpretation	94
6.3	Numerical simulations of gas tracer tests in an unsaturated shear zone.....	97
6.3.1	Water-soluble gases as partitioning tracers	97
6.3.2	Modelling gas tracer tests at the Grimsel Test Site	101
6.4	Achievements and outlook	107
7	Geophysical surveys	109
7.1	Field campaigns and test equipment.....	109
7.2	Test results.....	112
7.2.1	Brine injection test (between November 15 th and 19 th 1999)	112
7.2.2	Gas injection test (between February 1 st and 4 th 2000).....	115
7.3	Modelling results	117
7.4	Evaluation of achievements and outlook.....	119
8	Summary and conclusions	121
8.1	Equipment developments and refined test procedures	121
8.2	Transport processes in the GAM shear zone	123

References	129
Acknowledgements	135

List of Tables

Tab. 1.1:	Report outline and list of authors.....	5
Tab. 3.1:	Core drilling campaigns for property tests in the GAM shear zone.	16
Tab. 3.2:	Liquid permeability of matrix core.....	26
Tab. 3.3:	Summary of Matrix and Shear Zone Data.....	32
Tab. 4.1:	Summary of the hydraulic tests performed in the GAM shear zone: pulse injection tests (PI).....	52
Tab. 4.2:	Summary of the hydraulic tests performed in the GAM shear zone.....	53
Tab. 4.3:	Hydraulic parameters obtained from PI data of the June 1995 test campaign.....	59
Tab. 4.4:	Hydraulic parameters obtained from RI data by means of automatic calibration based on Jacob approximation of Theis solution at late time.	62
Tab. 5.1:	Summary of test configurations and bibliographic references.	71
Tab. 5.2:	Summary of the results of solute- and particle-tracer tests.....	77
Tab. 5.3:	Geostatistical inversion of the solute tracer tests PT1 to PT5 including a-priori hydraulic information.	79
Tab. 6.1:	Overview Gas Tracer Tests.	91
Tab. 6.2:	Tracers used in GAM gas tracer tests.....	92
Tab. 6.3:	Capillary pressure and relative permeability parameters.....	103

List of Figures

Fig. 1.1:	Schematic representation of an emplacement cavern for low-level waste.	1
Fig. 2.1:	GAM tracer test programme – experiment concept.....	8
Fig. 2.2:	GAM – experimental set-up at the Grimsel Test Site.....	9
Fig. 2.3:	Tunnel map of the GAM site in the AU tunnel after Wyss (1996).....	11
Fig. 2.4:	(left) Core sample CoGAM98-001 comprising several brittle structures that are filled with fault gouge material, (right) GBIPS borehole image of borehole GAM98-02 (detail of the shear zone section).....	12
Fig. 2.5:	The location of the GAM boreholes in the plane of the GAM shear zone.	13
Fig. 3.1:	Tunnel map with the location of the core samples.	17

Fig. 3.2:	Photograph of (left) CoGAM98-001 showing open epoxy-filled fractures within inner core and (right) CoGAM98-002 showing no noticeable coring-induced damage. Lower left shows core removal by previous borehole.	18
Fig. 3.3:	Illustration of subcoring technique. Small diameter holes were used to perforate the annulus before coring.	18
Fig. 3.4:	Core drilling with the improved drilling technique: (a) drilling scheme and (b) core sample CoGAM98-05.	19
Fig. 3.5:	Overburden Permeameter Porosimeter (a) in a temperature-controlled cabinet, and (b) view of cabinet interior showing pressure vessel (core holder) and hydraulics.	20
Fig. 3.6:	Automated Two Phase Flow (ATPF) apparatus shown with components labeled.	21
Fig. 3.7:	Porosity versus effective confining stress for matrix core.	24
Fig. 3.8:	Klinkenberg test series on matrix core with an effective confining pressure of 2.0 MPa.	25
Fig. 3.9:	Klinkenberg permeabilities as a function of effective confining pressure for matrix core.	26
Fig. 3.10:	Measured bulk porosity and calculated shear zone porosity as a function of effective confining pressure.	28
Fig. 3.11:	Shear zone gas permeability as a function of effective confining pressure.	28
Fig. 3.12:	Calculated shear zone liquid permeability as a function of effective confining pressure.	29
Fig. 3.13:	Effective gas and water permeability as a function of water saturation.	30
Fig. 3.14:	Capillary pressure as a function of water saturation.	31
Fig. 3.15:	Measured core porosity and calculated shear zone porosity as a function of applied effective confining pressure.	31
Fig. 3.16:	Schematic representation of laser scanning confocal microscopy set-up (Fredrich 1999).	33
Fig. 3.17:	Specimen Co-GAM98-002-1A. Low magnification view of region within several mm-wide macroscopic shear zone (768×512 with 2.055 micron pixel size; 1.578×1.052 mm).	34
Fig. 3.18:	Three-dimensional rendering of void space in sample CoGAM98-002-1A.	35
Fig. 3.19:	Sample CoGAM98-002-1A. Image within shear zone showing (a) block-like microcracking in phenocrysts, and (b) sharp transition to region with no porosity.	35
Fig. 3.20:	Sample CoGAM98-001-2.	36
Fig. 3.21:	X-ray image of shear zone, looking down axis of 9 mm core.	36
Fig. 3.22:	Photograph of the artificial fracture model.	38
Fig. 3.23:	The experimental set-up for visualisation of transport in artificial fractures.	39
Fig. 3.24:	Tracer distributions at five different time steps. From left to right: (a) empty exponential, (b) empty fractal, (c) filled exponential, and (d) filled fractal models.	40

Fig. 3.25:	Gas invasion at 3 different time steps (dimensionless time, expressed as the fraction of injected pore volume): (a) empty fracture and (b) filled fracture.	41
Fig. 3.26:	Section face of the core at the inlet side.	43
Fig. 3.27:	Variation of pore size distribution filled by water during miscible flooding by deuterated water.	44
Fig. 3.28:	Variation in pore size distribution filled by water during gas flooding.	44
Fig. 3.29:	Upper face of the core before processing.	45
Fig. 3.30:	Dry sample radiography.	46
Fig. 3.31:	Ratio of the saturated sample tomography to the drained sample tomography for a selected volume.	47
Fig. 4.1:	Typical packer test procedures applied for hydraulic characterisation of rock formations.	50
Fig. 4.2:	Equipment used for hydrotesting at the GAM site: (a) downhole equipment – hydraulic and mechanical packer systems and (b) surface equipment for pulse tests and constant rate head tests.	51
Fig. 4.3:	Pulse test analysis by type curve matching: (a) Cooper family curves, (b) semi-log plot of pulse test data and (c) match of the test data with the best-fit type curve.	55
Fig. 4.4:	Analysis of flow dimension: diagnostic plots for linear flow (Cartesian plot), radial flow (semi-log plot) and spherical flow (square root plot).	56
Fig. 4.5:	Diagnostic analysis of flow dimension and flow boundaries by log-log derivative representation of a constant rate test.	57
Fig. 4.6:	Parameter estimation based on straight line analysis approaches: example of a constant rate test performed in the GAM shear zone.	58
Fig. 4.7:	Parameter estimation based on straight line analysis approaches.	60
Fig. 4.8:	Preferential hydraulic connections obtained by the analysis of storativity data from the constant injection tests (interpretation approach after Meier et al. 1998).	63
Fig. 4.9:	The 483 transmissivity zones forming the two-dimensional flow model with size $184 \times 184 \text{ m}^2$	65
Fig. 4.10:	Logarithm of transmissivity fields obtained by geostatistical inversion of data from RI1, RI2, RI3, RI4, RI5 and steady-state heads for different anisotropy ratios.	66
Fig. 5.1:	Layout of the tracer injection equipment.	69
Fig. 5.2:	Layout of the tracer extraction system.	70
Fig. 5.3:	Borehole locations and dipole configurations of the particle and solute tracer tests.	72
Fig. 5.4:	Uranine input concentration record during PT1. The concentration is given in parts per billion (ppb).	73
Fig. 5.5:	Combined solute and particle tracer test PT1.	74

Fig. 5.6:	Solute and particle tracer tests PT2 and PT3: Breakthrough curves of the solute and particle tracers at the extraction borehole.....	76
Fig. 5.7:	Geostatistical inversion of tracer tests PT1 to PT3.....	80
Fig. 5.8:	Geostatistical inversion of tracer tests PT4 and PT5.....	81
Fig. 5.9:	Longitudinal dispersivity as a function of θ	82
Fig. 5.10:	The ratio of the pre-asymptotic, $\alpha_L(\varepsilon)$, to the asymptotic longitudinal macrodispersivity, $\alpha_L(\varepsilon = 0)$, as a function of ε in two and three dimensions.....	83
Fig. 5.11:	Simulations in three fractures at different time steps (dimensionless time in terms of porevolume injected/PVI).....	84
Fig. 5.12:	Solute recovery curves at the extraction borehole as a function of dimensionless time ($\tau =$ mean arrival time).....	86
Fig. 5.13:	Solute recovery curves at the extraction borehole averaged over 20 realisations as a function of dimensionless time.....	87
Fig. 6.1:	Schematic illustration of the dissolution-diffusion mechanisms addressed.....	90
Fig. 6.2:	Layout of the borehole intersections with the GAM shear zone. The arrows indicate the dipole flow fields in which the gas tracer tests were carried out.....	92
Fig. 6.3:	Schematic view of the experimental layout.....	93
Fig. 6.4:	Ar, Xe, He and SF ₆ breakthrough curves recorded during GTT2 run#4: (a) log-log plots and (b) semi-log plots of the normalised gas concentrations.....	96
Fig. 6.5:	Ar, Xe, He, SF ₆ and H ₂ S breakthrough curves during GTT3: (a) run#8 with a gas injection rate of 75 ml(STP)/min and (b) run#9 with a gas injection rate of 300 ml(STP)/min.....	97
Fig. 6.6:	Quasi-steady-state gas saturation distribution for different fracture conceptual models.....	99
Fig. 6.7:	Effective gas saturation as a function of mass recovery at the extraction well for different realisations and conceptual models.....	101
Fig. 6.8:	Modelling of gas tracer test GT2 run # 4.....	104
Fig. 6.9:	Measured breakthrough curves, blind prediction and calibrated breakthrough curves for the four gas tracers used in Run#4 (Ar, He, Xe and SF ₆ respectively).....	107
Fig. 7.1:	Basic test arrangement during the brine and gas injection tests in the GAM shear zone: (a) 3-D view of the GAM site with the geophysical boreholes and (b) projection of the geophysical boreholes G1S-G5S and G4N on the shear zone plane.....	110
Fig. 7.2:	Configuration of the ground penetrating radar array. The borehole antenna is moved along boreholes G1S-G5S and G4N, respectively. The ground antennae have fixed positions at tunnel surface.....	111
Fig. 7.3:	Baseline radar measurements along borehole G2S on November 16 th (16:01): (a) stacked time section and (b) migrated time section.....	113
Fig. 7.4:	Georadar surveys during the brine injection test between November 15 and November 19, 1999.....	114

Fig. 7.5:	Baseline radar measurements along borehole G1S on January 31 st (16:01): (a) stacked time section and (b) migrated time section.	115
Fig. 7.6:	Georadar surveys during the gas injection test on February 1 – 4, 2000.....	117
Fig. 7.7:	Simulation of a time section in the reflection mode, using a simplified ray tracing approach:	118
Fig. 7.8:	Comparison measurement (coloured background) and calculations (white dots) for antenna in borehole G2S; the tunnel is indicated by the green dots, the shear zone by the yellow dashes.	119
Fig. 8.1:	Descriptive structural model of the GAM shear zone on different scales:	125
Fig. 8.2:	The descriptive structural model of the GAM shear zone forms the basis for the conceptual transport model. The three conceptualisations in the upper section were utilised for illustrating possible microstructural controls of macroscopic transport processes.....	126

1 Introduction

1.1 Background and scope

In deep underground disposal of radioactive waste, gas escape through the host rock formation is a key issue in the assessment of repository performance. In the post-operational phase, gas (mainly hydrogen, methane and carbon dioxide) will be generated in the emplacement tunnels due to anaerobic corrosion of metals and chemical and microbial degradation of organic substances. Gas production in the disposal area may affect the performance of the repository (cf. Figure 1.1):

- When the gas release rate is lower than the gas production rate in the emplacement tunnels, an unacceptable accumulation of gas could be generated in the tunnels. The resulting pressure build-up could have a negative effect on the barrier function of the host rock itself (opening of existing fractures, generation of new fractures) and on the engineered barrier system (e.g. failure of tunnel sealing).
- Gas overpressures in the emplacement tunnels could enhance expulsion of contaminated groundwater from the disposal area into the geosphere.
- Enhanced transport of radionuclides in the gaseous phase could take place along preferential pathways, leading to excessive activity in the biosphere.

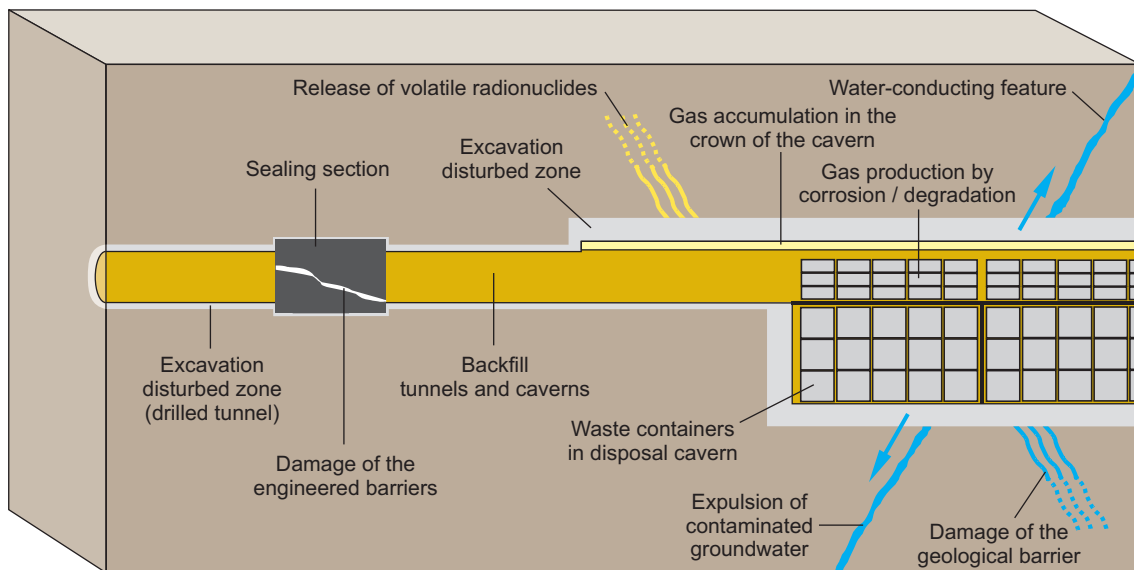


Fig. 1.1: Schematic representation of an emplacement cavern for low-level waste.

In fractured hardrock such as granite or indurated sedimentary rock in tectonic regimes, gas transport from the emplacement tunnels through the geosphere occurs preferentially along discrete water-conducting features (e.g. shear zones). Gas transport in these water-conducting features is a two-phase flow process; the continuity and spatial distribution of pore spaces ("heterogeneity"), the pore size distribution and the interfacial forces of the three phases gas-water-rock have a significant influence on gas transport. Gas transport in a shear zone is focused along those channels with the highest transmissivity and aperture.

To date, quantitative description of gas transport in fractured formations has not yet been accomplished in a satisfactory way. The main difficulties to be resolved when simulating two-phase flow processes in fractured rock are:

- description of the internal heterogeneity of the individual water-conducting features. The influence of channelling along preferential flow paths is even more pronounced than for single-phase fluid flow, because gas transport takes place more or less exclusively along the most transmissive channels. Due to capillary forces, channels with small pore sizes are occupied by the wetting fluid (water).
- determination of effective mass exchange coefficients of the relevant components of the system. Mass exchange may occur between all three phases (gas-water-rock). It depends on the spatial distribution of water and gas along the water-conducting features (i.e. specific surfaces of the contact areas liquid-solid, liquid-gas, gas-solid) and on the solubilities and diffusivities of the different components (based on Henry's law, Fick's law), but also on state variables of the liquid phase (initial content of dissolved/free gas, initial pressure).
- assessment of network effects due to the intersection of different water-conducting features.

1.2 Expectations of the agencies

The experiment 'GAs Migration in Shear Zones' (GAM) was an international research project carried out at the Grimsel Test Site (GTS) within the framework of Investigation Phase V (1997 - 2004). Four radioactive waste management organisations participated in the GAM experiment, namely ANDRA, ENRESA, NAGRA and Sandia National Laboratories (SNL) for the US Department of Energy (DOE). The experiment team consisted of 15 members, including delegates of the participating organisations and research groups from the Swiss Federal Institute of Technology / Zurich and from the Technical University of Catalonia / Barcelona.

Participation of the organisations in the GAM experiment was motivated by a common interest in basic research in the field of multi-phase transport mechanisms in fractured hard-rock. Beyond this, each organisation placed emphasis on specific aspects in the context of their national waste disposal programmes. A short summary is given below.

ANDRA

In the context of the field investigations, ANDRA intended to extend the gas tracer tests to at least one different time and length scale. The work was carried out in collaboration with the field contractor of the previous gas tracer tests and a French company. This arrangement allowed training French experimentalists, while ensuring consistency between the previous data and the data from the extended test(s).

ANDRA interests in modelling / interpretation focused on two-phase flow and property modelling aspects on different scales. The aim of the work was to model two-phase compositional flows within the shear zone (fracture) on a very fine scale where the different materials (e.g. matrix, channels, gouges) will be represented. Scaling-up aspects were also studied to derive two-phase flow properties suitable for simulating the experiments on coarser scales. The upscaling of two-phase flow included the simulation of the gas tracer tests. Different codes of stochastic simulation, multiphase flow simulation and two-phase flow property upscaling were applied for the fine scale modelling of flow and transport in the shear zone.

ENRESA

In the Spanish concept for geological disposal of HLW in granitic rock, the generation of gas by anaerobic corrosion of steel canisters is the most important source of gas production. If the repository is saturated when canister failure occurs, hydrogen will be produced from the reaction of iron with water. In an initial stage, hydrogen production and water intrusion will occur simultaneously. Once the hydrogen pressure is higher than the hydrostatic pressure, the resulting gas outflow might mobilise radionuclides, open preferential pathways in the host rock and degrade the buffer material.

In early 1998, the so-called ENRESA 2000 project was launched to assess the performance of the above-mentioned repository in granite. Through participation in the GAM project, ENRESA aimed to obtain a detailed understanding of multi-phase flow processes and their correct conceptualisation and modelling by validating the BRIGHT code (Olivella et al. 1996) against a reliable, high-quality, in-situ data set.

Nagra

Nagra's interest in the GAM experiment is strongly related to the performance assessment (PA) issues of groundwater flow and gas-related processes in a L/ILW repository in a fractured host rock. The models developed to assess the performance of the planned repository require (i) an appropriate conceptualisation of groundwater flow and two-phase flow processes in the host rock and (ii) upscaled hydraulic and two-phase flow parameters on the site scale. The GAM experiment is expected to provide important input for the validation of such models.

For the investigation of gas-related phenomena in the previous Wellenberg project, a process model was developed to simulate the different phases of the repository evolution (Senger et al. 1998). These include: (i) the construction / operation phase resulting in desaturation of the host rock due to the pressure decrease and ventilation in the caverns, and (ii) the post-closure phase after backfilling and sealing of the caverns resulting in resaturation of the host rock and the caverns and in the release of waste-generated gas. For both periods, determination of effective hydraulic and two-phase flow parameters of the host rock on the hectometre scale is critical for the assessment of the repository concept. Reliable conceptualisations of two-phase flow processes and upscaling procedures for the parameters acquired within the framework of site characterisation are required as input for the process model.

Numerical simulations of regional groundwater flow at the Wellenberg site were based on a stochastic model of the hydraulic conductivity distribution in the host rock (Wellenberg K-model, cf. Marschall et al. 1998b). In the Wellenberg K-model, effective hydraulic conductivities have been determined on a hectometre scale, based on the hydraulic characterisation of the water-conducting features in the investigation boreholes at the site. The effective parameters are derived by upscaling local hydraulic conductivity measurements using fracture network models on the block scale (Lanyon et al. 1997). An important input parameter for this upscaling procedure is knowledge of the so-called channelling factor, a quantity which describes the internal heterogeneity of the water conducting features. It is expected that the present investigations will provide input for the conceptual understanding of channelled flow in fractures.

Sandia National Laboratories for US Department of Energy

The Waste Isolation Pilot Plant (WIPP) project in the United States has embarked on an International Research and Development programme. The overall objectives of this programme are to (i) provide focused development of mutually beneficial cooperative projects and technical

exchanges that will drive advances in areas of common scientific interest and (ii) help ensure that international technical developments are appropriately considered in iterative WIPP recertifications. Specific scientific disciplines that have been identified as important for assessing the future behaviour of the WIPP repository include two-phase flow testing and analysis (DOE/CAO International Research and Development Plan). WIPP technical objectives for participating in the GAM project include development and testing of quantitative experimental and modelling tools for assessing multi-phase fluid flow in relatively tight, fractured rocks. Multi-phase fluid flow in anhydrite interbeds plays an important role in fluid flow between the WIPP repository and the surroundings host rock. Fractures within these interbeds are the primary fluid-conducting features. Brine inflow to repository excavations, brine and gas outflow due to waste-generated gas and fluid migration from petroleum drilling operations beyond the site boundaries towards WIPP are all fluid flow scenarios that are important for future recertification assessments for WIPP; all of them involve multi-phase flow through relatively tight, fractured rock. Through participation in the GAM experimental programme, the WIPP project will contribute to, and benefit from, the collaborative development of experimental and multi-phase model assessment technologies that will extend beyond currently available technology.

1.3 Report outline and authors

The GAM technical team (GAM experiment team plus associated contractors) formed a group of more than 30 members, including experiment delegates, research groups and associated contractors. Within the framework of the 7th GAM experiment team meeting in Paris (June 9 – 10, 2000), the structure of the final project report was elaborated and the teams of contributing authors were nominated. It was agreed to subdivide the report into 8 chapters with 5 technical sections (Chapters 3 – 7). The teams of authors of the different chapters are given in alphabetical order in Table 1.1. The compilation and final editing of the report was jointly performed by Ivan Lunati and Paul Marschall.

The GAM project report references a multitude of internal project documents, which were elaborated in the course of the experiment. A complete list of internal GAM project documents is found in Marschall (2006).

Tab. 1.1: Report outline and list of authors

Chapter	Authors
Chapter 1: Introduction	N. Brodsky ⁸ , M. de Combarieu ² , P. Marschall ⁷ , J.C. Mayor ⁴ , P. Meier ²
Chapter 2: The GAM experiment - concept and experiment programme	I. Lunati ^{3,5} , P. Marschall ⁷
Chapter 3: Laboratory investigations of core samples	N. S. Brodsky ⁸ , J. T. Fredrich ⁸ , P. Marschall ⁷ , J. C. Stormont ¹⁰ ,
Chapter 4: Hydraulic characterisation of the shear zone	J. Carrera ¹¹ , J. Jodar ¹¹ , W. Kinzelbach ⁵ , I. Lunati ^{3,5} , P. Marschall ⁷ , P. Ramajo ¹¹ , T. Trick ⁹
Chapter 5: Solute and particle tracer tests	S. Attinger ⁵ , J. Carrera ¹¹ , M. Garcia ⁶ , J. Jodar ¹¹ , K. Kennedy ⁷ , W. Kinzelbach ⁵ , I. Lunati ^{3,5} , J.C. Mayor ⁴ , P. Ramajo ¹¹ , T. Fierz ⁹
Chapter 6: Gas tracer tests	S. Attinger ⁵ , J. Carrera ¹¹ , T. Fierz ⁹ , M. Garcia ⁶ , J. Jodar ¹¹ , K. Kennedy ⁷ , W. Kinzelbach ⁵ , I. Lunati ^{3,5} , J.C. Mayor ⁴ , P. Ramajo ¹¹
Chapter 7: Geophysical surveys	I. Lunati ^{3,5} , P. Marschall ⁷
Chapter 8: Synthesis and conclusions	P. Marschall ⁷
¹ Albert-Donié Geo-Consult, Wettingen, Switzerland ² Andra, Paris, France ³ EPFL, Laboratory of Soil and Environmental Physics, Lausanne, Switzerland ⁴ Enresa, Madrid, Spain ⁵ ETH- Swiss Federal Institute of Technology, Zürich, Switzerland ⁶ FSS International, Chaville, France ⁷ Nagra, Wettingen, Switzerland ⁸ Sandia National Laboratories, Albuquerque, New Mexico ⁹ Solexperts, Schwerzenbach, Switzerland ¹⁰ University of New Mexico, Albuquerque, New Mexico ¹¹ UPC - Technical University of Catalonia, Barcelona, Spain	

2 The GAM experiment – concept and experiment programme

2.1 Aims and concept

Quantitative description of solute and gas transport in fractured formations is still a topic of basic research. The main difficulties to be resolved when simulating multi-phase flow processes in fractured rock are (i) the description of the internal heterogeneity of the individual water-conducting features, (ii) the determination of effective mass exchange coefficients of the relevant components of the system and, finally, (iii) the assessment of network effects due to the intersection of different water-conducting features. The GAM experiment gave emphasis to the first two items, namely assessment of heterogeneity and mass transfer in a single fracture. The investigation of fracture network effects was beyond the scope of the project. The specific objectives of the GAM experiment were:

- development / evaluation of advanced site characterisation methodologies for investigation of solute and gas transport in fractured rock. Special focus was placed on visualisation of flow channelling on the laboratory and field scales (internal heterogeneity of shear zones),
- development and validation of upscaling procedures and derivation of effective parameters for single- and two-phase flow processes in fractured media,
- development of consistent conceptual and numerical models for (single-phase) solute and gas transport.

The experiment was launched as an integrated research project on solute, particle and gas transport in a single fracture, which is characterised by a heterogeneous internal structure (shear zone). The experiment concept consists of four elements: (i) solute, particle and gas tracer tests in a shear zone of the GTS, (ii) visualisation of the in-situ tracer experiments using high frequency ground-penetrating radar techniques, (iii) laboratory experiments with core samples and, finally, (iv) integrated interpretation of laboratory and field results.

Tracer tests in the GAM shear zone

The field investigations were carried out in a section of the GAM shear zone which is approximately 4×6 m and has been characterised by a total of 20 boreholes (see section 2.2). The field investigation programme consisted of hydraulic single-hole and crosshole tests, gas threshold pressure tests and tracer tests with a set of complementary tracers. Non-sorbing solute tracers in combination with particle tracers (micro-spheres, phages, nano-spheres) and gas tracers (He, Xe, Ar, SF₆) have been used because their different migration behaviours permit investigation of different domains within the multi-porosity shear zone structure (Fig. 2.1). Particle tracers are focused on the main flow channels, showing no diffusion into the matrix or stagnant pores. Non-sorbing solute tracers are governed by advection-dispersion processes and respond to the entire system of connected porosity. Finally, a gas phase predominantly migrates along those flow channels with large pore radii. In addition, rates of mass transfer of the gas tracer across the gas/water interface are specific to each gas tracer and to the flow path.

In-situ visualisation of flow paths

In-situ visualisation of flow paths during solute and gas tracer testing was another key aspect of the GAM experiments. For this purpose, a series of boreholes was drilled parallel to the GAM shear zone at a distance of 1 m (Fig. 2.2). Radar reflection and transmission measurements were conducted in these boreholes using a high frequency borehole probe, combined with several

surface probes, positioned at the tunnel surface. Radar surveys were carried out before and during tracer testing (solute tracer tests with brine and gas injection tests with nitrogen). The spread of the injected tracer plume was inferred from amplitude differences in the transmission / reflection traces between a zero measurement (prior to tracer injection) and the subsequent surveys during injection.

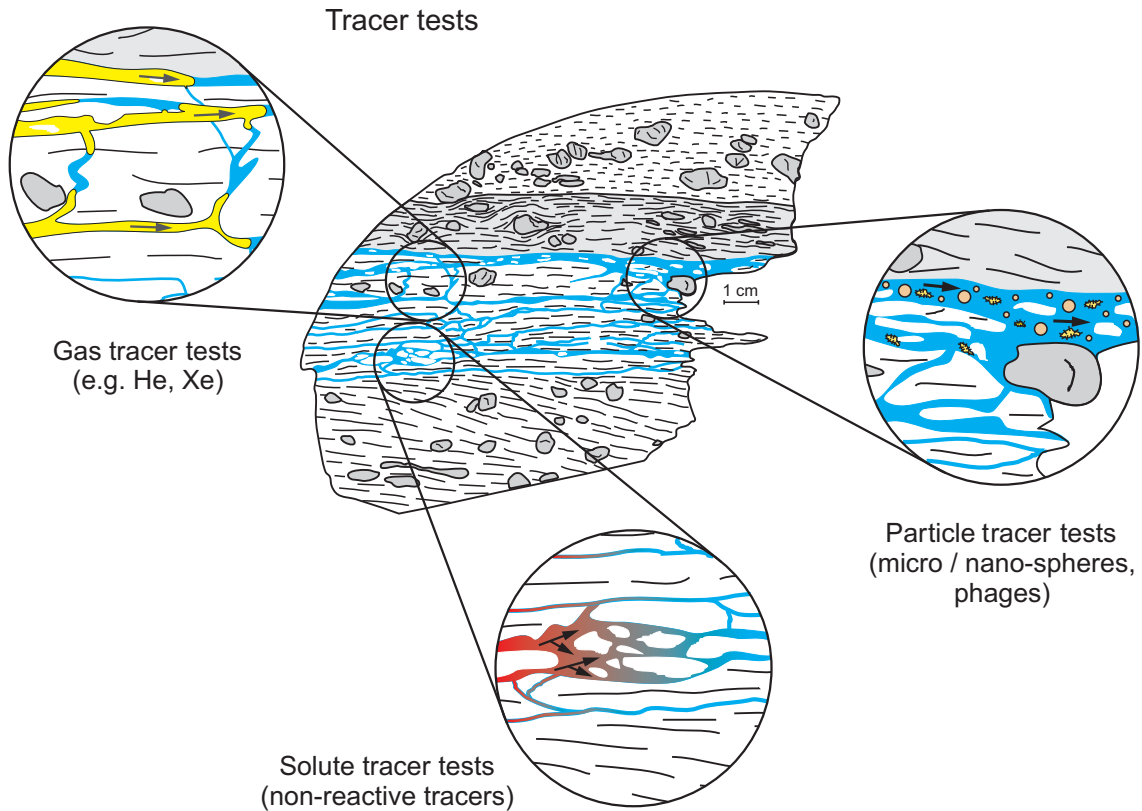


Fig. 2.1: GAM tracer test programme – experiment concept.

The internal structure of the GAM shear zone is made up of a complex system of flow channels of variable size and extent. Solute tracers, gas tracers and particle tracers explore different domains of the multi-porosity shear zone structure.

Laboratory studies

The laboratory tests were focused on three issues: (i) development of new coring techniques to recover undisturbed shear zone samples, (ii) material property tests (porosity, permeability, two-phase flow parameters), and (iii) visualisation of pore spaces and of transport processes in a shear zone sample. The impact of microstructural properties (size and connectivity of flow channels on the microscopic scale) of the shear zone samples on macroscopic transport properties (intrinsic permeability, accessible porosity) was highlighted.

Integrated interpretation and modelling

The integrated interpretation of the GAM field and laboratory studies included development of comprehensive conceptual models of solute / gas migration in heterogeneous shear zones. As part of these conceptual models, constitutive relationships between microstructural properties

and microscopic flow and transport parameters (e.g. permeability-porosity relationships) were a key issue. Analytical and numerical tools for upscaling of flow and transport properties were developed (core scale to experimental scale).

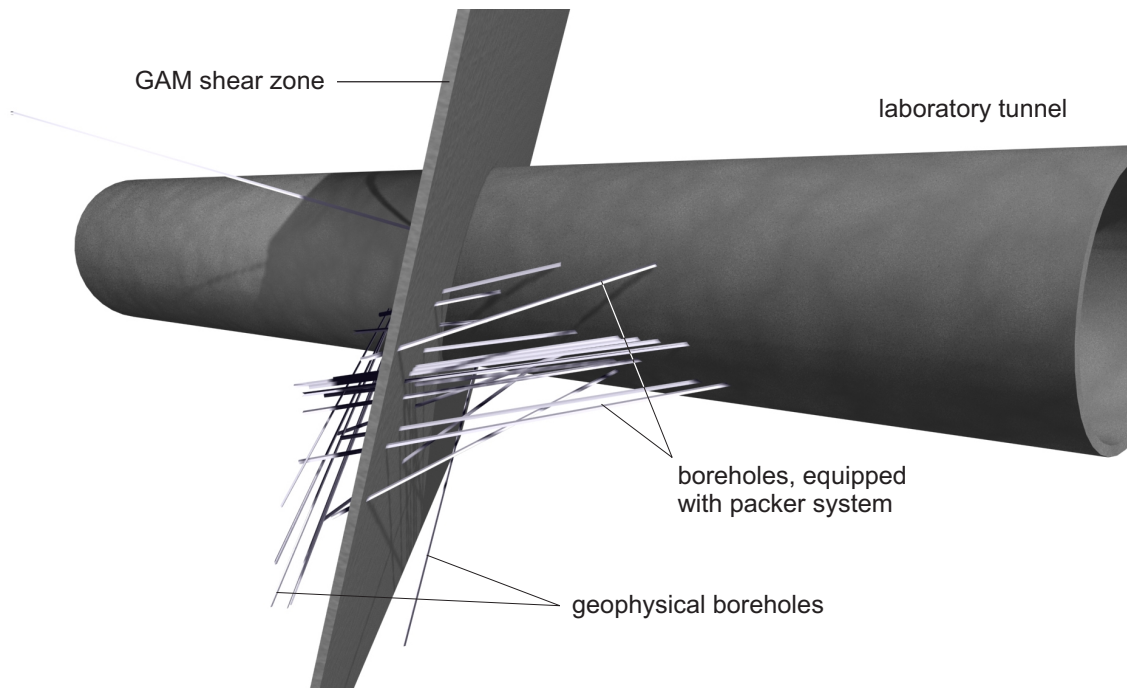


Fig. 2.2: GAM – experimental set-up at the Grimsel Test Site.

On the site scale, the GAM shear zone is a quasi-planar structure that has been explored by a total of 20 boreholes. A fan-like array of boreholes was drilled parallel to the shear zone at a distance of 1 m.

2.2 The GAM experimental site

The GAM experimental site is located in the AU tunnel in the southern part of the GTS. The GAM shear zone (formerly called the FRI shear zone) is a subvertical feature with an extent of at least several decametres – fractured traces of the shear zone were mapped not only in the AU tunnel but also in the main access tunnel and in the VE tunnel. In the AU tunnel, the GAM shear zone can be represented by a planar feature, striking at an azimuth of 141.5N and dipping at 71°. The intersection point at the floor of the AU tunnel is at TM144.2 m (for details see project document GAM-28 / Marschall, 2006).

Geological setting of the GTS

The GTS in the Central Swiss Alps is located in the southern part of the Central Aar Massif, around 400 m below ground surface. The rocks in this area are almost exclusively granitic, the northern part of the GTS being located in Central Aare granite and the southern part in the Grimsel granodiorite. The age of solidification of the granites is approximately 290 – 300 Ma; subsequently the rocks were intruded by sets of lamprophyres and aplites (250 Ma ago).

The whole Aar Massif was subjected to strong alpine deformation and metamorphism. The dominant overprinting of the rocks occurred some 20 – 25 Ma ago, associated with ductile

deformation, indicated by a cleavage of variable intensity (orientated NE - SW), by ductile shear zones and mylonites.

During the following uplift (which is still ongoing) and subsequent cooling, the deformation changed from ductile to brittle behaviour, resulting in fractures and fault breccias. Brittle deformation concentrated along the old cleavage planes, NE-SW striking shear zones and along the lamprophyre / granite contacts. At present, these brittle structures represent the main groundwater flow paths at the site. A comprehensive overview of the geology of the GTS is given in Keusen et al. (1989).

In the central and the southern parts of the GTS, the frequency of discontinuities is significantly lower than in the northern part, the dominant rock type changing from a slightly deformed homogeneous Central Aare granite to Grimsel granodiorite. Brittle structures are linked to the ductile shear zones, largely parallel to the cleavage. The shear zones in the southern part of the GTS have been characterised in great detail by Majer et al. (1990), Bossart & Mazurek (1991) and Vomvoris & Frieg (1992).

Geology of the GTS shear zones

Most of the shear zones in the southern part of the GTS (MI shear zone, GAM shear zone, VE shear zone) exhibit a similar structure. The features are steeply dipping and the strike is predominantly NE-SW. Macroscopically, the shear zones are characterised by:

- zones of ductile deformation with a thickness ranging from decimetres (e.g. MI zone) up to 10 m (VE shear zone). The ductile zones are generally characterised by high cleavage intensity with mica-rich mylonite bands. Most of the shear zones have extents of decametres up to hundreds of metres.
- Brittle fault breccia horizons with a thickness of a few millimetres to 1 cm and more. The fault breccia horizons are located in the zones of greatest ductile deformation, with an orientation parallel to the cleavage. They contain fine-grained, cohesionless gouge material. Frequently, several more or less parallel fault breccia horizons with undulating shape are observed. Fault gouge horizons may either intersect each other or are connected by fine channels along grain boundaries or sheet silicates.

The porosity of the fault gouge horizons is estimated at 10 - 30 vol %, although has never been measured at the laboratory (Bossart & Mazurek 1991). Recent studies as part of the TPF experiment (Marschall et al. 1998, Croisé et al. 1998) showed that the aperture distribution across the brittle structures is typically described by a log-normal distribution with mean values of about 0.2 - 0.5 mm and a cumulative thickness in the cm range.

The porosity of the ductile part of the shear zones is comparable to matrix porosity (typically < 1 %).

As verified by hydrotests and tracer tests, the flow paths along the shear zones are well connected over distances of decametres. Interconnections in the range of hecto- to kilometres are considered likely. The connectivity to the rock matrix along both sides of the shear zones is weak but, nevertheless, detectable.

The average transmissivity values of the different shear zones are highly variable. This is also true for the internal transmissivity distribution along the shear zones. Meier et al. (1998) analysed a set of hydraulic tests in the MI shear zone. Point measurements of transmissivity ranged from 1×10^{-10} to 5×10^{-6} m/s. The geometric mean was in the range $2 - 4 \times 10^{-7}$ m²/s.

Hydrotests in the GAM zone as part of the TPF and GAM experiments (Marschall et al. 1998a, Gemperle 1999a, b) showed point values in the range 7×10^{-11} to 1×10^{-9} m²/s, with a geometric mean of $2 - 5 \times 10^{-10}$ m²/s.

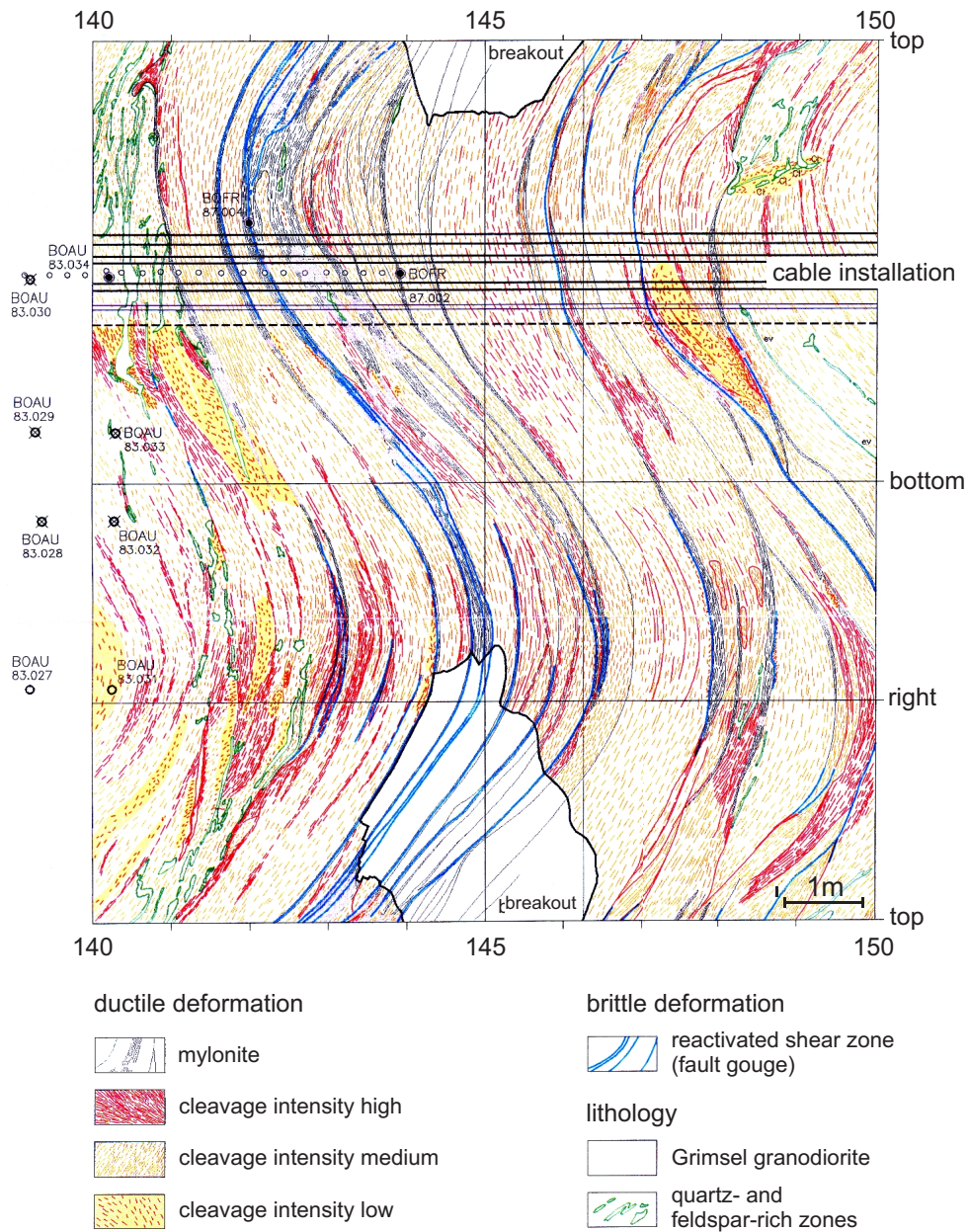


Fig. 2.3: Tunnel map of the GAM site in the AU tunnel after Wyss (1996). The blue structures represent the reactivated shear zones which are (partly) filled with fault gouge.

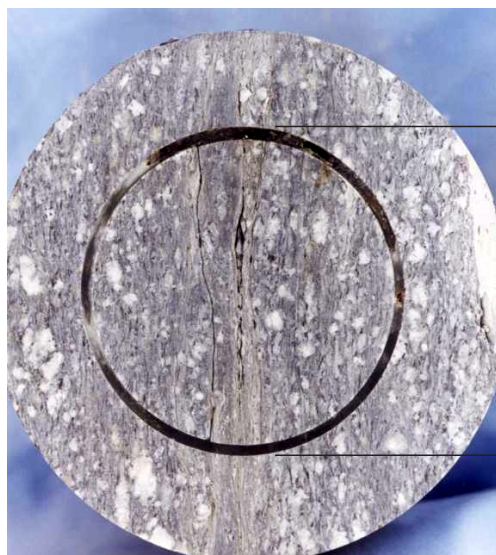
The GAM shear zone

The GAM shear zone is oriented parallel to the regional cleavage trend. It dips sub-vertically towards the SE and its thickness varies between 1.00 and 3.50 m. The mapped lithologies and structures are shown in Figure 2.3. A clear distinction can be made between ductile and brittle structures:

- ductile type of deformation (alpine greenschist metamorphism and development of the regional cleavage) characterised by structures such as the cleavage, granitic mylonites with quartz ribbons, mineral stretching lineations, extension veins and quartz recrystallisation. The porosity and hydraulic conductivity of the ductile structures are both very low ($n < 1\%$, $K \approx 1 - 5 \times 10^{-12}$ m/s).
- subsequent brittle type of deformation (post-metamorphic regional uplift), forming a fracture network which is filled with fault gouge material. In the GAM shear zone, 2 to 6 fractures filled with fault gouge material can be observed (Fig. 2.3, blue traces). Some of the fault gouge horizons, ranging from a few tenths of mm to a maximum of 0.5 mm in width, can be traced over the whole tunnel cross-section. The small-scale mapping also demonstrates that these diverging fractures may merge to 1 – 2 fractures, resulting in an interconnected fracture network. This connectivity may further be enhanced by the flat-lying extension veins, which have undergone brittle reactivation or are only partially mineral-filled.

In the GAM shear zone, three brittle structures were detected, which can be followed more or less continuously over the entire tunnel cross-section (see Figure 2.3). These three major features are approximately 0.6 m apart from each other and were hit in most of the GAM boreholes (see section 2.3). The one in the middle was selected as the target feature for the GAM experiment, because it showed the highest transmissivities and good spatial continuity. As part of the GAM site characterisation programme, core samples were taken from the shear zone (project documents GAM-18, GAM-24, GAM-35&36 / Marschall 2006) and high resolution imaging tools (EPIBS) for logging the boreholes (BLM 1999). The small-scale variability of this structure is remarkable: Figure 2.4 shows a high resolution image of the borehole wall in borehole GAM 98-02 and an 8-inch core, which was drilled along the target feature (cf. section 3.1).

Core sample



Borehole image

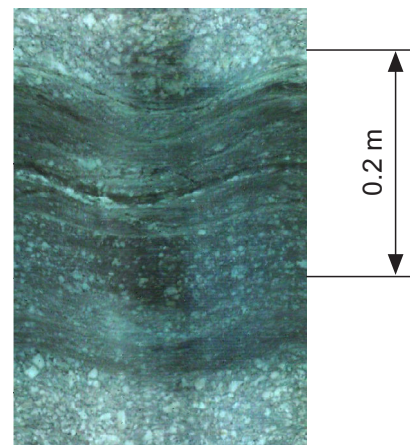


Fig. 2.4: (left) Core sample CoGAM98-001 comprising several brittle structures that are filled with fault gouge material, (right) GBIPS borehole image of borehole GAM98-02 (detail of the shear zone section).

2.3 Instrumentation of the site

Geoscientific investigations have been carried out at the GAM site (formerly FRI / TPF site) since 1984 (Majer et al. 1991, Marschall & Croisé 1999). To date, the GAM shear zone has been characterised by a total of 20 boreholes. Most of the boreholes are oriented subhorizontally with a diameter of 86 mm or 35 mm, respectively (project document GAM-28; cf. Marschall, 2006), intersecting the GAM shear zone at some distance along the hole. Figure 2.5 shows the intersection points of these boreholes with the plane of the shear zone. A fan-like array of boreholes was drilled parallel to the shear zone at a distance of about 1 m from the target structure (5 boreholes to the south, 1 borehole to the north). These boreholes were used in the course of the radar surveys for logging the site with the borehole antenna. Orientations, diameters and lengths of all boreholes are documented in the GAM project documents GAM-28- and GAM-25 (Marschall 2006).

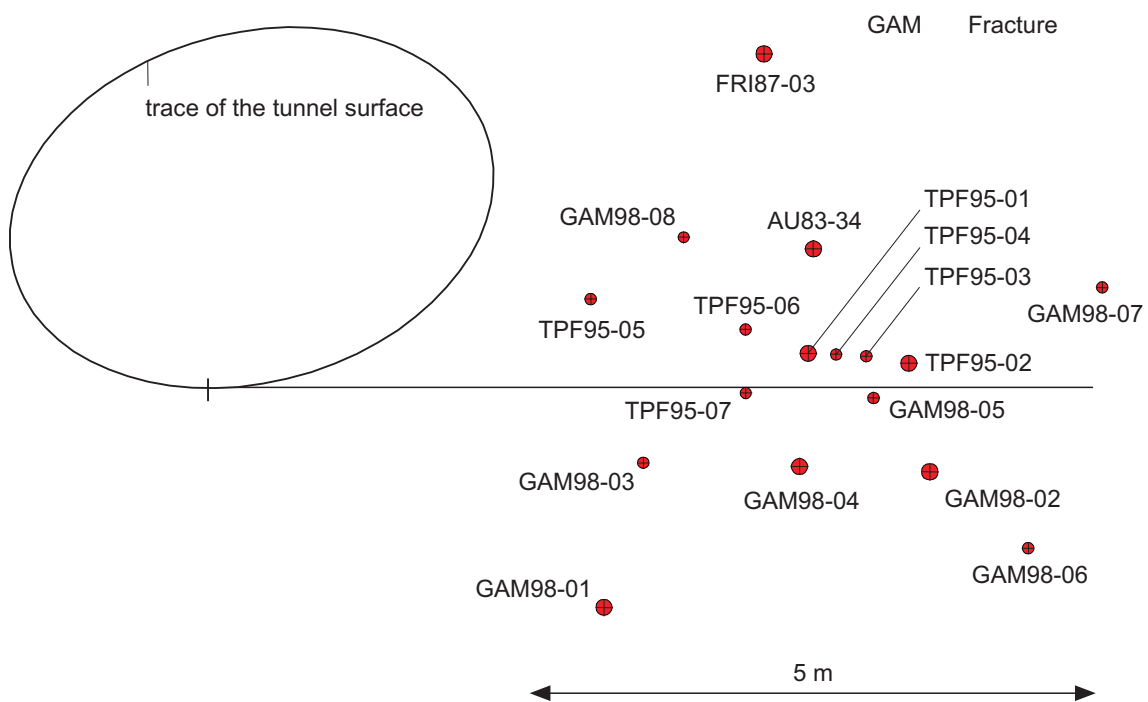


Fig. 2.5: The location of the GAM boreholes in the plane of the GAM shear zone.

After drilling, all boreholes except the geophysical boreholes were equipped with single- or multi-packer systems, aimed at hydraulic separation of the GAM shear zone. Three types of packer systems were used:

- conventional hydraulic single- and multi-packer systems (FRI87-01 and -03, FRI89-01, GAM98-01)
- mechanical single-packer systems (AU83-34)
- hydraulic triple-packer systems (borehole diameter 86 mm), specially designed for gas injection tests. The middle interval (interval 2) has a fixed length of 36 cm and the interval volume is as low as ≈ 0.5 l. Each packer module is controlled individually through independent control lines. Each interval has both a pressure measurement line and a fluid injection line. Water is used as an inflation medium for long-term measurement applications.

- mechanical mini-packer systems (borehole diameter 35 mm) comprising a mechanical double-packer system with a fixed length 40 cm straddle. The 40 cm straddle is designed to isolate the shear zone. A third mechanical packer is added to the instrument string at the borehole mouth to isolate the matrix interval (I3). No measurement lines are connected to the I3 interval. Interval I2 has both a pressure measurement line and a fluid injection line. Interval I1 has only a single pressure line.

A detailed description of the borehole instrumentation is given in Gemperle (1999a).

2.4 GAM investigation programme

The GAM experiment, as an integrated research project, closely links the experimental work on the laboratory and field scale with an extensive data analysis and interpretation task. The investigation programme was sub-divided into the following scientific tasks:

- Laboratory studies with core material from the GAM shear zone, such as material property tests and flow visualisation experiments (chapter 3)
- In-situ programme in the GAM shear zone, comprising hydraulic crosshole tests (chapter 4), single (liquid) phase tracer tests with solutes and particles (chapter 5) and, finally, gas tracer tests (chapter 6)
- Geophysical surveys of the shear zone during the tracer experiments (chapter 7)
- Integrated interpretation of laboratory and field experiments (chapter 8)

3 Laboratory investigations of core samples

There is multiple evidence that flow and transport processes in the GAM shear zone are strongly affected by the microstructural characteristics of the brittle deformation structures (Figure 2.3) – determining factors are the spatial variability of fracture aperture, the interconnectedness of the brittle features and the fracture infill. Characterisation of the microscopic heterogeneity of the reactivated shear zone was therefore the focus of the laboratory investigations, together with fundamental laboratory experiments of transport processes in heterogeneous fractures. In this context, recovery of undisturbed rock samples turned out to be an indispensable prerequisite for reliable property tests on core samples. The GAM laboratory programme consisted of the following sub-tasks:

- Recovery of undisturbed core samples from the GAM shear zone (section 3.1)
- property tests on core samples from the GAM shear zone (section 3.2). Special emphasis was given to porosity and permeability (gas and water permeability, relative permeability)
- visualisation of the three-dimensional microgeometry of the pore structure (section 3.3)
- visualisation of single- and two-phase flow transport processes through replicas of heterogeneous fractures (section 3.4).

3.1 Development of core recovery techniques

3.1.1 Core drilling campaigns in the GAM shear zone

A total of 6 core drilling campaigns were conducted as part of the GAM laboratory programme, complemented by a drilling campaign that had been carried out within the framework of the previous TPF experiment (Fischer et al. 1998). All cores were drilled from the tunnel surface parallel to the shear zone plane. The purpose of the drilling campaigns was (i) to improve the drilling and core recovery techniques and (ii) to provide core samples for Sandias's property test programme. Table 3.1 presents an overview of the drilling campaigns and Figure 3.1 shows a tunnel map with the location of the core samples. Further information can be found in the internal project documents GAM-12, GAM-21, GAM-24, GAM-35 and GAM-36 (Marshall, 2006).

3.1.2 Recovery of CoGAM98-001 and CoGAM98-002

Core recovery was carried out at the GAM site from January to February 1998. Two cores, both cored parallel to the shear zone, were recovered. The core recovery technique was innovative in that after an approximately 100 mm diameter core had been drilled, it was not broken off from the host rock. Instead, the annulus between the core and the rock matrix was filled with an epoxy resin to protect the inner core. After the resin hardened, the sample was overcored using a 200 mm diameter core barrel and then broken off. For CoGAM98-001, the inner subcore was 400 mm in length and drilled using fresh water as the drilling fluid. CoGAM98-002 was drilled in a similar manner to CoGAM98-001, but was dry drilled to prevent flushing of the fault gouge, and the inner core was only drilled to a depth of 150 mm before the annulus was filled with epoxy resin. CoGAM98-002 intersected a previous borehole. During drilling of the annulus, the previous borehole very likely provided a pathway for removal of drill cuttings and thereby facilitated the coring operation.

After the overcores were broken off, the cores were placed in plastic containers and covered with epoxy resin for protection during shipping. The shipping boxes were damaged, but the epoxy resin protected the core. The epoxy was very difficult to remove from the core, except where duct tape had been applied to the specimen surfaces.

Tab. 3.1: Core drilling campaigns for property tests in the GAM shear zone.

Core ID	Date of recovery	Length (m)	Diameter (mm)	Reference	Remarks
CoTPF95-002	Sept. 95	0.50	107	Fischer et al. (1996)	Overcoring technique
CoGAM98-001	Jan. 98	0.40	170 subcore: 102	- GAM 12 - - GAM 21 -	Wet drilling, overcoring technique (Sandia's property tests)
CoGAM98-002	Feb. 98	0.40	170 subcore: 102		Dry drilling, overcoring technique (Sandia's property tests)
CoGAM98-003	Aug. 98	0.40	220	-	Test sample: matrix
CoGAM98-004	Oct. 98	0.43 – 0.59	146 subcore: 109	- GAM 24 -	Modified overcoring technique (Sandia's property tests)
CoGAM98-005	Oct. 98			- GAM 36 -	Modified overcoring technique (ETH particle tracer test)
CoGAM99-001	Mar. 99	0.35 – 0.45	150 subcore: 99	- GAM 35 -	Modified overcoring technique (NMR tests by ETH)

3.1.3 Laboratory specimen preparation

For CoGAM98-001, the inner subcore appeared to have been damaged during drilling of the annulus. Pre-existing fractures were opened and epoxy resin filled some interior fractures (Fig. 3.2 left). CoGAM98-002, which had been dry drilled and had intersected a pre-existing borehole, showed no noticeable infilling of epoxy from the annulus (Fig. 3.2 right).

Initially, an attempt was made to subcore 38 mm diameter samples of the shear zone from CoGAM98-002 by dry drilling. This damaged the core and core barrels. Dry sawing with a wire saw similarly damaged the wire. Subcore damage included the opening of fractures due to heat and vibration. Attempted improvements to the coring procedure included:

- Using dry ice as a coolant. This only induced further cracking.
- Using helium gas as the coolant because it is able to better penetrate the rock. This approach met with some success.
- Using a segmented core barrel, i.e. one in which the tip is composed of 3 - 4 segments separated by 3 mm spaces. The spaces facilitated the flow of coolant and improved the coring operation.
- Using small diameter (6.35 - 9.53 mm) masonry bits to perforate the annulus before coring (see Figure 3.3). This resulted in less material for the core barrel to remove and additional pathways for the removal of drill cuttings. It therefore improved the coring procedure.

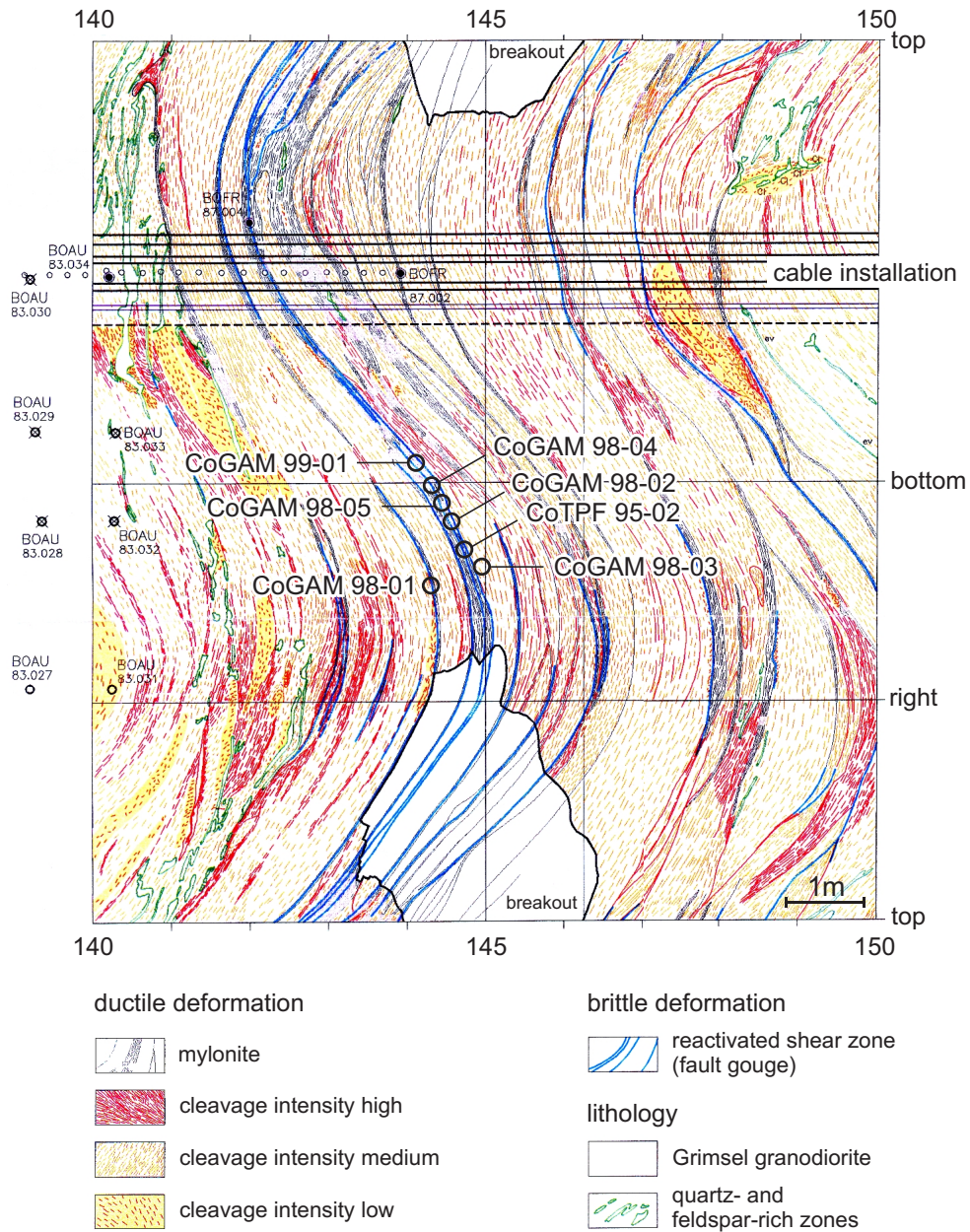


Fig. 3.1: Tunnel map with the location of the core samples.

Coring proceeded using the last 3 modifications simultaneously. Helium gas was used as the coolant while drilling a pre-perforated annulus using a segmented core barrel. With these techniques, core samples were successfully obtained outside the fracture zone for measurements of matrix properties and pore geometry. Within the shear zone, however, the rock became further damaged during coring even when all techniques were used simultaneously. It was then decided to use the inner subcores from both cores as porosity and permeability test specimens (cf. chapter 3.2).

The inner subcores were made into test specimens as follows:

1. Flat ends were sawed perpendicular to the core axes, forming the top and bottom of the test specimens.

2. A hole was drilled through the epoxy annulus parallel to the core axis. The specimen was placed on a table saw and the saw blade was fed through the hole. The saw blade was then reattached to the table saw.
3. The specimen was carefully rotated and the saw blade cut through the epoxy annulus, freeing the central core.



Fig. 3.2: Photograph of (left) CoGAM98-001 showing open epoxy-filled fractures within inner core and (right) CoGAM98-002 showing no noticeable coring-induced damage. Lower left shows core removal by previous borehole.

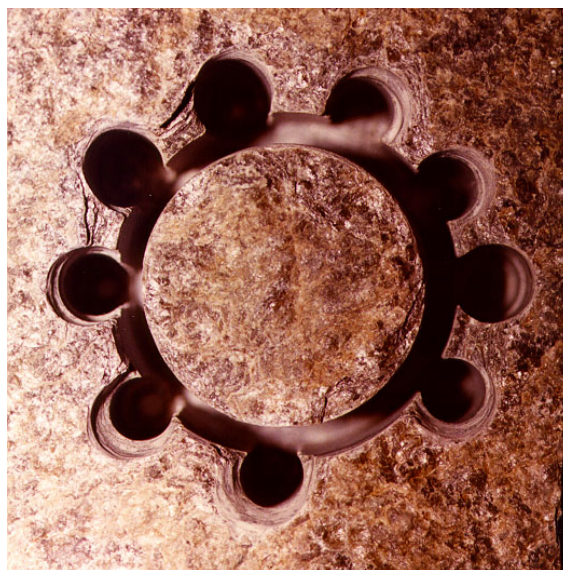


Fig. 3.3: Illustration of subcoring technique. Small diameter holes were used to perforate the annulus before coring.

3.1.4 Application of the improved core recovery technique

Based on Sandia's experience with tests on laboratory specimen preparation, a modified core drilling technique was adopted for the cores CoGAM98-003 to 98-005 and CoGAM99-001. A comprehensive description of the drilling procedure is given in the internal project documentation GAM-35 (Marschall, 2006). Here is a brief summary of the main steps:

- use small diameter (32 mm) masonry bits to perforate the annulus before coring. A total of 8 holes is realised by percussion drilling in a circular arrangement (cf. Figure 3.4).
- fill the small diameter boreholes with resin
- after hardening of the resin, drill the inner annulus with a 4-inch core barrel. A minimum amount of fresh water is used for cooling of the drill bit
- fill the inner annulus with resin
- after hardening of the resin, overcore the inner sample with a 6-inch core barrel
- break and recover the core

The modified drilling procedure was successful, providing excellent specimens without visible disturbances. In particular, no invasion of drilling fluid into the brittle structures was observed, which could have washed out the fault gouge material. Moreover, the core samples did not break apart along the fault gouge horizons as had happened with conventional core recovery techniques. The orientation of the drilling machine turned out to be the most difficult part of the drilling procedure, because the dip of the individual fault gouge horizons showed local variations. Hence, some of the specimens were not drilled exactly parallel to the fault gouge horizons.

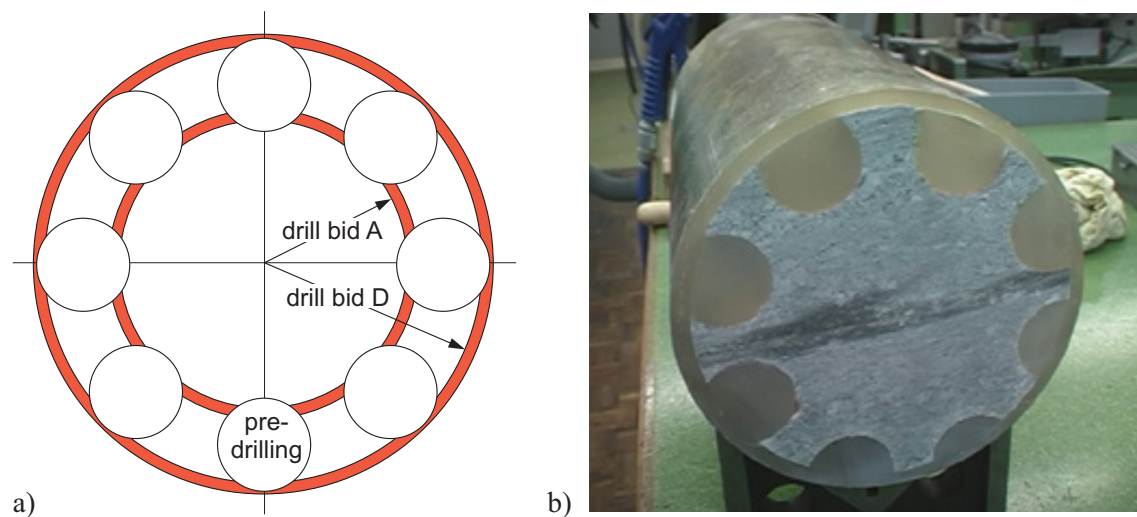


Fig. 3.4: Core drilling with the improved drilling technique: (a) drilling scheme and (b) core sample CoGAM98-05 (note: outer shell with rock material has been removed).

3.2 Determination of material parameters

Measurements of porosity and of gas, liquid and relative permeabilities and gas threshold pressure were made along the plane of the shear zone for the two test specimens CoGAM98-001

and 98-002. Measurements of porosity and permeability were also made on the matrix material that surrounds the shear zone. Additional subcores were obtained for visualisation and characterisation of the three-dimensional microgeometry (CoGAM98-004). Porosity and gas permeability measurements were completed on one such subcore. Sandia's property tests are documented in Brodsky et al. (2000).

3.2.1 Experimental set-up

Two measurement systems were used to conduct the flow measurements. The Overburden Permeameter-Porosimeter, or OPP (Figures 3.5), is designed to measure gas permeability and porosity on cores from 25 mm to 152 mm in diameter and lengths up to 254 mm. Hydrostatic confining (overburden) pressures up to 20 MPa and pore pressures up to 14 MPa can be applied. The OPP is contained within an incubator to allow control of test temperature. The system control and data acquisition is done by means of a personal computer. Helium gas was used for all porosity and single-phase permeability measurements using the OPP.

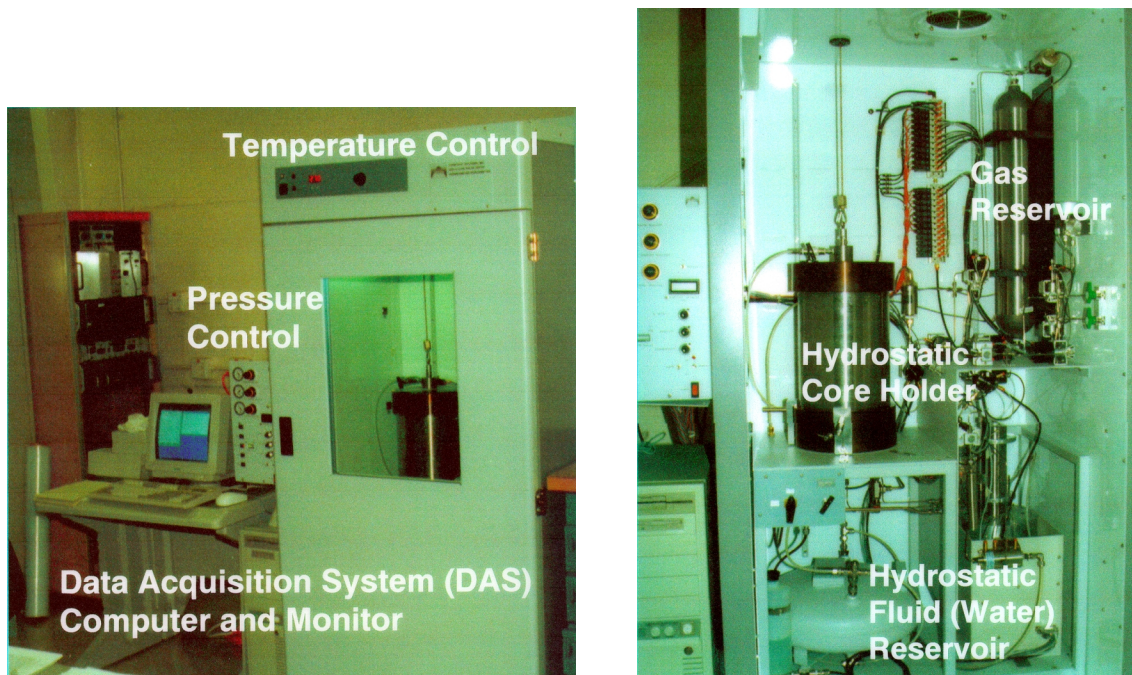


Fig. 3.5: Overburden Permeameter Porosimeter (a) in a temperature-controlled cabinet, and (b) view of cabinet interior showing pressure vessel (core holder) and hydraulics.

The Automated Two-Phase Flow device, or ATPF (Fig. 3.6), is designed to perform steady-state liquid and gas permeability measurements, transient relative permeability measurements and capillary pressure - saturation tests on cores from 25 mm to 152 mm in diameter and lengths up to 254 mm. Hydrostatic confining (overburden) pressures up to 20 MPa and pore pressures up to 14 MPa can be applied. The ATPF is contained within an incubator to allow control of test temperature. The system control and data acquisition is done by means of a personal computer. Nitrogen gas was used for all measurements (relative permeability, capillary pressure) with the ATPF.

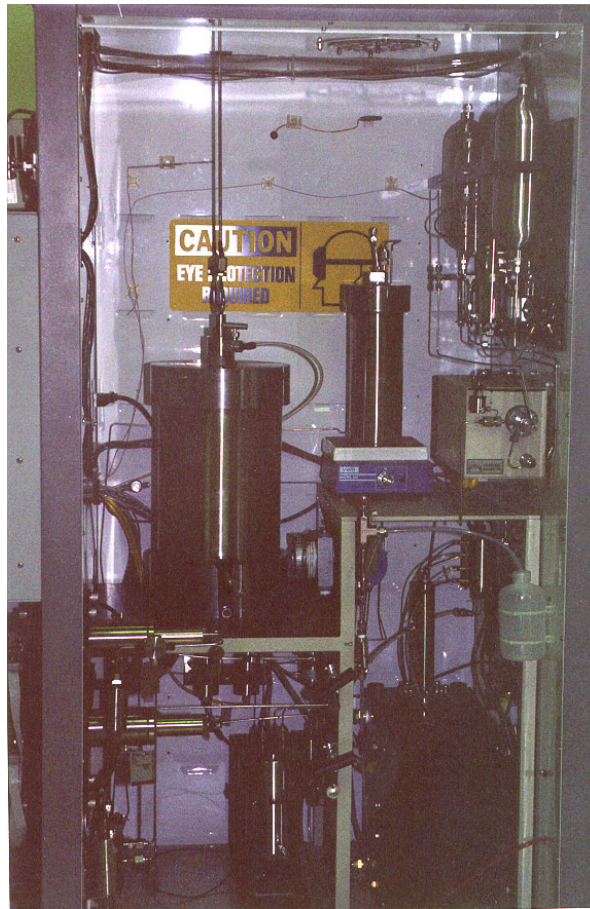


Fig. 3.6: Automated Two Phase Flow (ATPF) apparatus shown with components labeled.

3.2.2 Experimental methods

Porosity

Porosity is determined using the gas expansion technique. After the specimen is placed in the OPP, the confining pressure is applied and a pore pressure is established in the specimen and the associated test system (the volume of tubing and valves adjacent to the core). Once equilibrium of the pore pressure is achieved, the core is exposed to a reservoir of a known volume. The system pressure adjusts (decreases) as gas moves into the additional volume of the reservoir. The test is terminated once the pressure stabilises at its final value. Knowing the volume of the reservoir and the test system, the pore volume can be calculated from the measured pressure change. The volume of the test system is determined by means of a calibration test that utilises a solid machined steel cylinder in place of a specimen. The calibration is then verified over the operating range by testing steel cylinders with central holes of known dimensions in place of a rock core.

The porosity is determined from the measured pore volume and core volume as:

$$\Phi = \frac{V_p}{V_i} \quad (3-1)$$

where Φ is the porosity, and V_p and V_i are the pore volume and initial total specimen volume, respectively. The OPP has the capability to measure porosities in the range of 0.1 % to 30 %.

Gas permeability

Gas permeability measurements were made with the OPP using the pressure decay technique. For these measurements, the OPP is configured such that there is an upstream and a downstream reservoir. The upstream reservoir is relatively large compared to the pore volume and test system volume, and is referred to as an infinite volume reservoir. The downstream volume is much smaller and can be switched between different known volumes to adjust the resolution of the OPP from about 10^{-15} m^2 to 10^{-21} m^2 .

A confining pressure is first applied to the core, followed by the establishment of the desired pore pressure in the core and the test system. The infinite reservoir is then isolated from the core and its pressure is increased by a specified amount to produce a pressure pulse. Once the increased pressure equilibrates in the infinite reservoir, the pulse is exposed to the core. Gas flows through the core and into the downstream reservoir. The pressure difference across the core is monitored as it decays with time. The rate of decay is dependent on the rock permeability as well as test system parameters such as the downstream reservoir volume. The permeabilities given below were interpreted using the method of Bourbie and Walls (1982). This technique is more applicable to rocks with low permeabilities than the exponential solution of Brace et al. (1968).

Gas permeability measurements in low permeability media can be affected by the Klinkenberg, or molecular slip, phenomenon, due to interaction between the gas molecules and the flow path wall. Because of this effect, the measured gas permeability is greater than the intrinsic permeability by an amount inversely proportional to the pore pressure. By conducting tests at different pore pressures, a correction for this effect can be developed. If the measured permeabilities are plotted as a function of inverse pore pressure, then the intercept of the straight line fit through the data at infinite pressure corresponds to the intrinsic gas permeability.

Liquid permeability

After the core is placed in the ATPF and a confining pressure applied, the test system and the core are vacuum-saturated with the liquid of choice (in this case water containing dissolved solids as described in section 3.3). The desired pore pressure is then established by means of a pair of precision pumps. These pumps are used to increase the pressure on the top of the core, while the downstream pressure is maintained with a regulator. At least one pore volume of liquid is forced through the core prior to initiating the permeability test to promote full saturation of the core. The flow rate of liquid is measured with the pumps, and is used to interpret permeability once it achieves a constant rate. The ATPF is designed to measure steady-state liquid permeability in the range of 10^{-15} m^2 to 10^{-21} m^2 .

Relative permeability

Relative permeability measurements were conducted in the ATPF device using an unsteady-state technique. The test begins with the core being subjected to a confining pressure and saturated with liquid at the desired pore pressure. Gas is then introduced to the top of the core at a pressure greater than the pore pressure. The gas displaces liquid from the core, eventually leading to breakthrough of gas through the core (that is, continuous gas flow through the core). The displaced fluid from the bottom of the core is separated into its liquid and gas fraction by

means of a gravimetric separator. The liquid displaced from the core is weighed and the amount of gas produced is measured by venting it into reservoirs and monitoring the pressure build-up. For relative permeability tests, the ATPF is configured so that the pressure in the line downstream of the core will increase as fluid moves through the core and into this line until the gas breaks through the core and activates a pressure relief regulator. Thus, the pressure difference across the core can decrease during the test until gas production is observed. The test is terminated after the ratio of gas flow to liquid flow reaches a pre-determined level.

The data are interpreted in terms of relative permeability using the method of Jones and Roszelle (1978). Data reduction requires input of the core pore volume and intrinsic liquid permeability. Another important parameter required for data reduction is the test system volume between the core and separator which produces a “lag” in the arrival of gas. Pre-test volume measurements on the ATPF yielded a downstream volume of 1.9 cm³. A processing program for use with data produced from the ATPF device was used for the data interpretation.

Capillary pressure as a function of saturation

Capillary pressure - saturation tests are conducted in the ATPF. A confining pressure is applied to the core and liquid is circulated through the core to ensure that it is saturated. Gas is introduced at the top of the core under a pressure greater than the pore pressure. The difference in gas and liquid pressures is the capillary pressure. Under a sufficient capillary pressure, the gas will displace water. A porous ceramic membrane, saturated with liquid, is located at the base of the core. The membrane will remain saturated with liquid until a characteristic threshold capillary pressure is reached. Liquid that is displaced from the core is collected and weighed, permitting the saturation to be calculated. The capillary pressure – saturation tests are conducted by progressively increasing the capillary pressure and de-saturating the specimen. The maximum capillary pressure that can be imposed is equivalent to the threshold pressure of the membrane, which was specified as 1.5 MPa for these tests.

Liquid permeant

The liquid used for liquid and relative permeability and capillary pressure tests was produced by dissolving ground Grimsel core in distilled water. Ground rock was recovered during specimen coring and placed in a large flask of distilled water at room temperature. The flask was placed on an automatic stirring device for several days. The liquid was then poured through a 0.45 µm filter so that only clear liquid remained. This clear liquid was used as the permeant.

3.2.3 Results – testing of core matrix

A subcore was removed from CoGAM98-001 that did not contain any macroscopic shear zone material. The subcore was 38.1 mm (1.5 in) in diameter and 56 mm (2.2 in) in length and was subcored using the techniques described in section 3.1.3. Measurements of porosity and gas permeability were completed on this specimen. The purpose of measuring these matrix properties was to facilitate correcting bulk property measurements (measurements made on specimens that contained both shear zone and matrix material) and to determine shear zone properties.

Porosity measurements

Eighty-four separate porosity measurements were made on the matrix core during March through August, 1999. Helium was used as the test fluid for all tests. The confining pressure was varied from about 3 MPa to over 15 MPa. For most of the tests, the initial pore pressure was about 1.4 MPa. The final pore pressure depends on the rock pore volume as well as the test system volumes. Using the standard OPP configuration, the final pore pressure for these tests was approximately 0.2 MPa.

Porosity as a function of effective confining pressure is given in Figure 3.7. The effective confining pressure was taken as the confining pressure minus the final pore pressure. The data are fit with a straight line ($R^2 = 0.81$), although other functions could be readily fitted to the data as well. The porosity values are in the range of about 0.25 % to 0.50 %, with a trend of decreasing porosity with increasing confining pressure.

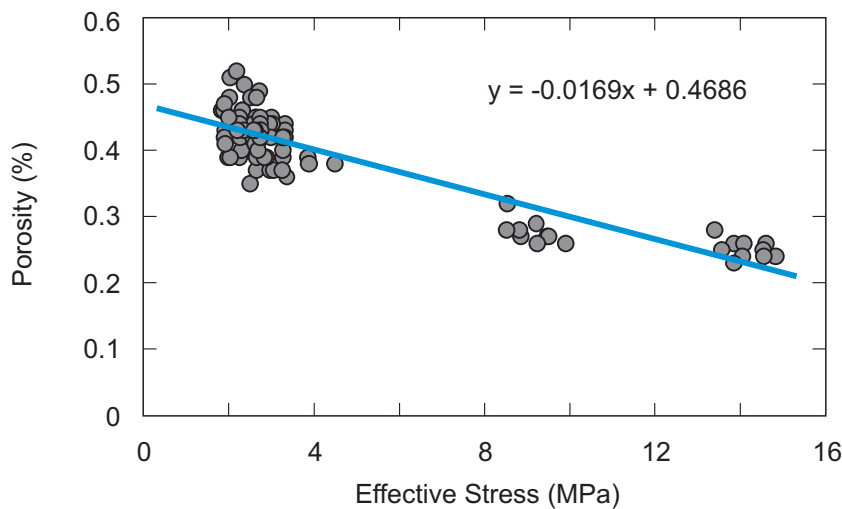


Fig. 3.7: Porosity versus effective confining stress for matrix core.

Gas permeability measurements

Eight series of gas permeability measurements were conducted for the purpose of obtaining the Klinkenberg or intrinsic gas permeability. These test series will be referred to as Klinkenberg series. Each test series involved conducting a number of gas permeability tests at constant effective confining stress but different pore pressures. In this way, the permeability can be determined independently of the gas slip phenomenon. During each test series, the pore pressure was varied from about 0.7 MPa to 2.2 MPa. The confining pressure was adjusted so that effective confining pressure remained approximately constant at 2 MPa during six of the test series, 8.5 MPa for one test series and 13.5 MPa for another test series. Each test series results in a single Klinkenberg permeability value.

Results from a typical Klinkenberg test series are shown in Figure 3.8. This test series consisted of five gas permeability tests conducted at an effective confining pressure of about 2.0 MPa. When permeability is plotted as a function of the inverse of the pore pressure, the intercept at infinite pressure yields the Klinkenberg or intrinsic gas permeability.

Another test series was conducted with a constant pore pressure of 1.5 MPa, but variable confining pressure. Because the pore pressure was held constant, these data cannot be interpreted as a Klinkenberg series. Instead, a Klinkenberg correction was developed from the previously described Klinkenberg series and applied to these data. The Klinkenberg series data can be fitted to a straight line (see Figure 3.8 above) which can be expressed as

$$k = k_k \cdot \left(1 + \frac{b}{P}\right) \quad (3-2)$$

where k is the measured permeability and k_k is the Klinkenberg permeability (y-axis intercept on Figure 3.8), b is a constant (the Klinkenberg correction parameter, which is related to the slope of the straight line in Figure 3.8) and P is the pore pressure. The average value of b was determined from the six Klinkenberg test series conducted at 2 MPa effective confining pressure, because the effective confining pressure was similar to those used in the test series with variable confining pressure.

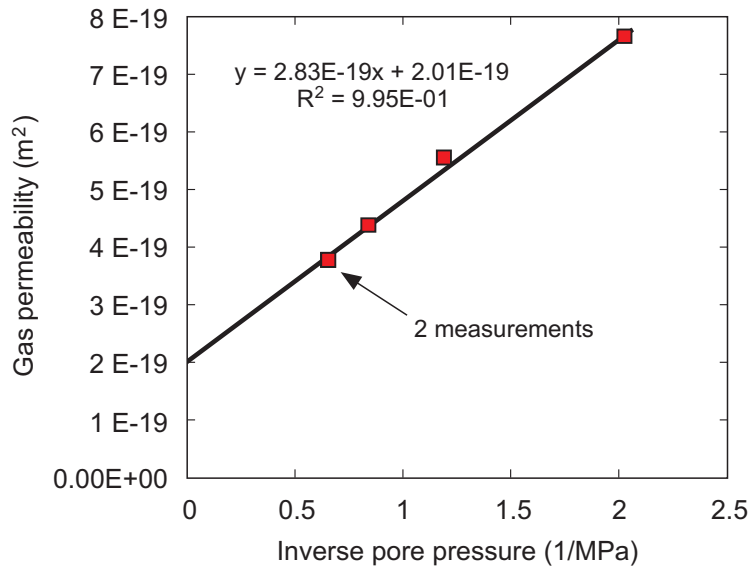


Fig. 3.8: Klinkenberg test series on matrix core with an effective confining pressure of 2.0 MPa.

A compilation of the Klinkenberg permeabilities is given in Figure 3.9. This compilation includes both the permeabilities derived from the test series at constant effective stress, as well as the corrected permeabilities from the test series with constant pore pressure. These data indicate that the gas permeability of the matrix decreases by nearly two orders of magnitude as the effective confining stress is increased from about 2 MPa to about 15 MPa.

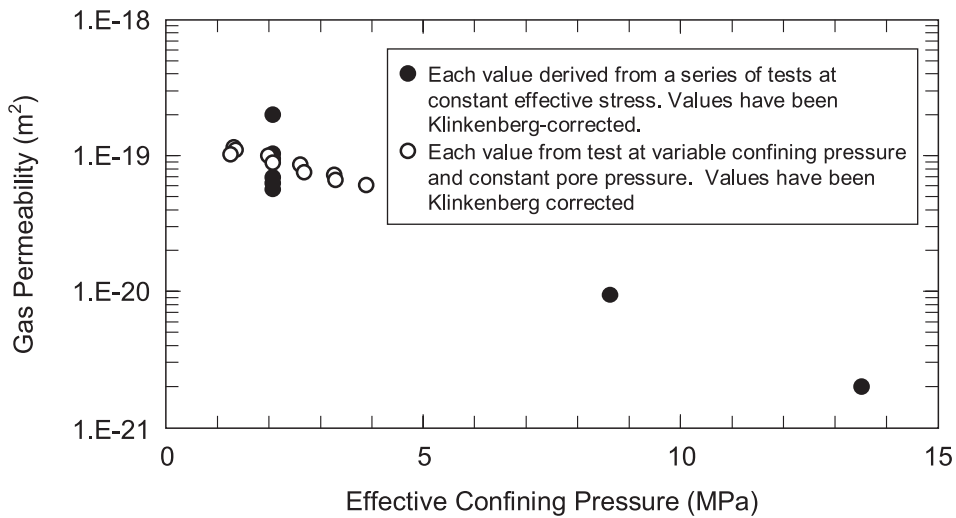


Fig. 3.9: Klinkenberg permeabilities as a function of effective confining pressure for matrix core.

Liquid permeability

Liquid permeability tests were conducted on the matrix core in the ATPF. Because of the very small pore volume of the specimen, the amount of water that moved through the core was small and consequently the measurements were near the resolution of the system. A summary of the liquid permeability measurements is given in Table 3.2 below.

Tab. 3.2: Liquid permeability of matrix core.

Confining pressure (MPa)	Pore pressure (MPa)	Pressure Drop Across Core (MPa)	Permeability (10 ⁻¹⁹ m ²)
5.5	3.4	0.2	3.9
4.1	1.4	1.0	3.0
4.5	1.4	1.0	2.9
4.5	1.4	0.7	2.4

Relative permeability

A number of relative permeability tests were attempted. During these tests, progressively greater capillary pressures (gas pressures) were imposed on the core. The results suggested that some water could be displaced from the core, but continuous gas flow was not established. The principal problem with the tests was related to the very small pore volume of the core (0.3 ml).

Weighing the core suggested that water had been displaced from the core during the relative permeability measurement such that the saturation of the core was about 65 %. The core was then placed in the OPP to measure the gas permeability at this saturation in order to provide a single point in the permeability-saturation relationship for the matrix core. However, the permeability of the core to gas was below the resolution of the test equipment (10 - 21 m²).

3.2.4 Results – testing of shear zone

Tests were performed on each of the two cores recovered from the GAM shear zone in February 1998. Photographs are given in Figures 3.2a and b and the method of subcoring is given in section 3.1.2. Each of these cores contained both shear zone and matrix materials.

Porosity – CoGAM98-001

Two sets of gas porosity measurements were conducted during two periods: the first was during August – September 1998 and the second during July-August 1999. The first set of measurements consisted of seven tests conducted at confining pressures between 2.8 and 4.1 MPa. Nine porosity measurements were made during July-August 1999. During these measurements, the confining pressure was varied from 3.4 to 13.5 MPa. For all measurements, the initial pore pressure was about 1.4 MPa and the final pore pressure was about 0.2 MPa.

The measured or bulk porosity of the core consists of the porosity of the shear zone material and the porosity of the matrix material. The measured porosity can be corrected to yield the shear zone porosity by subtracting the matrix material contribution:

$$\Phi_s = \frac{(\Phi_b - (1 - \chi) \cdot \Phi_m)}{\chi} \quad (3-3)$$

where Φ is the porosity and the subscripts s, m and b refer to the shear zone, matrix and bulk material, respectively. χ is the fraction of the core that consists of shear zone material.

The bulk porosity and the shear zone porosity calculated from equation 3-3 are given in Figure 3.10 as a function of effective confining pressure. The shear zone fraction was estimated from visual observations as 20 %. The matrix porosity was adjusted for confining pressure using the straight line fit to the matrix porosity data given in Figure 3.7. All but one of the calculated shear zone porosity values are in the range of 2 to 3 %. The single exception was a value of about 1% obtained at a ~ 14 MPa confining pressure.

Gas permeability – CoGAM98-001

Gas permeability measurements were conducted during August 1998 and then again in July 1999. The gas permeabilities were obtained from Klinkenberg test series; that is, a number of tests conducted at constant effective stress but variable pore pressure in order to derive the Klinkenberg-corrected permeability. These data were also corrected for the effective area of the shear zone in a manner similar to that used to calculate the shear zone porosity. Because the matrix permeability is more than two orders of magnitude lower than that measured, the effective shear zone permeability (k_s) can be calculated from the interpreted Klinkenberg permeability (k) as

$$k_s = \frac{k}{\chi} \quad (3-4)$$

Results from these tests are summarised in Figure 3.11. The measurements conducted at the same effective confining pressure indicate that the gas permeability decreased from 2 to $3 \times 10^{-15} \text{ m}^2$ during August, 1998 to about $5 \times 10^{-16} \text{ m}^2$ during July 1999. The data obtained during July 1999 indicates a decrease from about 5×10^{-16} to $2 \times 10^{-16} \text{ m}^2$ as the effective confining pressure was increased from about 2 to 14 MPa.

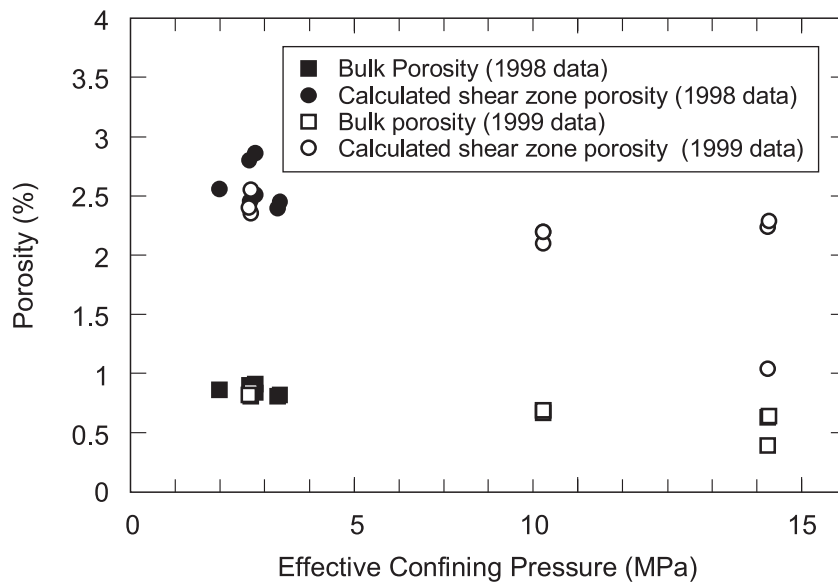


Fig. 3.10: Measured bulk porosity and calculated shear zone porosity as a function of effective confining pressure.

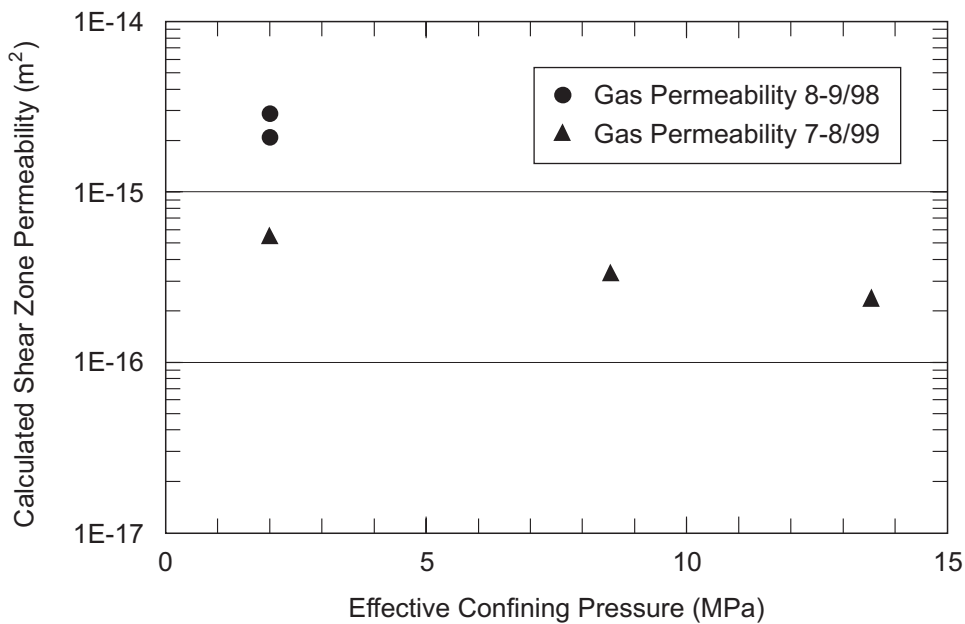


Fig. 3.11: Shear zone gas permeability as a function of effective confining pressure.

Liquid permeability – CoGAM98-001

Liquid permeability measurements were made during September 1998, and again during November 1998. The three measurements made during September were made with a confining pressure of 3.5 MPa and a pore pressure of 1.4 MPa. The measurements made during November were performed under a range of confining pressures from 3.5 to 5.5 MPa and pore pressures from 1.4 to 4.8 MPa. The measured liquid permeabilities are corrected to yield an estimate of the shear zone permeability using equation 3-4. Results are summarised in Figure 3.12. The tests conducted at the same effective confining pressure indicate that the liquid permeabilities

decreased by almost an order of magnitude from nearly 10^{-15} to 10^{-16} m² from September to November. It is possible that the liquid permeant caused swelling of any clay minerals and thereby decreased permeability, or that fine particles of rock in the permeant ($< 0.45 \mu\text{m}$) blocked flow through the finer pore structures. The data suggest a possible moderate decrease in permeability with an increase in effective confining pressure.

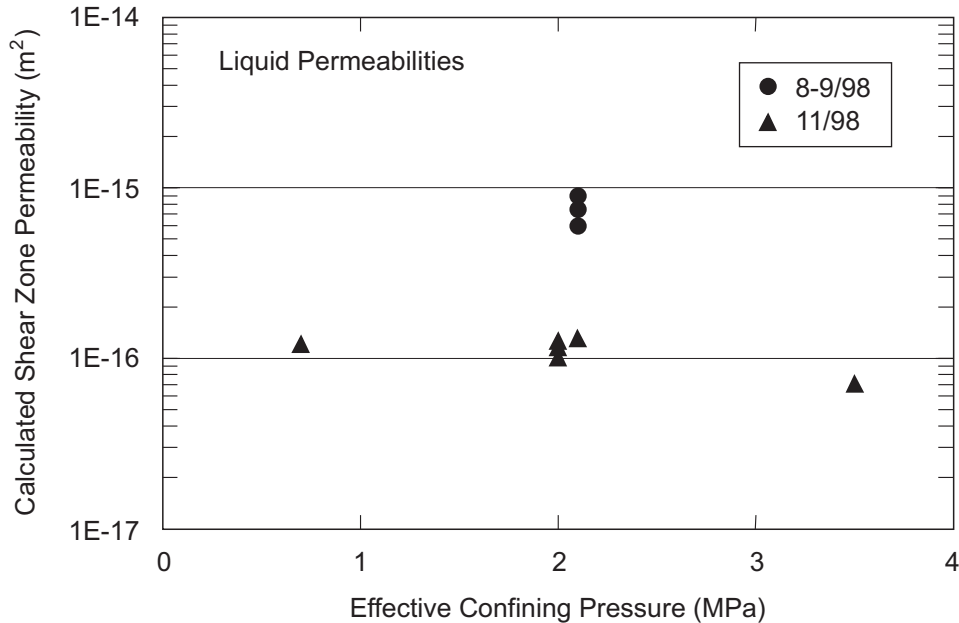


Fig. 3.12: Calculated shear zone liquid permeability as a function of effective confining pressure.

Relative permeability – CoGAM98-001

Two sets of relative permeability measurements were made: the first during September 1998 and the second during December 1998. The initial test was conducted with a confining pressure of 5.5 MPa, a pore pressure of 3.5 MPa and a differential gas pressure of 297 kPa. The second test was conducted with a confining pressure of 5.5 MPa a pore pressure of 3.5 MPa and a differential gas pressure of 862 kPa.

The test data, interpreted as effective gas and water permeability, are shown in Figure 3.13. It was assumed that the gas movement was principally through the shear zone; consequently, the intrinsic permeability assumed for the data reduction method was that calculated for the shear zone. Consistent with the observed changes in permeability over time (see Figure 3.12), the intrinsic permeability was assumed to be 7.5×10^{-16} m² and 1.3×10^{-16} m² for the first and second data sets, respectively.

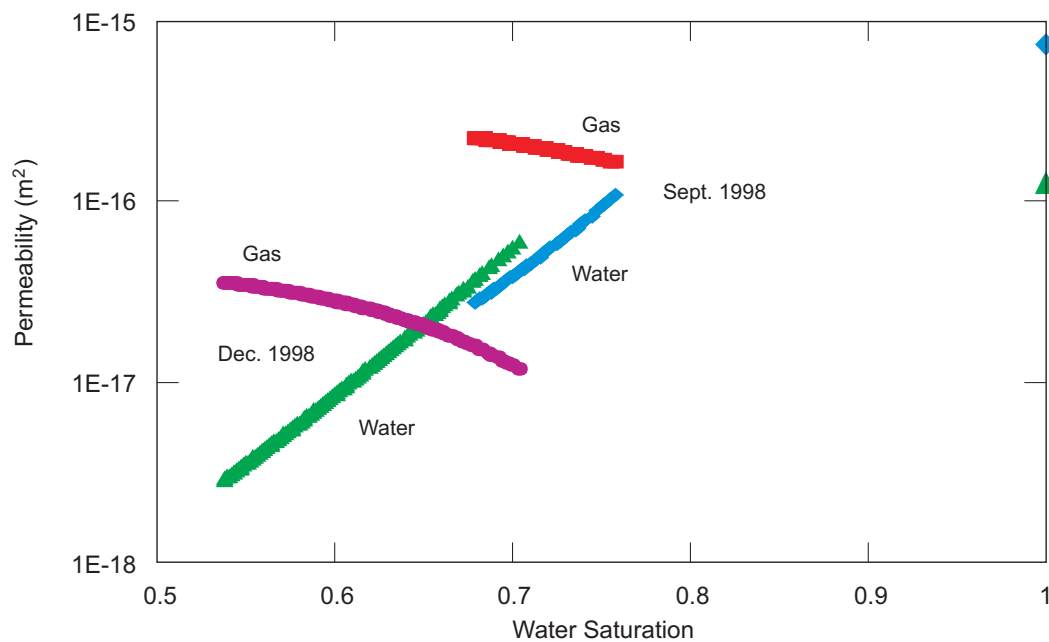


Fig. 3.13: Effective gas and water permeability as a function of water saturation.

Capillary pressure-saturation tests – CoGAM98-001

Two capillary pressure-saturation tests were conducted during February 1999. These tests were conducted with a confining pressure of 5.5 MPa and a pore pressure of 3.5 MPa. Both tests were conducted with gas displacement pressures of up to about 0.5 MPa, beyond which gas apparently moved past the ceramic plate and precluded collecting further data. The data from the two tests, shown in Figure 3.14, are comparable until a saturation of about 0.8 is reached. The data from the first test indicate that the water saturation does not decrease much below 0.8, whereas for the second test the saturations are much lower at comparable capillary pressures.

Porosity – CoGAM98-002

CoGAM98-002 was 107 mm (4.22 in.) in diameter. It was too large for the standard 101.6 mm (4 in.) fixturing available for the OPP and ATPF. The specimen was therefore epoxied into an aluminium ring such that it could be accommodated by the standard 152.4 mm (6 in.) fixtures. The aluminium ring did not transmit changes in confining pressure to the specimen.

Porosity measurements were made on this core during April 1999. Ten measurements were made with varying effective stress applied to the core, ranging from 1.9 MPa to 6.1 MPa. The measured porosity values can be adjusted to yield estimates of the shear zone porosity. The fraction of the core that was estimated to comprise the shear zone was 32 %. The porosity results are given in Figure 3.15.

These results indicate that the porosity did not change appreciably with applied stress. However it cannot be excluded, that the aluminium ring did not transmit the applied stress to the core. Thus, these values could be considered porosities for an unconfined core.

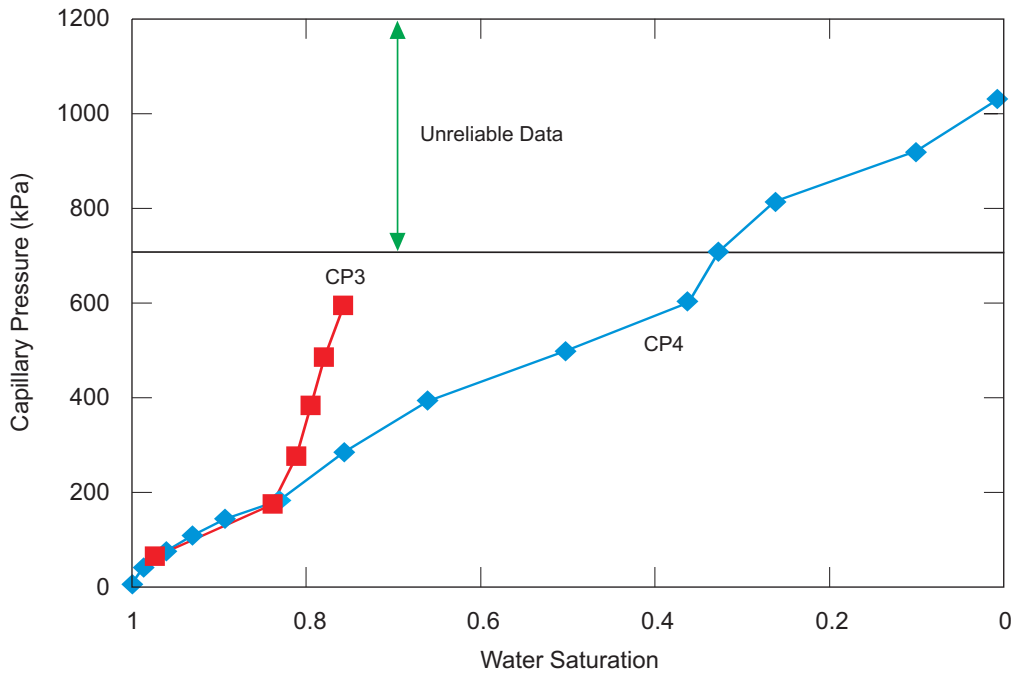


Fig. 3.14: Capillary pressure as a function of water saturation.

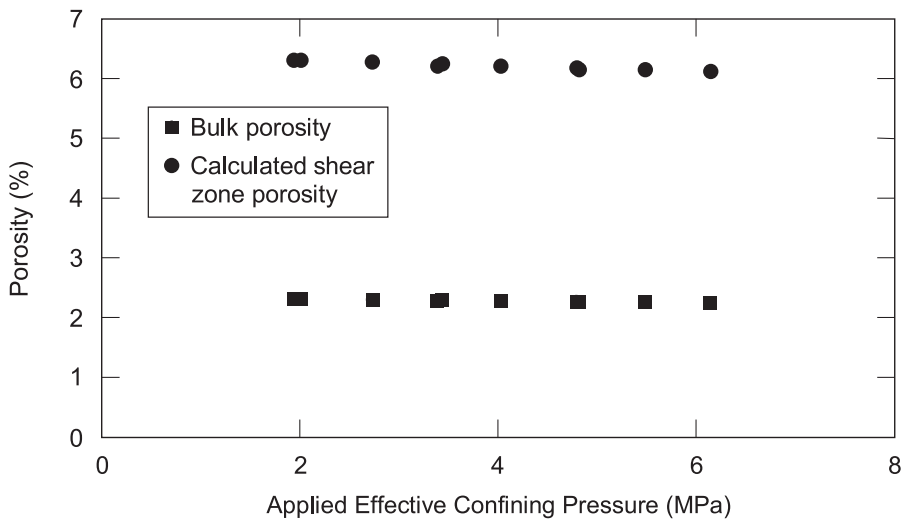


Fig. 3.15: Measured core porosity and calculated shear zone porosity as a function of applied effective confining pressure.

Note, it cannot be excluded that the effective actual effective confining pressure remained near zero because the aluminium ring did not transmit stress.

Gas permeability – CoGAM98-002

This core proved too permeable to utilise the OPP and the pulse decay measurement approach. A gas permeability measurement was attempted in the ATPF using the steady-state method. The permeability of this core was at the upper limit of the ATPF as well, but a permeability of between 1×10^{-15} and $5 \times 10^{-16} \text{ m}^2$ was estimated from the data. Using equation 3-4 to convert the measured values to those for the shear zone, these data imply a gas permeability of the shear zone of the core under unconfined conditions in the range of 3×10^{-15} to $1.5 \times 10^{-15} \text{ m}^2$.

3.2.5 Summary and interpretation of property tests

The matrix and shear zone data are summarised in Table 3.3. Shear zone porosities measured on CoGAM98-001 were between 2 and 3 % and decreased as effective confining pressure increased; the values are lower than those reported by Fischer et al. (1998) of approximately 5 %. This may be due to the fact that Fischer et al. tested under unconfined conditions, whereas CoGAM98-001 was tested under pressure.

Klinkenberg-corrected single-phase gas permeabilities within the shear zone ranged from 10^{-16} to $3 \times 10^{-15} \text{ m}^2$; liquid permeabilities were comparable and ranged from 7×10^{-17} to $\sim 10^{-15} \text{ m}^2$. Permeabilities measured on CoGAM98-002, which was tested essentially in the unconfined state, were more comparable to those reported by Fischer et al. (10^{-14} to 10^{-13} m^2). Differences in specimen geometry may also affect results. Fischer et al.'s test specimens were smaller in length (20 - 40 mm) than those tested here, which may have resulted in a larger fraction of the specimen volume being affected by specimen preparation-induced damage.

Relative permeabilities to both gas and liquid were measured for saturations between 54 and 76 percent (shear zone samples). Threshold gas pressures were measured for saturations between 50 and 100 percent.

The measured matrix porosities are somewhat lower than the previously reported accessible porosity of Grimsel granodiorite of about 1 % (Schneebeli et al. 1995). The measured permeabilities are also lower than the permeabilities derived from field measurements at the Grimsel site. Gimmi et al. (1997) reported the permeability of the Grimsel granodiorite as about $3 \times 10^{-18} \text{ m}^2$ from field desaturation experiments. This permeability was similar to values interpreted from evaporation and ventilation data from the Grimsel site (Bossart et al. 1994). Borehole injection tests at Grimsel yield permeabilities from $4 \times 10^{-19} \text{ m}^2$ to $2 \times 10^{-17} \text{ m}^2$ (Heiniger 1992).

The data shown here indicate that applied load influences measured porosities and permeabilities. Changes in properties are observed over the pressure range of 0 - 15 MPa for both the matrix and shear zone.

The data demonstrate a capability to measure porosity, single-phase and relative permeabilities and gas threshold pressures for low permeability materials under confined conditions.

Tab. 3.3: Summary of Matrix and Shear Zone Data.

	Porosity (%)	Permeability (m^2)		Length (mm)	Effective Confining Pressure (MPa)	
		Gas	Liquid		Gas	Liquid
Core 1 (Shear Zone)	~ 2 - 3	$\sim 2 \times 10^{-16}$ to $2\text{-}3 \times 10^{-15}$	7×10^{-17} to 10^{-15}	158	2 - 14	0.7 - 3.5
Core 2 (Shear Zone)	~ 7	$1.5 - 3 \times 10^{-15}$	No Test	58	0	No Test
Matrix Core	0.25 - 0.5	2×10^{-21} to 2×10^{-19}	$2.4 - 3.9 \times 10^{-19}$	56	1 - 13.5	2 - 3

3.3 Visualisation of pore space distribution

3.3.1 Scope and relevance

Basic solute and two-phase flow experiments in artificial fractures demonstrated the significant impact of microstructural characteristics on transport processes in heterogeneous shear zones (cf. section 3.4). Visualisation and characterisation of the microgeometry of the rock, comprising both brittle and ductile deformation structures, is therefore a key element in conceptualisation of transport phenomena in heterogeneous shear zones. Visualisation techniques allow classification of microstructures and may give a qualitative picture of the interconnectedness of different classes of microstructural features. Typical sizes of pore throats can be estimated and the spatial continuity of brittle structures can be inferred.

3.3.2 Experimental methods and results

Two types of core imaging techniques were applied to these cores. Laser confocal microscopy provided high resolution images of the pore structure within the shear zone and also within the matrix material. X-ray imaging provided lower resolution information and was primarily used to assess the viability of applying this technique to the GAM shear zone.

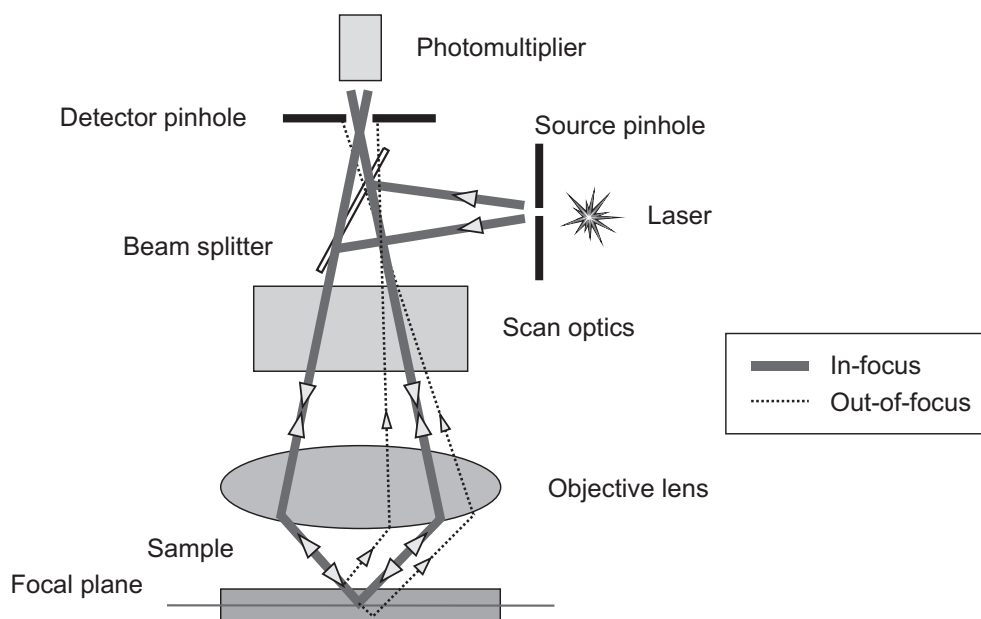


Fig. 3.16: Schematic representation of laser scanning confocal microscopy set-up (Fredrich 1999).

Laser scanning confocal microscopy (LSCM)

Laser scanning confocal microscopy (LSCM) is illustrated schematically in Figure 3.16. As noted by Fredrich et al. (1995), the technique has been used extensively in the biological sciences and has had more limited applications to nonbiological (solid) materials (Kobayashi and Shockey 1991). The distinguishing feature of LSCM is that both illumination and detection are confined to a single location on the specimen at any one time. Resolutions in the x-y plane of 200 nm and in the z direction of $< 0.1 \mu\text{m}$ can be obtained. 3D imaging is obtained by

scanning at successively increasing focal depths and using commercially available image analysis software to reconstruct the image.

Two cores, each 25.4 mm (1 inch) in diameter, were prepared for imaging. Specimen CoGAM98-002-1A was subcored from CoGAM98-002 and contained a portion of the localised shear zone. During subcoring, this specimen did not remain intact but separated into two halves along the shear zone. Specimen CoGAM98-001-2A was subcored from CoGAM98-001. This specimen comprised the matrix material that surrounded the localised shear zone.

The dry subcores were placed under a vacuum and submerged in an ultra-low-viscosity, slow-curing epoxy. The epoxy was doped with a suitable fluorochrome whose fluorescent wavelength matched that of the excitation light source. The vacuum degassed the epoxy and release of the vacuum forced it into the rock's interconnected void space. Once the epoxy cured, the rocks were sectioned and polished using standard abrasive techniques. Two sections were prepared for confocal microscopy from each subcore (located approximately one inch apart). The sections were oriented perpendicular to the axis of the subcores.

During LSCM, the prepared surfaces were illuminated with laser light. Because most minerals do not fluoresce, images of the pore structure were obtained. Observations suggest that the porosity distribution is extremely heterogeneous, although similar features are seen in the microscopy samples from the two sections from each subcore. Porosity is concentrated in the shear zone, but significant interconnected porosity also exists in regions spatially removed from the macroscopic shear zone.

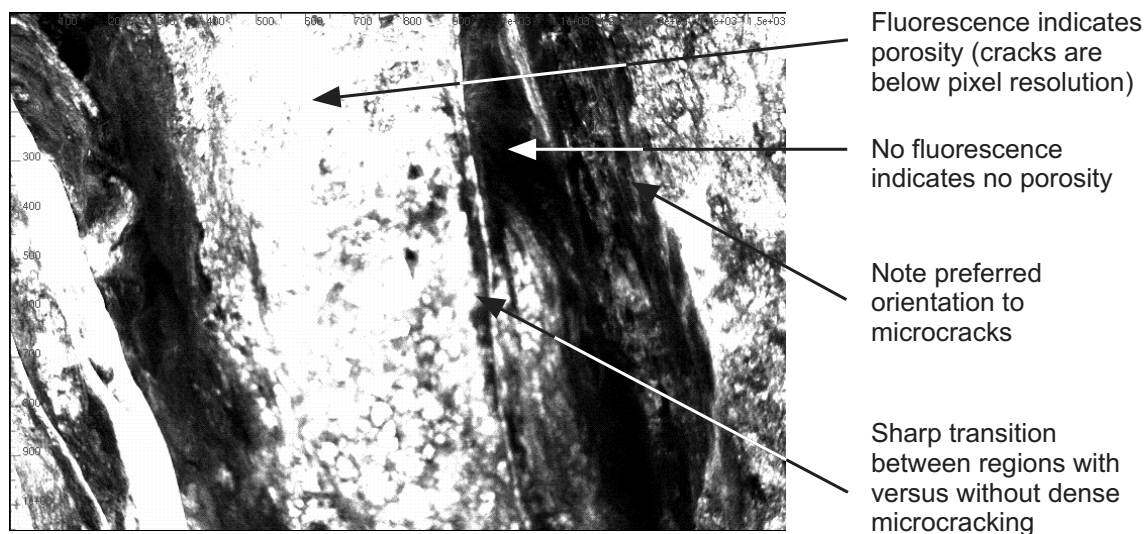


Fig. 3.17: Specimen Co-GAM98-002-1A. Low magnification view of region within several mm-wide macroscopic shear zone (768×512 with 2.055 micron pixel size; 1.578×1.052 mm).

Figure 3.17 is an image of the pore structure within the macroscopic shear zone. Bright areas indicate fluorescence and therefore represent pore space filled with epoxy. Dark areas represent the absence of fluorescence and therefore represent the intact rock mass. Sharp transitions between the rock and pore space are noted as is a preferred microcrack orientation. Figure 3.18 is a 3-dimensional reconstruction of the void volume within a section of the macroscopic shear zone viewed from below. The heterogeneous pore size distribution is evident. The shear zone is highly complex and much of the porosity is contained in an extremely fine microcrack structure

at the micron to submicron scale, with preferred orientation. The heterogeneity of the shear zone is also shown in Figure 3.18. Figure 3.19 shows localised regions of intense microcracking and interconnected porosity existing outside the shear zone with sporadic distribution.

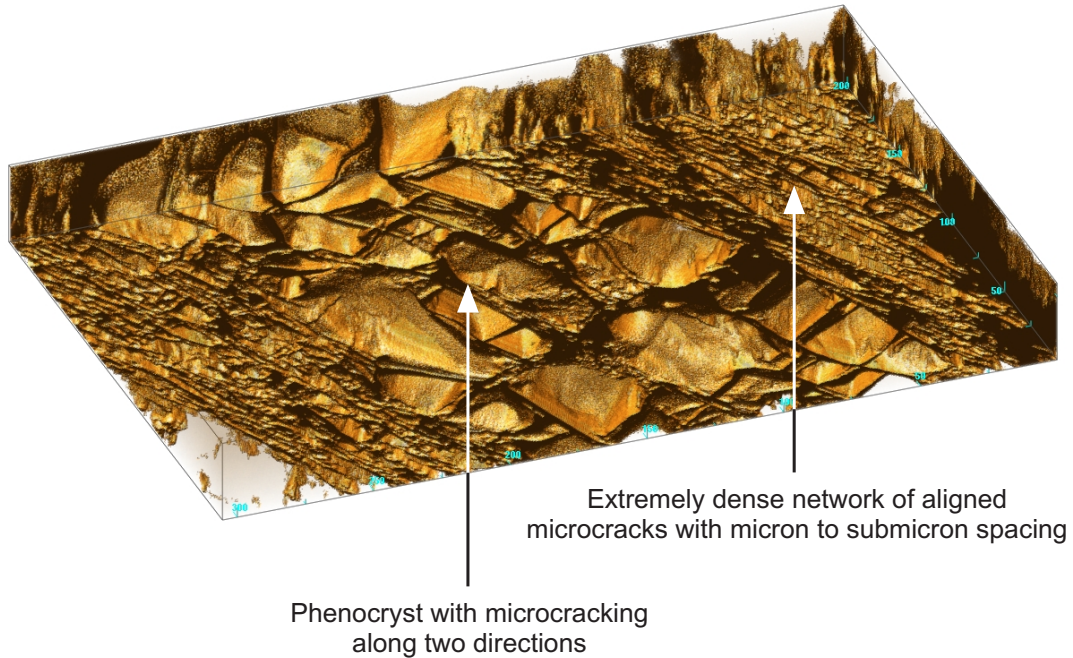
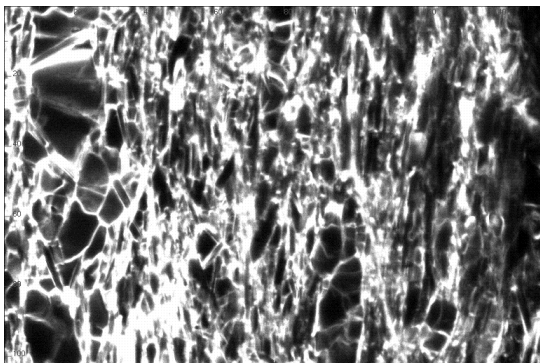


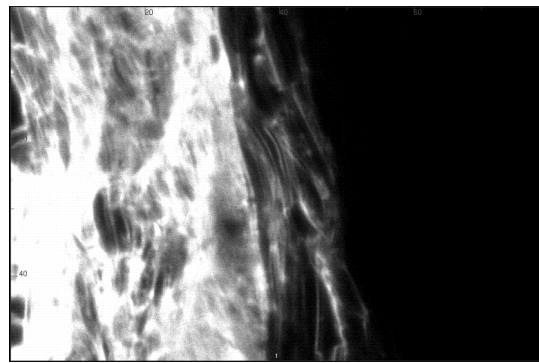
Fig. 3.18: Three-dimensional rendering of void space in sample CoGAM98-002-1A.

Higher magnification view of region within macroscopic shear zone illustrating bimodal porosity distribution within shear zone. 76 optical sections; $768 \times 512 \times 76$ with 0.40 micron cubic voxels; $305 \times 204 \times 30$ micron.

Sample 25.2.98.2-1A



a) 768×512 , with 0.200 micron pixel size;
 154×103 micron



b) 768×512 , with 0.103 pixel size;
 79×53 micron

Fig. 3.19: Sample CoGAM98-002-1A. Image within shear zone showing (a) block-like microcracking in phenocrysts, and (b) sharp transition to region with no porosity.

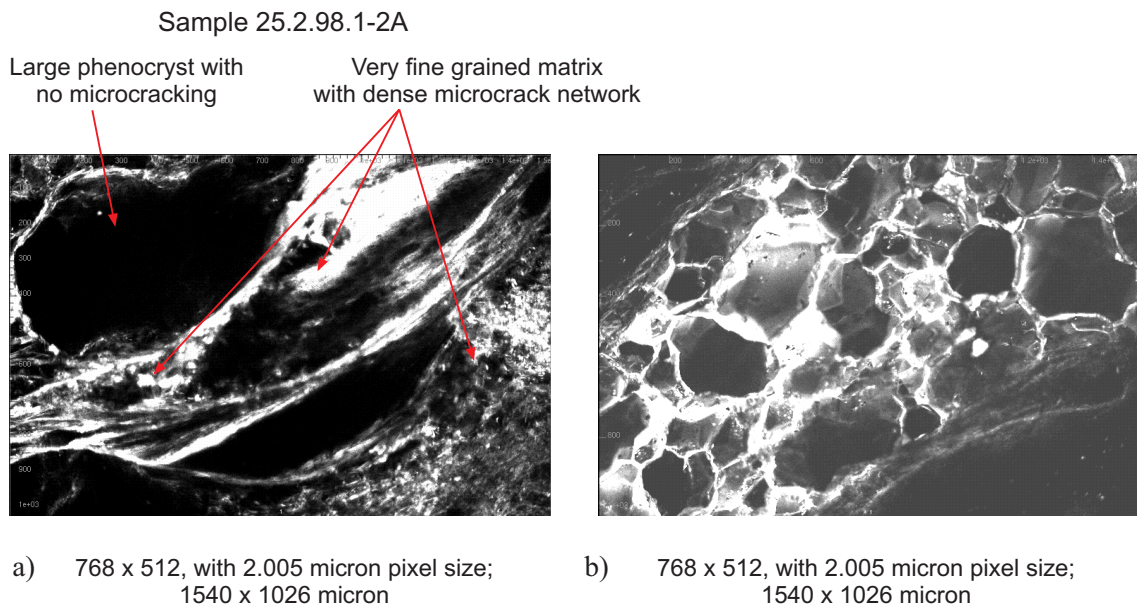


Fig. 3.20: Sample CoGAM98-001-2.

Microcracking in region outside shear zone. (a) Low magnification view showing structures similar to those within the shear zone but less well developed. (b) Phenocryst with blocky microcracking within shear zone, with intense microcracking in surrounding finer grained matrix.

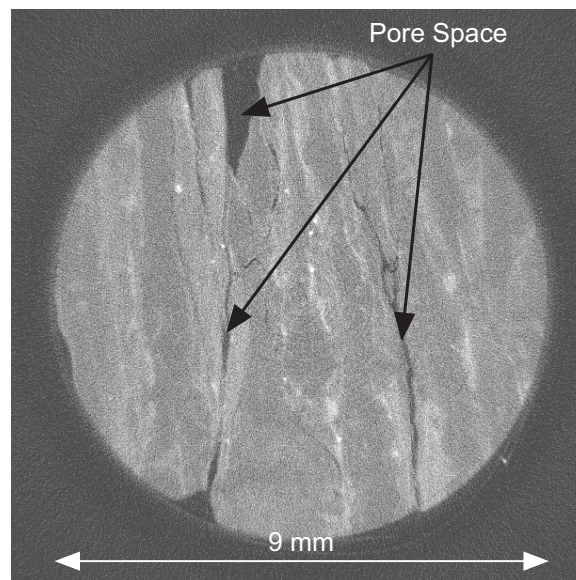


Fig. 3.21: X-ray image of shear zone, looking down axis of 9 mm core.

X-ray imaging

A 9 mm diameter subcore that intersected the reactivated shear zone was taken from CoGAM98-001. The subcore was fragile and fell apart during coring. It was taped together and imaged using X-ray techniques at Argonne National Laboratories. A resulting photograph is shown in Figure 3.21. The dark areas are the larger voids within the reactivated shear zone

horizons. These features form the main pathways for solute and gas transport. X-ray scans along the axis of the specimen indicate, even on this small scale, that the reactivated zones cannot be seen as simple, continuous features, but comprise a rather irregular pattern of microscopic joints. In some cross-sections, the reactivated shear zone consists of a single joint, whereas in other places nearby it spreads into a complex network. The resolution of the technique was 19 microns.

3.3.3 Interpretation and conclusions

Microstructural observations showed that porosity, although concentrated in localised shear zones, also exists outside these zones where it occurs sporadically as highly concentrated regions of relatively intense interconnected voids. The porosity is dominated by a complex, very fine microcrack network with micron to submicron crack spacing. The highly localised, channeled pore structure is consistent with the relatively high permeability measured, given the matrix porosity of less than 1 %.

3.4 Visualisation of transport and two-phase phenomena

3.4.1 Scope and relevance

Solute and two-phase flow experiments through artificial fractures were conducted at ETH Zürich (Soerensen 1999, Su and Kinzelbach 1999). The purpose of these experiments was to demonstrate the impact of fracture heterogeneity and fracture infill on mass transport. The experiments highlight the enormous differences between transport of miscible and immiscible fluids, respectively. Clear evidence is seen that solute and gas tracers explore different domains of a multi-porosity structure (cf. section 2.1).

A further laboratory study concentrated on the delimitation of the domains of fluid flow in the GAM shear zone (Chen & Kinzelbach 2002, Lunati et al. 2003). For this purpose, core specimens from the GAM shear zone were scanned with nuclear magnetic resonance and neutron radiography.

3.4.1 Experiments in artificial fractures

Two artificial physical fractures were constructed to visualise the tracer transport in a heterogeneous fracture (Su and Kinzelbach 1999). Systematic laboratory experiments were performed in the set-up, consisting of two horizontal plexiglass plates with dimensions of 400 mm × 400 mm (Figure 3.22). The upper plate was flat, whereas a numerically generated aperture field was milled into the lower plate. The heterogeneous aperture fields of both fractures were normally distributed on a grid of 513 × 513 pixels and had the same mean aperture (0.52 mm) and the same standard deviation (0.2 mm). However, the covariance functions of the two fields were different. In one case the aperture was a stationary random field with an exponentially decaying covariance function (exponential model); in the other case the covariance function was non-stationary with power-law decay (fractal model).

The transport experiments were first performed in the empty models, then repeated after filling the models with glass beads, which played the role of a fault gouge (Sørensen 1999, Lunati et al. 2003).

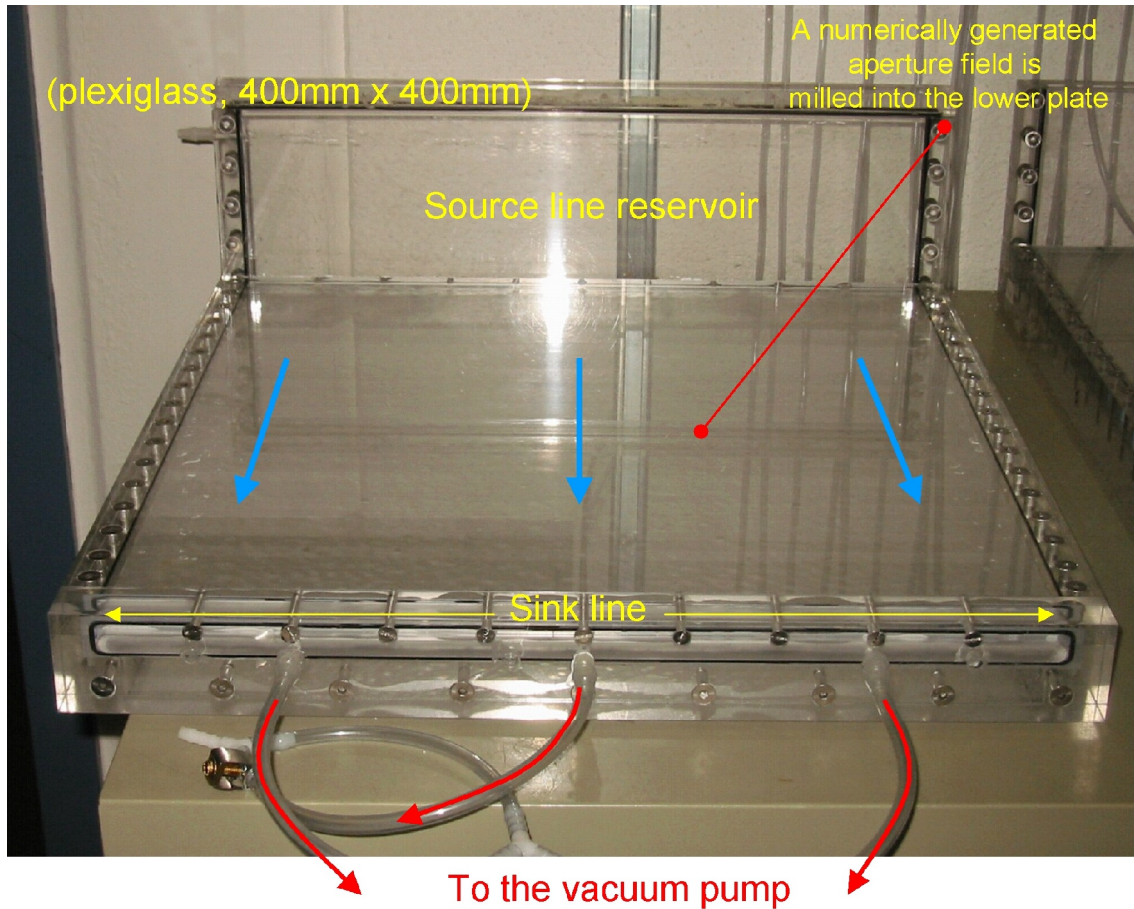


Fig. 3.22: Photograph of the artificial fracture model.

Experimental procedure: the empty fractures

The fractures were flushed first with CO₂ then with degassed and desalinated water until CO₂ bubbles were no longer visible in the fracture. The saturated fracture was mounted on the experimental set-up consisting of a cold light source, which uniformly lights the plexiglass plates from below, and a CCD camera set 1.2 m above the model, which records the flow phenomena and is controlled from a PC (Figure 3.23). The fracture was sealed on two opposite sides, while the other two slides were in contact with two reservoirs: the sink line reservoir was sealed and connected to a pump that controlled the outflow; the source line reservoir was open. The pressure was kept at a constant value slightly higher than atmospheric pressure (15 cm H₂O) in order to avoid deformations of the plexiglass plates and keep the model tight. A solution of a deep blue dye (Hexacol - E133) was added to the open reservoir, while a small flow of clear water into the sealed reservoir were applied to prevent diffusion and mixing of the dye into the model. Then the flux is reversed and the solution starts flowing into the fracture. Variations in the intensity of the emerging light are recorded by the digital camera and converted into concentrations by a light transmission technique, which basically detects the presence of the tracer from changes in the intensity of the emerging light due to the different absorption coefficients of the solution and pure water.

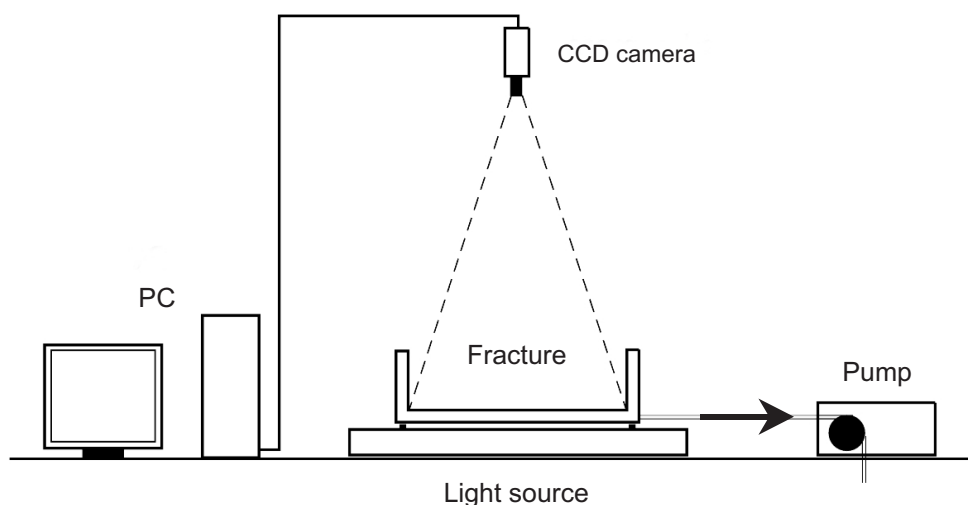


Fig. 3.23: The experimental set-up for visualisation of transport in artificial fractures.

The spatial distributions at five different time steps are shown in Figures 3.24a and b for the exponential and the fractal model, respectively. The flow was from left to right, and the solute (black) is continuously injected into the pure water-filled fracture from the left side. Even though both models show a very heterogeneous front, there were remarkable qualitative differences. In the exponential model, an average front displacement could be easily identified and, even if perturbations of this average displacement grew with time, they appeared evenly distributed in space. In the fractal model, distinct flow and no-flow regions were recognised; the existence of these regions was due to the long-range correlation of the aperture. The fractal nature of the medium, with a non-vanishing, scale-dependent correlation, suggested that a similar pattern would also be observed in situ at a larger scale.

Experimental procedure: the filled fractures

The experiment was repeated adding fine glass beads as a suspension to the degassed, desalinated water during the model saturation stage. The diameter of the glass beads ranged from 0.06 to 0.09 mm. Due to pumping and gravity they were transported downwards, filling the fracture which was tilted vertically and yielding a porosity of 40%. After that, the experimental procedure was the same as for the empty fractures. The spatial distributions of the solute at five different time steps are shown in Figures 3.24c and d for the exponential and fractal model, respectively. Dramatic changes in the solute transport occurred when the models were filled with glass beads: in both models a well defined average solute movement was observed and deviations from this average front were small and evenly distributed.

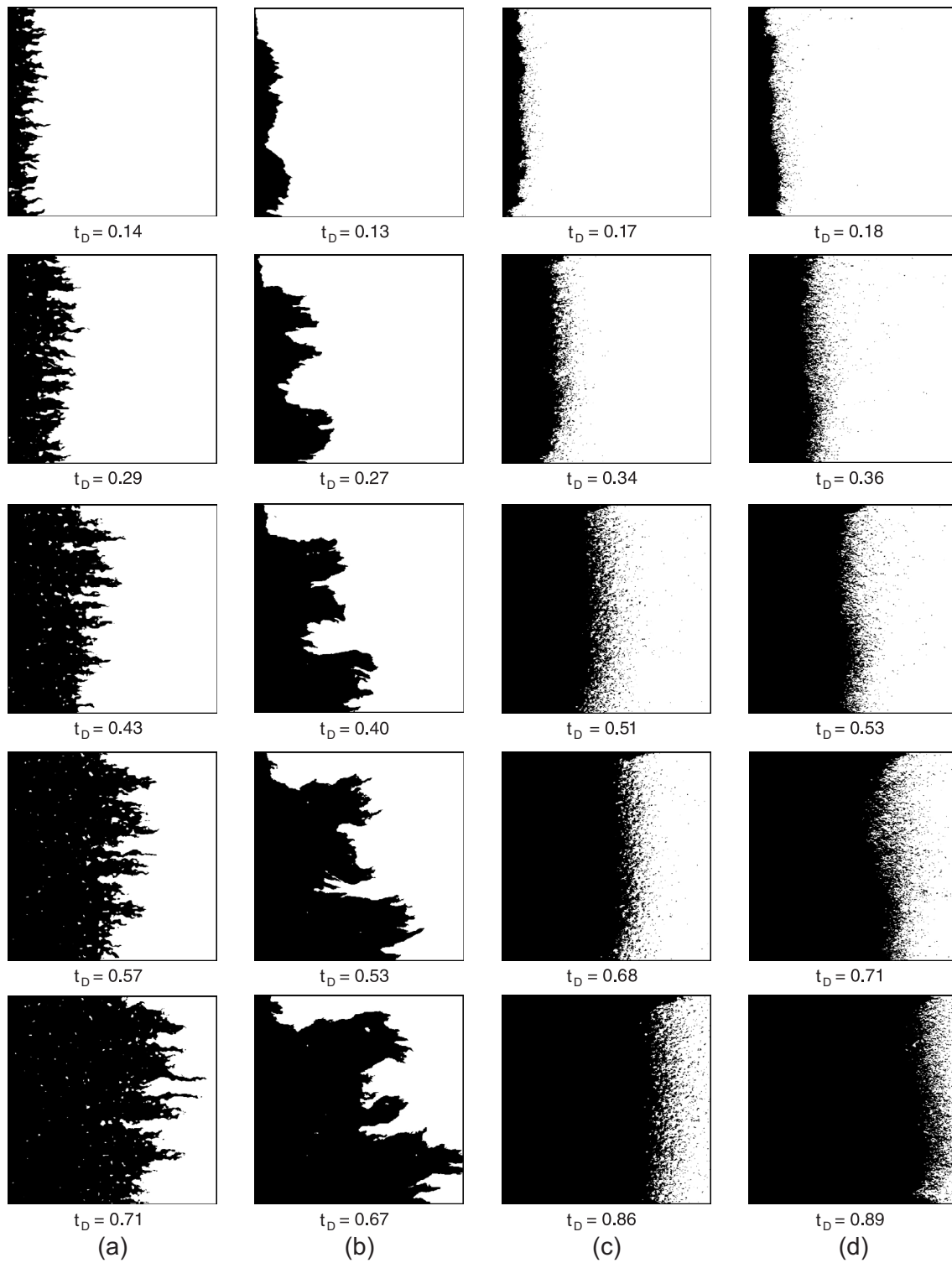


Fig. 3.24: Tracer distributions at five different time steps (dimensionless time, expressed as the fraction of injected pore volume). From left to right: (a) empty exponential, (b) empty fractal, (c) filled exponential, and (d) filled fractal models.

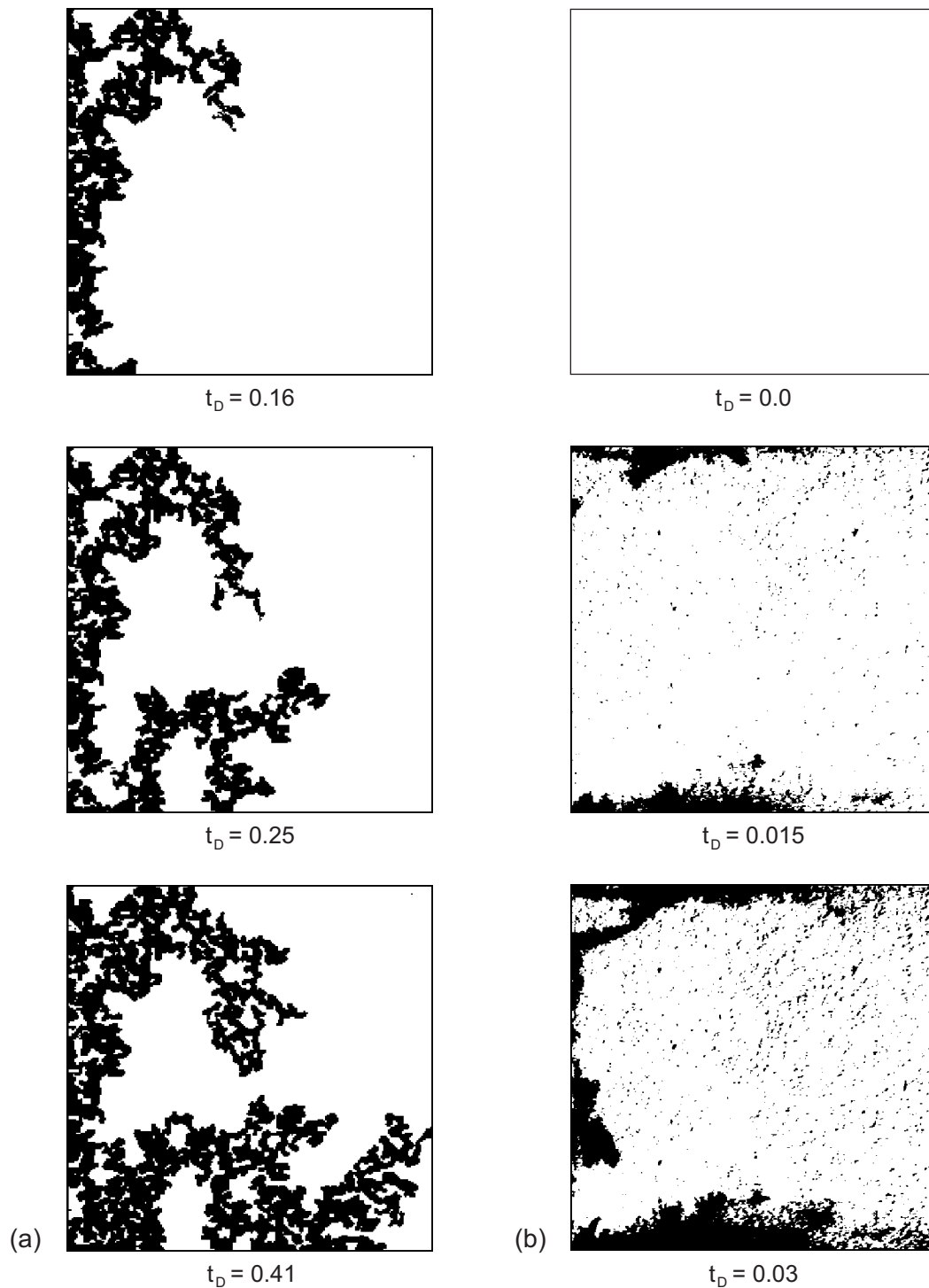


Fig. 3.25: Gas invasion at 3 different time steps (dimensionless time, expressed as the fraction of injected pore volume): (a) empty fracture and (b) filled fracture.

The two-phase flow experiment

An analogous series of experiments were performed for immiscible flow; in particular, drainage of the empty and the filled fractures was considered (Sørensen, 1999; Neuweiler et al. 2004). At the beginning of the experiment, the source line reservoir was open and filled with air at

atmospheric pressure, such that the air-water interface was located exactly at the fracture entrance. When the pump was activated, water was extracted at the sink line and the air-water interface moved into the fracture. The fracture pixels were invaded by air when their entry pressure dropped below atmospheric pressure. The morphology of the air-water interface was reminiscent of the invasion percolation theory as can be observed in Fig. 3.25a.

When the experiment was repeated in the fractures filled with glass beads (a similar experimental procedure to that in empty fractures was followed), the results showed striking boundary effects. The systematically larger pores adjacent to the wall provided a preferential path for air flow and were invaded first (Fig. 3.25b). Air breakthrough was observed before the presence of a continuous air path through the fracture was detected: the air flow took place through narrow throats that were unresolved by the acquired CCD images. While these intrinsic boundary effects were quite disappointing from an experimental point of view, they clearly showed how small-scale heterogeneity could dominate immiscible displacement and represent an indication that two-phase flow in the shear zone can exhibit extreme behaviour triggered by discontinuities in the fracture properties.

In general, two-phase displacement experiments showed much more heterogeneous behaviour than the tracer experiments, which indicated the limited applicability of continuum models to immiscible displacement.

Conclusions

The experimental observations showed that the behaviour of a tracer was much smoother and more regular after the fractures were filled with glass beads, which played the role of a homogeneous fault gouge material. This was due to the linear relationship between pore volume and transmissivity that caused pore velocity not to be directly dependent on the transmissivity, but only indirectly through the hydraulic gradient – a much smoother function due to the diffusive behaviour of the flow equation acting as a filter.

3.4.2 Non-destructive measurements on Grimsel cores by NMR and Neutron Tomography

Nuclear magnetic resonance measurements of single- and two-phase flow

Nuclear magnetic resonance (NMR) provided a tool for non-destructive investigation in a granite core containing a section of the GAM shear zone (Chen and Kinzelbach 2002). The length of the sample was 17 cm and the diameter of the section accessible to the flow was about 10 cm (Figure 3.26). The NMR measurements were based on the property of hydrogen nuclei, which align their magnetic moment to an applied magnetic field and produce a net magnetisation. A radio frequency pulse perturbed the position of the hydrogen magnetic moments. Once the pulse stopped, they regained the original orientation by relaxation. From the transverse relaxation time of the nuclei, information on the size of the water-filled pores could be obtained. Due to the paramagnetic properties of granite, only low-intensity magnetic fields could be applied, which prevented the measurements from having a good spatial resolution and allowed only information on the pore statistical distribution in the core to be obtained.



Fig. 3.26: Section face of the core at the inlet side.

The core sample was first dried at 40°C for more than one week then, saturated with distilled water under vacuum conditions. The single-phase flow experiment was performed by injecting deuterated water at two different constant flow rates (1 and 4 ml/min). As deuterium nuclei (^2H) had a different resonance frequency to hydrogen nuclei (^1H), pores filled with deuterated water were not detected and vanished from the pore size distribution spectrum obtained by NMR. The experimental results are shown in Figure 3.27, which shows the size distributions of the water-filled pores at different stages of the deuterated water injection and water saturation.

The two-phase flow experiment was performed by injecting nitrogen gas into the saturated core under different pressure conditions. Nitrogen gas-filled pores produced no NMR signal at the resonance frequency of hydrogen nuclei and vanished from the pore size spectrum. The water-filled pore size distributions at different average water saturations are shown in Figure 3.28. At low gas pressure, corresponding to high water saturation, mainly large pores were desaturated by gas. With an increase in gas pressure, water saturation in small pores also decreased gradually.

Comparing Figures 3.27 and 3.28, it can be observed that changes in the size distribution of water-filled pores monitored with NMR were more homogeneous during miscible flooding than immiscible flooding. In miscible flooding, the large and small range of the pore size distribution decreased simultaneously, indicating that deuterated water invaded both types of pores at the same time. In the immiscible flooding process, the large pores were preferentially invaded by gas. Gas breakthrough occurred quickly at extremely low gas saturation (2 % of total pore volume), indicating preferential pathways. Water saturation decreased gradually with the increase in injection pressure. In comparison, the process of miscible flooding by deuterated water was much more homogeneous, deuterated water breakthrough occurring slowly at higher deuterated water saturation (27 % of total pore volume). Note that the cross sectional area belonging to the shear zone is $A_f = 15.7\%$ (obtained from image processing).

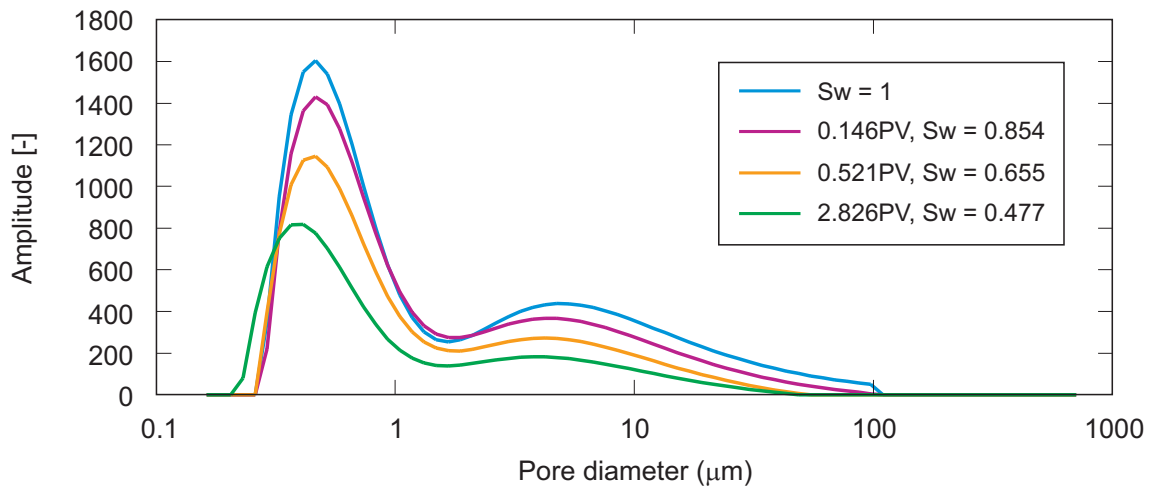


Fig. 3.27: Variation of pore size distribution filled by water during miscible flooding by deuterated water.

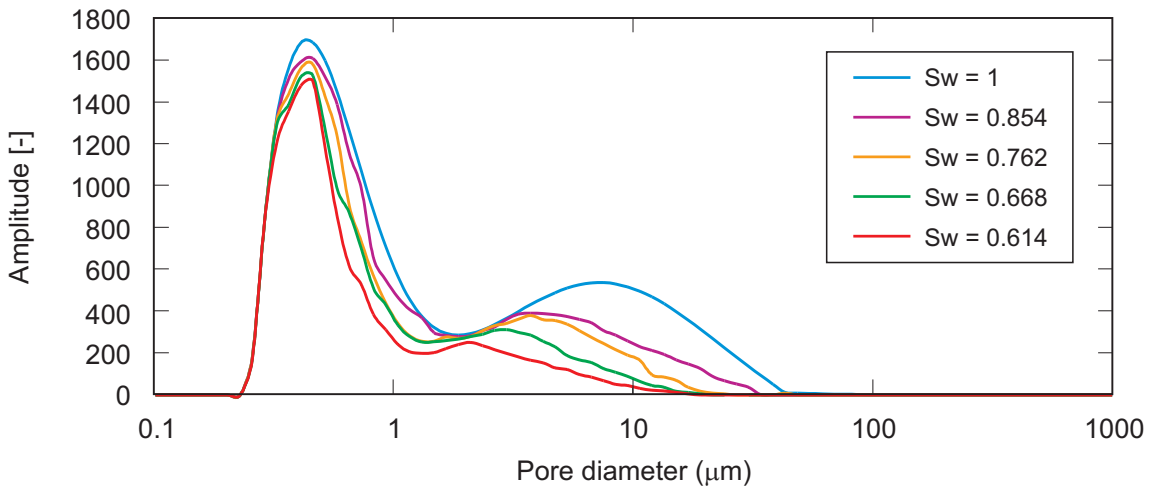


Fig. 3.28: Variation in pore size distribution filled by water during gas flooding.

Visualisation of capillary imbibition and drainage by neutron radiography

Lunati et al. 2003c, d (see also Lunati 2003) used neutron radiography to investigate two-phase flow in a core sample containing a fracture filled with a non-cohesive fault gouge material. Due to the weak interaction with matter, thermal neutrons are highly penetrating and could be used as a non-destructive probe for complex structures such as porous media. Since different materials have different macroscopic cross-sections that produce different attenuations, by comparing the incident and transmitted beams information about the sample composition can be obtained. As protons have an extremely large cross-section, neutron radiography represents a powerful tool for investigating water content distributions.

The experiments were performed at the NEUTRA radiography facility of the Paul Scherrer Institute in Villigen (AG, Switzerland – <http://neutra.web.psi.ch/>). The incident beam of thermal neutrons was produced by the spallation source SINQ; it had a neutron flux of 7.7×10^6 n/cm²s and a collimation ratio of 350. The transmitted beam was recorded by a Peltier cooled CCD camera as a 2D projection of the object with a spatial resolution of 115×115 μm² determined

by the camera lens used. The sample was fixed on a rotating table, which permitted a rotation in small angular steps over 180° and allowed the reconstruction of fully 3D information from the 2D projections by computer tomography (CT).

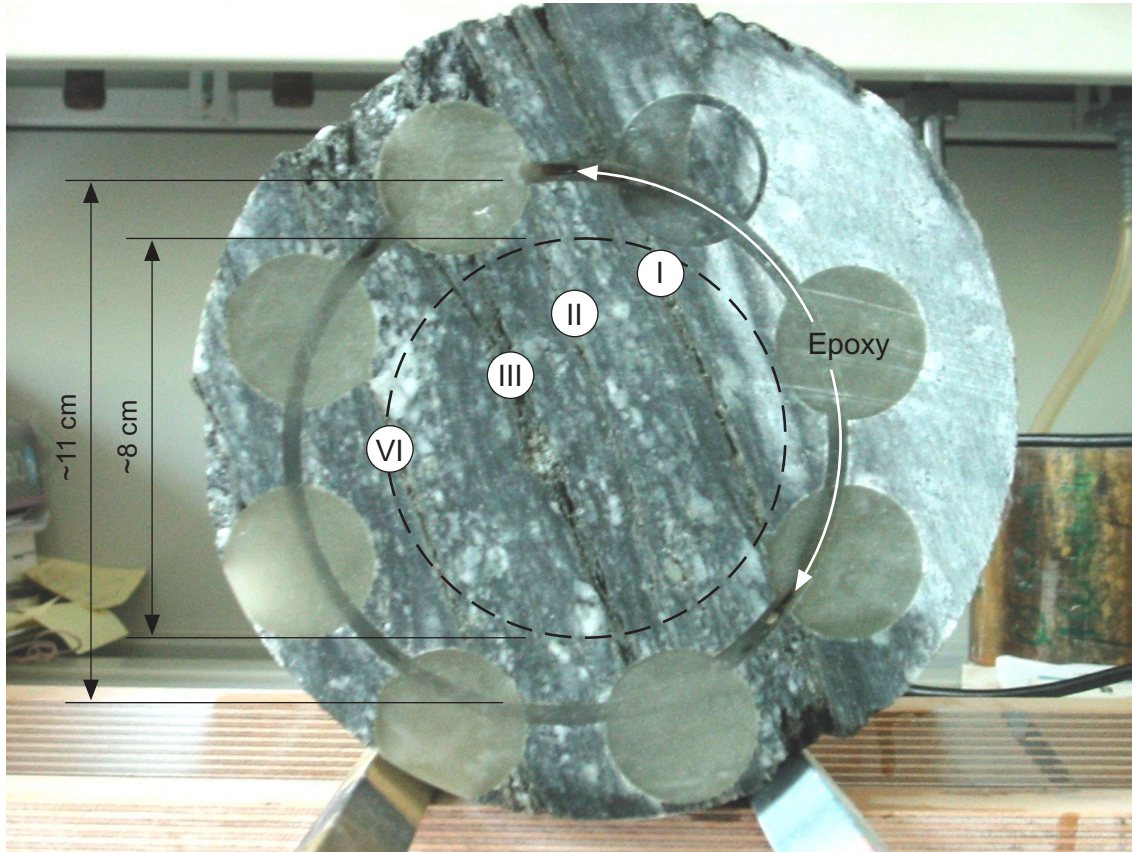


Fig. 3.29: Upper face of the core before processing.

Four fractures are visible; the fracture selected for the experiment is designed at II. The dashed-line circle approximately represents the sub coring position.

A core sample from the GAM shear zone containing four separate fractures (Figure 3.29) was subcored to obtain a cylinder with a height of 16 cm and a diameter of 8 cm. In order to perform the experiment in a single fracture and avoid secondary flow, a layer of silicon was spread on the two faces of the sample except the area corresponding to fracture II (Figure 3.29). First, the core was dried at 40° for about two weeks and fully 3D image was acquired by neutron tomography. Then, the bottom of the sample was brought in contact with water and capillary imbibition started. The wetting front displacement was observed at different time steps by 2D radiography. Each image was normalized by the radiography of the dry sample, such that differences from the dry state were highlighted and water distribution resulted (Figure 3.30). The front rose rapidly and, after a few minutes, the water phase was irregularly distributed. After that, an increase in moisture content in the already wet regions was observed. A tendency for water to accumulate at the boundaries was also observed. Once the imbibed sample could be considered in a quasi-steady state, a tomographic image was acquired and compared with the tomography of the dry sample, which showed a non-uniformly distributed water phase.

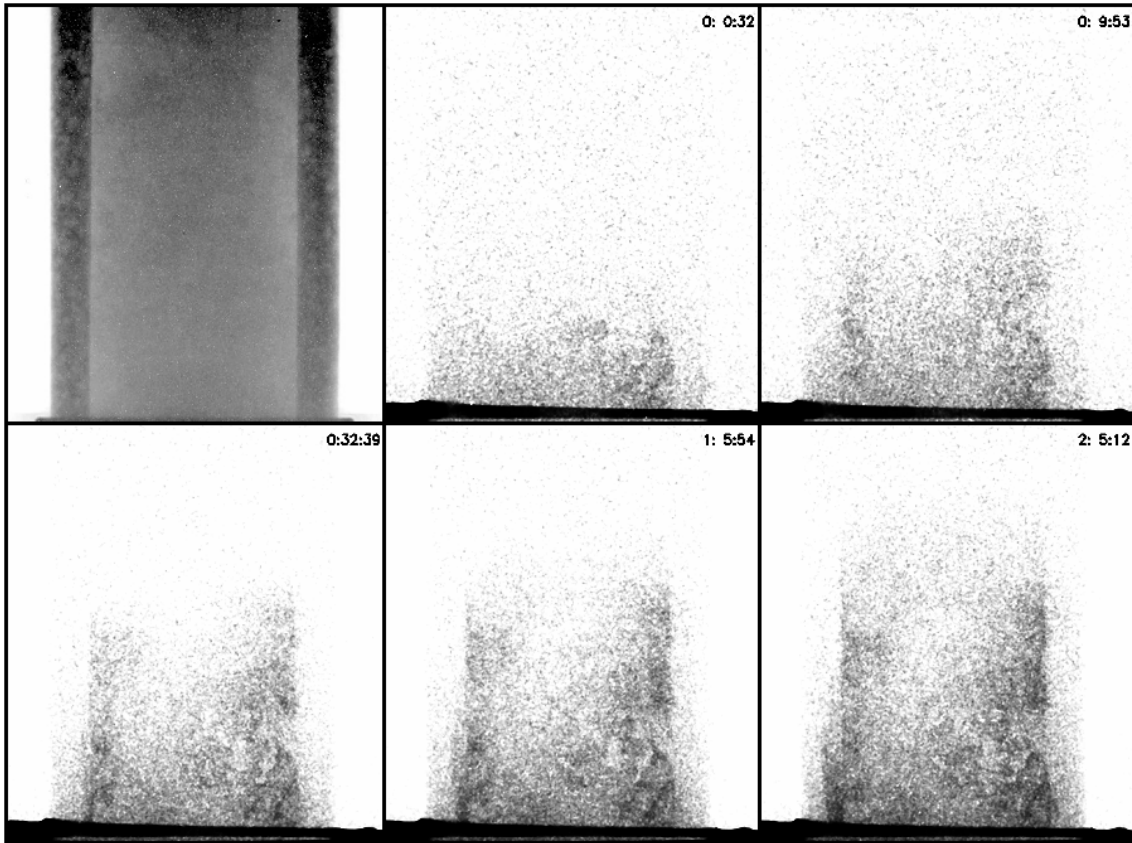


Fig. 3.30: Dry sample radiography.

Top-left corner: Dry sample radiography, projection in the direction perpendicular to the flow. Top-centre to bottom-right corner: ratios of the radiography at different times after capillary imbibition started to the dry sample radiography (top-left corner). These ratios show the water content (black) in the core at different time steps after imbibition started.

For the water displacement experiment, the sample was first dried at 40°C for over a month, then saturated under vacuum conditions with degassed water and flushed for over 30 hours. The acquired tomographic image showed an incomplete saturation of the fracture selected for the experiment. In contrast, the other fractures were partially filled with water, despite the care taken to avoid flow in all fractures. The large amount of water in the saturated sample strongly reduced the transmission of neutrons and made the signal to noise ratio worse than in the capillary rise experiment. Little could be observed by 2D radiography and no satisfactory measurement of the air front displacement was achieved. After draining the core for 1 hour by injecting air at 1.5 bar pressure, a tomographic image was acquired. Figure 3.31 shows the ratio of the saturated sample tomography to the drained sample tomography, which highlights the water distribution. The fracture was well visible and lay in a vertical plane in the middle of the volume, where darker regions corresponded to regions drained by air injection. This was evidence for an unevenly distributed air phase after drainage and testified to air flowing through preferential pathways.

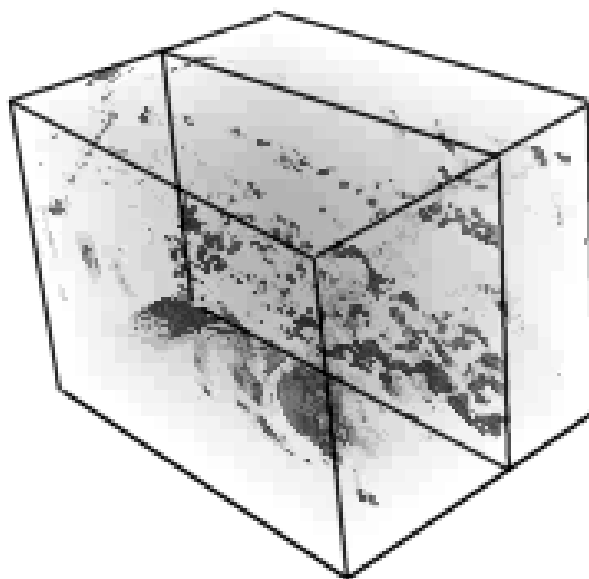


Fig. 3.31: Ratio of the saturated sample tomography to the drained sample tomography for a selected volume.

Black corresponds to a higher water content in the saturated sample than in the drained sample, thus to regions drained by air injection. Fracture II is well visible and lies in a vertical plane in the middle of the volume.

4 Hydraulic characterisation of the shear zone

A comprehensive hydraulic test programme was conducted to characterise flow and transport properties of the GAM site. Special emphasis was placed on determining the spatial variability of transmissivity in the shear zone. Reliable estimates of storage coefficient and static formation pressure distribution were further aims of the the hydrotest campaigns.

Section 4.1 gives an introduction into the applied hydrotest methods and presents a brief overview of the field programme. The hydrotest data base comprises a multitude of pulse tests, constant head and constant rate tests, which were performed between 1995 and 2000. According to Nagra's standard procedures for field testing, the first step in hydrotest interpretation was a diagnostic test analysis, conducted by the field contractor as part of the field reporting. Diagnostic hydrotest analyses (section 4.2) provide first rough estimates of hydraulic formation parameters and give further insight into formation characteristics (spatial variability of hydraulic parameters, hydraulic boundaries). However, during this early stage of data interpretation the picture of the hydraulic conditions at the site may still be immature and information from other test campaigns is not included. Therefore, a refined interpretation procedure is required which integrates further site-specific information (section 4.3). In this context, the joint interpretation of hydrotests with different injection boreholes and the analysis of crosshole responses are of particular value. Geostatistical methods are adopted to estimate the transmissivity distribution in the shear zone.

4.1 Field testing

4.1.1 Test equipment and experimental procedure

During the GAM site characterisation campaign, pulse injection tests, constant rate injection tests and constant head injection tests were performed. The different types of packer tests significantly differ from each other with regard to the radius of investigation and reliability of parameter estimates. In the following section, a brief review of experimental methods and field equipment is presented.

Figure 4.1 gives an overview of frequently applied packer test procedures. A pulse injection test (PI) comprises a sudden pressure pulse within the test interval caused by quick injection of water and monitoring the response of the system to the perturbation of the pressure field. The pressure recovery curve is mainly controlled by the hydraulic properties in the vicinity of the well, such that the pressure curve as a function of time can be used to provide an estimate of the interval transmissivity and system compressibility. In contrast, constant rate injection tests (RI) and constant head injection tests (HI) investigate the properties of a larger portion of the medium around the injection borehole. They consist of water injection, either at constant flow rate or at constant pressure, into a borehole over a period varying from several hours to several days. The test duration depends essentially on the hydraulic properties of the formation. During injection, the area of influence of the well extends to increasingly larger portions of the medium whose hydraulic pressure is perturbed. The pressure response to the forcing water injection is monitored at the injection well, as well as at other observation boreholes. Then injection stops and pressure recovery is observed for a time that is typically 2 to 4 times longer than the injection period. Both pressure increase and pressure recovery can be analysed by means of diagnostic plots, providing information about the hydraulic properties and the dimensionality of the flow, which can help in discussing the appropriate flow model to be employed. Moreover, cross-hole test analysis can be performed to evaluate interference reactions between the

boreholes and to assess possible heterogeneities in the shear zone properties, which may result in preferential pathways and channel flow.

Slug tests represent another convenient type of packer test; this test requires a minimum of surface test equipment. In the context of the GAM site characterisation activities, slug tests were not performed.

When static formation pressure is high, withdrawal tests may be the preferred approach, because withdrawal testing reduces the risk of borehole clogging by mud invasion. At the GAM site, withdrawal testing was not feasible due to the low static formation pressure.

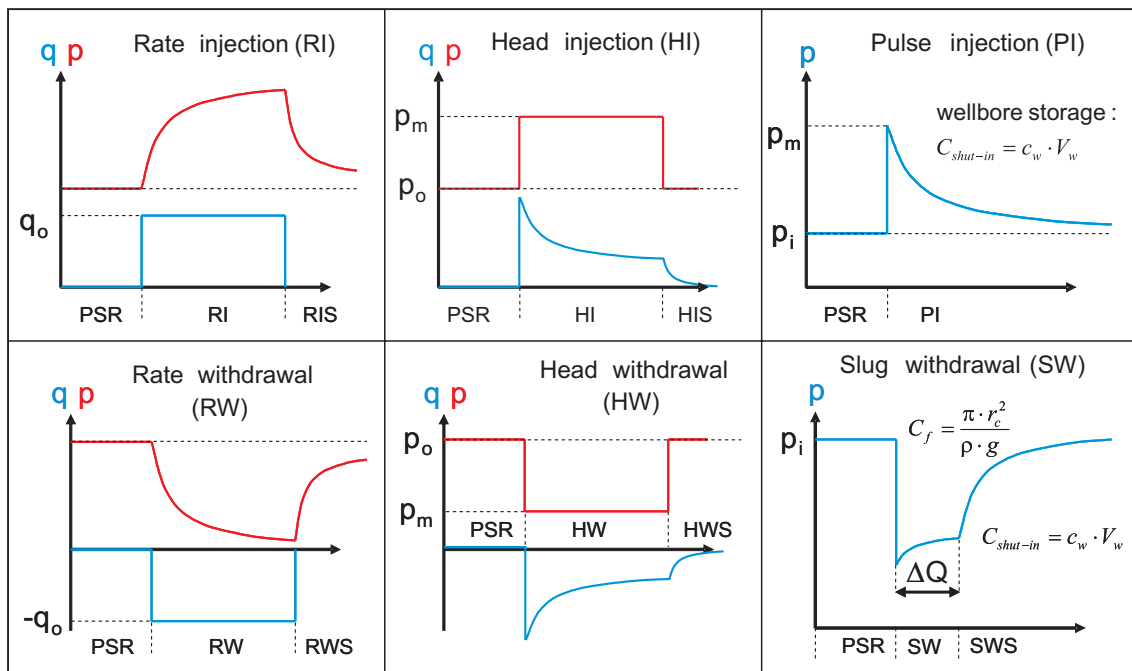


Fig. 4.1: Typical packer test procedures applied for hydraulic characterisation of rock formations.

The choice of the test procedure is based on the test objectives, on the formation characteristics and, last but not least, on the technical specifications of the (surface) equipment.

As mentioned in section 2.3, most of the boreholes at the GAM site were instrumented with hydraulic or mechanical double packer systems (cf. Figure 4.2a). Packer testing was only carried out in the test intervals which had been placed such that they packed off the reactivated shear zone. The surface equipment for packer testing consisted of a pressurised vessel, a flow controller unit and a simple flowboard (Figure 4.2b and c). Complementary measurements of the weight of the injected fluid were carried out to check for consistency with the flowmeter readings.

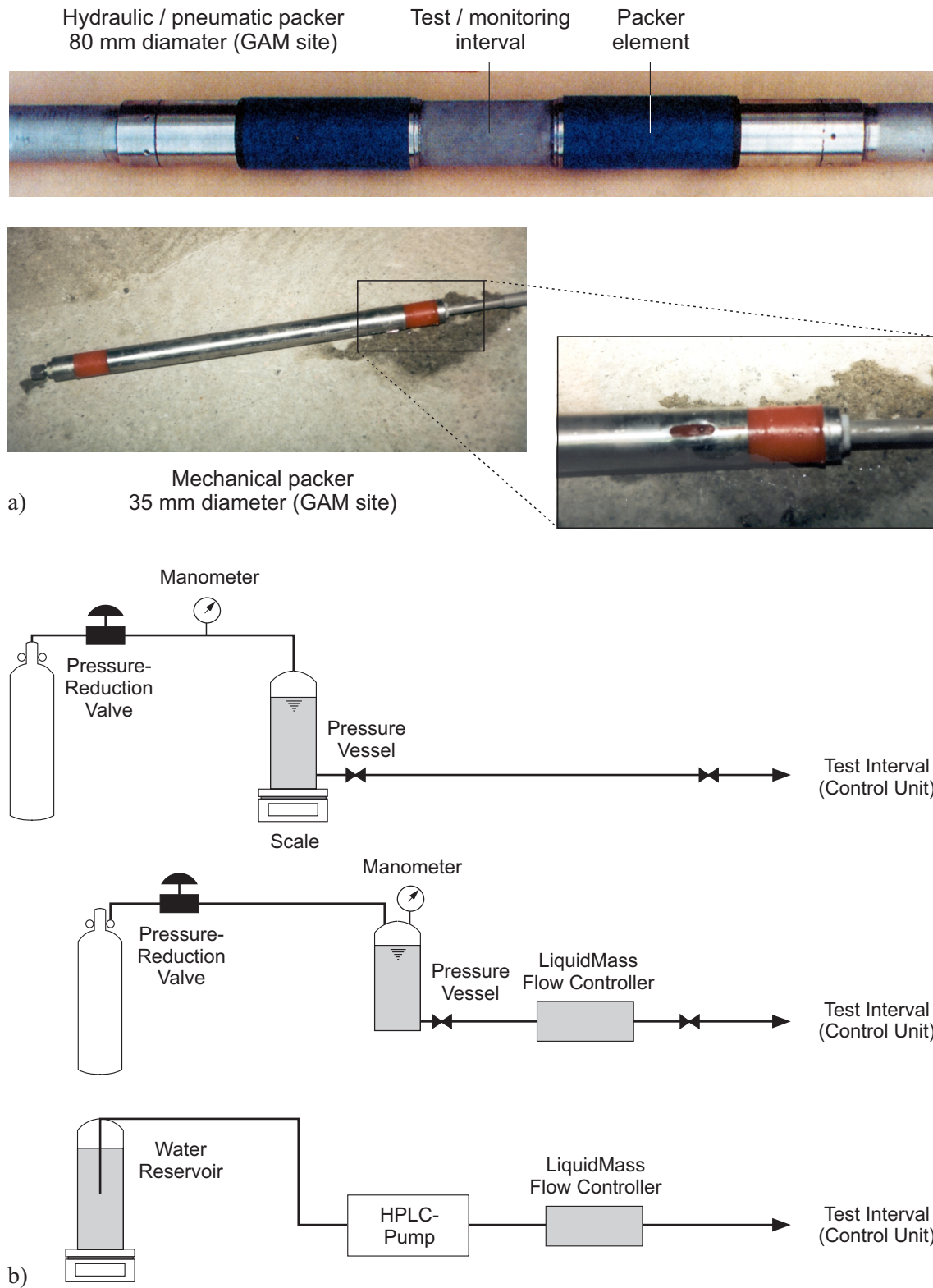


Fig. 4.2: Equipment used for hydrotesting at the GAM site: (a) downhole equipment – hydraulic and mechanical packer systems and (b) surface equipment for pulse tests and constant rate head tests.

4.1.2 Overview of the hydraulic test campaigns

Several hydraulic test campaigns were performed in the GAM shear zone, both during the former TPF project (Wyss 1996) and as part of the GAM project (Gemperle 1999b, Fierz & Piedevache 2000, Trick 2000 and Trick 2001). These measurements extend over a period of five years from January 1995 to December 2000 and include single borehole tests as well as cross-hole hydraulic tests. In particular, within the GAM experiment a first campaign was performed in November 1998 to characterise the hydraulic properties in the intervals of the newly drilled boreholes GAM98-002 and 98-004 (Gemperle 1999b). Additional hydraulic tests were performed during the three gas tracer test campaigns (GT1: Fierz and Piedevache 2000; GT2: Trick 2000; GT3: Trick 2001), with the main purpose of achieving well defined initial conditions required as a precondition for the subsequent gas threshold pressure test and the gas tracer test (i.e. to guarantee full saturation of the shear zone and displace any brine injected during the preceding solute tracer test). A summary of the hydraulic tests performed at the GAM site is given in Tables 4.1 (pulse tests) and Table 4.2 (constant head and rate tests), together with the corresponding references.

Tab. 4.1: Summary of the hydraulic tests performed in the GAM shear zone: pulse injection tests (PI).

Date	Boreholes	References
June 1995	TPF95.001 to TPF95.007	Wyss (1996)
November 1998	GAM98.002 and GAM98.004	Gemperle (1999b)
January 2000	GAM98.002	Fierz & Piedevache (2000)
December 2000	GAM98.001 GAM98.003 to GAM98.008	Trick (2001)

Tab. 4.2: Summary of the hydraulic tests performed in the GAM shear zone.

Cross-hole tests performed at constant-rate injection (RI) and constant-head injection (HI).
 ↓ indicates the injection borehole, whereas ⊙ denotes the observation boreholes.

Borehole	Crosshole hydraulic tests							
	Jun 95 (Wyss 1996)		Nov 98 (Gemperle 1999b)		Jan 00 (Fierz & Piedevache 2000)	Aug 00 (Trick 2000)	Dec 00 (Trick 2001)	
	RI1/HI1	RI2/HI2	RI3/HI3	RI4/HI4	RI5	RI6/HI6	RI7	RI8
AU83.034	⊙	⊙	⊙	⊙	⊙	⊙	⊙	⊙
FR87.001	⊙	⊙	⊙	⊙	⊙	⊙	⊙	⊙
FR87.003	⊙	⊙	⊙	⊙	⊙	⊙	⊙	⊙
FR89.001	⊙	⊙	⊙	⊙	⊙	⊙	⊙	↓
TPF95.001	↓	⊙	⊙	⊙	⊙	⊙	⊙	⊙
TPF95.002	⊙	↓	⊙	⊙	⊙	⊙	⊙	⊙
TPF95.003	⊙	⊙						
TPF95.004	⊙	⊙	⊙	⊙	⊙	⊙	⊙	⊙
TPF95.005	⊙	⊙	⊙	⊙	⊙	⊙	⊙	
TPF95.006	⊙	⊙	⊙	⊙	⊙	⊙	⊙	⊙
TPF95.007	⊙	⊙	⊙	⊙	⊙	⊙	↓	⊙
GAM98.001			⊙	⊙				
GAM98.002			↓	⊙	↓	⊙	⊙	⊙
GAM98.003			⊙	⊙		⊙	⊙	⊙
GAM98.004			⊙	↓	⊙	↓	⊙	
GAM98.005			⊙	⊙	⊙	⊙	⊙	⊙
GAM98.006			⊙	⊙	⊙	⊙	⊙	⊙
GAM98.007			⊙	⊙	⊙	⊙	⊙	⊙
GAM98.008			⊙	⊙	⊙	⊙	⊙	⊙

4.2 Diagnostic analysis

4.2.1 Fundamentals

Diagnostic analysis is the first step in the interpretation of packer test data. Usually, diagnostic test interpretation is part of the field reporting, aimed at providing a quick overview of the test results. This section gives a brief introduction, with emphasis on the following aspects:

- Flow model identification
- Characterisation of hydraulic boundaries (inner and outer boundaries)
- Rough estimates of hydraulic parameters

The purpose of the different types of packer tests was discussed in section 4.1. Thus, pulse tests are mainly suited for rough parameter estimates with a rather limited radius of investigation. Constant rate and head tests, on the other hand, are preferred for comprehensive characterisation of flow dimension and boundary conditions. In the following sections, the fundamentals of diagnostic packer test analysis are reviewed.

Pulse tests and slug tests

The classic analysis of pulse injection tests (PI) is based on Cooper's type curves (cf. Cooper & Papadopulos 1997, de Marsily 1986, Grisak et al. 1985). The ratio of the pressure change to the initial pressure change caused by the injection pulse is plotted versus the dimensionless time:

$$\beta = \frac{T \cdot t \cdot \pi}{C \cdot \rho_w \cdot g} = \frac{\beta t}{r_c^2} \quad (4.1)$$

where T is the transmissivity, C is the wellbore storage coefficient, ρ_w is the density of water and g is the gravitational constant. The type curves of the Cooper family are determined by a second parameter:

$$\alpha = \frac{\pi \cdot r_w^2 \cdot S}{C \cdot \rho_w \cdot g} = \frac{r_s^2}{r_c^2} \quad (4.2)$$

where r_w is the borehole radius (see Figure 4.3a), r_c is the radius of the casing and S is the storativity. The specific storage S_s can be derived from the storativity as $S_s = S/l$, where l is the length of the test interval.

Classic pulse and slug test analysis is based on a type curve matching procedure. First, the normalised pressure change P/P_0 is plotted on a logarithmic time scale (Figure 4.3b). Subsequently, the semi-log plot of the data is matched with the Cooper type curves (Figure 4.3c). The storativity S can be computed from the parameter α and the transmissivity from the dimensionless time for $\beta = 1$.

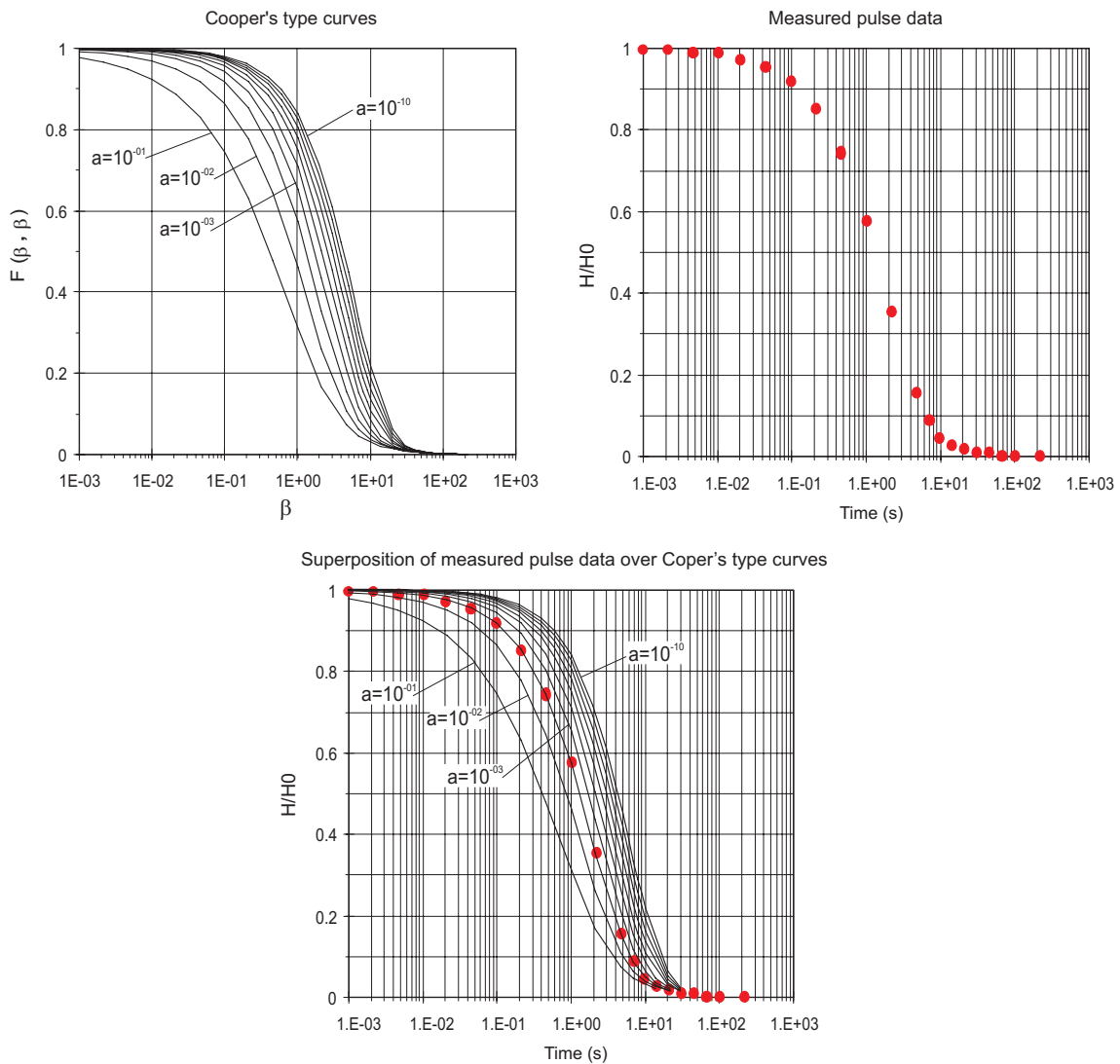


Fig. 4.3: Pulse test analysis by type curve matching: (a) Cooper family curves, (b) semi-log plot of pulse test data and (c) match of the test data with the best-fit type curve.

Constant rate and constant head tests

Advanced techniques have been developed in the field of hydrocarbon exploration for the diagnostic analysis of constant rate and constant head tests. Key references in this respect are Pickens et al. (1987) and Horne (1995). In this report, the diagnostic approach is applied for the analysis of constant rate tests. However, by the use of deconvolution techniques the approach is applicable to any type of packer tests (constant head tests, variable rate tests), as shown by Bourgeois & Horne (1993). Three aspects of diagnostic analysis will be discussed in more detail:

- (1) Analysis of flow dimension
- (2) Refined analysis of flow model
- (3) Parameter estimation

Analysis of flow dimension: the generalised concept of flow dimension has been introduced by Barker (1988). The flow dimension characterises the dissipation of a pressure perturbation from the source (borehole) into an infinite space. Three bounding cases of pressure dissipation are shown in Figure 4.4, namely linear, radial and spherical flow.

The flow dimension concept is of special importance when fractured rock or heterogeneous formations are being tested (Walker & Roberts 2003). Assuming a packer test is conducted in fractured rock where the test interval intersects a single fracture normal to the fracture plane, evidence for radial flow is seen when the fracture transmissivity is homogeneous. Deviations from radial flow conditions may indicate heterogeneous distribution of hydraulic properties in the vicinity of the test interval: flow could take place along a small number of localised flow channels (linear flow) or, at the other extreme, flow is spread in all directions by the effect of a superimposed network of background fractures (spherical flow). In any case, a simple flow dimension analysis provides valuable information about the flow system in fractured rock.

For a constant rate test, the flow dimension can be inferred by a series of diagnostic plots of the pressure transients during the pressure build-up phase. The graphs comprise a Cartesian plot, semi-log plot and square root plot. Assuming that the pressure transients are not disturbed by the effect of an outer boundary (see next section), the late time asymptotes are indicative for the flow dimension as shown in Figure 4.4.

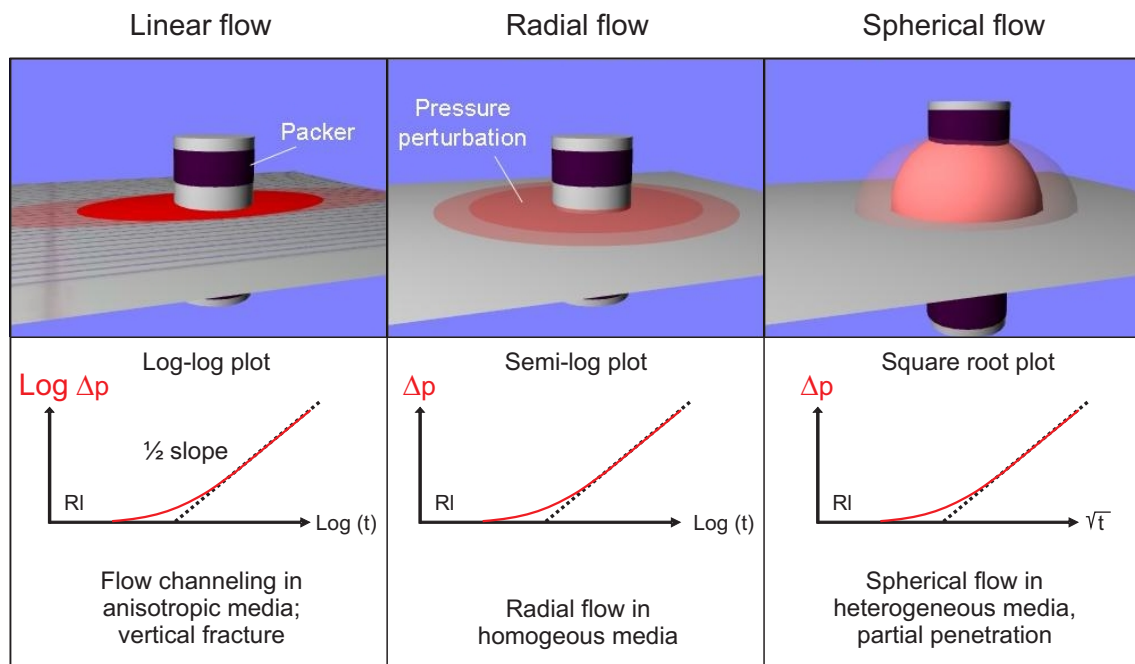


Fig. 4.4: Analysis of flow dimension: diagnostic plots for linear flow (Cartesian plot), radial flow (semi-log plot) and spherical flow (square root plot).

Refined analysis of flow model: the pressure transients are not only indicative for the flow dimension but may also characterise the near-borehole boundary conditions, the outer boundary conditions or the presence of complex flow responses (e.g. dual porosity systems). Such a refined analysis is performed by means of derivative plots (see e.g. Horne 1995). They consist of a simultaneous representation on the same graph of the logarithm of the pressure change ($\log \Delta p$) and $t \log \partial p / \partial t$ versus the logarithm of the time elapsed since injection started ($\log t$). The

advantage of this type of log-log plot is the ability to display, in a single graph, many characteristics of the system. Figure 4.5 shows some features of a typical log-log derivative plot (example from Horne 1995). Analysis of the early time data characterises the near-borehole conditions (e.g. wellbore storage, skin effects, fractured well), while the mid-term data are characteristic for the formation characteristics (homogeneous system, dual porosity system). Eventually, the late time response may indicate the existence of an outer boundary (e.g. intersection with a sealing fault / high permeability fault).

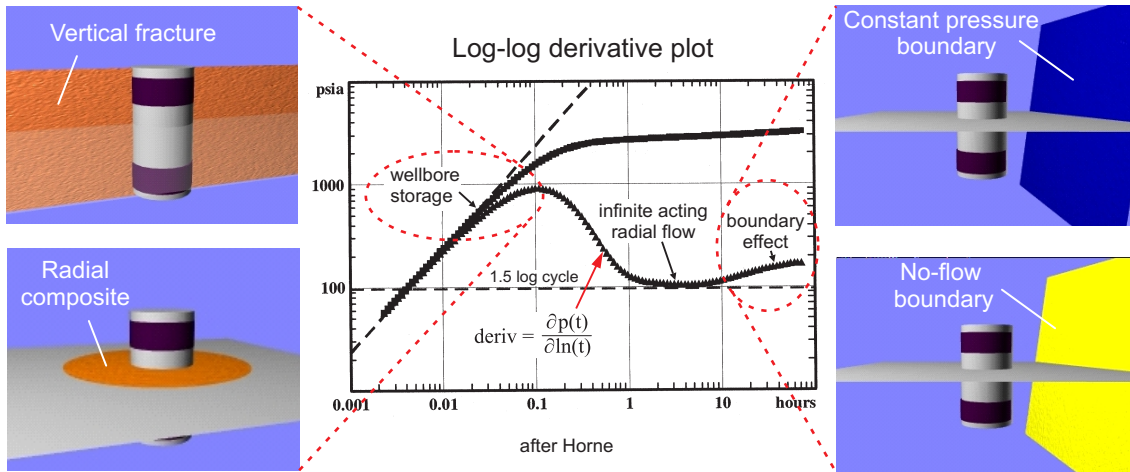


Fig. 4.5: Diagnostic analysis of flow dimension and flow boundaries by log-log derivative representation of a constant rate test.

Parameter estimation: For radial flow conditions, constant rate injection tests (RI) and constant head tests (HI) can be interpreted with the Jacob's method, which is a straight line matching technique based on a late-time approximation of the Theis solution (see e.g. de Marsily 1986). This analysis is applicable to the observation borehole as well as to the injection borehole. It consists of plotting the ratio of the pressure change to the flow rate versus the logarithm of t/r^2 , where r is the borehole radius for the injection borehole or the distance from the injection well for an observation borehole. Since the logarithmic approximation holds for the Theis solution at late time, the pressure change approaches a straight line. T can be estimated from the slope of the regression line per log cycle (note: ΔP is the piezometric head in [m], Q is the flow rate in [m^3/s]):

$$T = \frac{0.183}{\left. \frac{\Delta P}{Q} \right|_{\log \text{ cycle}}} \quad (4.3)$$

while the storativity is estimated from the zero pressure change intercept t_0/r^2

$$S = \frac{2.25 \cdot T \cdot t}{r^2} \quad (4.4)$$

Figure 4.6 shows a semi-log plot of a constant rate test performed in the GAM shear zone. Slope and intercept of the late time asymptote are the parameters to be determined. Interval transmissivity and storativity are inferred according to equations (4-3) and (4-4).

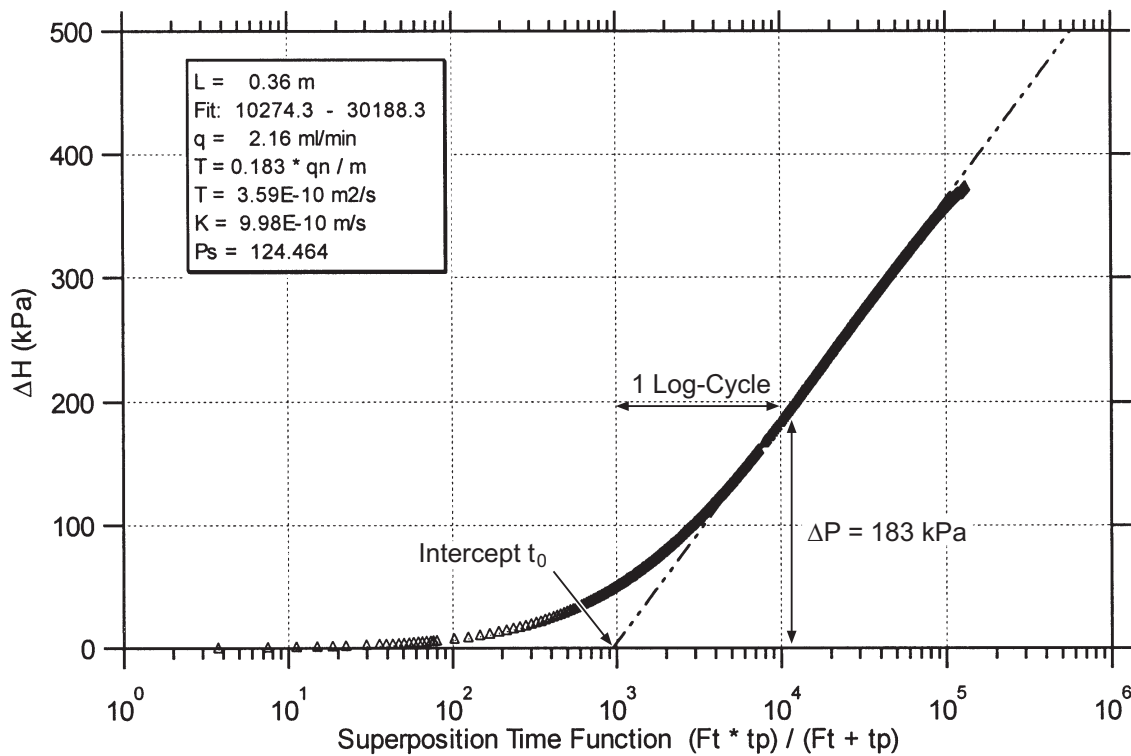


Fig. 4.6: Parameter estimation based on straight line analysis approaches: example of a constant rate test performed in the GAM shear zone.

4.2.2 Results

The extensive campaign of pulse injection tests in June 1995 was interpreted by Wyss (1996) using classic type curve matching techniques based on Cooper solutions. The data were re-interpreted as part of the GAM project using inverse modeling techniques (Ramajo et al. 2001). Two different automatic calibration approaches were considered: first the wellbore storage coefficient C was defined as a non-fitting parameter corresponding to the values used in Wyss (1996). In a second step, C was defined as an additional fitting parameter. The parameters estimated by different calibration methods are compared in Table 4.3. A strong local variability of the transmissivity field was observed: estimated transmissivities varied over three orders of magnitude (10^{-11} - 10^{-8} m²/s). A generally good agreement among the three methods was observed with regard to transmissivity identification. In contrast, different methods showed striking differences in the estimated storativity values, which suggested that estimates were unreliable. This might reflect the intrinsic uncertainty in estimating storativity from single well tests or might be due to local field heterogeneities around the well that make the homogeneous model used for interpretation inaccurate (Meier et al. 1998).

Data from constant rate injection (RI) and constant head tests (HI) were first analysed by means of log-log derivative plots and subsequently calibrated by means of Jacob's semi-logarithmic approximation. Figures 4.7a and b show the derivative plot and the semi-log plot of data from RI6 measured at borehole TPF95.002. The straight-line corresponding to the approximate Jacob's solution is also plotted. Derivative plots for data measured at the injection borehole GAM98.002 during RI3 and at the injection borehole GAM98.004 during RI4 are shown in Figures 4.7c and 4.7d, respectively.

Tab. 4.3: Hydraulic parameters obtained from PI data of the June 1995 test campaign.

The fitting parameters T and S are obtained by different fitting approaches: (i) manual calibration of S and T with fixed wellbore storage coefficient C (note: $Sw = C \cdot \rho_w \cdot g$) as reported by Wyss (1996), (ii) automatic calibration of T and S with fixed Sw and (iii) automatic calibration of T, S and Sw.

	Type curve matching			Automatic interpretation					
	Wyss (1996)			non-fitting parameter Sw			fitting parameter Sw		
	T(m ² /s)	S	Sw(m ²)	T(m ² /s)	S	Sw(m ²)	T(m ² /s)	S	Sw(m ²)
TP95.001	4.40E-09	1.18E-06	1.37E-07	8.11E-09	2.64E-08	1.37E-07	1.82E-09	1.46E-05	4.87E-08
TP95.002	2.70E-09	1.51E-06	1.76E-07	4.33E-09	1.21E-06	1.76E-07	1.68E-09	7.26E-06	1.15E-07
TP95.003	8.10E-11	3.75E-06	7.64E-08	9.45E-11	3.57E-06	7.64E-08	7.73E-09	7.69E-06	7.27E-08
TP95.004	2.30E-09	5.29E-06	1.07E-07	1.67E-09	1.37E-05	1.07E-07	3.97E-10	2.89E-04	6.07E-08
TP95.005	1.10E-11	1.34E-04	1.37E-07	1.25E-11	1.37E-04	1.37E-07	1.10E-11	1.80E-04	1.32E-07
TP95.006	1.10E-10	5.39E-05	2.74E-07	5.13E-08	1.03E-04	2.74E-07	7.66E-11	1.72E-04	2.60E-07
TP95.007	2.60E-08	1.54E-06	1.56E-07	6.17E-08	9.36E-13	1.56E-07	3.26E-08	2.09E-08	1.05E-07

An extended crosshole analysis of the log-log plots showed the presence of heterogeneous regions within the shear zone. Indeed, in many observation boreholes the infinite acting radial flow (IARF) conditions were never achieved. Two major groups were identified: the boreholes in the upper shear zone (AU83.34, FR87.001, FR87.003, TPF95.006, GAM98.007 and GAM98.008) and the boreholes in the lower shear zone (TPF95.001, TPF95.002, TPF95.004, TPF95.007, GAM98.003, GAM98.005 and GAM98.006). The boreholes in the upper shear zone showed a delayed first response and no IARF conditions; the boreholes in the lower shear zone showed a middle time negative half slope – which might indicate radial flow conditions or leakage occurring from the transitional zone around the fracture – followed by late-time stabilisation of the derivative reflecting a slow transition to radial flow. The diagnostic plots of boreholes GAM98.002 and GAM98.004 of RI3 and RI4 (Figs. 4.7c and 4.7d) showed an early time half slope, which suggested initial linear flow conditions, whereas at later time no clear IARF conditions appeared.

The hydraulic parameters estimated from RI tests (i.e. transmissivities and storativities) are summarised in Table 4.4. The comparison with Table 4.3 reveals more homogeneous transmissivity values calibrated on data from RI than those obtained by the interpretation of the PI tests. Considering, for instance, the June 1995 test campaign, transmissivity values from PI data range from 1.1×10^{-11} to 6.2×10^{-8} m²/s, whereas transmissivity from long-term RI data range from 8.6×10^{-11} to 5.1×10^{-10} m²/s. Comparable results were obtained by Wyss (1996), Gemperle (1999b) and Meier et al. (1998).

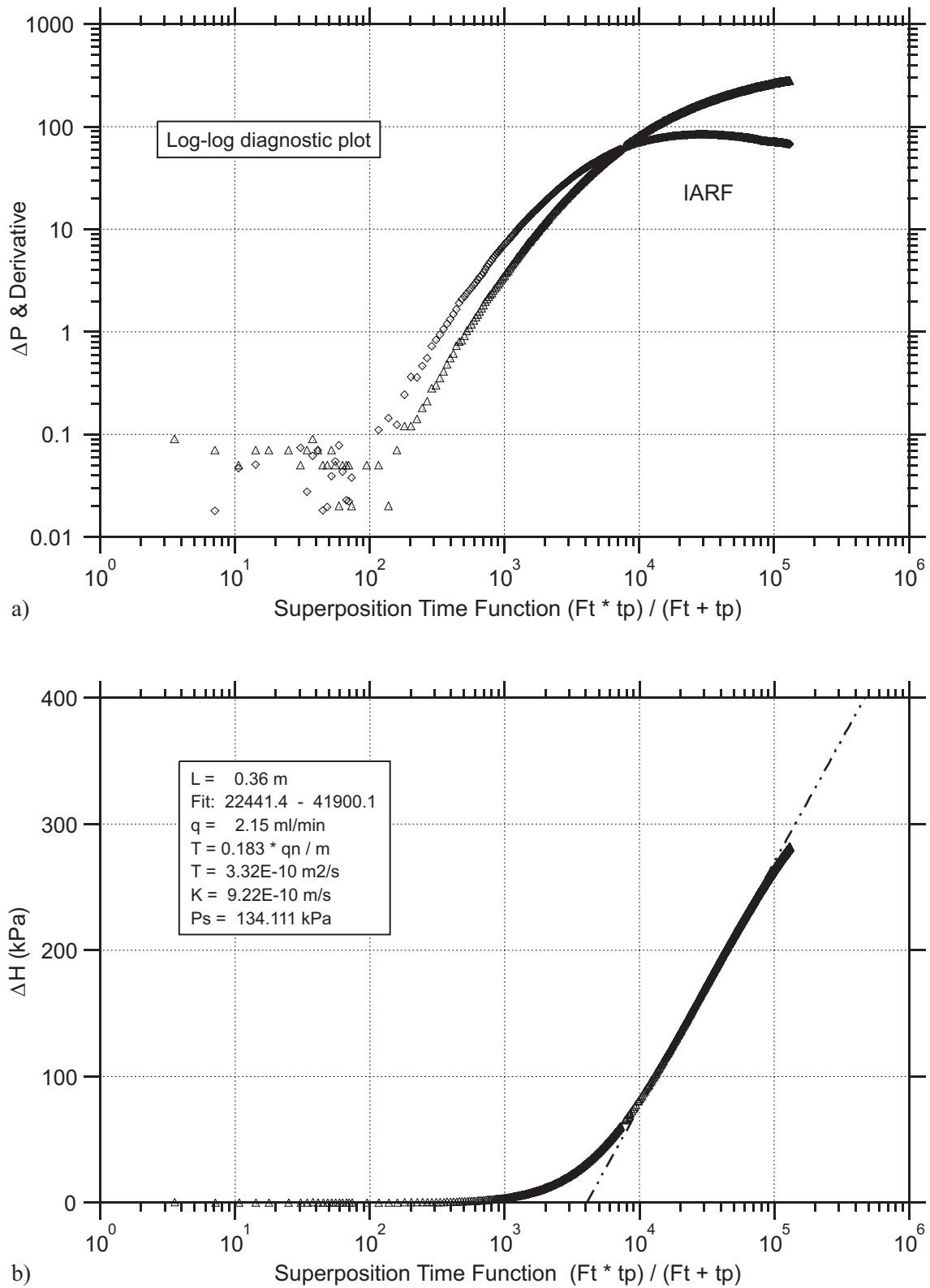


Fig. 4.7: Parameter estimation based on straight line analysis approaches.
Example of constant rate tests performed in the GAM shear zone: (a) derivative plot of test RI6 in TPF95.002, (b) semi-log of test RI6.

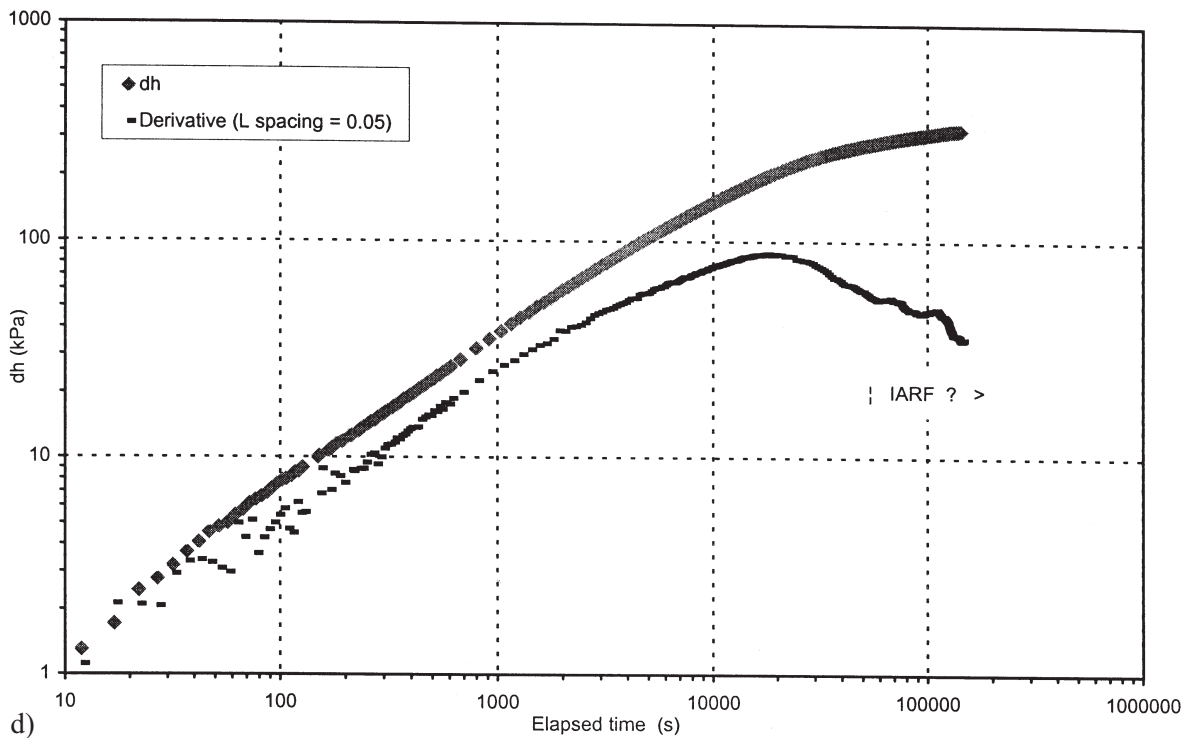
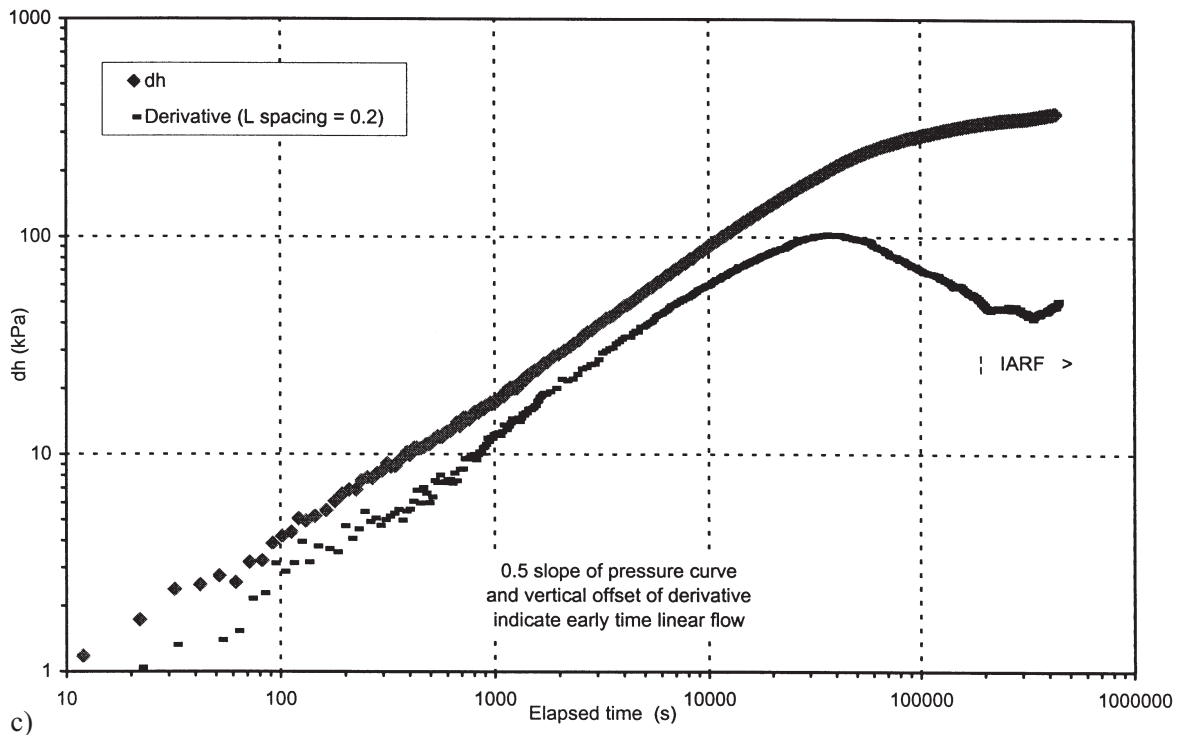


Fig. 4.7: (Cont.) Parameter estimation based on straight line analysis approaches.

Example of constant rate tests performed in the GAM shear zone: (c) derivative plot of test RI3 in GAM98.002 and (d) derivative plot of test RI4 in GAM98.004.

Tab. 4.4: Hydraulic parameters obtained from RI data by means of automatic calibration based on Jacob approximation of Theis solution at late time. ↓ indicates the injection boreholes.

Borehole	Constant rate injection tests									
	RI1		RI2		RI3		RI4		RI5	
	T [10 ⁻¹⁰ m ² /s]	S [10 ⁻⁶]	T [10 ⁻¹⁰ m ² /s]	S [10 ⁻⁶]	T [10 ⁻¹⁰ m ² /s]	S [10 ⁻⁶]	T [10 ⁻¹⁰ m ² /s]	S [10 ⁻⁶]	T [10 ⁻¹⁰ m ² /s]	S [10 ⁻⁶]
TPF95.001	↓	↓	4.06	1.35	3.85	2.05	6.27	2.75	2.89	3.13
TPF95.002	2.72	3.27	↓	↓	3.36	4.70	5.35	1.68	2.48	10.1
TPF95.003	2.40	12.3	4.66	7.13						
TPF95.004	3.85	18.1	4.27	4.25	3.93	2.56	6.29	2.50	3.72	3.89
TPF95.005	0.86	2.24	0.88	1.41	2.24	2.34	1.98	4.17	14.7	36.1
TPF95.007	2.84	5.20	5.06	0.70	3.66	1.05	5.82	2.44	3.92	1.29
GAM98.001					1.83	4.40	1.67	8.26		
GAM98.002					↓	↓	5.81	0.98	↓	↓
GAM98.003					2.27	397	2.85	9.33	338.63	9085
GAM98.004					3.63	2.19	↓	↓	3.88	3.12
GAM98.005					3.40	6.60	5.48	3.33	2.55	13.7
GAM98.006					11.00	20.6	10.90	2.01	3.26	115
GAM98.007					9.19	66.7	16.10	28.3	5.49	54.5
GAM98.008					5.68	10.0	10.10	11.2	7.41	18.3

4.2.3 Interpretation of the results

The analysis of the hydraulic rate injection tests revealed an unrealistically large variability in the storativity coefficients and a moderate variability in the transmissivity values when compared to the values obtained from PI data. The latter is an obvious consequence of the different test durations. RI tests contain spatially averaged information about the hydraulic properties of the rock formation, yielding an estimate of the effective transmissivity of the shear zone, whereas PI tests are expected to provide point transmissivities at the borehole location. The late time RI data considered by the Jacob analysis correspond to a region of influence in the metre range around the injection borehole, eventually covering the entire GAM site (Figure 4.8). Notably, the transmissivity values obtained from RI data are generally smaller than those obtained from PI data. In some cases, this observation was interpreted as an effect of small-scale heterogeneities around the borehole, such as a negative skin effect due to drilling and subsequent borehole flusing (Gemperle 1999b). However, it cannot be excluded that the higher variability of PI transmissivities originates from the heterogeneity of the GAM shear zone itself.

The large variability in the storativity field can be interpreted as the effect of heterogeneity of the transmissivity field rather than real fluctuation of the storativity field. Meier et al. (1998) studied the effects of using Jacob interpolation in a heterogeneous medium. They showed that Jacob interpretation, which assumes a homogeneous medium, still provided robust estimates for the effective transmissivities, whereas storativity estimates were unreliable. The fluctuations of

the inferred storativity field rather reflected different connectivities between the observation boreholes and the injection well: better connected boreholes showed a faster response to the injection signal, yielding an apparent storativity, which is smaller than the actual value. The tests RI3, RI4 and RI5 (Table 4.4) suggested an excellent connection between TPF95.002 and TPF95.007, between GAM98.002 and TPF95.007 and between GAM98.004 and GAM98.002. These preferential connections are illustrated in Figure 4.8. The existence of a channel between boreholes GAM98.004 and GAM98.002 is also supported by the half-slope behaviour at early time that was observed in the log-log interference derivative plots of RI3 and RI4 and indicated linear flow conditions (cf. Figure 4.7b and c).

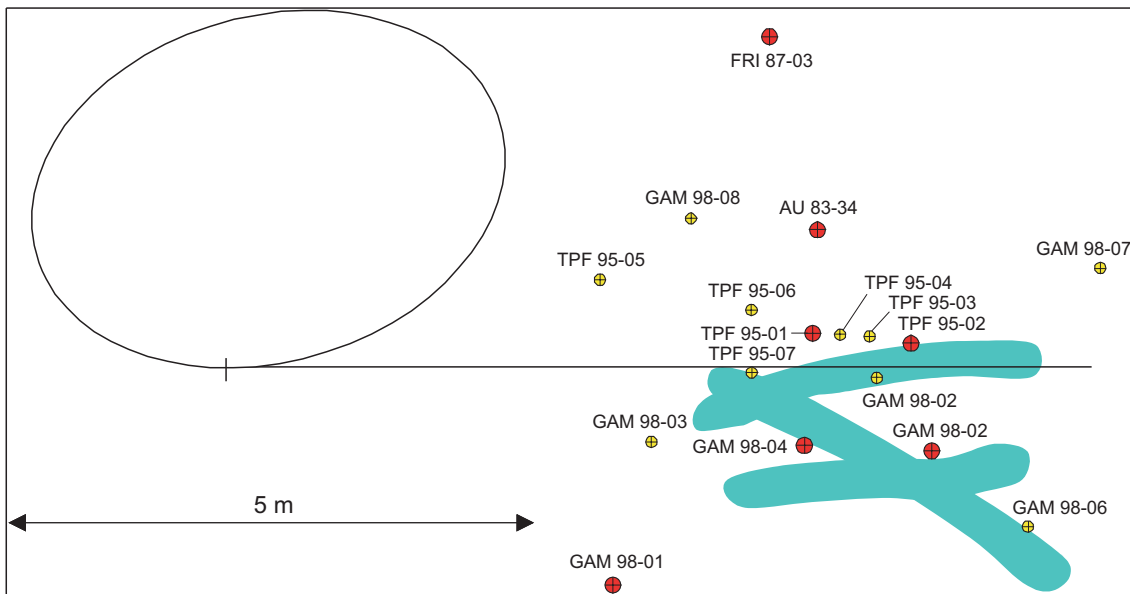


Fig. 4.8: Preferential hydraulic connections obtained by the analysis of storativity data from the constant injection tests (interpretation approach after Meier et al. 1998).

The diagnostic analyses showed various effects which can be interpreted as the results of heterogeneity on different scales: strong spatial variability of transmissivities identified from PI data, unrealistically dispersed storativity values, no IARF conditions in several boreholes, indications for channel flow both from very small storativity values and from early time half slope of the drawdown during RI. All these observations suggest a complex structure of the conductivity field in the shear zone, calling for a more complex interpretation and modelling tool that represents, in an appropriate manner, the spatial variability of the hydraulic parameters in the GAM shear zone.

4.3 Geostatistical inversion of hydraulic tests

4.3.1 Methodology

Geostatistics provides an efficient tool to deal with heterogeneity. The main assumption is that hydraulic parameters are random variables with well defined statistical properties, which are known a-priori. These variables have to be estimated via an inverse procedure in such a way that they are able to reproduce the available data (i.e. drawdown at the observation boreholes

during hydrotests) and eventually to predict the behaviour of the system under different conditions. The maximum likelihood estimation (MLE) was selected to identify the flow parameters. The latter are not supposed to be intrinsically random, but simply unknown: they are uncertain due to the lack of information and error measurements, but the model itself is still deterministic. Given a specific model structure to be known a-priori, MLE identifies among all possible set of parameters the optimum set as the most likely without requiring that the model is able to reproduce the system exactly. The main advantage of MLE is that a-priori information about the parameter statistics can be included in a rather simple manner (Carrera & Neuman 1986). This allows conditioning of the results of the geostatistical inversion both on head and transmissivity measurements. This means that the estimated transmissivity field coincides with the punctual measurements of T at the points at which they are available and yields an accurate simulation of the heads at the observation borehole.

Because of the scarcity of data, the choice of the model to be applied as well as the choice of the sets of parameters that are able to fit the measured data is virtually infinite. In order to avoid over-parameterisation and to reduce uncertainty, one has to reduce the number of parameters to be identified. The choice of an appropriate conceptual model plays an important role in this process and a wrong conceptualisation of the system can prevent the estimated parameters from being predictive, besides being able to reproduce the available measurements.

Since the thickness of the shear zone is negligible compared to its lateral extent, a two-dimensional model appears to be appropriate for reproducing head measurements. The domain was a square of $184 \times 184 \text{ m}^2$ centred on the access gallery, which was divided into 483 internally homogeneous zones (Figure 4.9). These zones are characterised by variable size, with a finer discretisation in the central region of the domain. This allows for obtaining a more detailed description of the region where measurements are located and avoiding an unrealistic number of parameters to be estimated for the outer region where no data are available; on the other hand, it reduces the influence of uncertain boundary conditions, by moving them away from the central area of interest. Whereas transmissivity varies from one block to the other, storativity was assumed to be homogeneous over the entire domain because it was shown by diagnostic analysis that the values obtained from conventional hydrotests are unreliable (Meier et al. 1998). Different boundary conditions were employed for steady-state data and for transient data from injection tests. Constant head at the outer boundaries and leakage at the tunnel were applied in the case of steady-state conditions. In the case of transient conditions, no-flow at the gallery, prescribed flow rate at the well and constant drawdown at the outer boundaries were imposed. Since no measurement at the boundaries was available, the hydraulic heads at the four corners of the domain were estimated during the inverse procedure and interpolated linearly.

A-priori information on the transmissivity of the heterogeneous zones, which is necessary for non-linear MLE of model parameters, was obtained from the analysis of pulse injection tests, which provides an estimation of the interval transmissivity. These data were interpolated by block kriging using the code KRINET (Olivella & Carrera 1987). The scarcity of data from the pulse injection tests did not allow for estimating a variogram for the punctual transmissivity measurements available in the shear zone, so that an exponential variogram was postulated with a sill $\sigma_{\ln T}^2 = 7.4$ and no nugget effect. As base case, a variogram with a range of 3.0 m in the horizontal and 0.3 m in the vertical direction was considered. The assumption of the anisotropic correlation function was based on the qualitative information about the preferential orientation of the highly connected zones. In order to compare the effects of the variogram on the identified field, other horizontal to vertical range ratios were considered (i.e. 0.5/0.3, 0.5/0.5, 1.0/0.3, 1.0/0.5 and 1.0/1.0). Data from RI1, RI2, R3, RI4, RI5 and steady-state heads were simultaneously used for parameter calibration. Data from RI6 were not used in the joint interpretation because some anomalous hydraulic responses were identified.

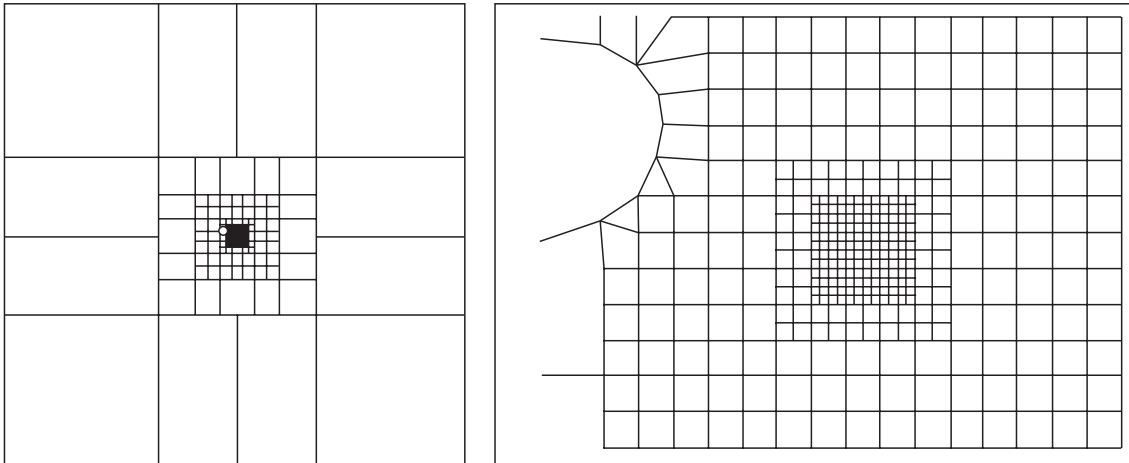


Fig. 4.9: The 483 transmissivity zones forming the two-dimensional flow model with size $184 \times 184 \text{ m}^2$.

Left hand side: full model. Right hand side: the most refined central part of the domain close to the tunnel.

4.3.2 Results

The transmissivities obtained by geostatistical inversion are shown in Figure 4.10. Despite the different statistical properties (i.e. anisotropy ratio) and the local pattern of the transmissivity, all fields are equally well conditioned, which means that differences between measured and calculated heads are smaller than the measurement errors (Ramajo et al. 1999). This indicates that the basic structure of the grid was captured; on the other hand it is evident that the solution of the inverse problem conditioned on the available data is non-unique. For the most part of the domain, the flow parameters are unconditioned because measurements were performed only at a few discrete locations. Hence, additional information and data could drastically change the structure of the transmissivity field, especially in regions far from observation boreholes.

The heterogeneity of the inverted fields reflects the heterogeneity of the point measurements (PI) of the transmissivity with its large spatial variability (Table 4.3). The joint inversion, as well as the diagnostic analysis, suggests the presence of preferential paths within the shear zone, which are characterised by high hydraulic conductivity. The results of the different approaches are consistent. In particular, all the transmissivity fields reproduce the good hydraulic connections between TPF95.002 and TPF95.007, GAM98.002 and TPF95.007, GAM98.004 and GAM98.002, which were identified by analysis of the storativity coefficients.

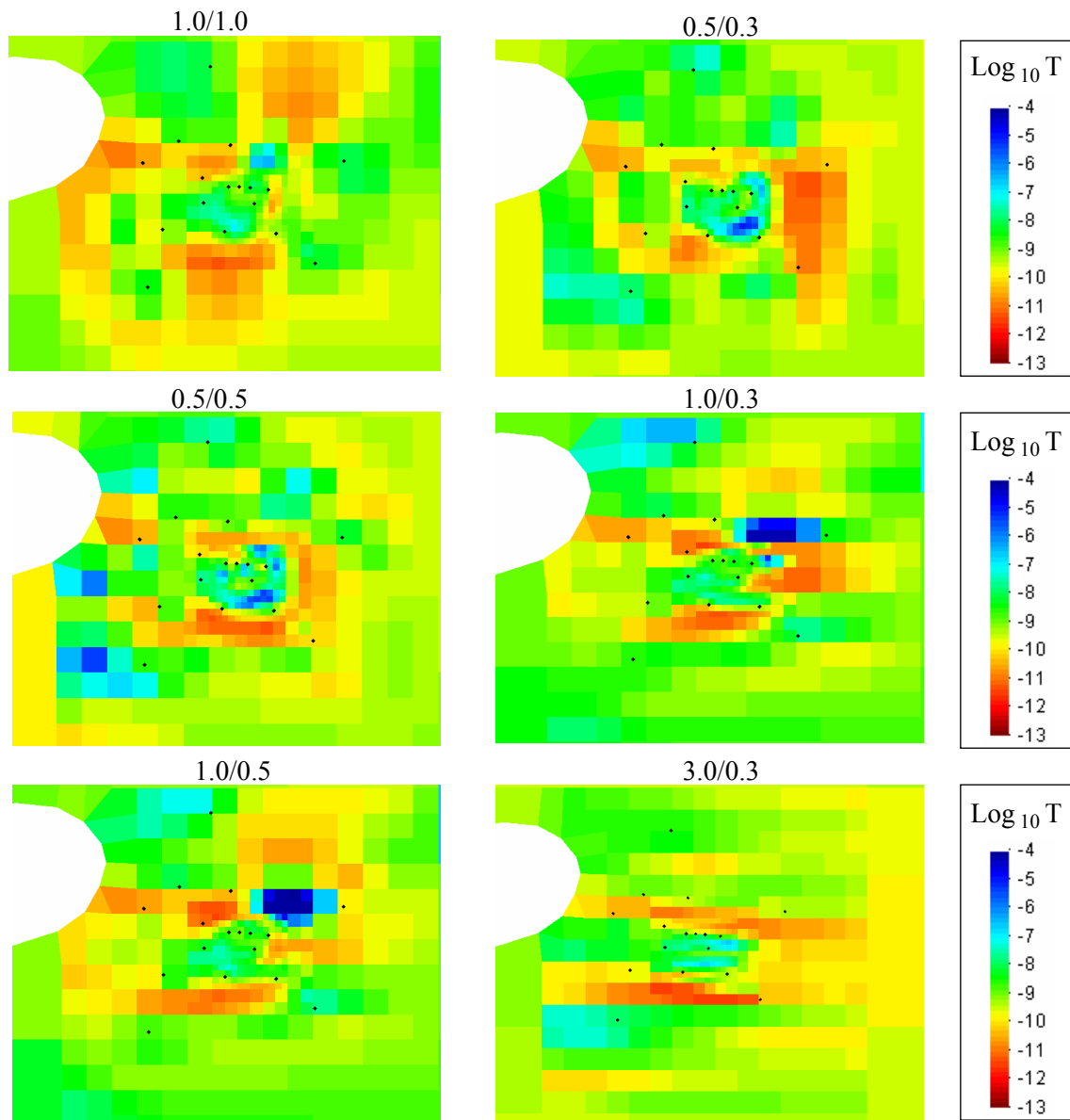


Fig. 4.10: Logarithm of transmissivity fields obtained by geostatistical inversion of data from RI1, RI2, RI3, RI4, RI5 and steady-state heads for different anisotropy ratios. The ratio of horizontal to vertical range of each field is indicated above the LogT map.

5 Solute and particle tracer tests

The design and performance of the solute and particle tracer tests in the GAM shear zone turned out to be a demanding task in various aspects. The short transport distances between 1 and 2 m and the low pore volume of the shear zone increased the need for precise mass balances of the injected and extracted tracers, respectively. The heterogeneity of the shear zone, on the other hand, impaired the design of the tests and introduced a considerable degree of uncertainty in the test interpretation. Hence, the tracer test programme was not only aimed at characterising the GAM shear zone, but, in a broader sense, at developing in-situ tracer test techniques and refining the interpretation tools. Equipment developments focused on the optimisation of the solute tracer injection procedure and on devices for the quasi-continuous detection of both solute and particle tracers. Innovative tracer test configurations (e.g. reversed flow fields) were investigated and numerical design calculations were initiated in support of the test optimisation. The in-situ tracer test results fed into the overall interpretation and synthesis procedure, in that they helped to refine the conceptual picture of flow and transport processes in the GAM shear zone. Last but not least, theoretical studies were devoted to the problem of upscaling of transport parameters in heterogeneous porous media.

Section 5.1 introduces the objectives of the tracer test programme and outlines the basic experiment concept. A summary of the field activities is presented in section 5.2, comprising the experimental set-up, test configurations, test procedures and a complete overview of test events in tabular form (dates, duration, test identification). Subsequently, a qualitative discussion of the experimental results is initiated, emphasising the distinct signatures of small-scale heterogeneities which are observed in the tracer test data. Section 5.3 is devoted to the quantitative interpretation of the solute tracer test data using the method of geostatistical inversion. Section 5.4 presents a theoretical appraisal of property upscaling of fluid flow in heterogeneous porous media. Finally, a brief summary of achievements is given in section 5.5.

5.1 Rationale, concepts and restrictions

Tracer tests are well known field methods for the characterisation of the transport behaviour of groundwater flow systems. As illustrated in section 2.1, a variety of complementary tracer test techniques is available, imaging different aspects of mass transfer in a heterogeneous porous medium. The use of complementary tracer test techniques for comprehensive characterisation of transport processes requires not only advanced field methods and measuring systems, but also refined interpretation approaches for the test analysis. The in-situ tracer test programme as part of the GAM experiment gave emphasis to both aspects, equipment development and development of interpretation tools. The specific objectives were:

- development and testing of advanced tracer injection / extraction systems, allowing for precise control of flow rates and injected / extracted tracer concentrations,
- improvement of modelling tools for the geostatistical inversion of solute tracer test data
- qualitative and quantitative characterisation of the spatial variability of transport properties in the shear zone and development of upscaling procedures,
- acquisition of data in support of the design for the successive gas tracer tests.

The need for precise mass balances of the injected and extracted tracers, respectively, is motivated by the fact that the effective pore volumes of the transport paths through the GAM shear zone are generally small when compared with the mixing volumes in the injection / extraction

systems. Consequently, the transport characteristics of the shear zone are masked to some extent by the mixing processes in the injection / extraction systems. The corresponding parameter uncertainties can be reduced by providing well defined flow and tracer injection conditions. The equipment developments focused, therefore, on injection devices which allow for a constant injection rate and a step-like input function for the solute concentration.

Various technical, financial and time constraints had to be met when planning the tracer test programme in the GAM shear zone. Thus, the total duration of the in-situ tracer test campaign was limited to a period of 9 months and some of the tracer detection devices were available only for a single tracer test. Furthermore, borehole locations and borehole instrumentation were given and should not be changed during the experimental phase, unless equipment failure was observed. Within this framework, the design options for dipole tracer tests can be broken down into the following categories:

- Choice of dipole direction
- Choice of injection / extraction ratio and flow rates
- Choice of the tracer

The choice of the dipole direction was constrained by the location and instrumentation of the available boreholes. Thus, the 86 mm boreholes were better suited for tracer injection / extraction than the 35 mm boreholes, because the test intervals of the mini-boreholes could not be flushed. Dipole distances < 2 m were hardly feasible due to the long test durations.

The injection / extraction ratio was restricted to flow ratios ≤ 1 , because the tracer tests were aimed at reaching 100 % tracer recovery. On the other hand, in order to ensure the exploration of a substantial pore volume of the shear zone, all tracer tests were conducted with flow ratios close to 1. The range of possible extraction rates was largely constrained by the given hydraulic conditions at the GAM site: the low static formation pressure in the order of 0.2 MPa (absolute pressure) did not allow for high withdrawal rates.

The combined use of particle and solute tracers was motivated by the fact that these different types of tracers could reveal complementary information on the microscopic pore structure of the shear zone, leading to a conceptual description of the shear zone in terms of a multi-porosity structure. Due to their finite size, colloids are excluded from the smallest pore throats and are mainly transported in the main flow channels, showing no diffusion into the matrix or stagnant pores. In contrast, solute tracers are transported by advection-dispersion processes, exploring the entire system of connected porosity. The following tracers were used in the different tests:

- Non-sorbing solute tracers (Uranine, Naphthionate, Sulphurhodamine)
- Fluorescent latex microspheres (diameter 1 μm)
- Nanospheres (diameter 1 nm)
- Biocolloids consisting of different bacteriophages (H40, MS2, H6) with a size ranging from 20 to 350 nm.

Different fluorescent dyes as solute tracers were used to keep the detection limit for these tracers as low as possible. Any residual tracer concentrations from previous tests would have impaired the detection of the times of first tracer arrival by enhancing the noise level for tracer detection.

The online detection units for the micro- and nanospheres were only available for a single tracer test (PT1, cf. section 5.2.2). Less restricted was the use of the biocolloids. The disadvantage of these particles was the time-consuming sampling procedure and subsequent analysis in the laboratory. Biophages were applied in 3 of 5 in-situ tracer tests (tests PT1 to PT3, cf. section 5.2.2).

5.2 The field experiments

5.2.1 Experimental set-up and procedure

All tracer tests were conducted in a dipole configuration. The injection / extraction boreholes were equipped with triple packer systems. The tracer injection / extraction was performed through the centre interval of the triple packer systems. The general layouts of the injection and extraction equipment are shown in Figures 5.1 and 5.2, respectively.

The injection equipment consists of the following elements:

- a water injection system
- a tracer circulation system

The water injection comprises a water source, a tracer reservoir, an injection HPLC pump and a flow-meter/controller. Water is supplied directly from a nearby borehole in order to ensure that water chemistry is comparable with the GAM conditions. During the tracer injection phase, water supply takes place through the tracer reservoir.

The circulation system includes a circulation HPLC pump, a flow-meter, two fluid exchange tanks and a fluorescence flow-through cell. The HPLC pump circulates water within the interval volume and the flow lines during the entire test sequence. Injection pressure is monitored continuously by a piezoresistive pressure transducer.

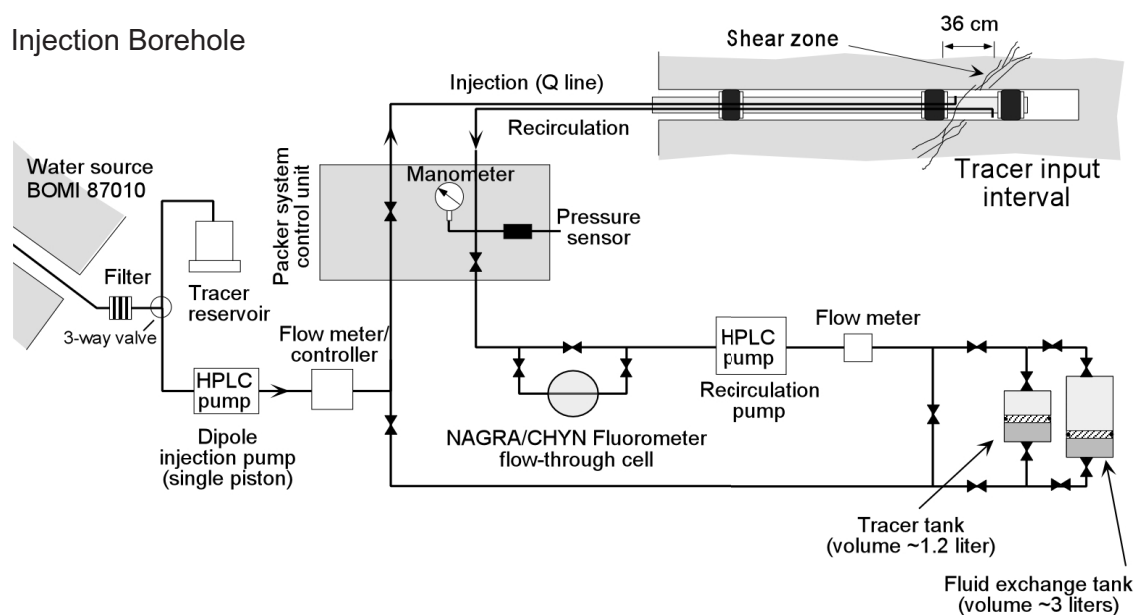


Fig. 5.1: Layout of the tracer injection equipment.

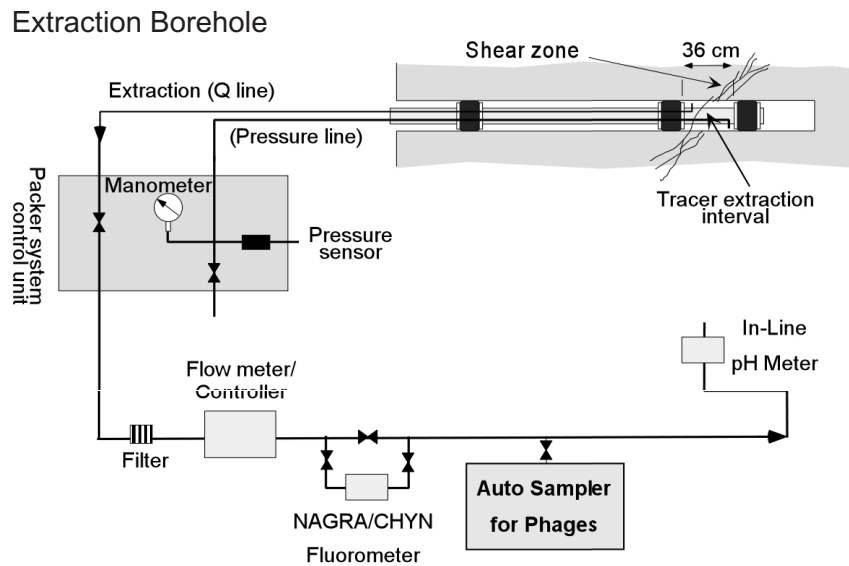


Fig. 5.2: Layout of the tracer extraction system.

The equipment at the extraction side is much simpler, consisting of a pressure line, which allows downhole pressure measurements, and an extraction flow line. Withdrawal is monitored and controlled with a flow controller, which maintains stable extraction rates. Tracer concentration measurements are performed with special devices in the extraction flow line. Concentrations of solute tracers and microspheres are measured in situ by online spectrofluorometry, while the concentration of bacteriophages is determined by laboratory analysis of automatically collected water samples. The total volumes of the extraction system (i.e. volume of the extraction interval, length and diameter of the extraction lines) were reduced as much as possible to minimise time delay between downhole tracer breakthrough and the breakthrough at the online measuring devices. For each tracer test the corresponding extraction volumes were documented to allow for the correction of the tracer arrival times (Kennedy 1999, 2000a and 2000b, Kennedy and Kleiner 2000).

The experimental procedure was the same for all solute and particle tracer tests. The procedure involved five steps:

- Establishing a stable dipole flow field at a constant flow rate.
- Replacement of the formation water in the test interval and in the lines. When starting the tracer injection, the bypass to the tracer tank was opened and the tracer was injected into the circuit until the first arrival of the tracer was detected at the flowthrough cell in the circulation line.
- Tracer injection and circulation. The bypass was closed and normal circulation was continued at a circulation rate which allowed complete mixing of the tracer within a timeframe of about 0.5 h.
- Removal of the tracer from the interval and the injection lines. In order to achieve a step-like input function, the tracer was removed as rapidly as possible at the end of the injection period by replacing it with the formation water contained in the fluid exchange tank. A similar procedure as for the start of the injection was applied.
- Continued injection of formation water over the duration of the test to maintain dipole flow conditions.

- Tracer concentration, flow rate and pressure at the interval were monitored during the entire test period. Since the triple packer system does not allow downhole measurements, pressure was monitored with a piezoresistive transducer in the circulation system.

5.2.2 Overview of tests and their configurations

The tracer tests performed in the GAM shear zone can be divided into two major groups: the earlier GAM solute and particle tracer tests performed between December 1998 and May 1999 and the solute tracer tests performed in August and September 1999. Each tracer test campaign was documented in a field report, presenting the test configuration, test procedures, test results, activity logbook and technical specifications of the instrumentation (Kennedy 1999, Kennedy 2000a & b, Kennedy and Kleiner 2000).

The earlier tracer tests PT1 to PT3 were characterised by a relatively long duration, from two weeks to a month, and by a complex instrumentation at the injection side. The optimisation of the instrumentation was a key issue, aiming at step-like input functions of tracer concentrations and well defined dipole flow conditions (Figure 5.1). Online detection devices for micro- and nanosphere measurements were used during the particle and solute tracer test PT1 between the boreholes GAM98.002 and GAM98.004 (Kennedy 1999). PT2 between boreholes TPF95.001 and GAM98.002 (Kennedy 2000a) and PT3 between boreholes TPF95.001 and GAM98.004 (Kennedy 2000b) were conducted only with biocolloids. The dipole configurations of PT2 and PT3 were less connected to each other and required significantly higher injection pressures than used during PT1, where the injection boreholes appeared to be particularly well connected.

Tab. 5.1: Summary of test configurations and bibliographic references.

Test		PT1	PT2	PT3	PT4	PT5
Tracers	Solutes	Uranine	Napthionate	Sulphur-hodamine	Uranine	Uranine
	Colloids	microsphere, nanosphere.	-	-	-	-
	Bacteriophages	H40	MS2	H6	-	-
Injection Borehole		GAM98.002	TPF95.001	TPF95.001	TPF95.004	TPF95.007
Extraction Borehole		GAM98.004	GAM98.002	GAM98.004	GAM98.004	GAM98.002
Inter-well distance [m]		1.2	1.7	1.2	1.1	1.9
Injection rate [ml/min]		1	1.5	1.6	1.5	1.5
Extraction rate [ml/min]		1	1.6	1.6	1.6	1.6
Tracer injection time [h]		20	30	17.5	4	4
Start / end of the test		9 Apr 99 to 5 May 99	4 May 99 to 27 May 99	5 Aug99 to 19 Aug 99	19 Aug 99 to 26 Aug 99	3 Sep 99 to 9 Sep 99
References		Kennedy 1999	Kennedy 2000a	Kennedy 2000b	Kennedy & Kleiner 2000	Kennedy & Kleiner 2000

In the second test phase between August and September 1999, another series of solute tracer tests was performed in the GAM zone. The principal differences from the earlier tests were the short duration and the absence of circulation at the injection interval. The purpose was to rapidly

characterise distances and directions in the shear zones that had not yet been tested and to evaluate the possibility of performing tracer tests with direct inline injection instead of the complex circulation system involved in previous tests. Several dipole configurations were considered, most of them producing anomalous pressure responses at the injection interval or no outflow at the extraction borehole. Two configurations were successful: PT4 between boreholes TPF95.004 and GAM98.004 and PT5 between boreholes TPF95.007 and GAM98.002.

A brief summary of the successful test configurations of both groups is given in Table 5.1. The borehole locations and the dipole directions are sketched in Figure 5.3. A comprehensive test description with technical details of the configurations and test procedures is found in the corresponding field reports (Table 5.1).

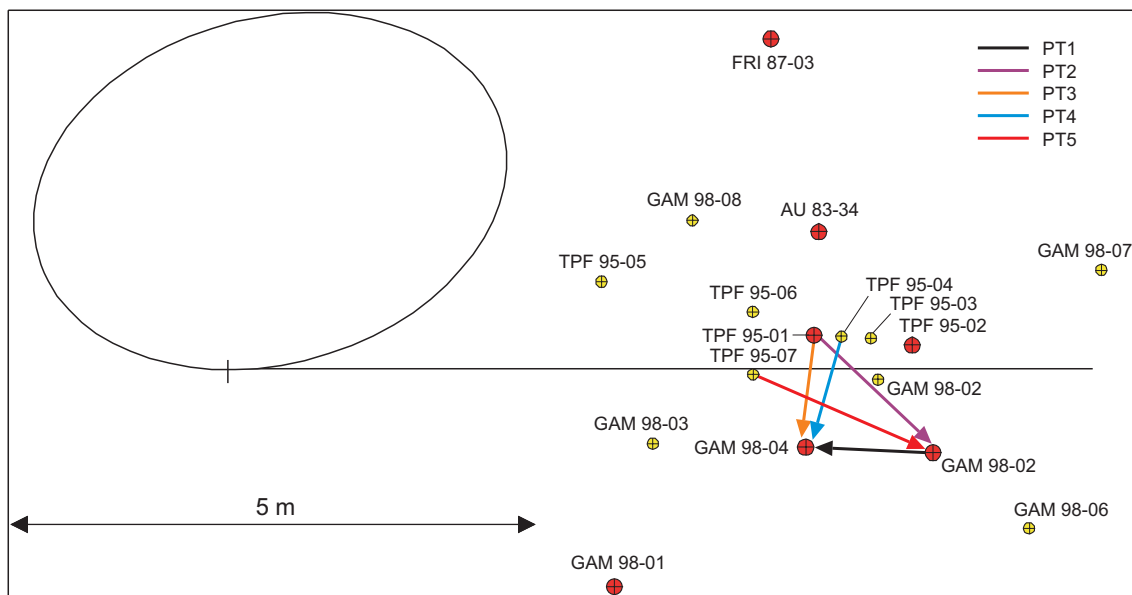


Fig. 5.3: Borehole locations and dipole configurations of the particle and solute tracer tests.

5.2.3 Tests results

The following section briefly highlights the experimental results obtained in the course of the solute and particle tracer test campaign between April and October 1999. Comprehensive documentation of all tests with graphical presentation of results and complete master databases on CD-ROM is given in the corresponding field reports (cf. Table 5.1).

From a technical point of view, no major problems were faced in the course of the solute and particle tracer tests PT1 to PT5. Stable dipole flow conditions were achieved in the shear zone by using electronic flow controllers, which guaranteed relatively constant injection and extraction rates over the entire duration of the tests. The dipole pressure field in the shear zone was less stable; pressure disturbances were mainly caused by external effects such as the ventilation conditions in the tunnel and seasonal fluctuations of groundwater level. A few pressure drops were related to technical problems with the injection pump.

Pre-tests were performed with different injection systems and different injections procedures. The tests showed that dilution effects in the test interval can be reduced significantly with the circulation system and the tracer injection procedure described in section 5.2.1. The rapid

formation water / tracer fluid exchange, followed by a continuous mixing process in the test interval, provided an excellent input signal of tracer concentration, characterised by short rise times and fall-off times and by a nearly constant tracer concentration during the injection period. Figure 5.4 shows the uranine input concentration record during PT1, which shows a variation of less than 2 % over the injection period.

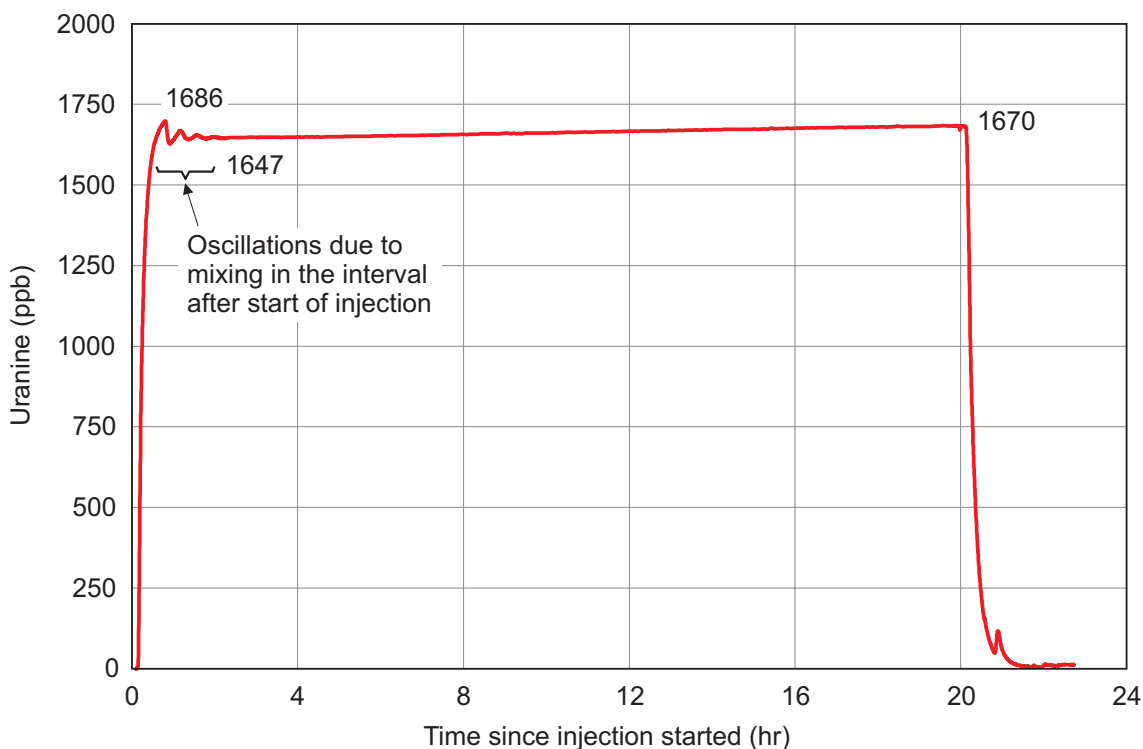


Fig. 5.4: Uranine input concentration record during PT1. The concentration is given in parts per billion (ppb).

On the extraction side, the main issue of concern was the minimisation of the total volume of the extraction system, which caused a time delay between downhole tracer breakthrough and the breakthrough at the online measuring devices. For this purpose, the fluorometer and the particle counter, respectively, were located as close as possible to the mouth of the extraction borehole. The volumes of the different components of the extraction system were documented in the field reports (Kennedy 1999, 2000a and 2000b, Kennedy and Kleiner, 2000). The downhole tracer breakthrough times were backcalculated by assuming plug flow through the extraction lines. The calculated offsets between downhole breakthrough and breakthrough at the detectors are documented in the field reports and ranged between 30 and 60 min, mainly depending on the extraction rate and the length of the extraction line.

Table 5.2 summarises the results of the tracer tests PT1 to PT5, including the average injection concentration, peak and normalised peak concentration in the extraction borehole, first arrival and peak arrival time and the total mass recovery in the extraction borehole. The arrival times correspond to the breakthrough at the detectors (fluorometer, particle counter, sampling port for phages).

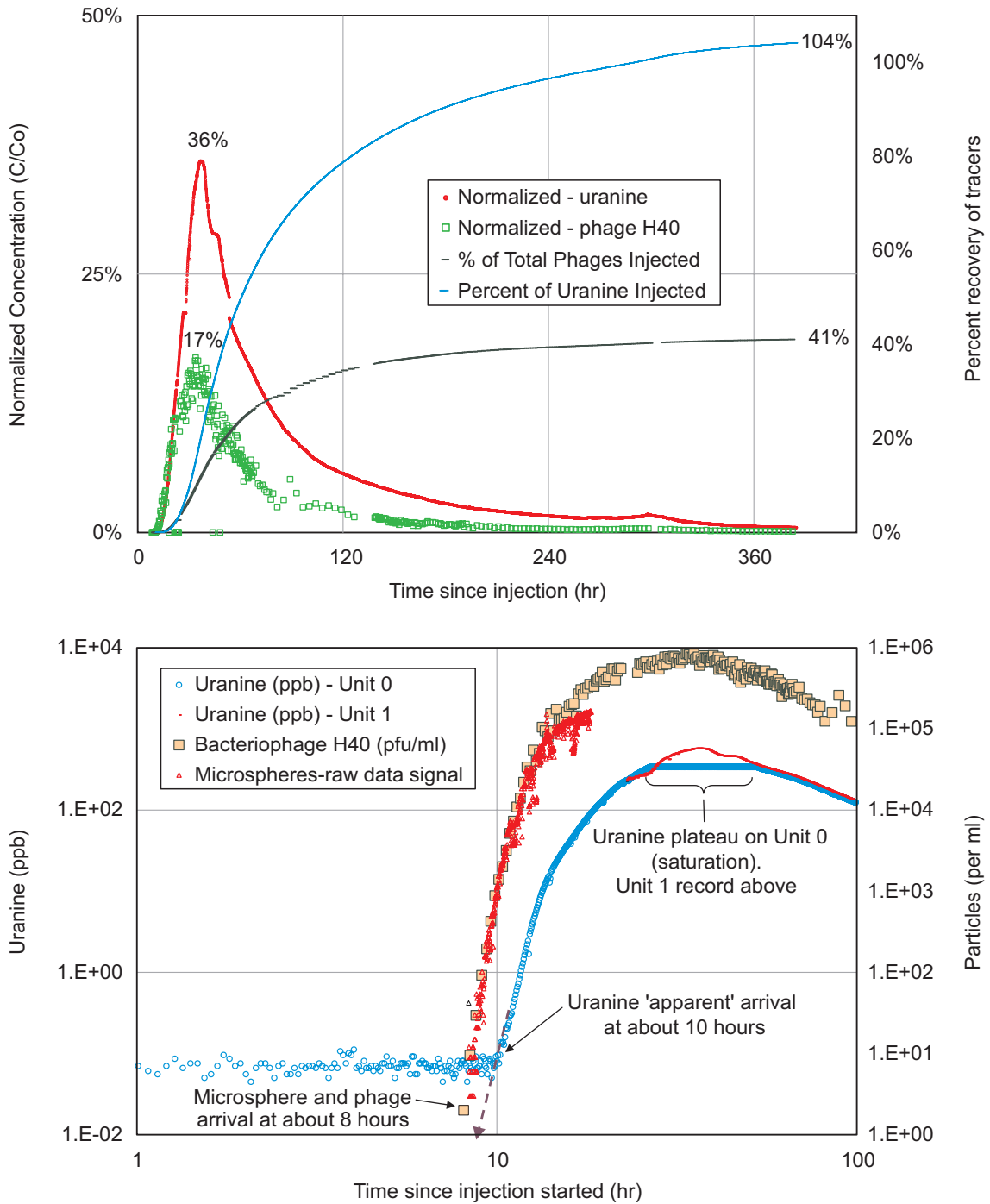


Fig. 5.5: Combined solute and particle tracer test PT1.

Top: breakthrough curves and total recovery, bottom: first arrival of Uranine and particle tracers on the log-log scale (further details in Kennedy 1999).

Tracer test PT1 was performed between boreholes GAM 98-02 and GAM98-03 with an interwell distance of about 1.2 m (Figure 5.3). Injection and extraction rate were about 1 ml/min (Table 5.1). Unexpectedly high breakthrough concentrations were recorded during PT1 with a normalised peak concentration of 0.34 for Uranine (Figure 5.5). The first arrival of the Uranine was detected after 9.5 h in the extraction fluorometer and the peak concentration was recorded

after 36.1 h. A mass recovery close to 100 % was reached at the end of the test after around 380 h. The particle tracers (micro- and nanospheres, phages) have significantly shorter breakthrough times of about 7 – 7.3 h (first arrival) and 32 – 34 h (peak arrival), but a distinct dependence of the arrival times on particle size is not observed. Even more surprising, the normalised peak concentrations of the phages and the nanospheres are nearly identical. Both the similar arrival times and the similar normalised peak concentrations indicate that particle exclusion is not a discriminating process for the adopted particle sizes (1 – 1000 nm). In other words, the typical width of the flow paths between the boreholes GAM98.002 and GAM98.004 is expected to be $\gg 1 \mu\text{m}$. The comparison of the arrival times and the normalised peak concentrations with the data for the solute tracer reveals another interesting aspect: the delay of the solute tracer indicates that the Uranine explores a larger pore volume of the shear zone. This secondary porosity seems to be characterised by small pore throats in the nanometer range, such that the pore space is not accessible for the nanospheres and phages.

The tests PT2 and PT3 were conducted with the tracer injection in borehole TPF95-01 and the extraction from the boreholes GAM98-002 and GAM98-04, respectively (cf. Figure 5.3). The inter-well distance was 1.7 m and 1.2 m. Injection and extraction rates were a factor of 1.5 higher than for PT1. Sodium naphthionate (PT2), sulphurhodamine (PT3) and the phages MS2 (PT2) and H6 (PT3) were injected as tracers. Micro- and nanospheres were not available for these test campaigns.

The tests PT2 and PT3 (Figure 5.6) were performed in the same area and on a similar scale as PT1. They exhibit some characteristic features, which support the assumption of a distinct small-scale heterogeneity of the pore space in the shear zone. Thus, mass recovery of phages is about two orders of magnitude lower than for PT1 (0.1 – 0.2 % recovery) and the extrapolated solute tracer recoveries are significantly less than 100 % (Kennedy 2000a and b). The peak concentrations at extraction occur earlier for bacteriophages than for the fluorescent dye, whereas the solute breakthrough exhibits a stronger spread. The observed differences suggest that solute and particle tracer transport in the flow fields of the tests PT2 and PT3 are controlled by different mechanisms. In particular, particle exclusion may be a more dominant process along the dipole directions of the tests PT2 and PT3.

The last two tests PT4 and PT5 between the dipoles TPF95-04 / GAM98.04 and TPF95-07 / GAM98-02 were carried out as pure solute tracer tests without particles. The inter-well distance was 1.1 m and 1.9 m, respectively. Injection and extraction rates were similar to PT2 and PT3, whereas the tracer injection time was considerably shorter than for the previous tests. The breakthrough curves of PT4 and PT5 are presented in Figure 5.7. A detailed description of the test procedures and the test results is given in Kennedy and Kleiner (2000).

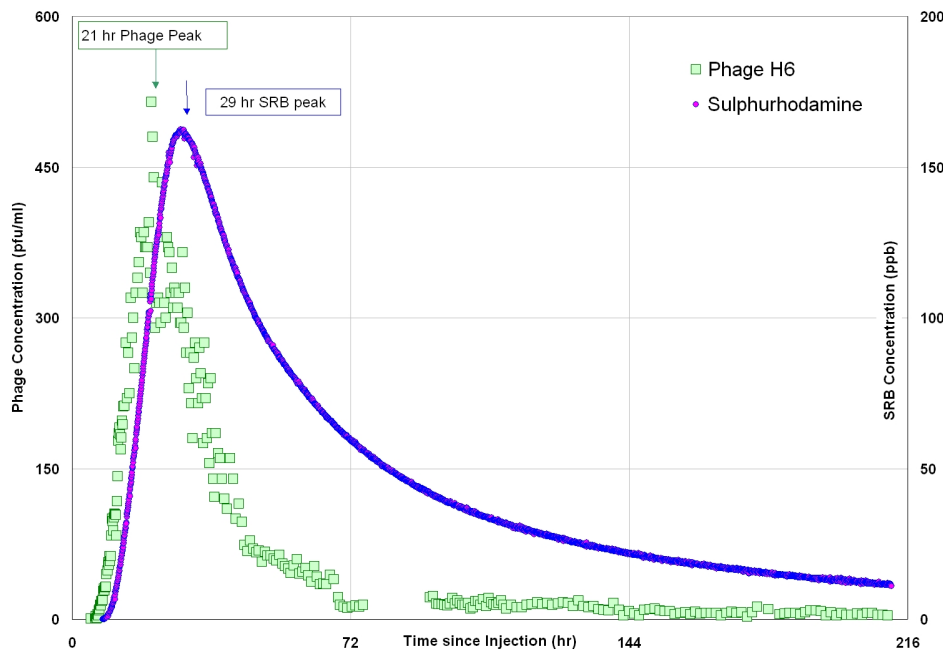
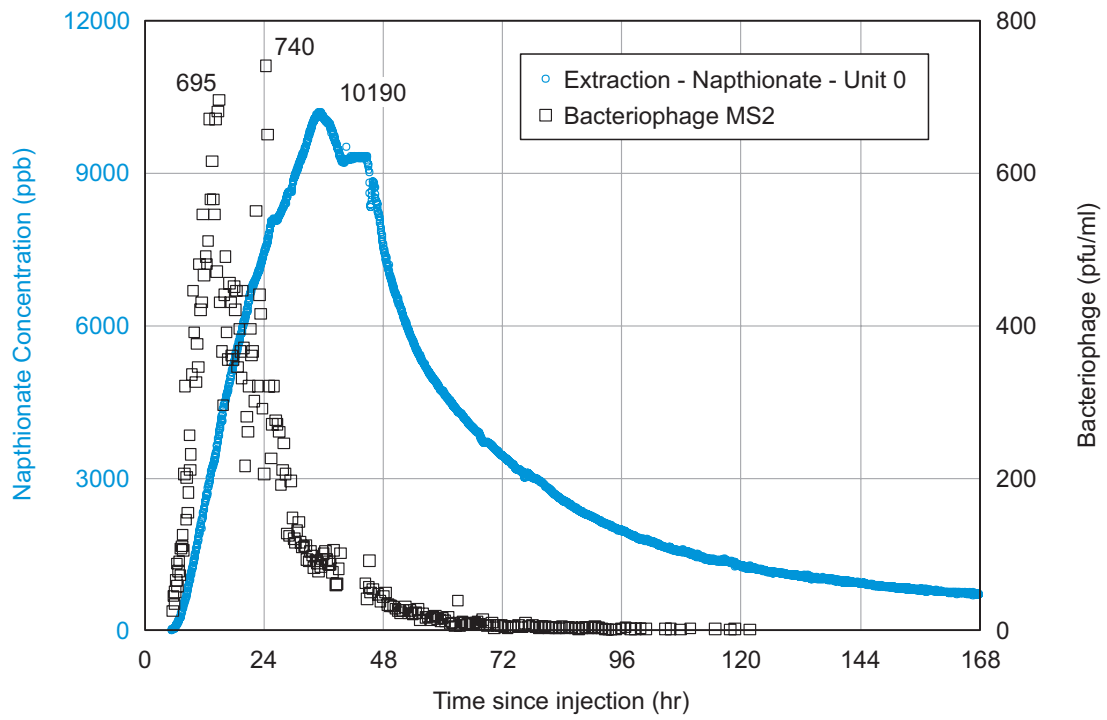


Fig. 5.6: Solute and particle tracer tests PT2 and PT3: Breakthrough curves of the solute and particle tracers at the extraction borehole.

Tab. 5.2: Summary of the results of solute- and particle-tracer tests.

		Average concentration at injection (C_0)	Peak concentration at extraction (C_{max})	Normalised peak conc. (C_{max}/C_0)	Time of arrival at detection device	Peak arrival time	Total mass recovery
PT1	Uranine	1650 ppb	558 ppb	0.34	9.5 h	36.1 h	90 – 104 % ^{a)}
	Microsphere	$2.4 \cdot 10^6$ sph/ml	n.d. ^{b)}	n.d. ^{b)}	7.3 h	n.d. ^{b)}	n.d. ^{b)}
	Nanosphere	$4 \cdot 10^{11}$ sph/ml	$8.5 \cdot 10^5$ sph/ml	2×10^{-6}	7.3 h	34 h	n.d.
	Phages H40	$4.6 \cdot 10^6$ pfu/ml	$8.6 \cdot 10^5$ pfu/ml	0.19	7 h	32 h	41 %
PT2	Naphthionate	28100 ppb	10190 ppb	0.36	4.5 h	34.7 h	64 %
	Phages MS2	$1.9 \cdot 10^5$ pfu/ml	696 pfu/ml	3.7×10^{-3}	< 5 h	14.3 h	0.2 %
PT3	Sulphurhodamine	983 ppb	163 ppb	0.17	7.1 h	27.2 h	58 %
	Phages H6	$8 \cdot 10^5$ pfu/ml	515 pfu/ml	6.4×10^{-4}	5.1 h	19.7 h	0.1 %
PT4	Uranine	76 ppb	6 ppb	7.9×10^{-2}	10 h	27 h	73 %
PT5	Uranine	150 ppb	11 ppb	7.3×10^{-2}	10 h	23 h	44 %

ppb – parts per billion

sph/ml – spheres per ml

pfu/ml – phages per ml

^{a)} 104 % mass recovery was obtained by Kennedy (1999)

^{b)} data loss due to unexpectedly high tracer concentrations (particle counter out of range).

5.3 Modeling of tracer tests including a-priori hydraulic information

The geostatistical inversion approach used for the interpretation of the hydraulic tests (section 4.3) was done by integrating the data of the five solute tracer tests. The fundamentals of the approach, the numerical implementation of the applied transport models and the results of the inversion procedure are described in greater detail in Ramajo et al. (1999, 2000, 2001, 2002). A brief summary of the interpretation of the tracer tests is given in the following sections.

Data from solute tests in the GAM shear zone were used to calibrate different models, which included a-priori information on the transmissivity field inferred from geostatistical inversion of hydraulic tests. Among the fields described in section 4.3, which were able to reproduce the hydraulic response of the fracture, one was chosen that had an anisotropy ratio 1.0/0.5. Storativity was homogeneous over the entire fracture. Constant head conditions were imposed at the outer boundary, no-flow conditions at the gallery and prescribed flow rate at injection and extraction boreholes. All transport parameters except pore volume were assumed to be constant in space. Three different models were considered to describe the specific pore volume (per unit of horizontal area), which is given by the fracture aperture b times porosity ϕ of the shear zone:

- the CONPHI model assumes spatially constant pore volume, i.e. $b \cdot \phi$;
- the KOZENY model assumes a relationship between porosity and transmissivity according to the Kozeny-Carman formula, i.e.

$$T = T_0 \frac{\phi^3}{(1-\phi)^2} \cdot \frac{(1-\phi_0)^2}{\phi_0^3} \quad (5.1)$$

- where $T_0=10^{-10}$ m²/s and $\phi_0=0.1$.
- the CUBIC model assumes that the porosity is equal to 1 (empty fracture) and that the pore volume varies as a function of the transmissivity according to a cubic law, i.e.

$$T = \frac{g}{\nu} \cdot \frac{b^3}{12} \quad (5.2)$$

where ν is the kinematic viscosity and g the gravity acceleration.

For each model, both a case with matrix diffusion (MD) and a case without matrix diffusion (NMD) were considered, such that in the end six different conceptual models were investigated. In MD models a sink/source term F_m is introduced, which represents the diffusive flux into/from the matrix at the interface, i.e.:

$$F_m = b\phi_m \cdot \frac{D_m}{b_m^2} \cdot \frac{\partial c_m}{\partial \eta} \Big|_{\eta=0} \quad (5.3)$$

where c_m is the concentration in the matrix, $2b_m$ the thickness of the matrix, D_m the molecular diffusion coefficient, ϕ_m the matrix porosity expressed as volume of the matrix void per unit of total volume and $0 < \eta < 1$ the dimensionless depth into the matrix.

Transport parameters were independently estimated from data for all five solute tracer tests performed in the GAM shear zone. The sets of transport parameters that best matched the measured breakthrough curves at the extraction borehole are shown in Table 5.3. In the NMD models, the longitudinal dispersivity α_L and the pore volume $b\cdot\phi$ were defined as fitting parameters for the CONPHI model. For the other two models, the fitting parameters were α_L and f , which is a dimensionless scaling factor for ϕ in the KOZENY model and for the fracture aperture (“transport aperture”) in the CUBIC model. For the MD models, $b\cdot\phi_m$ and D_m/b_m^2 were introduced as additional fitting parameters.

The models without matrix diffusion generally show a larger longitudinal dispersivity (α_L) than the models with matrix diffusion. The best-fit α_L values estimated for the models without matrix diffusion show a considerable spread (between 0.14 and 1.9 m for tests PT1 to PT5), which is an indication of the distinct heterogeneity of the shear zone on the scale of the tracer tests. For the models with matrix diffusion, the strong spread of the breakthrough curves is mapped in the D_m/b_m^2 parameter.

Another characteristic feature is observed for the fitting parameter $b\cdot\phi$ (CONPHI model) and the parameter f (CUBIC and KOZENY models), respectively: both parameters are larger when matrix diffusion is not considered. This is due to fact that the delay in tracer arrival has to be compensated by scaling the porosity ϕ when accounting for matrix diffusion. Specific pore volumes (CONPHI model) in the range 2.1×10^{-3} to 4.5×10^{-3} m for the models without matrix diffusion suggest transport in a very thin zone of the GAM shear zone. The corresponding f -parameters in the CUBIC model are between 55 and 90.

Tab. 5.3: Geostatistical inversion of the solute tracer tests PT1 to PT5 including a-priori hydraulic information.

Calibrated transport parameters for the six conceptual models providing the best match with measured breakthrough curves.

	PT1		PT2		PT3		PT4		PT5	
	CONPHI-NMD	CONPHI-MD								
$b\phi$ (m)	2.07E-03	1.80E-03	2.70E-03	1.80E-03	4.50E-03	2.70E-03	3.78E-03	2.34E-03	2.52E-03	8.46E-04
α_L (m)	1.50E-01	4.80E-03	5.50E-01	4.40E-01	5.00E-01	1.40E-01	2.00E-01	3.70E-02	1.50E+00	3.90E-03
$b\phi_m$ (m)		2.30E-04		8.30E-04		4.20E-03		1.40E-03		8.50E-04
$\frac{D_m}{b_m^2} (s^{-1})$		3.30E-06		2.50E-06		8.00E-07		3.60E-06		4.60E-06

	PT1		PT2		PT3		PT4		PT5	
	KOZENY-NMD	KOZENY-MD								
f(-)	4.00E-01	3.10E-01	4.10E-01	1.50E-01	7.00E-01	3.30E-01	6.20E-01	2.80E-01	3.50E-01	1.30E-01
α_L (m)	1.40E-01	1.00E-02	5.50E-01	8.00E-02	7.00E-01	9.70E-02	4.00E-01	1.60E-02	1.90E+00	1.00E-02
$b\phi_m$ (m)		2.80E-04		2.70E-03		5.00E-03		1.70E-03		1.50E-03
$\frac{D_m}{b_m^2} (s^{-1})$		2.60E-06		1.90E-06		7.00E-07		2.50E-06		1.50E-06

	PT1		PT2		PT3		PT4		PT5	
	CUBIC-NMD	CUBIC-MD								
f(-)	6.00E+01	4.00E+01	6.10E+01	3.00E+01	9.00E+01	3.50E+01	7.50E+01	3.80E+01	5.50E+01	1.50E+01
α_L (m)	1.50E-01	1.70E-02	7.00E-01	3.60E-01	7.00E-01	1.80E-02	3.50E-01	1.80E-02	7.00E-01	1.00E-02
$b\phi_m$ (m)		3.20E-04		1.40E-03		4.20E-03		1.81E-03		1.30E-03
$\frac{D_m}{b_m^2} (s^{-1})$		1.20E-05		2.70E-06		7.00E-07		2.10E-06		3.10E-06

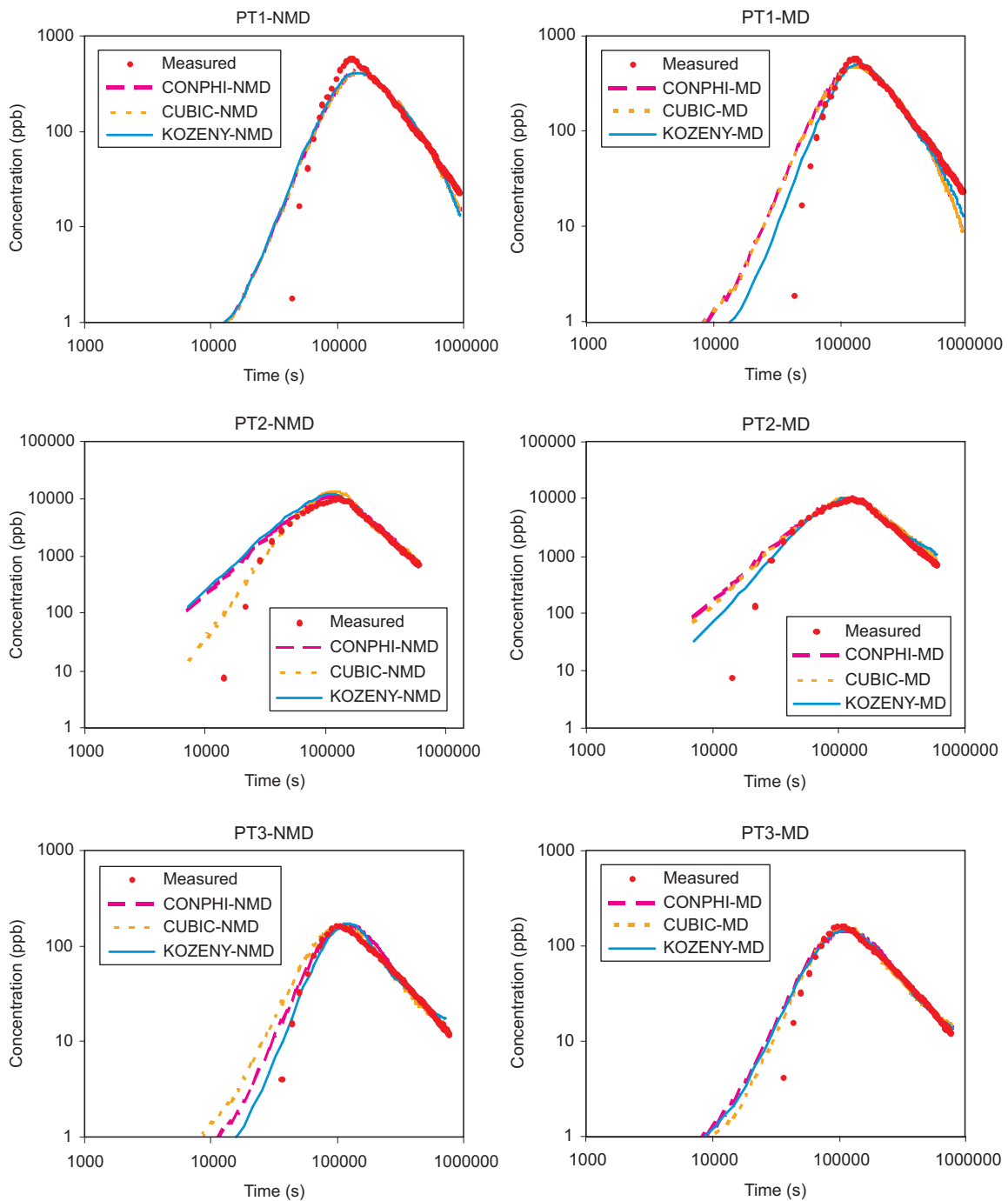


Fig. 5.7: Geostatistical inversion of tracer tests PT1 to PT3.

Comparison between measured breakthrough curves and breakthrough curves computed after the parameter calibration of the tracer tests PT1, PT2 and PT3 with the three models CONPHI, CUBIC and KOZENY. The models on the right hand side consider matrix diffusion (MD) and the models on the left hand side do not.

The measured breakthrough curves are shown in Figures 5.7 and 5.8, together with the breakthrough curves computed using the best-fit parameters. It is not surprising that differences between the different conceptual models are minor. The agreement between measured and computed breakthrough curves is generally better when using the CUBIC and the KOZENY

models together with the transmissivity field derived from the geostatistical inversion. The performance of these two approaches is very similar, which indicates that the solute tracer experiments are not suitable for an efficient discrimination between these two models.

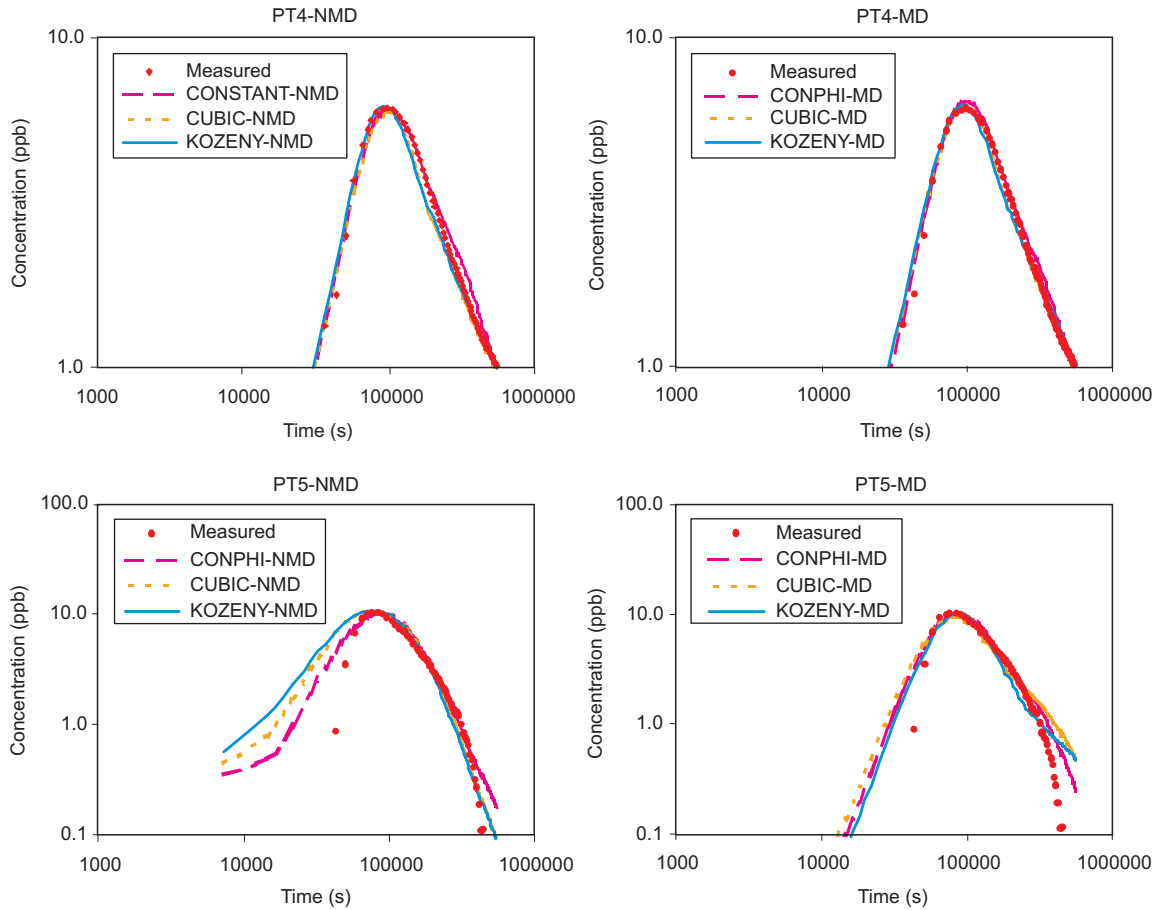


Fig. 5.8: Geostatistical inversion of tracer tests PT4 and PT5.

Comparison between measured breakthrough curves and breakthrough curves computed after the parameter calibration of the tracer tests PT4, and PT5 with the three models CONPHI, CUBIC and KOZENY. The models on the right hand side consider matrix diffusion (MD).

5.4 Theoretical study of solute tracer tests

The theoretical study of tracer tests was twofold. On the one hand, it was aimed at investigating scale effects of transport properties in a heterogeneous 2-D structure when inhomogeneous flow fields (dipole fields) are considered. On the other hand, the impact of the microstructure of the shear zone on solute transport was assessed: particular emphasis is given to the discriminative power of solute tracer tests to distinguish between fault gouge filled and open fractures.

5.4.1 Upscaling of solute transport in a non-uniform flow field

Part of the modelling activity was devoted to investigating the large-scale effects of small-scale velocity fluctuations, which are produced by small-scale variability of medium properties. The small-scale flow was assumed to be Darcian and characterised by a typical length λ , which

represents the heterogeneity scale of the medium and consequently the typical length of velocity fluctuations. The ratio of the small-scale length to the characteristic length L of the observation scale, $\varepsilon = \lambda/L$, is used to distinguish between two cases: an asymptotic case characterised by $\varepsilon < 1$ and a pre-asymptotic in which ε is finite.

The asymptotic case for a radial diverging flow field was studied by Neuweiler et al. (2001) by means of perturbation theory and by Attinger et al. (2001) by means of homogenisation theory. It was found with both approaches that the large-scale equation describing solute transport is still an advection-dispersion type equation in which the local dispersion coefficient is replaced by a macrodispersion coefficient. The latter describes the large-scale effects of small-scale fluctuations of the velocity field from the mean velocity that are not explicitly described, and depends on the mean velocity field.

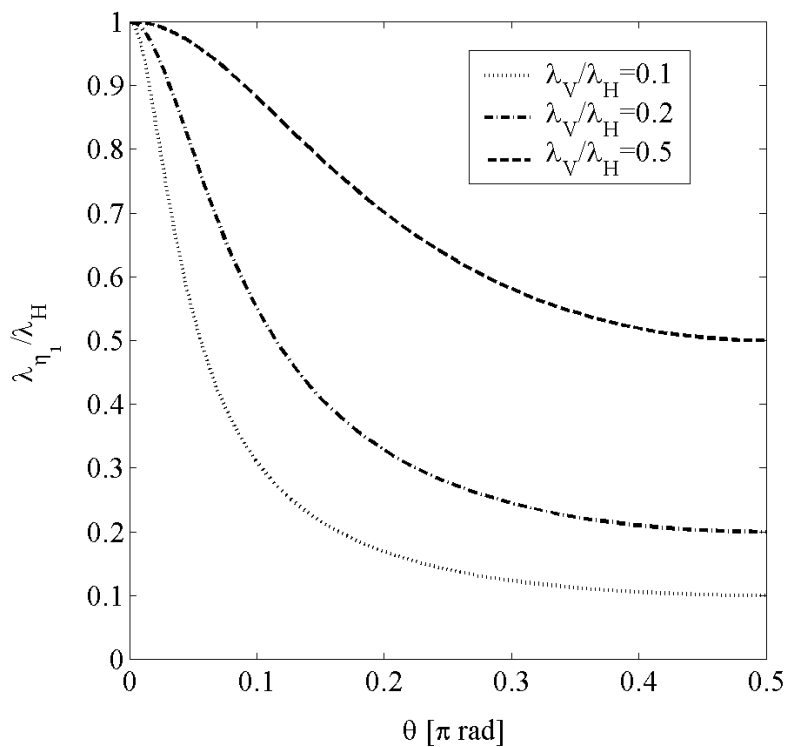


Fig. 5.9: Longitudinal dispersivity as a function of θ .

The asymptotic longitudinal macrodispersivity is proportional to the correlation length of the conductivity field in the flow direction, λ_{η_1} , and depends on the angle θ that the latter forms with the principal axes of anisotropy H and V . The results for three different anisotropy ratios, λ_V / λ_H , are shown.

Lunati et al. (2002) extended the analysis to arbitrary non-uniform flow fields. By homogenisation theory, they showed that the small-scale variability of the velocity field can be incorporated into a macrodispersivity field that depends on the mean velocity field. An important finding was that it is possible to define a macrodispersivity that is a medium property independent of the flow conditions if diffusion can be ignored. This means that a locally heterogeneous medium can be homogenised and treated as a homogeneous medium if the observation scale, L , and the heterogeneity scale, λ , are well separated. The macrodispersivity tensor (of fourth rank) depends only on the statistical properties of the local velocity field. If the medium is statistically isotropic, it is an isotropic tensor. This case formally coincides with the common pore-scale

dispersivity model. If the medium is statistically anisotropic the tensor is axially symmetric: it depends on the angle θ that the mean flow forms with the principal axes of anisotropy. The dependence of the longitudinal dispersivity on θ is shown in Figure 5.9.

If the heterogeneity scale has a typical length comparable with the dipole size, the two scales are no longer separated and ε has to be considered finite. This pre-asymptotic case was studied by heuristic extension of the homogenisation theory (Lunati et al. 2002). In this case, the macro-dispersive term describes only fluctuations from the mean velocity that occur on the smallest length scale, whereas the others are still explicitly described by the advective term. This leads to a macrodispersivity that is always smaller than in the asymptotic case (see Figure 5.10). If ε is finite, it is not a medium property, but a scale-dependent parameter. A comparison with the standard ensemble averaging approach shows that the latter does not consistently account for finite ε effects: it tends to overestimate the dispersion coefficient to be applied in the single realisation.

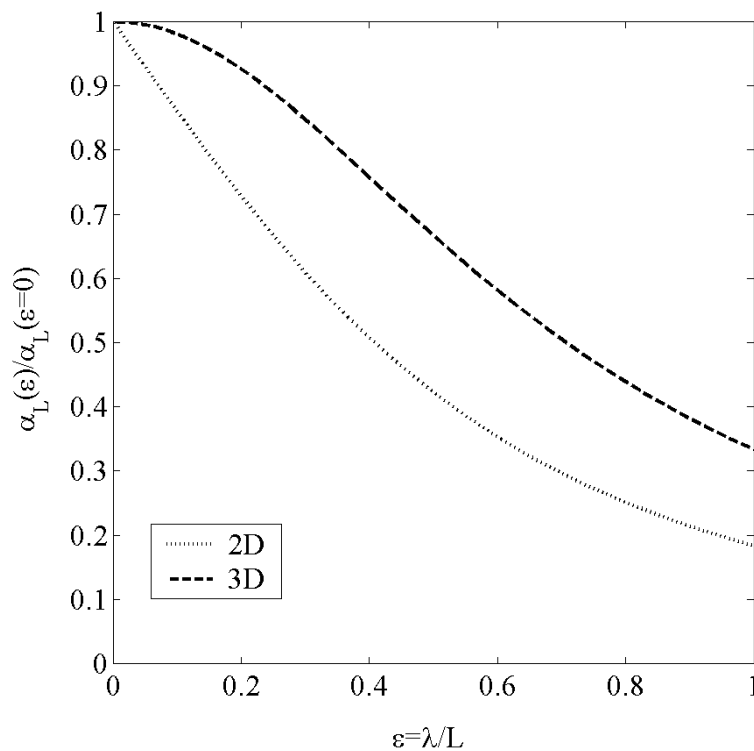


Fig. 5.10: The ratio of the pre-asymptotic, $\alpha_L(\varepsilon)$, to the asymptotic longitudinal macrodispersivity, $\alpha_L(\varepsilon = 0)$, as a function of ε in two and three dimensions.

5.4.2 Effects of pore volume-transmissivity correlation

Modelling the hydraulic response of the shear zone requires no specific description of the pore volume distribution. In contrast, the latter plays a fundamental role when transport phenomena are considered. Consequently, a correct description of the pore volume variability is needed to compute the pore velocity, which is the relevant velocity for the displacement of the solute front, from the Darcy velocity (specific flow rate).

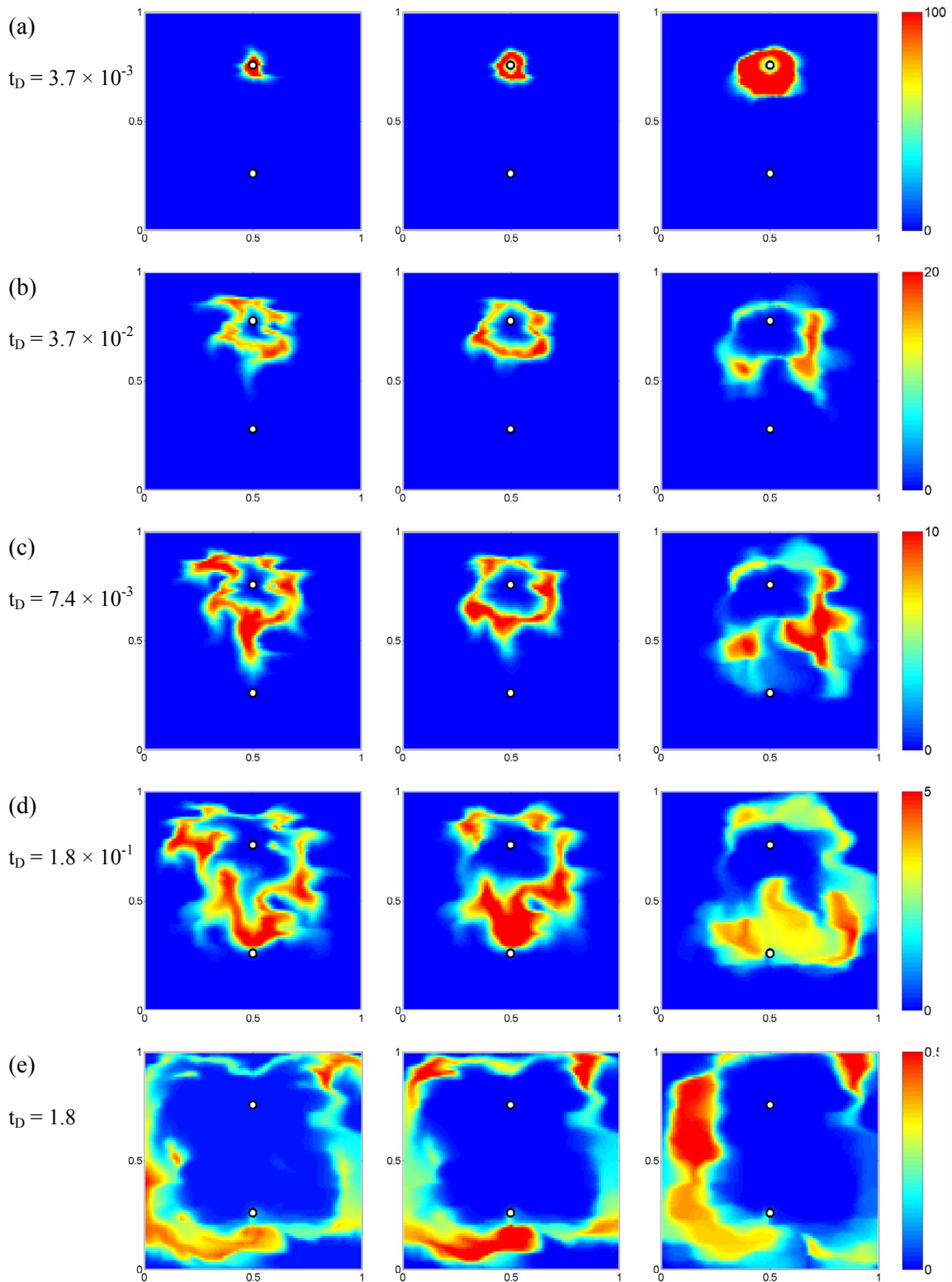


Fig. 5.11: Simulations in three fractures at different time steps (dimensionless time in terms of porevolume injected/PVI).

Evolution of an ideal-tracer pulse injection in dipole fields in three fractures with the same transmissivity field and total pore space, but with different pore space distribution (thickness porosity field). From left to right: parallel-plate filled with heterogeneous fault gouge, rough-walled empty fracture, rough-walled fracture filled with homogeneous fault gouge.

Lunati et al. (2003) investigated the effects of the correlation between pore volume and transmissivity fields. They considered two-dimensional models of a fracture that were hydraulically equivalent, but had a different pore volume distribution per unit of horizontal area, which is given by thickness times porosity, i.e. $b \cdot \phi$. Three simplified conceptual models were analysed, which had exactly the same transmissivity field T :

- A parallel-plate fracture filled with heterogeneous fault gouge (“UM model”). The fault gouge was assumed to have space dependent hydraulic conductivity, but constant porosity, which led to a pore volume constant in space and uncorrelated to the heterogeneous transmissivity field.
- A rough-walled empty fracture (“PCM model”). Assuming cubic law, the transmissivity is related to the third power of the fracture thickness and pore volume and the transmissivity fields were partially correlated ($T \sim b^3$).
- A rough-walled fracture filled with homogeneous fault gouge (“CCM model”). The fault gouge had constant hydraulic conductivity and porosity, such that the transmissivity variability was related linearly to the fracture thickness and the pore volume field and the transmissivity fields were perfectly correlated ($T \sim \phi b$).

Numerical simulations of tracer tests in a dipole flow field demonstrated that the transport process differs dramatically in the three fractures, even if they have exactly the same piezometric head and specific flow rate at any point of the domain. Figure 5.11 shows the result of one of these simulations and plots the responses of the three fractures to an instantaneous ideal tracer injection at the injection well. Striking differences can be observed in the evolution of the plume between the parallel-plate fracture (left side) and the rough-walled fracture filled with homogeneous material (right and side), which can be regarded as two limiting cases. The numerical simulations supported the results of laboratory experiments (see section 3.3.1), which demonstrated how the correlation between pore volume and transmissivity yields a much smoother and more homogeneous solute distribution. If perfect, the correlation causes pore velocity to be not directly dependent on the transmissivity, but only indirectly through the hydraulic gradient, which is a much smoother function due to the diffusive behaviour of the flow equation acting as a filter.

These differences make it important for site characterisation to be able to discriminate among different conceptual models by means of the information that is typically available in-situ. The possibility of discriminating on the basis of tracer breakthrough and recovery curves at the extraction well was studied by analysis of the results from the numerical simulations. This suggested that the possibility of discriminating among the models is subject to many constraints. In particular, the integral scale of the transmissivity field turned out to be a very critical parameter.

If the heterogeneity scale is small compared to the dipole size, the fracture can be homogenised, i.e. reduced to the homogeneous case, as was shown in section 5.4.1 by the Homogenisation Theory. The numerical simulations performed in fractures with the same transmissivity field and the same total pore volume showed that the rough-walled fracture filled with a homogeneous material showed an initially higher recovery compared to the other two fractures, to which correspond earlier first-arrival time and peak arrival time. This is illustrated in Figure 5.12, which plots the recovery curves for the three models of the fracture as a function of time, which is made dimensionless by the mean arrival time.

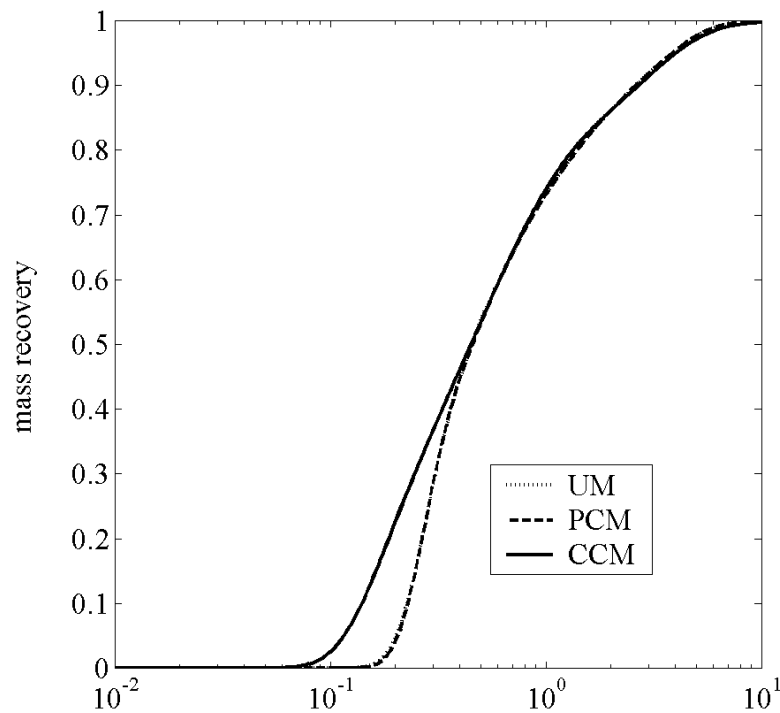


Fig. 5.12: Solute recovery curves at the extraction borehole as a function of dimensionless time (τ = mean arrival time).

UM, parallel-plate fracture with heterogeneous fault gouge; PCM rough-walled empty fracture; CCM, rough-walled fracture with heterogeneous fault gouge. Mean transmissivity 2×10^{-10} m²/s, log-transmissivity variance $\sigma_{\ln T} = 7.4$, correlation scale approximately 3×10^{-3} times the dipole size.

In all the cases in which the heterogeneity scale is comparable with the dipole size, it is impossible to discriminate among the different conceptual models, because the effects of local variability in transmissivity dominate those of the pore volume-transmissivity correlation. This prevents the identification of any qualitative difference between either the breakthrough curves or recovery curves of different models. This is well illustrated by Figure 5.13, which plots the ensemble-average of the recovery curve computed over 20 realisations of transmissivity fields with the same statistical properties. For each realisation the tracer tests was simulated using the three conceptual models. The ensemble-averaged recovery curves of the three conceptual models lie within the 69 % confidence interval of the parallel-plate model and are statistically indistinguishable.

Due essentially to the loss of information by missing at the extraction borehole, breakthrough curves from single tracer tests are not sufficient, in most practical cases, to identify the correct fracture model to be applied. Information needs to be integrated using data from several tracer experiments, which can be very useful particularly if they can provide information on the integral scale of the heterogeneity (e.g. tests with a different dipole size or orientation), or more promisingly by multi-tracer tests.

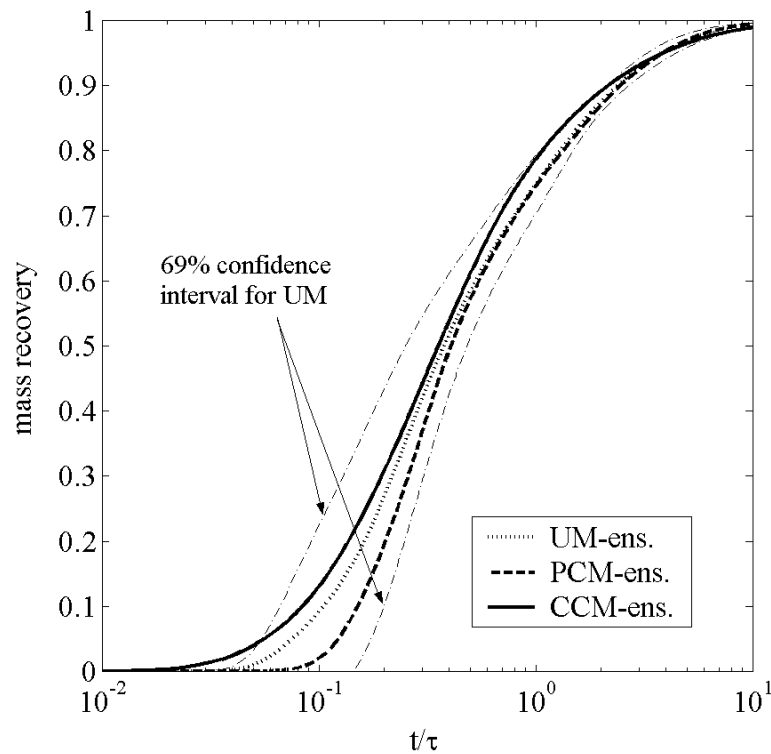


Fig. 5.13: Solute recovery curves at the extraction borehole averaged over 20 realisations as a function of dimensionless time.

UM, parallel-plate fracture with heterogeneous fault gouge; PCM, rough-walled empty fracture; CCM, rough-walled fracture with heterogeneous fault gouge. Mean transmissivity $2 \times 10^{-10} \text{ m}^2/\text{s}$, log-transmissivity variance $\sigma_{\ln T} = 7.4$, correlation scale approximately 0.07 times the dipole size.

5.5 Summary of achievements

The solute and particle tracer tests that formed part of the GAM experiment were designed for a variety of different purposes. Key aspects were (i) the development of innovative tracer test equipment, (ii) the improvement of modelling tools for tracer test analysis and (iii) the development of upscaling procedures for transport parameters in heterogeneous media. Some of the key achievements are highlighted here:

- The equipment related investigations concentrated on the development of tracer injection systems and on the testing of online particle counters. Excellent results were obtained with the new tracer injection and circulation system (Fig. 5.1), providing step injection functions with short rise times and stable injection concentrations. The particle counter devices for nano- and microspheres were available during the PT1 test campaign – the equipment worked well under in-situ conditions and the results of the particle tracer test provided complementary information of the transport characteristics of the shear zone. On the other hand, it is felt that the design of suitable test procedures needs further thought and the operation of the particle counters under in-situ conditions could be improved with regard to the robustness of the hardware and the user-friendliness of the calibration procedure.
- The interpretation of the solute tracer tests using the geostatistical inversion method allowed a consistent interpretation of both hydrotest and tracer test data. Different representations of the shear zone were used: (i) a fracture of variable transmissivity with a homogeneous infill,

(ii) a fracture with a heterogeneous infill and (iii) an open fracture. The 3 conceptual models provided matches of the tracer breakthrough curves which performed more or less equally well. Without further a-priori information, it was not possible to discriminate between the different models. The parameter estimation procedure revealed that a very small pore volume of the shear zone is accessible for the solute (specific pore volume in the order of $0.001 \text{ m}^3/\text{m}^2$ of the shear zone area).

- The theoretical studies on parameter upscaling revealed that a locally heterogeneous medium can be homogenised (i.e. treated as a homogeneous medium) if the observation scale and the heterogeneity scale are well separated. The macrodispersivity tensor depends only on the statistical properties of the local velocity field. If the heterogeneity scale has a typical length comparable with the dipole size (“pre-asymptotic case”), the two scales are no longer separated and the macrodispersive term describes only fluctuations from the mean velocity that occur on the smallest length scale, whereas the others are still explicitly described by the advective term. This leads to a macrodispersivity that is always smaller than in the asymptotic case, i.e. it represents a scale-dependent parameter.

6 Gas tracer tests

A numerical pre-study on the feasibility of an in-situ gas tracer test at the GAM site was conducted as part of the Grimsel Phase IV research programme (TPF experiment). The numerical simulations confirmed the general feasibility of a gas tracer test (dipole configuration with He and Xe as gas tracers and nitrogen as a carrier gas) and revealed the discriminating power of such tests. A clear separation of the breakthrough of the two gas tracers was seen, which was very sensitive to the accessible pore volume within the shear zone. The promising results of the pre-study initiated the launching of the GAM experiment within the framework of the Grimsel Phase V Programme.

Section 6.1 briefly summarises the aims and the concept of the gas tracer tests. An overview of the field experiments is given in section 6.2, comprising the test configurations, the experimental set-up and the experimental procedure. A summary of the results is also given and a preliminary interpretation is presented. Section 6.3 is dedicated to modelling issues, including a theoretical study on the discriminative power of gas tracer testing and an attempt to model the field tests at the GAM site.

6.1 Aims and concept

The assessment of gas tracer testing as an innovative in-situ technique for the characterisation of transport in heterogeneous groundwater systems was identified as a key task in the GAM experiment concept (cf. section 1.1). The issues of interest were of a basic nature, such as the technical feasibility of such tests, equipment requirements, the specific benefit compared with conventional tracer tests and, last but not least, the availability of numerical tools for the test interpretation. The specific objectives of the gas tracer tests can be summarised as follows:

- development and testing of equipment and test procedures for controlled gas tracer tests (injection / extraction systems and monitoring devices)
- evaluation of the specific benefit of gas tracer tests for characterisation of mass transport in heterogeneous groundwater flow systems
- collection of an experimental data base for the evaluation of numerical codes for the simulation of multiphase-multicomponent processes in groundwater flow systems

Due to the pioneering character of the experimental work, it was expected that the field data would provide mainly qualitative information on the transport behaviour of the GAM shear zone, rather than data that could help to constrain the transport properties in a quantitative manner. The use of reactive gas tracers was beyond the actual scope of the GAM experiment; nevertheless some pilot tests were conducted to assess the potential of such tracers for future experimental work (Carrera et al. 2000).

The experimental concept is based on the use of a tracer gas cocktail containing gases with different solubility and diffusivity. Due to their different solubility and diffusion coefficients, each tracer gas is expected to propagate differently in a groundwater flow field, leading to different breakthrough curves in terms of arrival time and shape. Figure 6.1 presents a schematic illustration of the complex transport processes within a partially saturated shear zone. Tracer transport takes place in the gas and water phases. Henry's law describes the gas-liquid interaction (solution – dissolution) of gases at the gas-liquid interface.

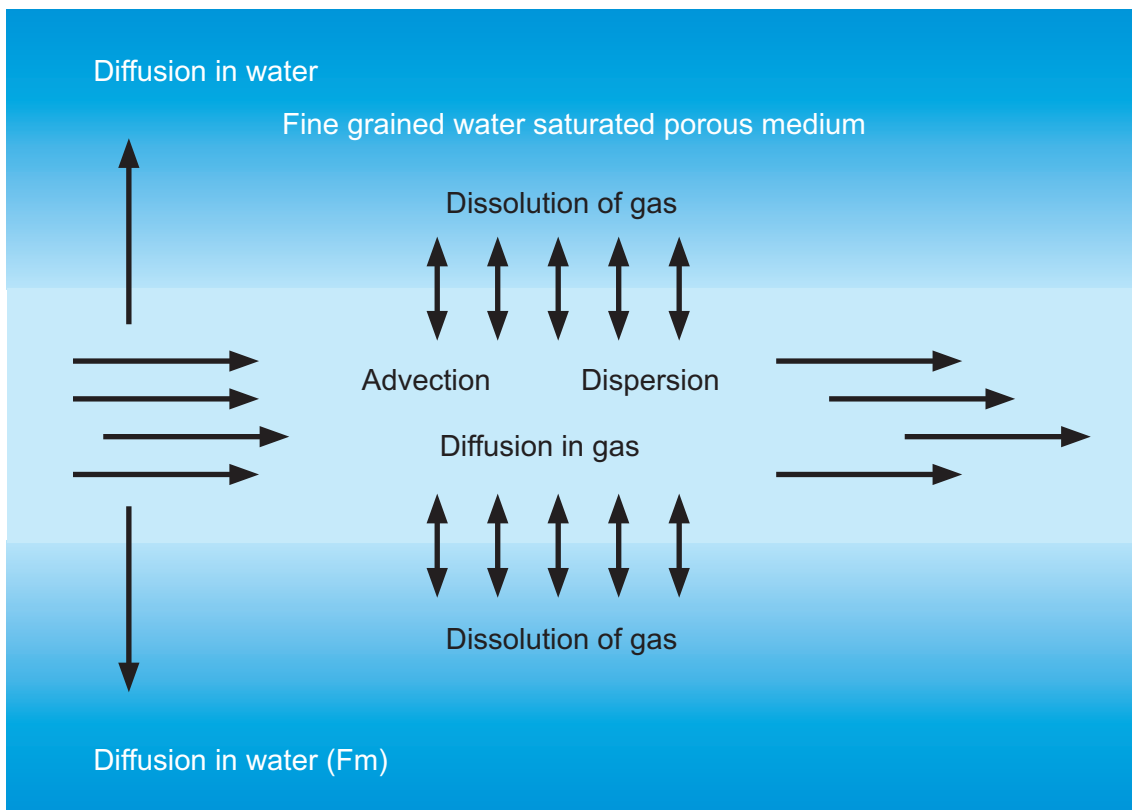


Fig. 6.1: Schematic illustration of the dissolution-diffusion mechanisms addressed.

6.2 The field investigations

6.2.1 Overview of gas tracer experiments

Three gas tracer test campaigns were realised within the framework of the GAM project between February and December 2000, namely GT1 (Fierz et al. 2000), GT2 (Trick et al. 2000) and GT3 (Trick et al. 2001). These 3 campaigns comprised a total of 11 gas tracer tests, which were performed in two dipole configurations with dipole distances of 1.1 m and 1.9 m, respectively. For the 1.9 m long dipole, gas tracer tests were conducted in both directions (see Figure 6.2). Different cocktails of gas tracers were injected: He and Xe in February, He, Xe, Ar and SF₆ in August and He, Xe, Ar, SF₆ and H₂S in December. Table 6.1 presents an overview of the gas tracer tests conducted and provides further details regarding the dipole configurations, flow rates and the applied gas tracers. Table 6.2 gives an overview of the solubilities and diffusion coefficients of the applied gas tracers.

For the first two sets of tracer tests (GT1 and GT2), the tracers were selected according to the following criteria:

- non-toxic and environmentally safe;
- non-reactive with the rock material in the shear zone and with the experimental equipment;
- chemically stable and not affected by the natural groundwater composition and the other tracer gases in the cocktail;
- detectable in small quantities, analysed online with standard mass spectrometers;

During the third campaign (GT3), H₂S was added to the tracer cocktail. Even though H₂S does not meet the first two criteria mentioned above (non-toxic, non-reactive), it was selected due to its solubility, which is more than one order of magnitude higher compared to the other tracer gases. The H₂S was used despite its toxicity, requiring special safety precautions, and despite its chemical reactivity, impairing the interpretation of the experimental data (possible metal corrosion in the injection / extraction intervals).

Tab. 6.1: Overview Gas Tracer Tests.

Run #	Date	Dipole		Gas flow rate / inj. [ml (STP) / min]	Dipole Distance [m]	Tracer used	Test cam- paign
		Injection borehole	Extraction borehole				
1	01.02. 2000	*GAM 98.002	*TPF 95.007	100** [50]	1.9	He, Xe	GT1
2	02.02. 2000	TPF 95.007	GAM 98.002	50	1.9	He, Xe	GT1
3	03.02. 2000	TPF 95.007	GAM 98.002	10	1.9	He, Xe	GT1
4	22.08. 2000	GAM 98.004	TPF 95.004	10	1.1	He, Xe, Ar, SF ₆	GT2
5	24.08. 2000	GAM 98.004	TPF 95.004	100	1,1	He, Xe, Ar, SF ₆	GT2
6	25.08. 2000	GAM 98.004	TPF 95.004	100 [10]	1.1	He, Xe, Ar, SF ₆	GT2
7	12.12. 2000	GAM 98.002	TPF 95.007	15	1.9	He, Xe, Ar, H ₂ S, SF ₆	GT3
8	14.12. 2000	GAM 98.002	TPF 95.007	75	1.9	He, Xe, Ar, H ₂ S, SF ₆	GT3
9	15.12. 2000	GAM 98.002	TPF 95.007	300	1.9	He, Xe, Ar, H ₂ S, SF ₆	GT3
10	18.12. 2000	GAM 98.002	TPF 95.007	300	1.9	He, Xe, Ar, H ₂ S, SF ₆	GT3
11	19.12. 2000	GAM 98.002	TPF 95.007	600	1.9	He, Xe, Ar, H ₂ S, SF ₆	GT3

* After tracer dosage the dipole direction was changed: the injection interval became the extraction interval and vice versa.

** Dipole injection flow rate after tracer dosage in parentheses.

Tab. 6.2: Tracers used in GAM gas tracer tests..

	He	Xe	SF ₆	Ar	H ₂ S
Mol. Weight	4.003	131.29	146.05	39.91	34.08
Solubility at 5°C [mole fraction/bar]	$7.5 \cdot 10^{-6}$ (1)	$1.5 \cdot 10^{-4}$ (1)	$9.2 \cdot 10^{-6}$ (2)	$3.8 \cdot 10^{-5}$ (1)	-
Solubility at 10°C [mole fraction/bar]	$7.3 \cdot 10^{-6}$ (1)	$1.2 \cdot 10^{-4}$ (1)	$7.3 \cdot 10^{-6}$ (2)	$3.3 \cdot 10^{-5}$ (1)	-
Solubility at 15°C [mole fraction/bar]	$7.2 \cdot 10^{-6}$ (1)	$1.1 \cdot 10^{-4}$ (1)	$6.0 \cdot 10^{-6}$ (2)	$3.0 \cdot 10^{-5}$ (1)	$2.3 \cdot 10^{-3}$ (3)
Molecular Diffusion Coefficient in water [m ² /s]	$6.3 \cdot 10^{-9}$	$2.2 \cdot 10^{-9}$	$1.2 \cdot 10^{-9}$	$2.0 \cdot 10^{-9}$	$1.3 \cdot 10^{-9}$
Molecular Diffusion Coefficient in gas (N ₂) [m ² /s]	$7.0 \cdot 10^{-5}$	$1.3 \cdot 10^{-5}$	$1.0 \cdot 10^{-5}$	$2.0 \cdot 10^{-5}$	$3.3 \cdot 10^{-5}$

(1) Benson and Krause 1976; (2) Cosgrove and Walkley 1981; (3) Dean 1994

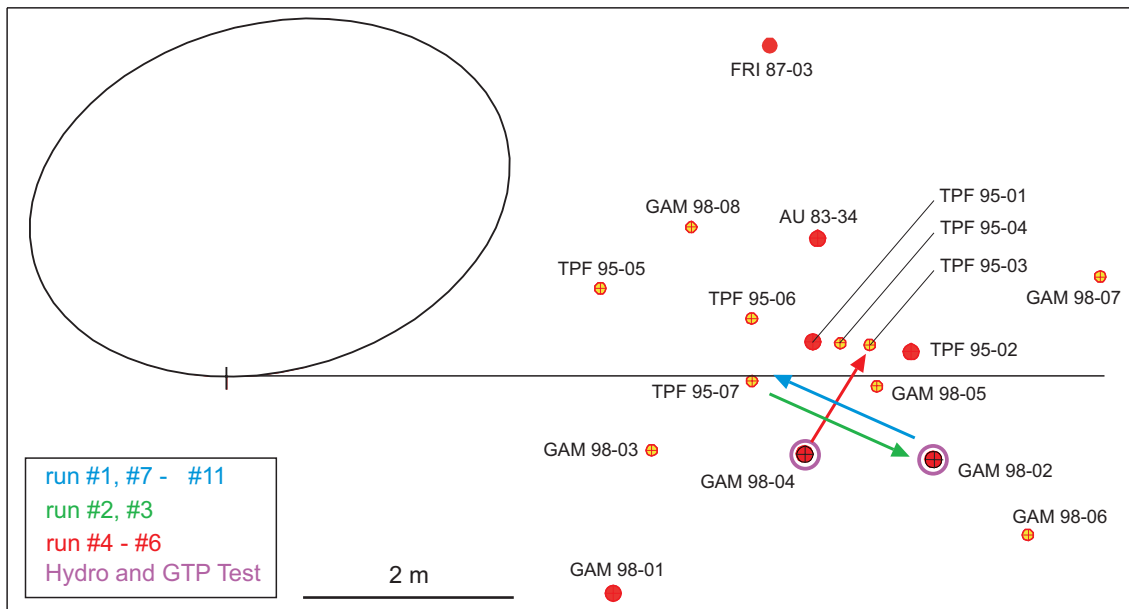


Fig. 6.2: Layout of the borehole intersections with the GAM shear zone. The arrows indicate the dipole flow fields in which the gas tracer tests were carried out.

6.2.2 Experimental set-up

High quality experimental data are required in order to identify the various gas transport processes within a partly saturated shear zone. Setting up the field experiment turned out to be a demanding task; special procedures had to be developed with respect to the control of dipole gas flow rates, the gas / water separation on the extraction side and the gas tracer detection. In addition, experimental artifacts such as tracer dispersion due to dead volumes in lines and packed-off intervals, or losses of tracer gas through gas leaks in the test equipment, had to be minimised.

A schematic drawing of the set-up is presented in Figure 6.3. Injection and extraction boreholes were equipped with triple packer systems. The packer systems isolated the borehole sections of the GAM shear zone. An optimised low-volume design was used for the shear zone intervals, which were equipped with two lines in order to perform gas-water exchange. The downhole equipment is described in detail in Gemperle (1999a). The surface equipment (consisting mainly of tracer detection equipment and of devices to establish and control a dipole flow field) is also represented in Figure 6.3. Gas flow controllers (Brooks type 5850S) and pressure vessels were used to create and maintain dipole flow fields. During the tracer runs, both gas and water outflows passing through the dipole extraction line were monitored. Before tracer analysis and measurement of the gas flow rate on the extraction side, water within the dipole extraction line was removed by a gas/water separator. The weight of the collected water was measured with a Mettler scale that was connected to the data acquisition system. Between the tracer test campaigns, the design of the gas water separator was improved several times. The final layout of the separator that proved reliable performance is documented in Trick et al (2000).

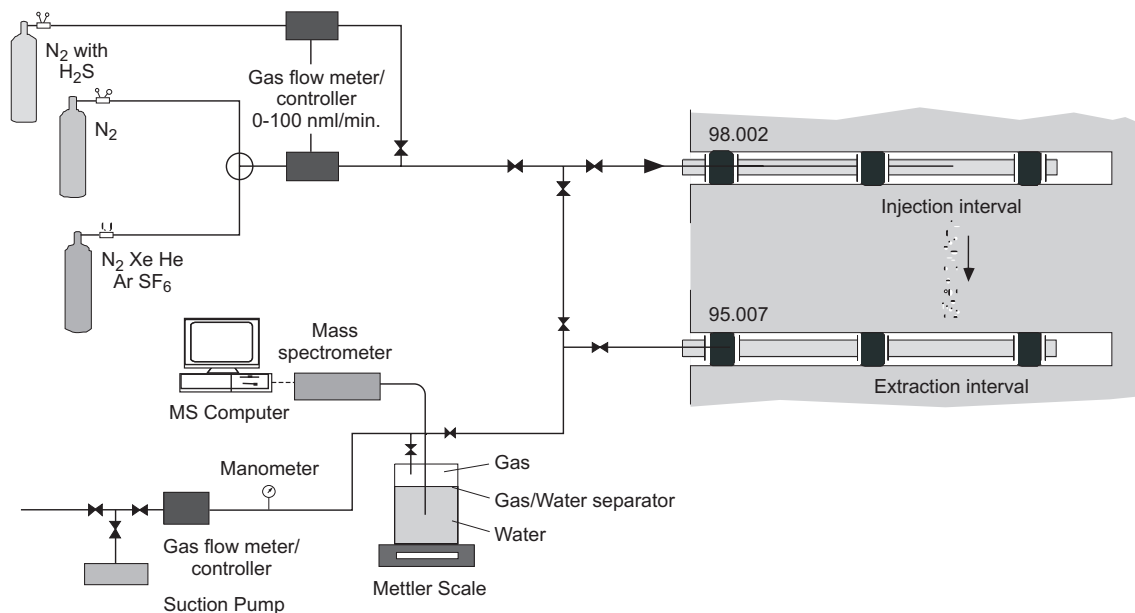


Fig. 6.3: Schematic view of the experimental layout.

Tracer gases were detected by a Balzers mass spectrometer, type Omnistar. The mass spectrometer was connected to the dipole extraction line by a capillary using a t-piece fitting. The suction rate through the capillary feeding the mass spectrometer was about 1 ml(STP)/min. Due to the required atmospheric pressure at the inlet of the capillary, no back-pressure could be set at the dipole extraction side. Therefore the test layout did not allow for variation of pressures within the shear zone.

Two independent data acquisition systems were part of the test set-up. The mass spectrometer was linked to a PC by a RS 232 serial interface. The mass spectrometer was operated using Balzers Quadstar 422 software, which allowed for configuration, calibration, data acquisition and data display. The second data acquisition system, a Solexperts GeoMonitor system, recorded gas and water flow rates and pressures in the various packed-off borehole sections of the GAM site.

6.2.3 Experimental procedure

A detailed test plan was prepared for each gas tracer campaign, which included input from modellers and experimentalists. The major steps were the following:

- Checking and – if necessary – modification of the site instrumentation in order to establish properly working downhole and surface equipment.
- Long-term (2 – 5 days) hydraulic constant rate injection test within the dipole injection borehole. The purpose of the hydraulic test was to achieve well defined initial conditions before starting the gas tracer test and to improve the hydraulic test characterisation of the site.
- Pressure recovery after the hydraulic test in order to reach quasi-stable pressure conditions.
- Performance of a Gas Threshold Pressure Test (GTPT) in the dipole injection borehole interval. First, the water in the test interval was replaced by nitrogen. Subsequently, the gas pressure within the test interval was set to the quasi-stable pressure measured prior to the water-gas exchange. Then, constant gas rate injection was started until the gas clearly started to displace water within the shear zone. The GTPT revealed the gas threshold pressure, which is defined as the pressure in the test interval when gas enters the shear zone. In addition, the performance of the GTPT represented the first step of dipole gas flow field establishment. The same gas injection rate was used for the GTPT and later for the dipole flow field.
- Open the extraction flow line in order to create a dipole flow field.
- Performance of gas tracer tests. As soon as quasi-steady flow and pressure conditions were achieved, tracer gas dosage was started. Tracer dosage was conducted by replacing the dipole input gas (pure nitrogen) by nitrogen spiked with the tracer gases (see Figure 6.3). After monitoring of the tracer breakthrough, the tracer dosage was stopped by changing the dipole input gas to pure nitrogen. Then, the tailing of the tracer breakthrough curves was monitored until background concentration or the detection limit was reached. Prior to a gas tracer test, the mass spectrometer was calibrated using the tracer gas cocktail bypassing the shear zone (see Figure 6.3). After the tracer test, the calibration was repeated in order to determine background or sensitivity drifts.
- Performance of additional runs without interruption of the dipole flow field. Variation of the dipole injection rates in order to run gas tracer tests with different velocities and tracer residence times within the shear zone.

6.2.4 Test results and preliminary interpretation

The field tests were successfully carried out under controlled hydraulic conditions. The established gas flow fields were quite stable, despite some fluctuations in the gas and water extraction rate due to intermittent gas / water flow in the extraction line. The online multiple gas tracer detection was realised by a mass spectrometer. For this purpose, the extracted gas/water mixture

was first separated in the gas/water separator. Subsequently, a small fraction of the gas flow was passed to the detector of the mass spectrometer, whereas the main gas flow was led to the gas flowmeter.

According to the results of the numerical pre-studies, gas tracer testing was expected to provide information about the spatial variability of the transport paths in the shear zone. In particular, a marked separation of the breakthrough curves of the different tracer gases was predicted (“chromatographic effect”) due to differences in the diffusion and, most notably, solubility coefficients (see Table 6.1). However, the retardation effects due to water solubility were much smaller than expected and the breakthrough curves observed for He, Xe, Ar and SF₆ during the gas tracer tests in the GAM shear zone were very similar. For these tracers, the breakthrough curves showed differences only at late time that can be related to the solubility coefficients, the more soluble tracer generally showing a more elongated tail of the curve.

This effect can be observed in Figure 6.4, which shows the normalised concentrations of all tracers at the extraction well recorded during GTT2 run#4. The tail of the breakthrough curve for Xe was more elongated and flatter at late time than those for SF₆ and He, whose solubilities are about 20 times smaller. Notice that the tails of SF₆ and He were similar as a result of their very similar solubilities at a temperature around 10°C. The recorded Ar breakthrough curve was more elongated than the breakthrough curve for Xe. This contrasts with the higher solubility of the latter, but the results might have been biased by the higher background concentration of Ar due to previous gas tests. Figure 6.4 clearly suggests that effects of molecular diffusion in the gas phases are not completely negligible at the experimental flow rate of 10 ml(STP)/min. Indeed, tracers with higher diffusion coefficients arrived earlier at the well and showed less steep increase in the concentration.

During GTT3, the highly soluble H₂S was added to the tracer cocktail. The shape of the breakthrough curve for H₂S was clearly different compared to the other tracers of the mixture. As can be observed in Figure 6.5, the first arrival of H₂S was strongly delayed, the normalised peak concentration much lower and the late time normalised concentration higher than He, Xe, Xe and SF₆. The comparison between Figure 6.5a and 6.5b also shows that variation of the dipole gas flow rates changed the tracer residence times. The longer the residence time the more distinct are the differences between the breakthrough curves of H₂S and the other tracers. Although a significant mass flux from the gas phase to the liquid phase took place during the experiment, the breakthrough curves for H₂S were strongly influenced by the reactivity of the tracer, such that the delayed arrival times and the pronounced tails cannot be entirely attributed to the solubility. The H₂S signal was unstable while calibrating the mass spectrometer by direct injection of the tracer mixture, which was a clear indicator that sorption on the steel surface of the line took place. The highly corrosive properties of H₂S suggest that chemical reactions took places within the equipment and in the formation. This is confirmed by the extremely low mass recovery for this tracer. For He, Xe, Ar and SF₆, after a relatively (depending on the dipole gas flow rate) short time, 100 % tracer recovery was reached in all experiments.

Figure 6.5b shows that the shape of the tail of the tracer changed when changing the flow rate and thus the residence time of the tracer gas within the shear zone. This was an indication that the kinetics of the dissolution is important and that equilibrium is not reached instantaneously. In such a case, the molecular diffusion in the water phase plays an important role, because a larger coefficient enables the tracer to penetrate a larger volume of water. If two tracers have the same solubility, the tracer with the largest diffusion coefficient is expected to be the most retarded.

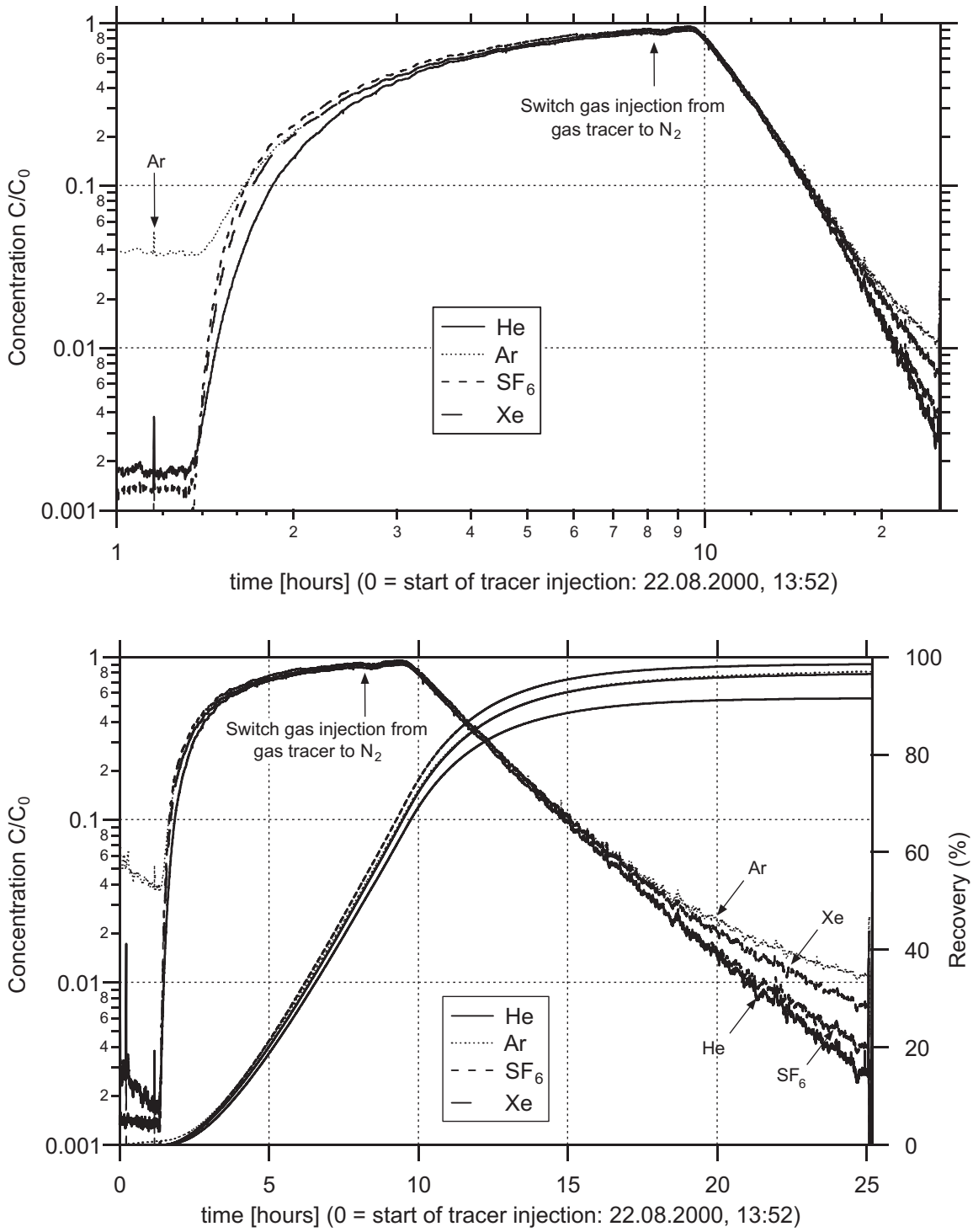


Fig. 6.4: Ar, Xe, He and SF_6 breakthrough curves recorded during GTT2 run#4: (a) log-log plots and (b) semi-log plots of the normalised gas concentrations.

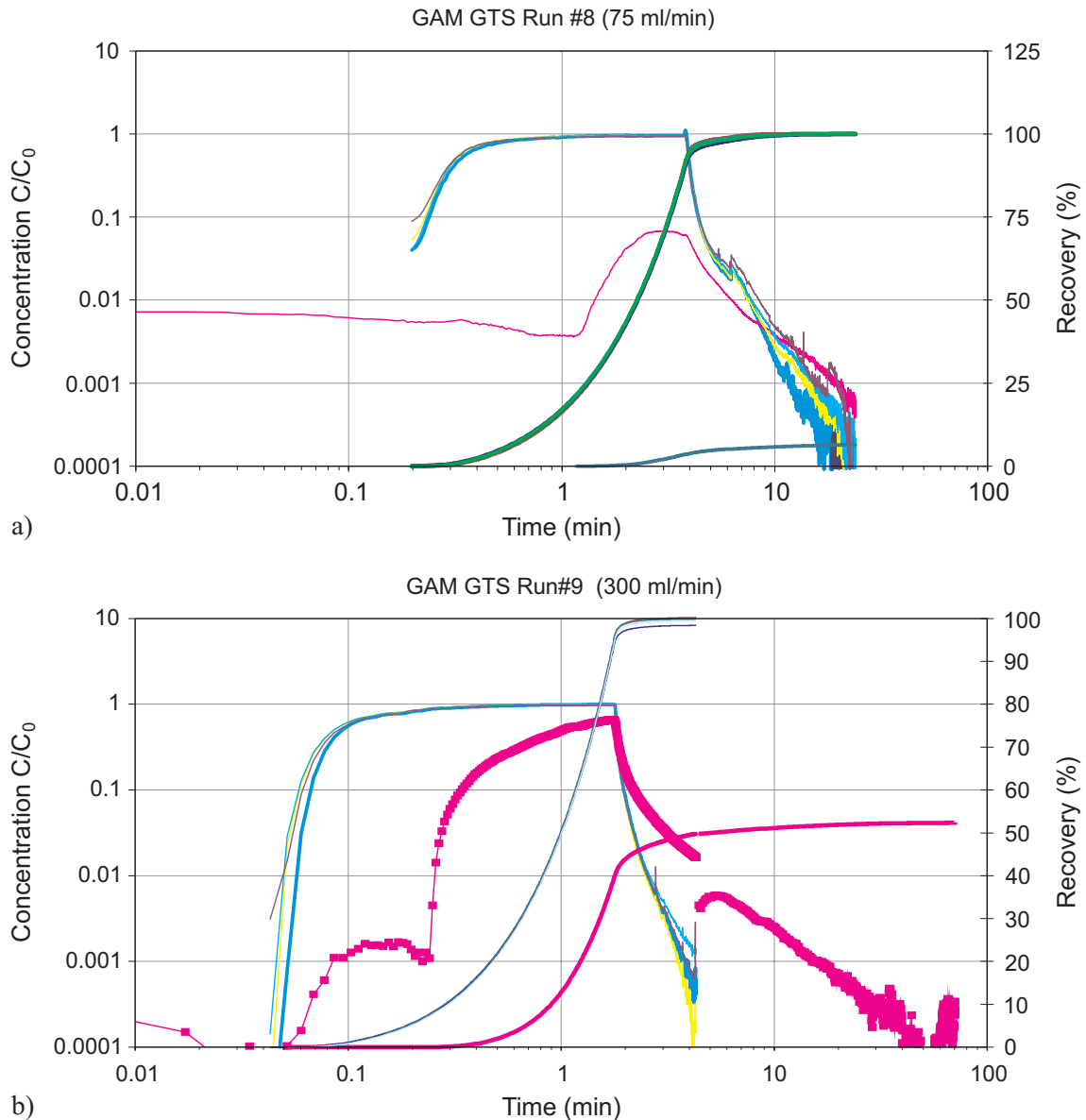


Fig. 6.5: Ar, Xe, He, SF₆ and H₂S breakthrough curves during GTT3: (a) run#8 with a gas injection rate of 75 ml(STP)/min and (b) run#9 with a gas injection rate of 300 ml(STP)/min.

6.3 Numerical simulations of gas tracer tests in an unsaturated shear zone

6.3.1 Water-soluble gases as partitioning tracers

The possibility of using information from gas tracer tests to estimate the fracture saturation was analysed numerically, together with the possibility of using this information to discriminate among different conceptual models (Lunati and Kinzelbach 2003a, 2003b, Lunati 2003). Indeed, Lunati et al. (2003) demonstrated that traditional solute-tracer tests might be inadequate under most realistic conditions to identify the most appropriate conceptual model to be applied. The same three models as in section 5.3.2 were considered, which have a different correlation between pore volume and transmissivity fields. The simulations were performed with the two

phase flow simulator TOUGH2 (EOS model). For comparability reasons, all three models are hydraulically equivalent (same transmissivity field), have the same total pore volume and the same capillary model (Brooks-Corey), except for the entry pressure distribution. Indeed, on the basis of microscopic considerations, the entry pressure p_d in the fracture can be related to the hydraulic conductivity K via the Leverett model, i.e. $p_d = K^{-1/2}$. This relationship implies that the correlation between pore volume and transmissivity tends to smooth the distribution of the gas-phase, because it reduces the correlation between transmissivity field, which is heterogeneous, and the entry pressure field, which becomes more homogeneous. The three models were characterised as follows:

- In the parallel-plate fracture (“UM model”) filled with a heterogeneous fault gouge, the transmissivity is proportional to the hydraulic conductivity. That results in a space-dependent entry-pressure field $p_d \sim T^{-1/2}$.
- In the rough-walled empty fracture (“PCM model”), the entry pressure is proportional to the inverse of the aperture, $p_d \sim 1/b$. Using the cubic law, it can be rewritten as $p_d \sim T^{-1/3}$.
- In the rough-walled fracture with a homogeneous fault gouge (“CCM model”), the entry pressure is spatially constant as a consequence of the homogeneity of the filling material. In this case transmissivity and entry pressure are uncorrelated.

Several gas tracer tests were simulated in synthetically generated single fractures. The ensemble of log normal transmissivity fields had a mean value $\text{Log}T = -9.7 \text{ m}^2/\text{s}$ and variance $\sigma_{\text{Log}T}^2 = 1.4$, which are the typical values obtained for the GAM fracture. Note that Lunati (2003) also considered a low-variance ensemble of transmissivity fields. The correlation length of the transmissivity field was about 0.034 times the size L of the domain, which was a square with no-flow boundary conditions imposed on the four sides. The dipole of size $L/2$ was placed in the middle of the domain.

First, the desaturation of the fracture by air injection was simulated. Air was injected at a constant mass rate Q in one borehole, while the other borehole was assumed to be at atmospheric pressure. When air injection started, the fracture was fully saturated and the gas phase occupied only the injection borehole. At the beginning, only water was produced at the extraction well, then the gas phase broke through and air recovery started. After a while, the gas saturation distribution and the velocity field within the fracture can be considered quasi-steady state, i.e. they vary slowly over the typical residence time of air in the fracture. The quasi-steady state gas saturation distributions for one realisation of the transmissivity field are shown in Figure 6.6 for all three conceptual models of the fracture. The numerical simulations show that the conceptual model adopted has striking effects on the fracture saturation via the entry pressure: in the parallel-plate fracture with heterogeneous fault gouge, gas flow takes place only in few discrete channels characterised by very high gas saturation and separated by fully water-saturated regions, whereas in the rough-walled fracture with homogeneous fault gouge, gas flow takes place in a more spread-out region where the gas saturation is considerably smaller than in the channels produced by the other model. The empty fracture model is in between, showing a pattern similar to the parallel-plate model, but characterised by a smaller variability of the saturation: extreme values are smoothed out by the partial correlation between pore volume and transmissivity, which in turn decreases the correlation between entry pressure and transmissivity.

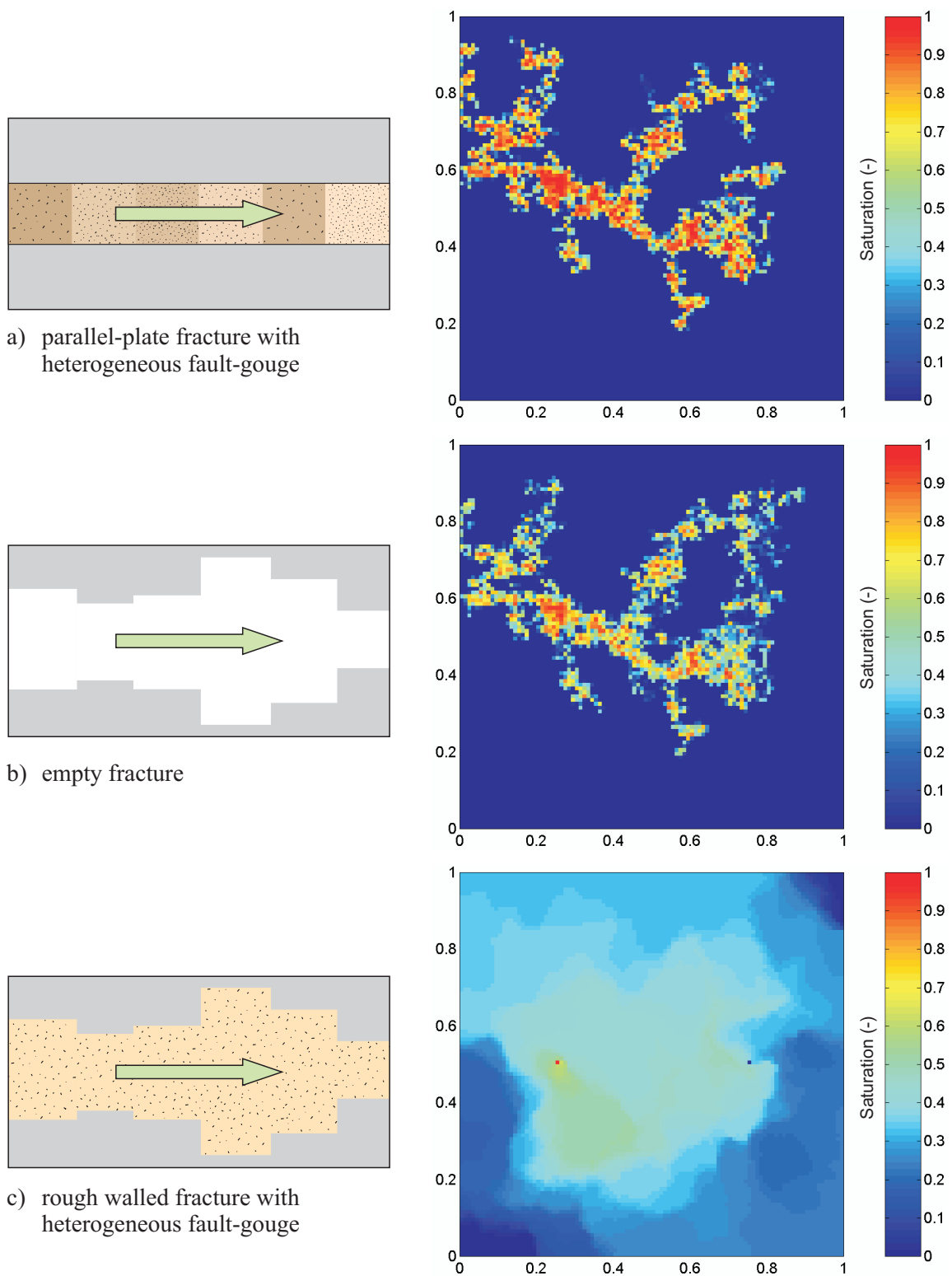


Fig. 6.6: Quasi-steady-state gas saturation distribution for different fracture conceptual models.

Corresponding to different correlations between pore volume and transmissivity: a) UM/parallel-plate fracture with heterogeneous fault gouge, b) PCM/empty fracture, and c) CCM/rough-walled fracture with homogeneous fault gouge.

These differences in the gas saturation can be very well observed by means of a gas tracer test in which at least two tracers with different water solubility are employed. Ignoring water flow and assuming that the quasi-steady state gas saturation and gas pressure fields remained constant, the responses of the three fractures to an instantaneous injection of gas tracer cocktail were simulated. Under these conditions, the only effect of the liquid phase is an exchange of tracer mass with the gas phase due to dissolution into water. Local instantaneous equilibrium was assumed between the tracer concentrations in the gas and in the liquid phases. This means that, within the cells of the numerical grid, all the water was available for dissolution and reached the equilibrium concentration stated by Henry's law instantaneously. Under these hypotheses, the transport of a soluble gas could be modelled as the transport of a linearly retarded tracer i with retardation coefficient given by

$$R_i = 1 + \frac{1 - S_g}{S_g} \gamma_i, \quad (6.1)$$

where the solubility factor γ_i depends linearly on the temperature and on Henry's constant of the tracer. The cocktail consisted of three gas tracers: an ideal tracer (id) and two soluble tracers, i.e. xenon, Xe, and hydrogen sulphide, H₂S. The main idea was to obtain an estimation of the gas saturation in the fracture using equation (6.1). The retardation factor of the tracer i can be computed by comparison between the mass recovery functions of the ideal tracer, $MR(t_{id})$, and of the soluble tracer, $MR(t_i)$, which represent the cumulative probability function of the residence time in the fracture. By identifying each streamline via the mass recovery at its arrival time, it is possible to compute a streamline-dependent retardation factor:

$$R_i(MR) = \frac{t_i(MR)}{t_{id}(MR)} \quad (6.2)$$

Writing equation (6.2), it was assumed that the arrival order of the streamlines was the same for different tracers. Inserting equation (6.2) into equation (6.1), a streamline-effective saturation can be computed by solving for S_g , which turns out to be the harmonic mean of the gas saturation along the streamline (weighted by the inverse of the velocity; Lunati & Kinzelbach, 2004).

The streamline-effective saturation computed according to equations (6.1) and (6.2) is plotted in Figure 6.7 for all models and realisations. The retardation factor of hydrogen sulphide was used to compute the effective saturation. Comparison of these plots with the saturation maps obtained from the numerical simulations definitely demonstrates that it is possible to obtain an excellent estimate of the fracture saturation by comparing the residence time distribution of two tracers, provided that equilibrium between the gas and the liquid phases is nearly instantaneous and that tracer transport is advection-dominated (as an example of this one can compare the saturation fields in Figure 6.6 with the corresponding curves, labeled with a star in Figure 6.7). It can also be observed that in the rough-walled fractures filled with homogeneous fault gouge, flow takes place in regions with lower gas saturation than in the other fractures, which implies that the gas phase is spread over a larger area of the fracture.

Data from tests with at least two soluble gas tracers provide additional information to that obtained by classic tracer tests. They also help to discriminate among the conceptual models, because they can reveal the presence of well separated channels within the fracture, which are normally observed in the parallel-plate and in the empty fractures. Indeed, most realisations produce a non-monotonic saturation curve when the parallel-plate fracture or the empty fracture models are adopted (Figure 6.7), which clearly proves that the gas saturation has a long correlation in the flow direction, typical of channel flow (Lunati and Kinzelbach 2003a, 2003b,

Lunati 2003). In extreme cases in which only one channel is present (shortcut), all models produce monotonic streamline saturation curves. However, whereas in the rough-walled fracture filled with homogeneous fault gouge flow is completely two-dimensional, in the other two fractures the flow in a channel is similar to mono-dimensional flow and the arrival time distribution is less dispersed.

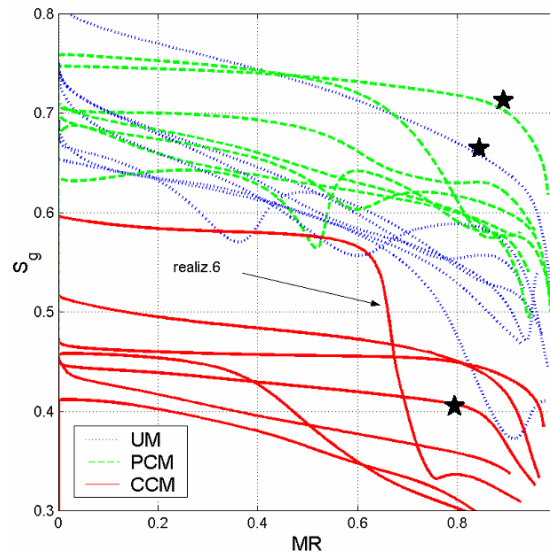


Fig. 6.7: Effective gas saturation as a function of mass recovery at the extraction well for different realisations and conceptual models.

UM: parallel-plate fracture with heterogeneous fault gouge, PCM: empty fracture, CCM: rough-walled fracture with homogeneous fault gouge. Data for hydrogen sulphide are used.

6.3.2 Modelling gas tracer tests at the Grimsel Test Site

Different conceptual models with increasing complexity were considered for modelling the gas tracer tests performed in the GAM shear zone. The aim of the simulations was, on the one hand, to perform a sensitivity analysis of the multitude of parameters needed to describe two-phase flow in the shear zone and, on the other hand, to compare the capability of different conceptual models to fit real data.

A first oversimplified model assuming a constant transmissivity field appeared inappropriate to reproduce experimental data. No set of parameters was able to adequately match the test results. In particular, this model showed problems in correctly reproducing the pressure response at most boreholes and reaching the experimental gas production rates. This proved the need to account for fracture heterogeneity by integrating into the model a-priori information from hydraulic tests.

In the following simulations, transmissivity fields obtained by geostatistical inversion of the hydraulic tests were used to construct conceptual models of fractures with a different pore volume distribution. A first sensitivity study was performed ignoring any relationship between the transmissivity and the entry pressure or between transmissivity and relative permeability (Garcia and Caussade 2001). According to laboratory experimental data, the capillary curve was defined as a piecewise linear function. Two models for relative permeabilities were tested: a van Genuchten model and a Grant model. Capillary pressure curves and relative permeability curves

were assumed to be constant over the whole domain. Only two of the conceptual models introduced in section 6.3.1 were considered to relate pore volume and transmissivity:

- the parallel-plate fracture filled with a heterogeneous fault gouge, with constant pore volume per unit of horizontal area (i.e. thickness times porosity) and heterogeneous hydraulic conductivity;
- the rough-walled empty fracture, with porosity $\phi=1$ and thickness defined by the cubic law ($b \sim T^{1/3}$).

The GAM shear zone was represented by a 2D simulation domain centred on borehole GAM98.004. The plane was assumed to be vertical and gravity effects were considered. Bottom, right and left boundaries of the domain were impermeable at a distance of 66 m from GAM98.004. Constant atmospheric pressure was assigned on the top boundary and on the tunnel boundary. The distance between the top boundary and GAM98.004 and the transmissivity at the tunnel/shear zone interface were adjusted to match the initial pressure data. A local grid refinement was applied to the central part of the domain with side length of 10 m. The models were calibrated on data from GT2 run#4, GT3 run#7 and run#8. The two were selected because they had better defined initial conditions, as they are the first runs of the GT2 and GT3 campaigns, respectively. The latter was retained because it was the first test showing a clear H₂S breakthrough. One of the calibrated models was also used to simulate the entire GT3 campaign, covering additional gas tracer tests not used for calibration (run #9 to #11).

The inverted transmissivity fields yielded major improvements compared to the homogeneous model: the experimental gas production rates were successfully simulated and pressure trends were also better reproduced. Pressures themselves generally remained unmatched, the simulated pressures showing higher variability than experimental pressures. Attempts to match the pressure slope (derivative) discontinuities observed during the long pressure fall-off that followed the multiple rate test at the end of GT3 also failed. Reasons were found in the complexity of the two-phase flow phenomena involved in the GAM gas tracer tests:

- Existence of a composite system with a restricted zone containing gas and surrounded by a fully water-saturated medium.
- Nearby constant pressure boundary with the tunnel, which clearly drains water.
- Gravity effects, with gas replaced by water during fall-off, leading to borehole storage changes and to pressure effects, gas pressures measured in boreholes becoming water pressures once gas has been replaced by water.

Differences among the inverted transmissivity fields were minor. A slight improvement in matching gas tracer breakthrough curves and pressure was obtained with transmissivity fields that have a horizontal correlation length of about 1m and moderate anisotropy characterised by a vertical correlation length 2 to 4 times smaller. The filled (parallel-plate) fracture and the empty fracture, associated with different pore volume distributions, yielded very similar results. This is in agreement with the simulations presented in section 6.3.1, which however considered spatially dependent entry pressure fields. Only a slightly higher retardation was detected in the tail of the breakthrough curves obtained with the empty fracture model. For both models, an average thickness times porosity of 7×10^{-4} m gave the appropriate breakthrough times.

For all calibrated models, poorly matched variables were the maximum concentration of H₂S at the extraction well and the gas/water ratio, which was systematically underestimated (overestimated water production). This might be due to the chemical properties of H₂S, which is reactive. This yields an irreversible decrease in tracer mass that could not be correctly reproduced by the model, which did not account for chemical reactions.

The effects of spatially varying capillary pressure curves were explored to improve the reproduction of water production rates and related gas/water ratios (Garcia and Caussade 2002). Indeed, in accordance to the results shown in section 6.3.1, they are expected to enhance fingering phenomena and channel flow for the gas phase. The simulation domain was the same as in Garcia and Caussade (2001). According to the previous sensitivity analysis, the transmissivity field with anisotropy ratio 1.0/0.5 was chosen among all the fields obtained by geostatistical inversion (Figure 4.5). The transmissivity field was transformed into a hydraulic conductivity field and into an aperture field assuming the two different conceptual models already used by Garcia and Caussade (2001). The third conceptual model introduced in section 6.3.1 was not considered of interest as it implies a spatially constant capillary model.

On the basis of the hydraulic conductivity fields, 24 conductivity classes were defined: the log-conductivity variation range was divided into 24 regular intervals, associated with the middle value of the interval. The same type of capillary pressure was assigned to all grid blocks characterised by conductivity values belonging to the same class. The Brooks-Corey model is adopted to describe the capillary pressure-saturation curves both for the empty and the filled fracture. For each interval, the entry pressure and the maximum capillary pressure are related to the middle conductivity value via the Leverett's model. This made the capillary pressure proportional to the inverse of the square root of the conductivity, i.e. $p_c = K^{-1/2}$. The same relative permeability curve was applied to the whole domain. However, two different cases were considered testing the Brooks-Corey model and the cross model, the latter assuming little interference between the two phases.

Introducing transmissivity-dependent capillary pressure curves further improved gas/water ratio predictions, but conserving the previous good matches. This was not enough, however, to reach and maintain high gas/water ratios as observed experimentally. Slippage effects of low-pressure gas flow might be introduced in order to improve the matching of experimental data.

A further improvement was achieved by considering gas-slippage effects (Klinkenberg effects), which yield different permeabilities for the gas and the liquid phases at low pressure. After a sensitivity study, Garcia and Caussade (2002) identified two sets of parameters as the best in matching experimental data. The gas/water ratios, the gas tracer breakthrough curves and the gas saturation maps obtained by simulating GT2 run#4 with these sets of parameters are compared in Figure 6.8. Both models assume a fault gouge-filled fracture. Details of capillary pressure and relative-permeability models are given in Table 6.3.

Tab. 6.3: Capillary pressure and relative permeability parameters.

Name	Rel. perm. model	Res. water saturation (-)	Max. rel. perm. (water)	Max. rel. perm. (gas)	Cap. pressure model	λ	Entry pressure (kPa)	Max cap. Pressure (kPa)
Tfield6FilledCase5	Cross	0.2	1.0	3.2	Brooks-Corey	3.0	20	80
Tfield6FilledCase13	Modified Brooks-Corey	0.0	1.0	3.2	Brooks-Corey	3.0	5	20

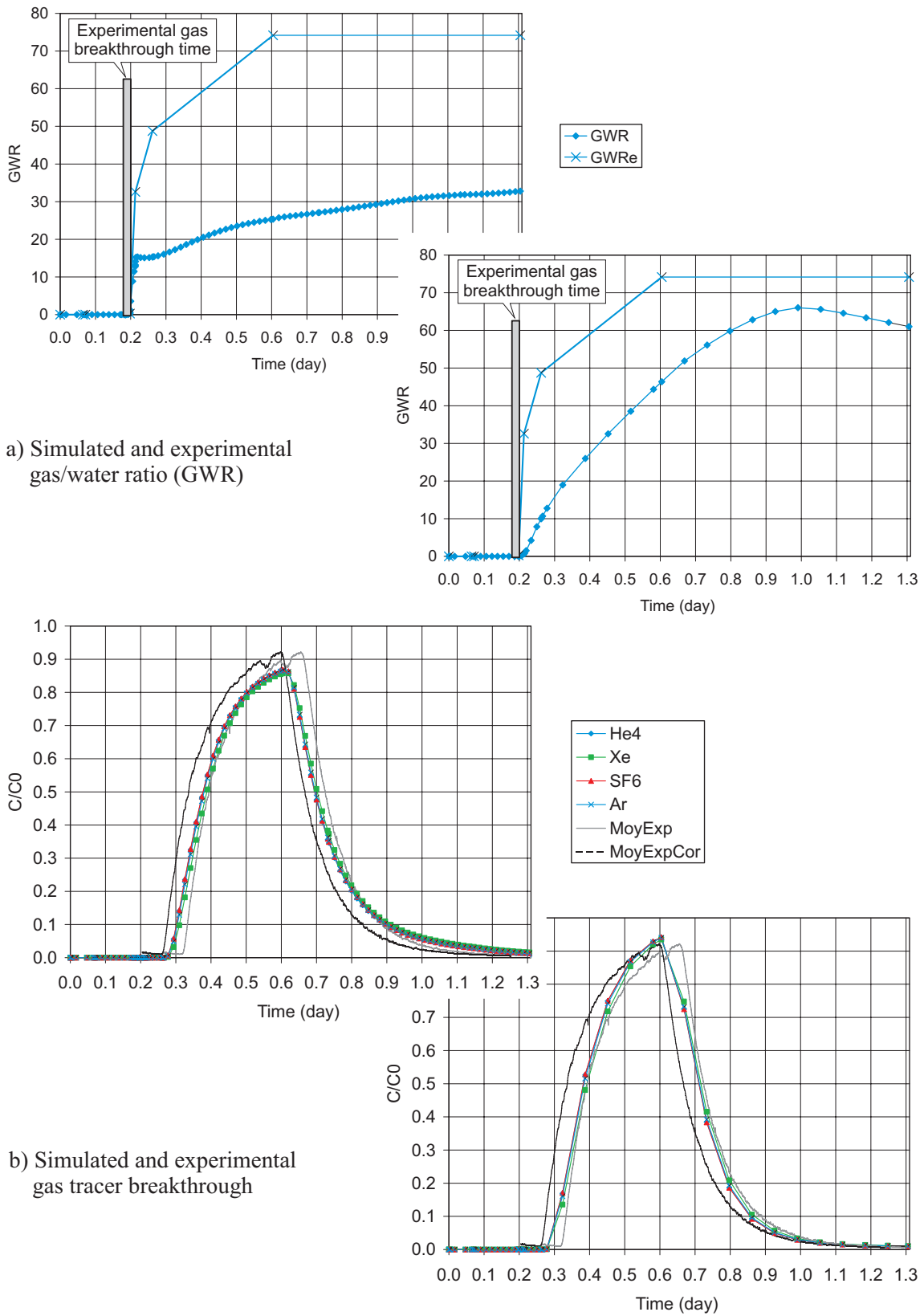
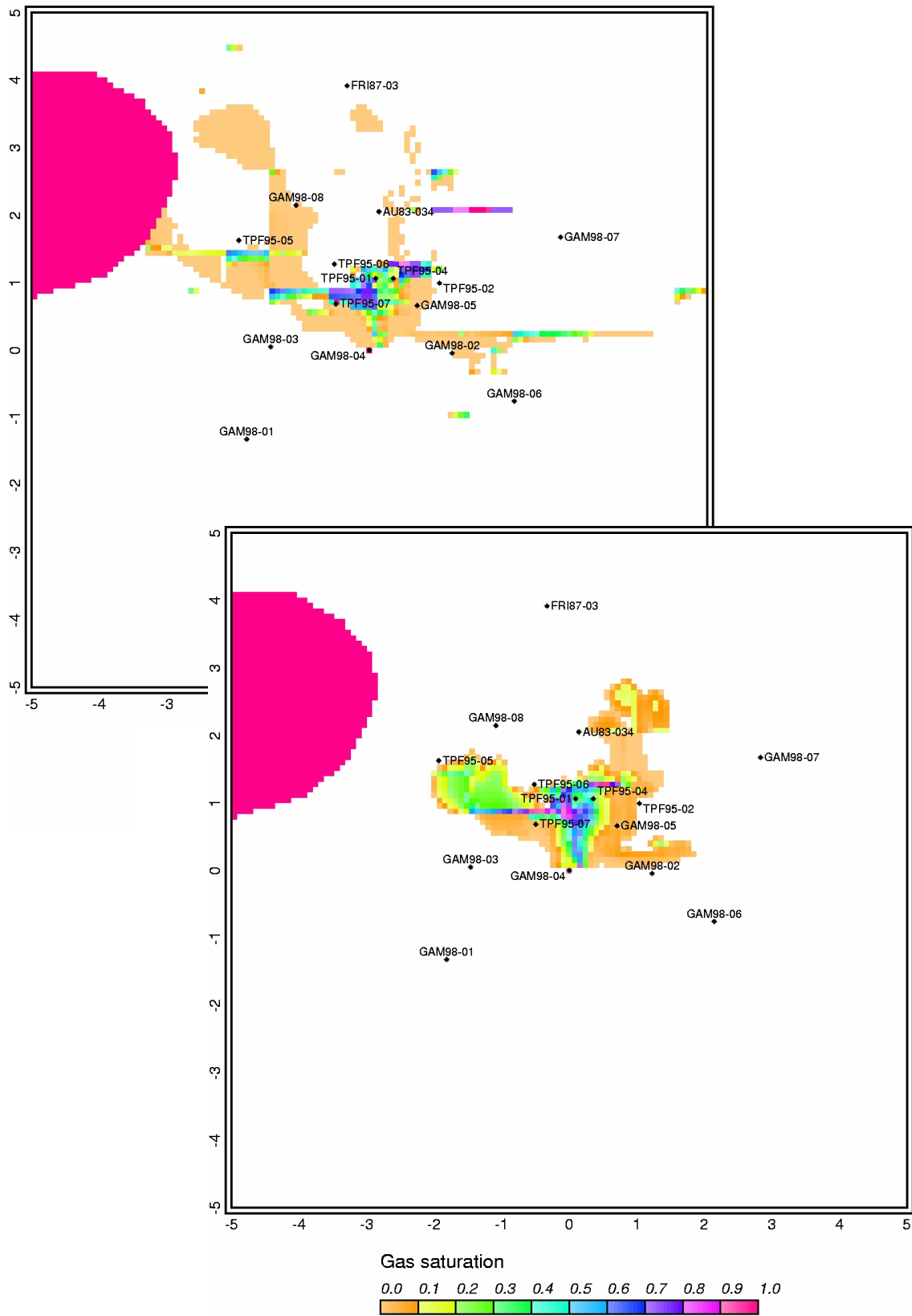


Fig. 6.8: Modelling of gas tracer test GT2 run # 4.

Gas/water ratios (a), the gas tracer breakthrough curves (b) and the gas saturation maps (c) obtained by simulating GT2 run#4 two sets of parameters best in matching experimental data (details of capillary pressure and relative permeability models are given in Table 6.3).



c) Gas saturation map.

Fig. 6.8: (Cont.) Modelling of gas tracer test GT2 run # 4.

Another conceptual model adopted to describe the gas tracer tests was a superimposition of the empty fracture and the fault gouge-filled models. The shear zone was divided into two regions:

- The mobile zone consisting of several open fracture paths was modelled as a single empty fracture with spatially dependent aperture computed according to cubic law from the geostatistically inverted transmissivity field (chapter 4). This structure was assumed to be completely unsaturated after the steady state dipole flow was established: water was present only in the form of a thin film wetting the fracture walls, which does not move. Gas tracer transport in the mobile zone was mainly advective and the contribution of the water film (molecular diffusion of dissolved tracer) was completely ignored.
- The immobile zone consisting of regions filled with fault gouge was assumed to be completely water saturated: due to the high gas entry pressure of the fine fault gouge, the gas is not able to displace water. Gas mass transfer between the immobile and mobile zones is assumed to be instantaneous and governed by Henry's law. Molecular diffusion is the only transport mechanism for dissolved gas tracer in the immobile zone.

These two regions formed a two-dimensional structure embedded in the rock matrix that was assumed impermeable to the flow.

First, gas migration between injection and extraction wells was simulated. Entry pressure was assumed to be dependent on the inverse of the aperture and capillary pressure was modelled by a linear-step curve. Once gas flow became steady-state, i.e. extraction gas flow rate through the extraction borehole was constant and pressures in the fracture were stationary, the gas tracer test was simulated: the gas tracer cocktail is injected at constant mass rate at the recharging well, whereas breakthrough curves at the extraction well are recorded.

Run #4 of GTT2 was selected for the simulation. The dipole flow field was created by injecting N_2 at a constant rate of 10ml(STP)/min in borehole GAM98.004 and imposing constant liquid and gas pressures of 0.1MPa in the extraction borehole TPF95.004.

Due to the fact that each gas tracer has different solubility and diffusivities, separate transport simulations were conducted for each gas contained in the tracer cocktail. As can be seen in Figure 6.9, none of the predicted breakthrough curves (dashed lines) fit reasonably well the observed breakthrough curves. The model fails to reproduce both peak concentration and tail slope of the breakthrough curves for all tracers. A calibration of the transport parameters was performed to obtain a better match between experimental and computed breakthrough curves. For all tracers, the best match was obtained by reducing the fracture apertures by a factor of 0.33 (Figure 6.9).

No significant separation effect was obtained in the simulations, according to the experimental data. Indeed, the chromatographic effects depend on the gas tracer properties such as solubility and diffusivity, as well as on the water content that is available for dissolution inside the fracture. Thus, this model suggested that a small water volume is available for dissolution over the residence time of the tracers.

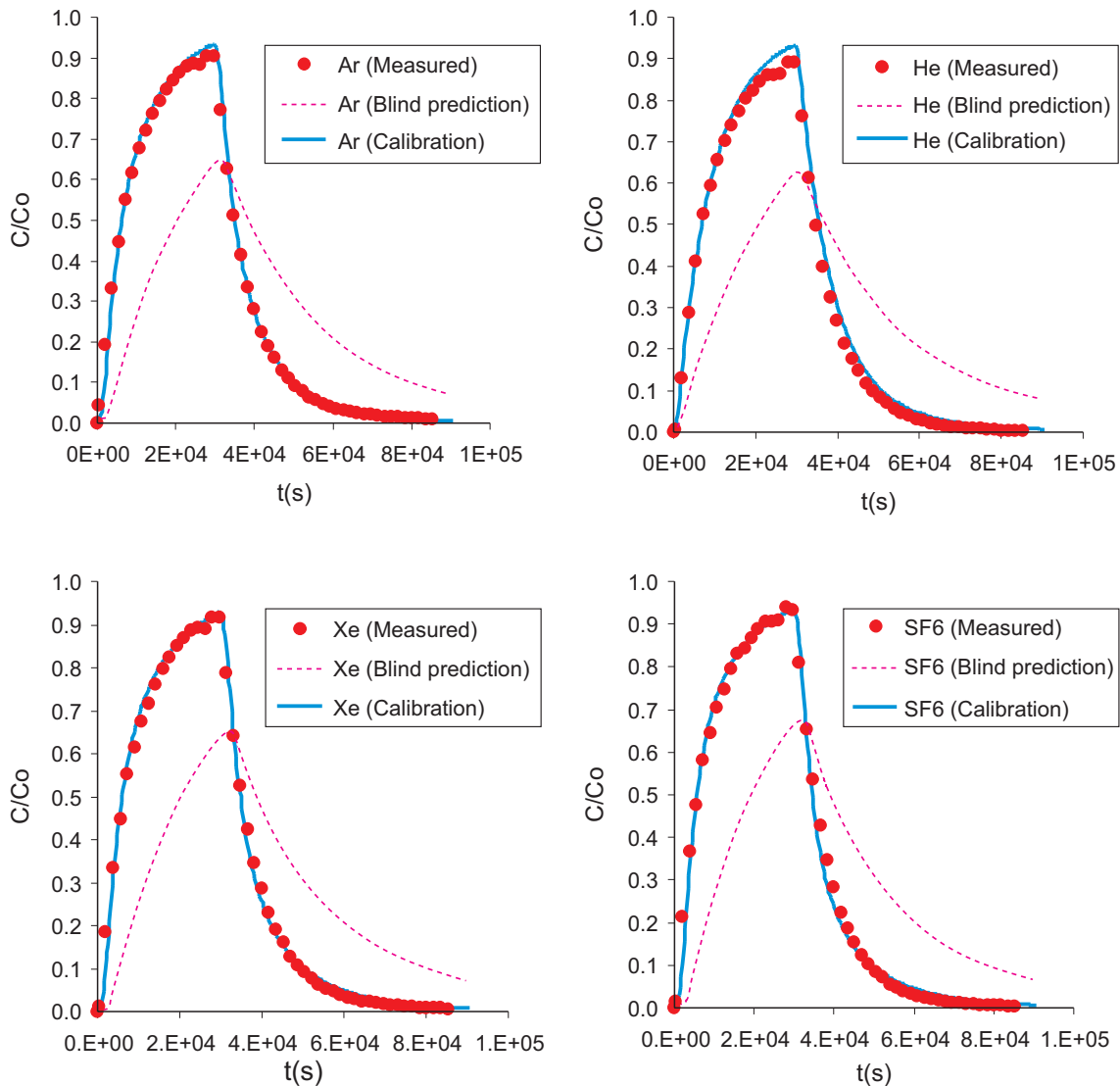


Fig. 6.9: Measured breakthrough curves, blind prediction and calibrated breakthrough curves for the four gas tracers used in Run#4 (Ar, He, Xe and SF₆ respectively).

6.4 Achievements and outlook

The technical achievements concentrated on the development of know-how in online gas tracer detection and on equipment refinements for combined gas/water extraction, which allowed stable gas flow fields over time periods of several weeks to be established. Furthermore, the dead volumes in the injection and extraction systems were minimised in order to reduce the impact of artificial dispersion in the breakthrough curves. In the final stage of the GAM experiment, reliable test equipment and mature test procedures were available for long-duration and well controlled gas tracer tests.

The main outcome of the experimental campaigns was that retardation caused by tracer solubility was smaller than expected. The expected separation of the gases with different solubility was based on the assumption of an efficient mass exchange along the gas paths due to the very large interface between the gas and the liquid phases. In contrast, the experiments showed that a significant separation of the tracers could be observed only in the tail of the breakthrough

curves. It is therefore concluded that the accessible water volume along the gas paths was small and the effect of dissolution over the typical time of the experiments was limited. The streamlines that contributed to the tails of the breakthrough curves may have experienced longer residence times in the shear zone, which allowed reaching deeper water showing some retardation due to water solubility. The observations suggest distinct channeling of gas flow along narrow pathways, as illustrated in the generic simulations in Figure 6.8a and 6.8b. Hence, the conceptualisations of a shear zone with heterogeneous fault gouge or even a rough-walled shear zone without fault gouge seem to be better suited to explain the gas transport processes in the GAM shear zone than the model of a fracture with homogeneous fault gouge infill.

A single case was represented by H_2S , which exhibited very different breakthrough curves compared to the other tracers. However, the different shape of the breakthrough curve cannot be attributed to the effect of water solubility only. H_2S is reactive and has corrosive effects on the metallic components of the set-up and on some minerals of the geological formation. Finally, H_2S was not considered a suitable tracer because data are difficult to interpret due to the combined effects of reactivity and solubility. Moreover, working with H_2S posed numerous practical problems due to dealing with a hazardous and corrosive chemical.

The interpretation of the experimental data benefited from the numerical modelling activity, which clearly showed the impact of a heterogeneous gas distribution on the tracer retardation. The capillary pressure, and in particular the spatial variability of the entry pressure, played a fundamental role in determining the gas saturation distribution within the shear zone. Different conceptual models of the shear zone were applied to simulate the gas tracer tests. Tracer breakthrough could be equally well matched with different conceptual models and with many sets of parameters, whereas other quantities (e.g. the gas/water production ratio, the pressure at the boreholes) were less successfully reproduced. In simulations where no significant retardation was observed, the breakthrough curve was mainly determined by the total cross-sectional pore volume of the gas phase along the gas paths, which controls the advective velocity. In this case, the breakthrough curve can be matched by fitting the thickness times porosity parameter, whereas the total porosity and the gas saturation in the medium do not play a significant role.

If solubility was significant, the gas-saturation within the shear zone played an important role on the resulting breakthrough curves, because the gas saturation affected the retardation of the gas tracer. On the other hand, it was theoretically demonstrated that data from tests employing tracers with different water solubilities could be used to estimate the fracture saturation if the solution process is known. The application of this technique to the experimental data was not attempted because of the important role played by kinetic effects.

According to the early arrival and the small retardations observed, gas flow in the shear zone was likely to take place within highly gas saturated channels. The gas phase concentrated in the larger porosity of the medium, possibly in a few open fractures present in the shear zone, and a small water volume are immediately available for gas dissolution over the experiment timeperiod.

7 Geophysical surveys

The applicability of non-destructive in-situ methods for the visualisation of solute and gas transport processes was evaluated as part of the preparatory phase of the GAM experiment. Such geophysical methods are seen as a key technology for inferring the length scale of heterogeneity in the GAM shear zone (cf. section 5.4). Seismic methods and ground penetrating radar were identified as possible techniques for monitoring a gas phase in the GAM shear zone. For the detection of solute tracers, seismic techniques are not suitable, whereas ground penetrating radar offers a chance for monitoring solutes if the salinity contrast between groundwater and tracer is sufficiently high. For this reason, the radar technique was selected for the in-situ visualisation tests in the GAM project.

Section 7.1 gives an overview of the georadar field campaigns, the applied test equipment and the basic test configurations. Technical details of the borehole probe and the ground antennae are discussed. Section 7.2 provides a brief summary of the results collected during the different measurement campaigns, with graphs of reflection and transmission measurements. Section 7.3 describes the efforts in modelling the radargrams using a simple ray tracing method.

7.1 Field campaigns and test equipment

The concept for high-resolution measurements with borehole radar equipment was elaborated in Marschall et al. (1998) and Albert (1999). A custom-made 1 GHz borehole probe had to be developed and tested, because standard borehole antennae do not allow for a spatial resolution in the decimetre range, which was required to image solute and gas transport in the GAM shear zone. In-situ tests of the georadar equipment were performed in October 1999 (Albert 1999), aimed at testing the transmission characteristics of the borehole antenna.

A radar survey during a radially diverging brine injection test was carried out between November 15th and 19th 1999 (Albert 2000a). The experiment started on November 15th with freshwater injection in borehole GAM98-02 at a constant injection rate of around 1.7 ml/min (salinity of freshwater: 0.11 mS/cm). The injection was maintained for more than 1 day to displace any remaining solute tracers from previous tracer experiments and to ensure uniform salinity in the shear zone. The brine injection started on November 17th at 11:00 (salinity of freshwater: 30 mS/cm). Just before the brine injection, the injection rate had been reduced to 0.5 ml/min. Tracer injection was continued until November 18th at 10:00, followed by freshwater injection at the same constant rate until November 19th 1999.

The next radar survey between February 1st and 4th 2000 (Albert 2000b) was aimed at visualising gas paths during the gas threshold pressure test in GAM98-02 and the subsequent gas tracer test GT1 (dipole test between GAM98-02 and TPF95-07). The injection of nitrogen gas started on February 1st at 9:46 at a mass flow rate of 100 ml/min (STP). On the same day at 14:06, borehole TPF95-07 was opened to establish the dipole gas flow field. Due to strong fluctuations of the gas outflow, a stable gas flow field could not be achieved. Therefore, it was decided to stop gas injection and to open borehole GAM98-02 (Feb. 1st, 20:23). Subsequently, the gas flow field was reversed by injecting nitrogen at a mass flow rate of 50 ml/min (STP) in borehole TPF95-07 (Feb. 1st, 21:00), with extraction from GAM98-02. A detailed description of the entire gas tracer test campaign is given in Fierz et al. (2000), comprising the corresponding test logbooks, the description of the different stages of the experiment and a summary of the test results.

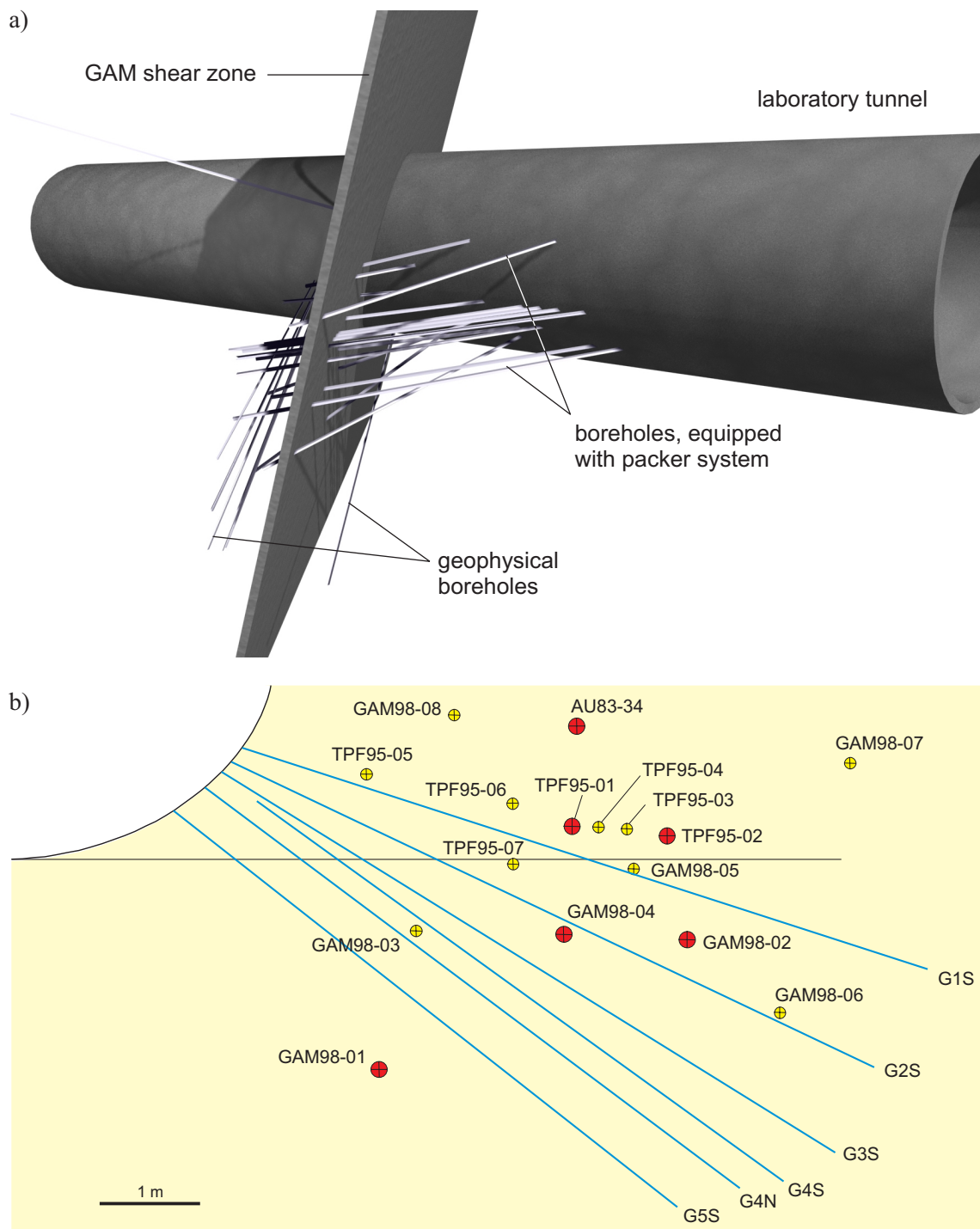


Fig. 7.1: Basic test arrangement during the brine and gas injection tests in the GAM shear zone: (a) 3-D view of the GAM site with the geophysical boreholes and (b) projection of the geophysical boreholes G1S-G5S and G4N on the shear zone plane.

Figure 7.1 presents a schematic sketch of the basic test arrangement which was used for both the brine and the gas injection experiment. At a distance of 1 m, a fan-like array of boreholes G1S to G5S had been drilled to the south of the shear zone, complemented by the single borehole G4N to the north. Any remaining water was pumped from the geophysical boreholes at the

beginning of the geophysical field campaign. The equipment consisted of a 4-channel SIR10 radar system with with the following antennae:

- two 500 MHz ground antennae (500 T: transmitter, 500 R: receiver),
- a 900 MHz ground antenna (900 T: transmitter, 900 R: receiver)
- a 1 GHz borehole antenna (TW 1000 T: transmitter, TW 1000 R: receiver).

The borehole antenna was fixed on a wooden rod to prevent rotation of the probe, while the ground antennae were positioned on the tunnel wall as shown in Figure 7.2.

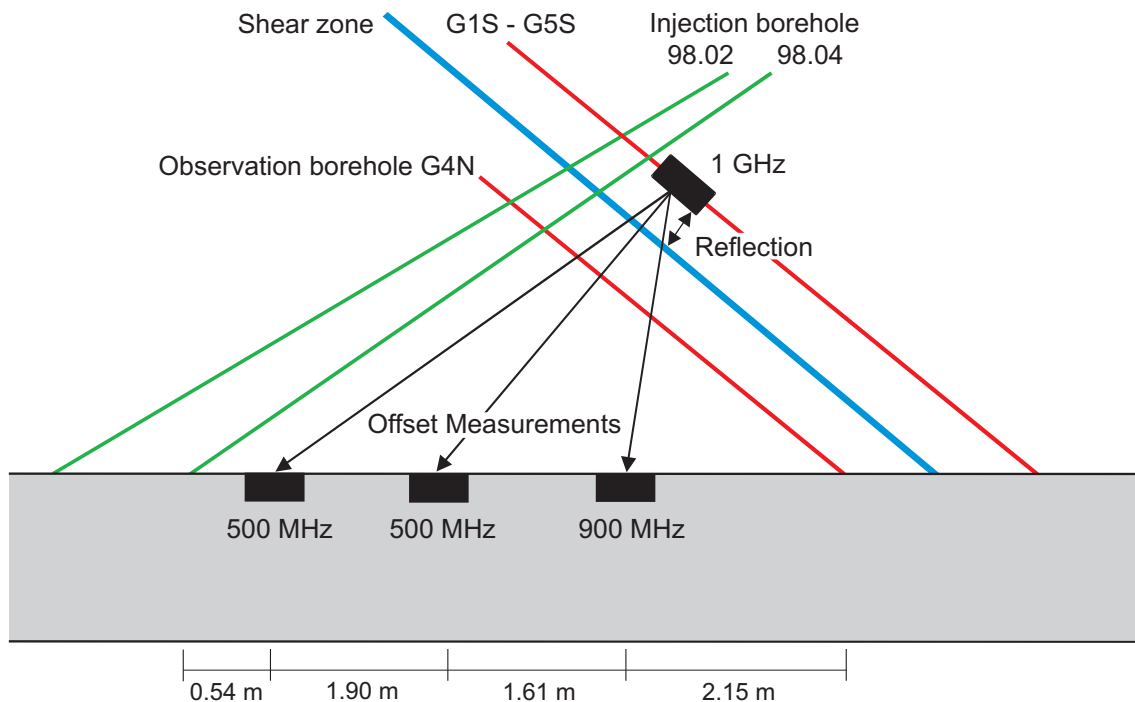


Fig. 7.2: Configuration of the ground penetrating radar array. The borehole antenna is moved along boreholes G1S-G5S and G4N, respectively. The ground antennae have fixed positions at tunnel surface.

Subsequent measurement series were performed before, during and after brine and gas injection, with the purpose of mapping changes in the radargram patterns due to the presence of brine or gas in the shear zone. Every measurement series included three different types of measurements: reflection mode, reflection in offset mode and transmission measurements. The reflection measurements were carried out in all boreholes (G1S-G5S & G4N) using the 1 GHz borehole antenna as transmitter and receiver. The reflection measurements in offset mode were performed from borehole G4N (borehole antenna 1 GHz) to the ground antennae (900 MHz, 500 MHz no1, 500 MHz no2). The expected time shift between direct wave and reflection from the shear zone was about 15 ns. The transmission measurements were performed from the boreholes G1S-G5S to the three ground antennae at the tunnel wall: the direct waves sent by the 1 GHz borehole antenna in the boreholes G1S – G5S travel through the shear zone and are then received at the ground antennae (900 MHz, 500 MHz no1, 500 MHz no2).

7.2 Test results

The field reports of the aforementioned georadar campaigns (Albert 2000a, 2000b) provide a brief summary of the test results, including radargrams of the raw data and a preliminary stage of data processing (stacking, migration, difference plots of time sections). Refined processing procedures were beyond the scope of the project.

The processing and interpretation of the raw data were complicated by a multitude of factors, such as the complicated test geometry, undesirable radar diffractions from the hydraulic borehole equipment, the time-consuming logging procedure with the borehole antenna and, last but not least, due to the limited knowledge about the actual tracer flow paths in the shear zone. The different modes of data recording (reflection mode, offset mode, transmission mode) exhibit some characteristic features, which need to be considered in the subsequent data interpretation.

In the reflection mode, much diffraction was observed in the logs of the borehole antenna, the diffraction images differing from borehole to borehole. In the processed radargrams (“migrated section”), the radial distance of the objects (diffractors) from the boreholes is displayed and it should be possible to image point and line diffractors. However, the complex diffraction pattern did not allow a direct image of the shear zone to be obtained by reflection measurements, which may be attributed to the following facts:

- The shear zone image was more or less horizontal, because the shear zone itself was parallel to the observation boreholes. Thus, the artificial, horizontal background overlaid the reflection signal of the shear zone, which was partially eliminated by the background removal.
- The metal installations created diffraction signals that were much stronger than the shear zone reflection signal.

The reflection measurements in the offset mode (borehole antenna in G4N) exhibit numerous different arrivals after the direct wave, most of them produced by diffractions of the metal installations (packer equipment). These signals showed changes with time, which could not be correlated with brine and gas injection sequences, respectively.

In the transmission mode, distinct changes were observed in the time sections, which could be clearly attributed to the brine and gas injection processes. However, the configuration of the antennae (cf. Figure 7.2) was not optimised for imaging the brine and gas flow field in the transmission mode.

7.2.1 Brine injection test (between November 15th and 19th 1999)

Baseline radar measurements were conducted during the freshwater injection on November 16th 1999. Figure 7.3 shows the baseline measurements along borehole GS2S in the reflection mode (left: stacked time section; right: migrated time section). In the stacked time section, distinct reflections from the tunnel wall are observed. Furthermore, multiple diffractions with their characteristic hyperbolic signatures can be related to the hydraulic instrumentation of the boreholes that intersect the GAM shear zone. The objects of interest such as the GAM shear zone and the diffractors cannot be imaged perfectly in the migrated time section (Figure 7.3b). This is explained by the combined effect of (i) the limited resolution of the radar and (i) the complexity of the site instrumentation.

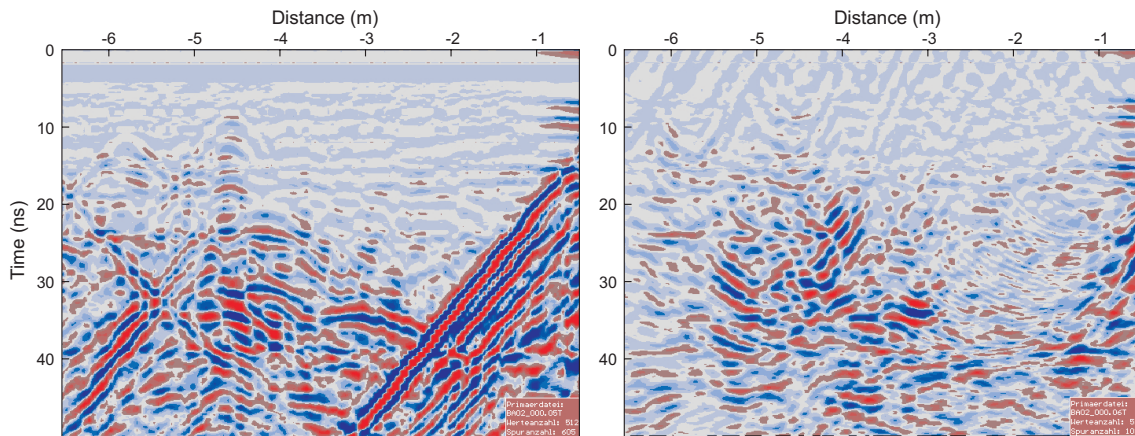


Fig. 7.3: Baseline radar measurements along borehole G2S on November 16th (16:01): (a) stacked time section and (b) migrated time section.

A series of radar measurements were conducted during the brine injection period between 17th and 19th November 1999. Notably, no significant changes were seen in the reflection mode and in the offset mode. In the transmission mode, however, distinct temporal variations were observed for all antennae configurations, which could be correlated with the brine injection. Figure 7.4 shows, along borehole GS1, a sequence of difference plots in the transmission mode (reference: baseline measurement on November 16th 1999). The difference plot of November 17th exhibits minor variations in the amplitudes (Figure 7.4b), whereas the strongest differential amplitudes are observed in the difference plot of November 18th about 20 h after the start of the brine injection (Figure 7.4c). A slightly different behaviour was observed for the boreholes G3S – G5S, where the strongest differential amplitudes were recorded on November 17th. These temporal and spatial changes in the transmission measurements are most likely a result of the complex mixing in the shear zone due to (i) the finite duration of the brine injection and (i) the strong transients in the flow field during the early stage of the brine injection.

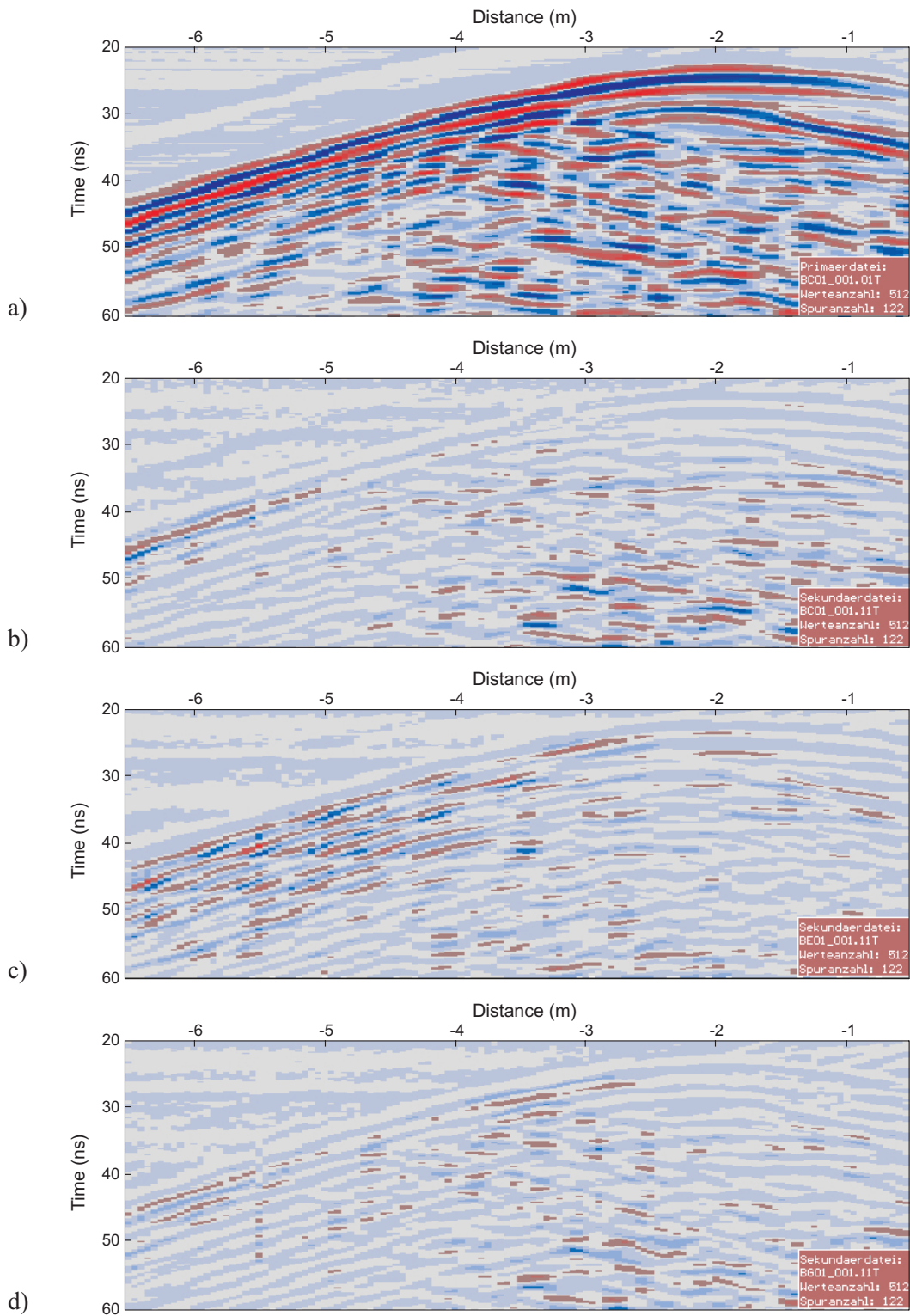


Fig. 7.4: Georadar surveys during the brine injection test between November 15 and November 19, 1999.

Transmission measurements along borehole GS1 with the 900 MHz ground antenna as receiver: (a) time section of November 17, 12:33, (b) difference plot of the time sections 17/11-12:33 and 16/11-14:52, (c) difference plot 18/11-08:00 and 16/11-14:52 and (d) difference plot 19/11-09:03 and 16/11-14:52.

7.2.2 Gas injection test (between February 1st and 4th 2000)

Baseline radar measurements were conducted before the start of the gas injection on the 31st of January. Configuration of the radar antennae and modes of data recording (reflection mode, offset mode, transmission mode) were the same as during the brine injection test.

Figure 7.5 shows the baseline measurements along borehole GS1 in the reflection mode (left: stacked time section; right: migrated time section). Piecewise reflections are observed for travel times of ~ 24 ns, corresponding to the distance of 1 m between borehole GS1 and the GAM shear zone. Diffractions of large amplitudes are superimposing the shear zone reflector.

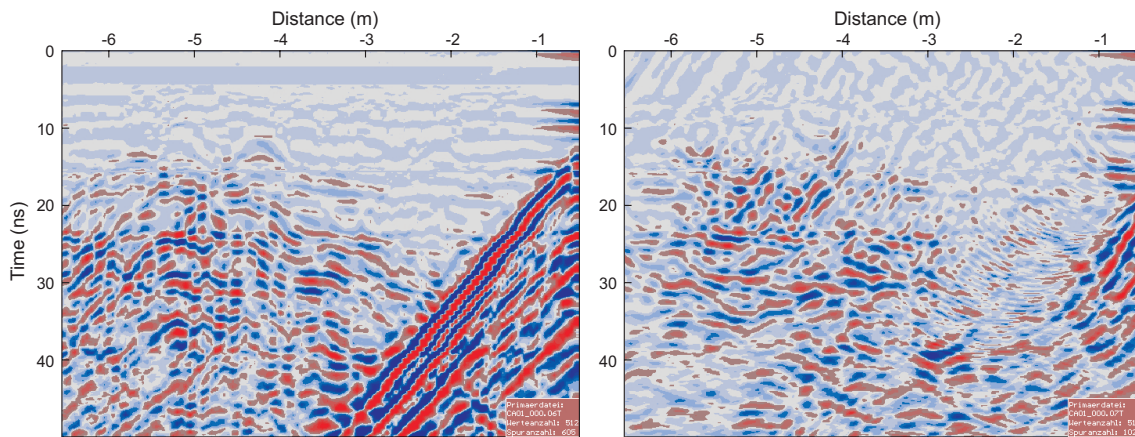
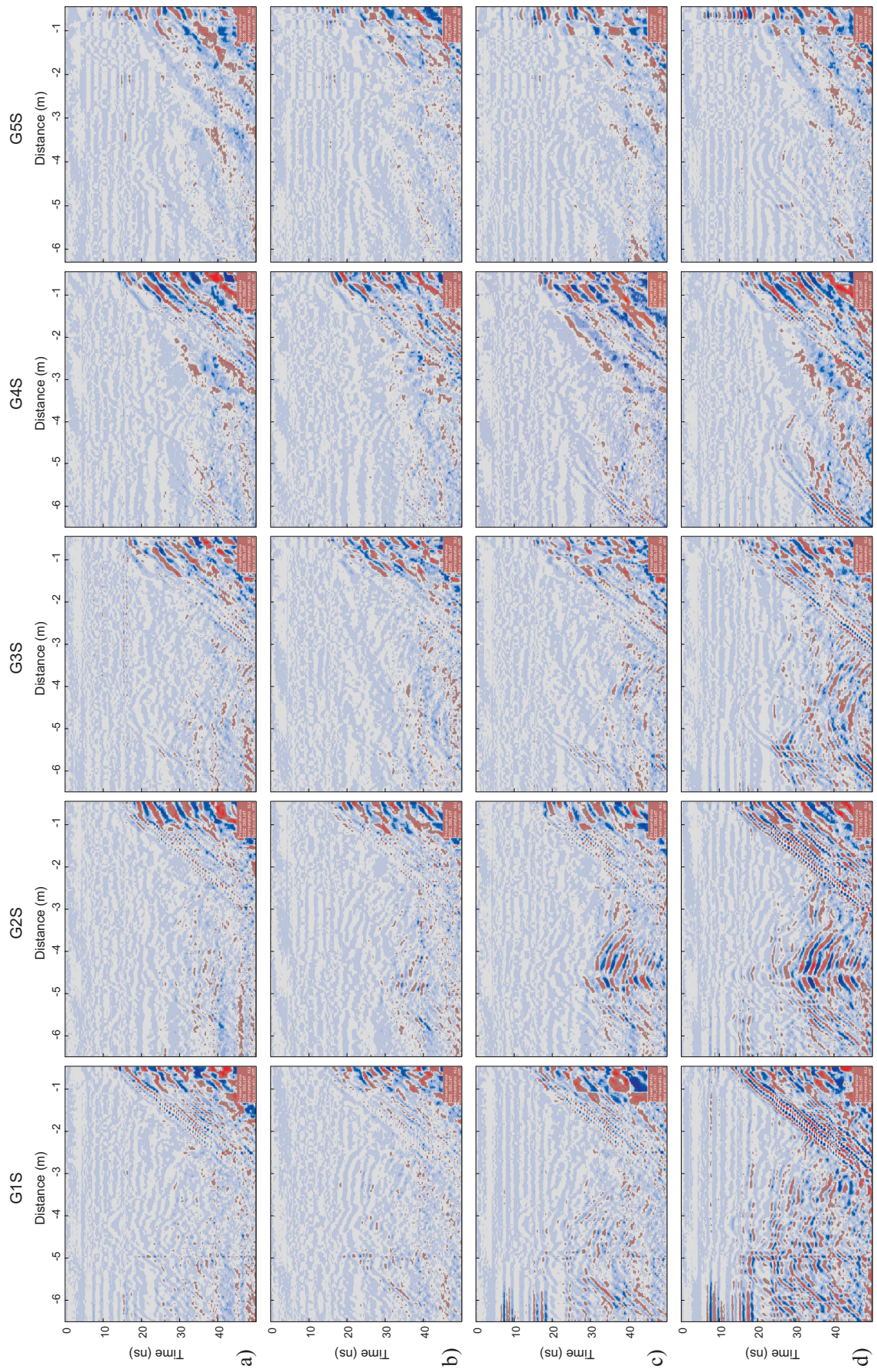


Fig. 7.5: Baseline radar measurements along borehole G1S on January 31st (16:01): (a) stacked time section and (b) migrated time section.

Four series of measurements were performed after the start of the gas injection on February 1st at 9:46. Figure 7.6 shows, for the boreholes GS1 to GS5 the difference plots in the reflection mode. The changes are small and more or less statistical in the first and second series of difference plots ($\sim 10:00$ and $\sim 12:00$ on the 1st of Feb.), but significant in the third ($\sim 15:00$ on the 1st of Feb.) and fourth series ($\sim 8:00$ on the 2nd of Feb.). In boreholes G1S, G3S and G4S, only amplitude variations of the diffractions are visible; these effects are most pronounced in borehole G1S.

Reflection measurements in the offset mode were conducted with the borehole antenna in G4N as the transmitter and with the ground antennae as receivers (Albert 2000b). In all offset measurements, numerous different arrivals were observed after the direct wave, probably produced by diffractions from the metallic borehole installations. The difference plots in the offset mode exhibit marked changes with time. However, a clear correlation of these changes with the effect of gas injection is not possible due to the complex geometric configuration of the site instrumentation.

Transmission measurements were conducted with the borehole probe in the boreholes G1S – G5S as the transmitter and with the ground antennae as receivers (Albert 2000b). No amplitude variation of the direct wave was observed in the difference plots of the first measurement series after gas injection ($\sim 10:00$ on the 1st of Feb.). However, in all subsequent measurement series marked amplitude changes were monitored, which increased with time. The strongest variations were observed for the boreholes G1S and G2S. As for the offset mode, it turned out to be difficult to explain the transmission measurements without an interpretation tool that considers the complex geometric configuration of the site instrumentation.



7.3 Modelling results

The georadar surveys in the GAM shear zone - and in particular the measuring campaign during the gas injection test in February 2000 – demonstrated in principle the feasibility of in-situ visualisation of transport processes by non-destructive methods such as radar technology. The injected gas phase could be clearly detected both in the reflection and the transmission mode. The difference plots in Figure 7.6 draw a plausible picture of the gas injection process in that they exhibit the most significant reflections along the boreholes G1S and G2S, which are close to the injection borehole GAM 98-002. On the other hand, it turned out to be a too ambitious aim to image the gas propagation process in the shear zone with the required spatial and temporal resolution. The purpose of the modelling task concentrated therefore on the basic understanding of some of the main features of the radargrams rather than on a rigorous inversion of the time sections. Synthetic radargrams were simulated in the reflection mode, aimed at imaging (i) the reflection of the GAM shear zone and (ii) the diffractions caused by the hydraulic instrumentation of the GAM site (project document GAM-61/Marschall 2006). A simplified ray tracing approach was applied for calculating the the travel time of the reflected / diffracted waves as shown in Figure 7.7. The approach did not account for multiple reflections and diffractions.

The electromagnetic permittivity of the medium was assumed to be $\epsilon = 5.65$, which yielded a wave velocity $v = 1.2 \times 10^8$ m/s. The experimental radargrams covered in all cases a borehole length of 6 m and a time range of 50 ns, which corresponded to a maximum reflection distance of 6.3 m from the antenna borehole, using the above-calculated velocity.

Figure 7.8 compares the experimental and the synthetic radargram for the radar log in borehole G2S. The plot was scaled assuming that the antenna is moved along borehole G2S from 0.5 m to 6.5 m depth, the wave velocity is 1.2×10^8 m/s and the measurement offset is -6.5 ns (-0.8 m travel distance). The tunnel and its multiple reflections were the dominant feature in the measurements in the lower-right part of the radargram. The horizontal structures represent those objects which are more or less parallel to the antenna borehole (GAM shear zone, boreholes G1S-G5S and G4N). With the visual help of the calculated results, some structures of the experimental radargrams can be related to specific boreholes, e.g. GAM98-06 which corresponded to the oblique straight line in the left part of Figure 7.8, or some of the hyperbolic curves, corresponding mainly to the group of TPF95 boreholes. The majority of the simulated reflectors and diffractors, however, cannot be assigned unequivocally to the corresponding experimental radargram.



Fig. 7.6: Georadar surveys during the gas injection test on February 1 – 4, 2000.

Reflection measurements along boreholes G1S – G5S: (a) difference plot of the time sections 31/01-12:00 and 01/02-10:00, (b) difference plot 31/01-12:00 and 01/02-12:00, (c) difference plot 31/01-12:00 and 01/02-15:00 and (d) difference plot 31/01-12:00 and 02/02-08:00.

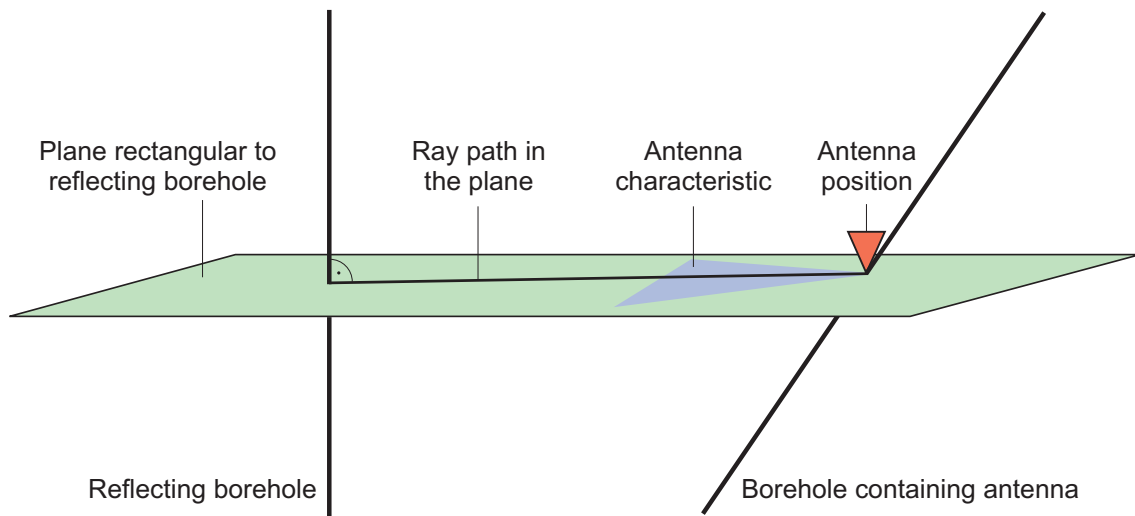


Fig. 7.7: Simulation of a time section in the reflection mode, using a simplified ray tracing approach:

Geometric configuration of the logged borehole and of the diffractor (e.g. borehole equipped with a multipacker system). The travel time of the diffracted wave is determined by the length of the ray path and by the velocity of the electromagnetic wave in the rock.

The synthetic radargrams calculated for the boreholes G1S and G3S – G5S exhibit patterns of reflections and diffractions which are similar to the radargram in Figure 7.8 (cf. Klubertanz & Schwarz 2000). As for the borehole G2S, only a few of the reflectors and diffractors in the synthetic radargram can be assigned clearly to the structures in the corresponding experimental time sections. The majority of structures in the experimental radargrams remain unrecognised, i.e. it is not possible to assign them to any of the potential reflectors / diffractors at the GAM site. This has several reasons:

- The complex geometry of the site instrumentation causes a multitude of superimposing reflections and diffractions which can hardly be separated.
- Exact geodetic surveys of the geophysical boreholes were not available; this fact introduces an additional degree of uncertainty in the synthetic radargrams.
- The structural characterisation of the GTS shear zones (section 2.2) revealed that the representation of the GAM shear zone as a planar structure is an oversimplification. The shear zone comprises several fault gouge horizons, which may form complex 3-D networks of potential fluid / gas flow paths.
- Only the basic data processing procedures were adopted for the interpretation of the radar measurements, including a simple background removal (cf. Albert 2000a, 200b). It cannot be excluded that the shear zone reflections were partly eliminated by the background removal procedure.
- The synthetic radargrams were calculated with a simplified ray tracing procedure which does not account for multiple reflections, or for a correct representation of the signal amplitudes. Advanced interpretation methods could have facilitated the comparison with the experimental radargrams.

In-depth interpretations of the radar measurements were beyond the scope of the GAM project. Nevertheless, it is believed that a more sophisticated re-interpretation of the existing data could

be an important step forward in the evaluation of the radar technologies as a non-invasive method for the visualisation of transport processes in heterogeneous media. Significant improvements in the interpretation process include a detailed geodetic survey of the geophysical boreholes, careful reprocessing of the radar raw data and the use of advanced modelling tools such as ray tracing methods or full wave inversion techniques. Data re-interpretation should also consider the data sets which were acquired in the offset mode and the transmission mode.

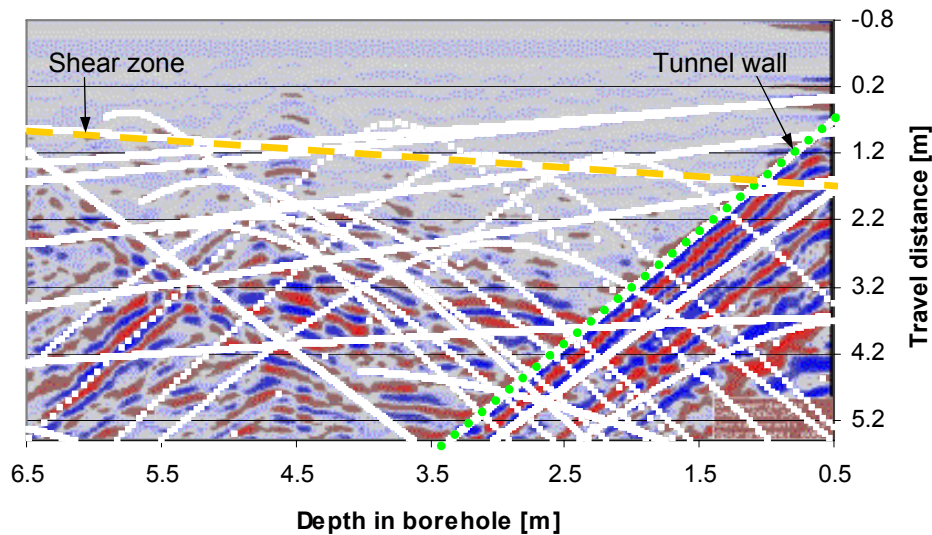


Fig. 7.8: Comparison measurement (coloured background) and calculations (white dots) for antenna in borehole G2S; the tunnel is indicated by the green dots, the shear zone by the yellow dashes.

7.4 Evaluation of achievements and outlook

Non-invasive geophysical methods are considered as a key technology for inferring, on the site scale, the characteristic length scale of variability of transport properties in fractured rock. The applicability of ground penetrating radar was tested within the framework of the GAM project; radar surveys were carried out in the course of a brine injection test and a gas injection test. The results of the two field campaigns can be summarised as follows:

- The radar survey of the brine test did not exhibit results which were sufficient to infer the propagation of the brine during the injection phase. Weak signatures of the brine injection were observed in the transmission mode but no response was recorded in the reflection mode.
- Encouraging results were obtained during the survey of the gas injection experiment. The gas injection phase could be detected in the reflection and transmission modes. Variations in successive radargrams can be correlated with the changing flow field during the gas injection phase. The field campaign proved in principle the applicability of georadar techniques for the in-situ visualisation of gas transport processes in fractured rock.
- The interpretation of the radargrams was complicated by the complexity of the test configuration at the GAM site. Of the multitude of potential reflectors and diffractors at the GAM site (shear zone, tunnel wall, hydraulic and geophysical boreholes), only a few could be identified unequivocally in the radargrams.

- The applied data processing procedures and the modelling tools which were available for the interpretation of the georadar measurements turned out to be insufficient. A more advanced data interpretation was beyond the resources of the project.

It is concluded that the two georadar surveys were not performed in a way which is needed for imaging transport processes in fractured rock with sufficient temporal and spatial resolution. Nevertheless, despite the limited success in visualising fluid and gas transport processes in the GAM shear zone, the georadar surveys have shown their potential in principle as a non-invasive imaging technique. Various improvements are recommended for future georadar surveys at the GAM site:

- Use of advanced modelling tools in the preparatory phase of the radar survey for the optimisation of the field campaign (e.g. ray tracing techniques, which can account for the complex site geometry).
- Technical optimisation of the georadar equipment on both the transmitter and the receiver side (probe characteristics of the borehole antenna, adjusted frequency ranges of transmitters and receivers, borehole logging procedure and data recording)
- Minimisation of electronic noise during the field campaign as a prerequisite for an effective processing of the data (background removal)

Drilling of additional geophysical boreholes could be beneficial to obtain a better coverage of the actual flow fields in the GAM shear zone. Precise geodetic surveys of all hydraulic and geophysical boreholes would be needed.

8 Summary and conclusions

The experiment ‘GAs Migration in Shear Zones’ (GAM) was an international research project which was carried out at the Grimsel Test Site (GTS) within the framework of Investigation Phase V (1997 – 2004). Four radioactive waste management organisations participated in the GAM experiment, namely ANDRA, ENRESA, NAGRA and Sandia National Laboratories (SNL) for the US Department of Energy (DOE). The experiment team consisted of 15 members, including delegates of the participating organisations and research groups from the Swiss Federal Institute of Technology / Zurich and from the Technical University of Catalonia / Barcelona. The project was aimed at investigating flow and transport processes in a heterogeneous shear zone with particular focus on the following aspects:

- visualisation of flow channelling on the laboratory and field scales (internal heterogeneity of shear zones),
- development of upscaling approaches and derivation of effective parameters for single and two-phase flow processes in fractured media,
- development of consistent conceptual and numerical models for (single phase) solute and gas transport.

The experimental and numerical investigations in the context of the GAM project fed into several masters theses and PhD theses at the Swiss Federal Institute of Technology / Zurich and the Technical University of Catalonia / Barcelona. Furthermore, the GAM-related studies gave rise to a considerable amount of papers published in peer-reviewed journals. Major achievements were made both in the development of field technologies for tracer testing and in the conceptualisation of transport processes in heterogeneous media. The key developments are highlighted and evaluated in the subsequent sections.

8.1 Equipment developments and refined test procedures

Essential aims in the GAM investigation programme were the development and testing of laboratory and field equipment for tracer testing, as well as the refinement of test procedures. Innovative laboratory technologies were applied, such as the Laser Scanning Confocal Microscopy and X-ray tomography (section 3.3), flow visualisation in artificial fractures, nuclear magnetic resonance measurements and neutron radiography (section 3.4). Novelties in field testing comprised the use of an online counter for the particle tracer tests and the georadar survey of gas and brine injection tests with a high frequency borehole antenna. Among the equipment developments, the following achievements are discussed here in greater detail:

- advanced drilling techniques for the recovery of well preserved core samples from the GAM shear zone
- tracer injection systems for pulse and step injection functions with short rise times
- gas tracer test methodology
- feasibility tests with high frequency georadar

Advanced drilling techniques

Previous core drilling campaigns through the shear zones of the GTS had been impeded by two major problems: (i) the invasion of drilling fluid washed out the fault gouge material and (ii) the

rock samples broke apart after core recovery due to the low cohesion of the brittle material. Based on Sandia's laboratory experiments (section 3.1), a new core drilling technique was tested at the GTS for the recovery of well preserved samples from the GAM shear zone. The applied method with annular pre-drillings, resin impregnation and overcoring (cf. Figure 3.4) provided excellent core specimens which remained mechanically stable and structurally intact. The good quality of the core specimens allowed detailed structural and hydraulic characterisation of the shear zone horizons, including X-ray tomography, NMR measurements, neutron tomography and solute and particle tracer tests as part of a column experiment.

Since its development within the framework of the GAM experiment, the new drilling technology has been used and further improved in a variety of other field experiments for the recovery of well preserved core samples in fractured rock formations (e.g. Mont Terri Research Programme; Thury & Bossart 1999).

New tracer injection systems

The early solute tracer experiments in the GAM shear zone revealed that the effective pore volume of the transport paths along the dipole flow fields was much smaller than the mixing volumes in the injection/extraction boreholes. Consequently, the characteristic transport properties of the shear zone were masked to some extent by the mixing processes in the injection/extraction systems. By a revised layout of the injection equipment (Figure 5.1), it was possible to achieve step-like input functions for the injected solute concentrations. The new injection system comprised a fluid exchange reservoir, pressure transducers and online tracer detectors for controlled circulation of the tracer fluid before the actual tracer injection started. Excellent input signals were achieved with this equipment configuration, with very short rise times of the step input function and a constant tracer concentration during the entire period of the tracer injection (cf. Figure 5.4).

The new tracer injection system has been established as standard equipment for tracer testing at the GTS, and has been used successfully in several tracer experiments of the GTS Phase VI Research Programme.

Gas tracer test technology

Theoretical studies have shown in principle that gas tracer testing should be an ideal method for characterising heterogeneous systems, because a gas phase migrates predominantly along those flow channels of a heterogeneous medium with the largest pore radii (section 6.3). Gas tracer tests in combination with solute tracer experiments are suitable for discriminating between competing concepts of transport processes (cf. section 8.2). Hence, the GAM experiment was aimed at assessing the value of the gas tracer test technology for future site investigation programmes.

Various challenges were faced in the gas tracer test programme in the GAM shear zone, both with regard to the equipment development and the experimental design. The technical developments concentrated on the adaptation of a mass spectrometer for online gas tracer detection and on equipment refinements for combined gas/water extraction, which allowed for establishing stable gas flow fields over time periods of several weeks. In the final stage of the GAM experiment, reliable test equipment and mature test procedures were available for long-term and well controlled gas tracer tests.

On the other hand, the experimental design of the gas tests was less successful: the expected separation of the gas breakthrough due to the different solubilities of the tracer gases was not observed. None of the investigated dipole flow fields was sufficiently long to allow for a significant mass exchange along the gas flow paths and thus for a retardation of the more soluble gas tracers. The lack of evidence for gas separation suggests distinct channelling of gas flow along a narrow flow path connecting the injection and extraction boreholes.

It is concluded that gas tracer testing represents a promising new technique for the characterisation of transport properties of fractured rock, which has undergone substantial improvements on the technical side. The design of such experiments, however, needs further thought. Future gas tracer tests at the GAM site should account for the site-specific conditions both by extending the length of the dipole flow fields and by the reduction of the injection and extraction flow rates.

High frequency georadar surveys

A custom-made georadar borehole antenna was tested in the GAM experiment to assess the potential of non-invasive geophysical methods for in-situ visualisation of transport processes in fractured formations. The results obtained during the survey of the gas injection PT1 were encouraging (section 7.2.2); the gas injection phase could be detected in the reflection and in the transmission mode. Variations in successive radargrams could be correlated with transients in the gas flow field, which indicated the general suitability of the method for imaging the propagation of the gas front in the shear zone. The interpretation of the radargrams was complicated by the complexity of the test configuration. A comprehensive analysis of the field data was not conducted due to limited project resources.

It is believed that the achievements made in the course of the GAM project will justify further efforts in the development of high frequency radar surveys as a tool for in-situ flow visualisation. The re-interpretation of the existing data sets with appropriate modelling tools is recommended as a first step for optimising the test configurations and test procedures. Furthermore, only limited additional investments in the infrastructure of the GAM site would be needed to improve the chance of success of future georadar surveys.

8.2 Transport processes in the GAM shear zone

Understanding of the complex flow and transport processes in the fractured crystalline rock formation of the GTS is inevitably linked to the microstructural characteristics of the individual shear zones which form the large-scale flow systems. The original aims of the GAM experiment were dedicated to the investigation of transport processes in a single heterogeneous shear zone on a 1 – 10 m scale, comprising:

- The structural characterisation of the connected pore space from the microscopic scale of the individual flow channels to the scale of tunnel mapping, where the shear zone is represented as a system of interconnected fault gouge horizons.
- Hydraulic characterisation of the shear zone in terms of a heterogeneous planar transmissivity field.
- Characterisation of solute and gas transport paths in the shear zone.

The unexpectedly low pore volume of the flow paths in the GAM shear zone caused major problems in the execution and analysis of the solute and gas tracer tests, because the tracer

volumes in the injection and extraction system exceeded the total pore volume of the flow paths in the shear zone. Hence, the mixing processes in the test equipment impaired the interpretation of the tracer tests and prevented a rigorous characterisation of the solute and gas transport properties of the shear zone. This fact led to an adjustment of some of the project aims and more emphasis was given to the understanding of the basic controls of fluid flow and mass transfer in heterogeneous flow fields rather than the estimation of transport parameters. In this context the specific issues of interest were:

- To develop a consistent approach of model abstraction from descriptive structural models on multiple scales towards flow and transport models, which describe mass transfer in a heterogeneous shear zone on the metre to decametre scale
- To assess the benefit of combined solute and gas tracer tests for discriminating between competing conceptual transport models.

Model abstraction process

The structural investigations in the GAM shear zone ranged from tunnel scale down to the microscopic characterisation of individual pore channels (cf. chapters 2 and 3). The integration of the descriptive studies draws the following conceptual picture of the shear zones in the southern part of the GTS:

1. On the site scale the shear zones can be identified as continuous, more or less planar structures over hundreds of metres. Geological tunnel mapping and borehole investigations provide a mature picture of the extent, orientation and spatial continuity of the shear zones.
2. Detailed tunnel mapping in combination with packer testing shows that groundwater flow is restricted largely to brittle structures, the so-called “fault gouge horizons”. A shear zone is made up of a series of fault gouge horizons which are arranged subparallel to each other and may have 2-D extensions in the metre to decametre range (cf. Figure 8.1b). The individual fault gouge horizons are weakly connected to each other and only a few of them exhibit a significant transmissivity.
3. A closer look at the pore space in a single fault gouge horizon reveals an interconnected network of flow channels of various apertures, embedded in a layer of more or less homogeneous fault gouge material (Figure 8.1c). On the timescales which were of interest for the GAM experiment, the zones of ductile deformation around the brittle structures do not exhibit a significant accessible porosity.
4. The complementary models on the two scales of observation can be converted into a simplified structural model, which describes the GAM shear zone as a heterogeneous 2-D structure (Fig. 8.1d). The pore space accessible for short-term tracer tests is restricted to the brittle parts of the shear zone (“fault gouge horizons”). These zones comprise both open flow channels and sections filled with compacted fault gouge material. The brittle parts of the shear zone are bound by low porosity mylonite (ductile deformation) and the unaltered granite matrix respectively.

Hydraulic testing in single-hole and crosshole configurations confirmed the heterogeneous transmissivity distribution in the GAM shear zone. However, neither the structural investigations nor the hydrotests could clarify unequivocally the impact of the fracture infill (“fault gouge”) on the transport behaviour of the shear zone. Evidence for both fault gouge filled fissures and open flow channels was found in the context of the tunnel mapping, drillcore analysis and borehole camera logs (cf. Figure 2.4). This led to some ambiguity in the elaboration of conceptual transport models, which had to be validated by in-situ solute and gas tracer tests.

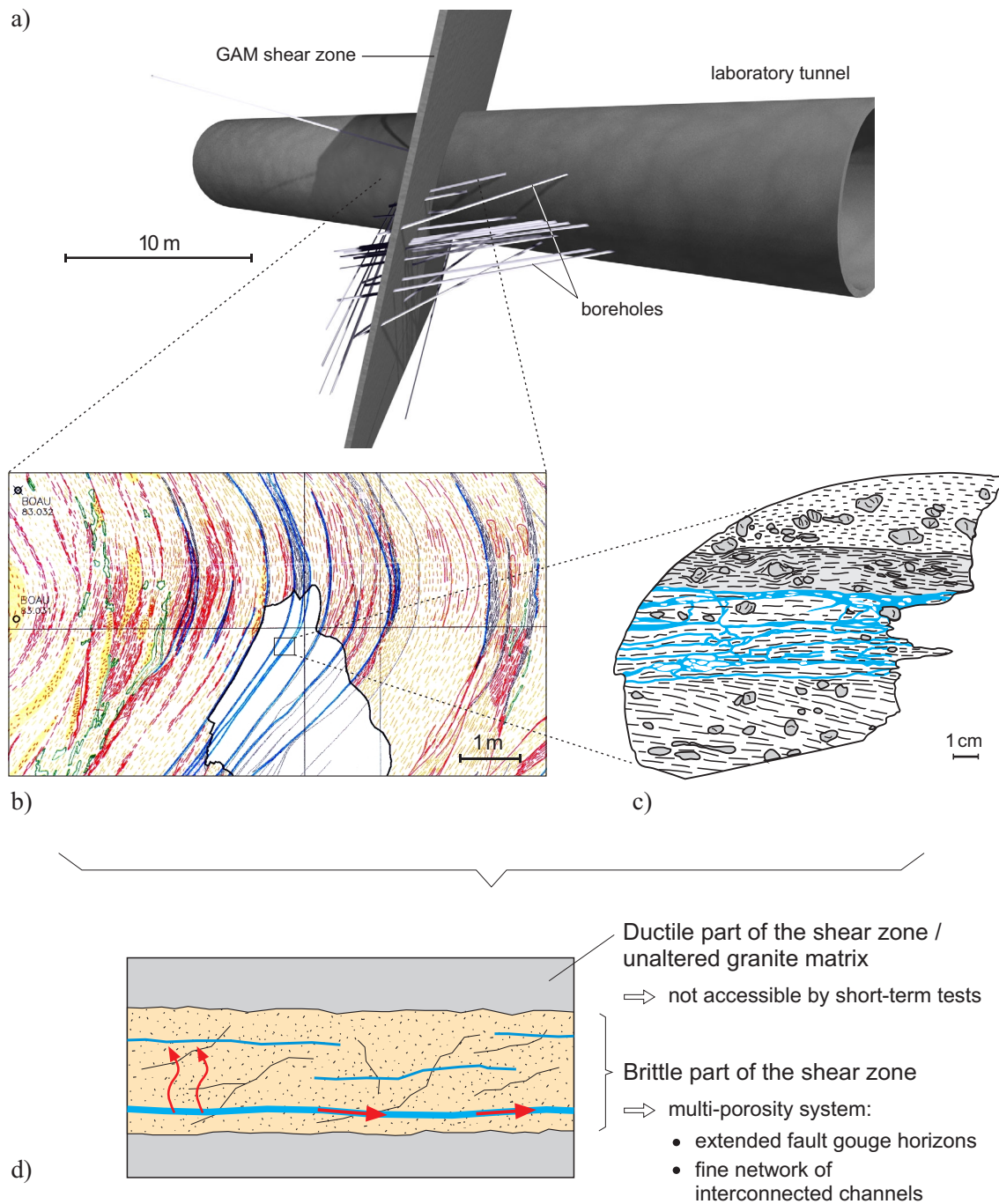


Fig. 8.1: Descriptive structural model of the GAM shear zone on different scales:

(a) the more or less planar structure can be followed on the site scale (b) the shear zone is made up of a series of fault gouge horizons which are arranged subparallel to each other and may have 2-D extensions in the metre to decametre range, (c) a single fault gouge horizon reveals an interconnected network of flow channels of various apertures, embedded in a layer of more or less homogeneous fault gouge material, (d) simplified structural model of the shear zone

The simplified structural model of the shear zone formed the basis for the definition of alternative conceptual transport models. Three bounding models were evaluated in greater detail to illustrate possible microstructural controls of macroscopic transport processes (cf. Figure 8.2):

1. a parallel-plate model with heterogeneous infill
2. a variable aperture model without infill
3. a variable aperture model with homogeneous infill

Further concepts such as dual porosity and dual permeability models were considered in principle, but were not implemented in numerical schemes.

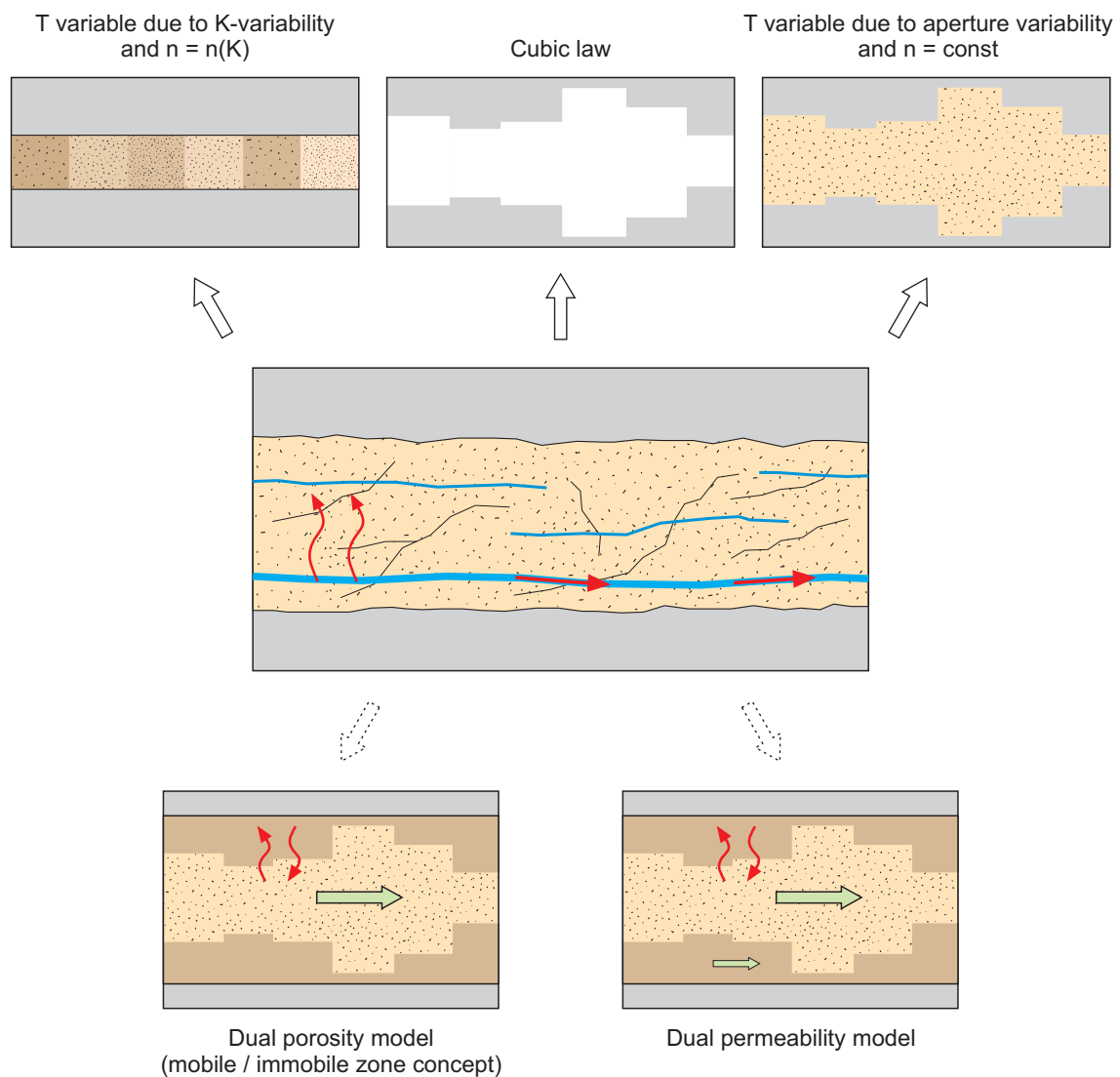


Fig. 8.2: The descriptive structural model of the GAM shear zone forms the basis for the conceptual transport model. The three conceptualisations in the upper section were utilised for illustrating possible microstructural controls of macroscopic transport processes.

Model discrimination

The interpretation of the solute tracer tests using the geostatistical inversion method allowed a consistent interpretation of both hydrotest and tracer test data. The three aforementioned conceptual transport models provided matches of the tracer breakthrough curves which performed more or less equally well. Consequently, without additional information it was not possible to discriminate between the different models.

High particle recovery during the in-situ particle tracer test PT1 and a rapid gas breakthrough during the gas injection tests suggest that a connected system of open channels exists in the GAM shear zone. These channels are believed to control transport behaviour of the shear zone during short-term tracer tests. Similar conclusions are drawn from the theoretical studies on gas transport in heterogeneous structures (cf. Figure 6.6). Rapid gas breakthrough and the low impact of solubility on the gas tracer breakthrough curves can be best simulated with those models which exhibit distinct flow channelling (i.e. open fracture or fracture with heterogeneous infill).

To date it is not clear whether these open channels are a real feature of the shear zones at the GTS or if they can be explained by artefacts, possibly caused by a wash-out of the fault gouge material during borehole drilling and tracer testing. Furthermore, the GAM in-situ experiments were not conclusive with respect to the continuity of these open channels on the large scale. Solute and gas tracer tests on a larger scale in time and space would be required to answer such questions.

References

- Albert W. (1999): Radar Measurements at the GAM Experiment Site – Feasibility Study - 7. + 8. Oct. 99. Nagra Aktennotiz, Nagra, Wettingen, Switzerland.
- Albert W. (2000a): Radar Measurements at the GAM Experiment Site – Brine Injection Test PT8 - 16. - 19. Nov. 99. Nagra Aktennotiz, Nagra, Wettingen, Switzerland.
- Albert W. (2000b): Radar Measurements at the GAM Experiment Site – Gas Injection Tests – 31. Jan. - 2. Feb. 2000. Nagra Aktennotiz, Nagra, Wettingen, Switzerland.
- Attinger S., Neuweiler I. & Kinzelbach W. (2001): Macrodispersion in radially diverging flow field with finite Peclet number 2. Homogenization theory approach, *Water Resour. Res.*, 37(3), 495-506.
- Barker J. A. (1988): A generalized radial flow model for hydraulic tests in fractured rock. *Water Resour. Res.*, 24(10): 1796-1804.
- Benson B. B. & Krause D. (1976): Empirical law for dilute aqueous solutions of nonpolar gases, *J. Chem. Phys.*, 64, 689-709.
- BLM Geophysiker and Ingenieure GmbH (1999): Optical imaging of borehole walls at the GAM site. Nagra Internal Report. Wettingen, Switzerland.
- Bossart P. & Mazurek M. (1991): Grimsel Test Site – Structural Geology and Water Flow-Paths in the Migration Shear-Zone. – Nagra Technical Report NTB 91-12; Nagra, Wettingen, Switzerland.
- Bossart P., Lang J. & Raz U. (1994): “Water Balance in Tunnel Sections,” In: Investigations of Hydraulic Parameters in the Saturated and Unsaturated Zone of the Ventilation Drift, Nagra Technical Report NT93-10, Nagra, Wettingen, Switzerland.
- Bourbie T. & Walls J. D. (1982): “Pulse Decay Permeability: Analytical Solution and Experimental Test,” *Society of Petroleum Engineers of AIME Journal*, October, pp 719-721.
- Bourgeois M. & Horne R. N. (1993): Model identification using Laplace space type curves. *SPE Formation Evaluation* (March 1993), 17-25.
- Brace W. F., Walsh J. B. & Frangos W. T., (1968): “Permeability of Granite under High Pressure,” *Journal of Geophysical Research*, Vol. 73, No. 6, pp. 2225-2236.
- Bredehoeft J. D. & Papadopoulos I. S., (1980): A method for determining the Hydraulic Properties of Tight Formations, *Water Resource Research*, v. 16, no. 1, p. 233-238.
- Brodsky N. S., Stormont J. C. & Fredrich J. T. (2000): Laboratory Measurements of Porosity, Gas Threshold Pressures, and Gas, Liquid, and Relative Permeabilities for Shear Zone Material from the Grimsel Test Site, Switzerland. Nagra Internal Report, Wettingen, Switzerland.
- Carrera J. & Neuman S.P. (1986): Estimation of aquifer parameters under transient and steady state conditions, I. Maximum likelihood method incorporating prior information. *Water Resources Research*, Vol. 22, Number 2, pp 199-210.

- Chen Q. & Kinzelbach W. (2002): An NMR study of single- and two-phase flow in fault gouge filled fracture, *J. Hydrol.*, 259, 236-245.
- Cooper H. H. & Jacob C. E. (1946): A generalized graphical method for evaluating formation constants and summarizing well field history, *Am. Geophys. Union Trans*, v. 27, no. 4., p. 526-534.
- Cooper H. & Papadopoulos I. S. (1967): Response of a finite diameter well to an instantaneous charge of water. *Water Resources Research*(27), 4: 526-534.
- Coscrove B. A. & Walkley J. (1981): Solubilities of gases in H₂O and 2H₂O, *J. Chromatography*, 216, 161-167.
- Croisé J., Marschall P. & Senger R. (1998): Gas-water flow in a shear zone of a granitic formation: interpretation of field experiments. *DisTec'98 – Tracer Hydrogeology*. Balkema, Rotterdam.
- Dean J. A. (1994): *Langes's handbook of chemistry*, McGraw-Hill,
- De Marsily G. (1986): *Quantitative Hydrogeology*, Academic Press Inc.
- Earlougher R.C. Jr., (1977): *Advances in well test analysis*, Soc. of Petroleum Engineers, Monograph Volume 5 of the Henry L. Doherty Series, 264 p.
- Fierz T. & Pidevache M. (2000): GTS V/GAM: Results of hydraulic tests and gas threshold pressure tests in GAM 98-002 (January/February 2000), NAGRA Internal Report, NAGRA NIB 00-14; Wettingen, Switzerland.
- Fierz T., Proust E., de Combarieu M. & Meier P. (2000): Gas tracer test series GT1 in the GAM shear zone, *Nagra Int. Rep.*, 00-30, Nagra, Wettingen, Switzerland.
- Garcia M. & Caussade (2001): Modelling and history matching of GAM gas tracer tests, ANDRA report ref. D RP 0FSS 01-001/A, 2001.
- Garcia M. & Caussade (2002): Integrating spatially varying capillary pressure functions in the simulation of GAM gas tracer tests, ANDRA report ref. D RP 0FSS 02-001/A, 2002.
- Gemperle R. (1999a): GTS V/GAM: Hydraulic testing in GAM 98.002 and GAM 98.004. NAGRA Internal Report 99-03, Wettingen, Switzerland.
- Gemperle R. (1999b): GTS/GAM: Hydraulic testing in GAM 98.002 and GAM 98.004, NAGRA Internal Report; Wettingen, Switzerland
- Grisak et al. (1985)
- Fischer U., Kulli B. & Flühler H. (1998): Constitutive relationships and pore structure of undisturbed fracture zone samples with cohesionless fault gouge layers. *Water Resources Research*, Vol. 34, No. 7, pp. 1695-1701.
- Fredrich J. T., Menendez B. & Wong T.-F. (1995): Imaging the pore structure of geomaterials, *Science*, 268, pp. 276-279.

- Fredrich J.T. (1999): 3D imaging of porous media using laser scanning confocal microscopy with application to microscale transport processes. *Phys. Chem. Earth*, 24, pp. 551-561.
- Frieg B. & Vomvoris S. (1994): Investigation of hydraulic parameters in the saturated and unsaturated zone of the Ventilation Drift. Nagra Technical Report NTB 93-10; Nagra, Wettingen, Switzerland.
- Gimmi T., Schneebeili M., Flühler H., Wydler H. & Baer T. (1997): Field-Scale Water Transport in Unsaturated Crystalline Rock. *Water Resources Research*, Vol. 33, No. 4, pp. 589-598.
- Heiniger P. (1992): Active and Passive Hydrological Testing in the VE Drift. In: Overview of Nagra Field and Modeling Activities in the Ventilation Drifts (1988-1990), Nagra Technical Report NTB87-14E, Nagra, Wettingen, Switzerland.
- Horne R. N. (1995): *Modern Well Test Analysis*, Petroway Inc., Palo Alto, CA, USA
- Jones S. C. & Roszelle W. O. (1978): "Graphical Techniques for Determining Relative Permeability from Displacement Experiments," *Journal of Petroleum Technology*, Vol. 30, No. 5, pp. 807-817.
- Kennedy K. (1999): GTS/GAM – Solute and particle tracer tests PILOT and PT1 in the GAM shear zone (Dec 1998 to April, 1999). Nagra Internal Report; Wettingen, Switzerland.
- Kennedy K. (2000a): GTS/GAM – Solute and particle tracer tests PT2 in the GAM shear zone (May 1999). Nagra Internal Report; Wettingen, Switzerland.
- Kennedy K. (2000b): GTS/GAM – Solute and particle tracer tests PT3 in the GAM shear zone (May 1999). Nagra Internal Report; Wettingen, Switzerland.
- Kennedy K. & Kleiner A. (2000): GTS/GAM – Solute Tracer Tests PT4 & PT5 in the GAM Shear Zone (August, September 1999). Nagra Internal Report; Wettingen, Switzerland.
- Keusen H. R., Ganguin J., Schuler P. & Buletti M. (1989): Grimsel Test Site – Geology. – Nagra Technical Report NTB 87-14E; Nagra, Wettingen, Switzerland.
- Kobayashi T. & Shockey D. A. (1991): *Adv. Mater. Proc.* Vol. 140, 28 (November, 1991) and 24 (December 1991): *Trans. Soc. Prof. Well Log Anal.*, Thirty-third Annual Logging Symp. Paper No. 9926, Oklahoma City, OK, 14 to 17 June 1992 (Soc. Prof. Well Log. Anal., Houston, TX, 1992.)
- Lanyon G. W., Marschall P., Vomvoris S., Jaquet O. & Mazurek M. (1997): Effective property determination for input to a geostatistical model for regional groundwater flow: Wellenberg T-K. Presented at the 3rd International Äspö Seminar, Oskarshamn, Sweden, 10 - 12 June 1998: Characterisation and Evaluation of Sites for Deep Geological Disposal of Radioactive Waste in Fractured Rocks.
- Lunati I., Attinger S. & Kinzelbach W. (2002a): Macrodispersivity for transport in arbitrary non-uniform flow fields: Asymptotic and pre-asymptotic results. *Water Resources Research*, 38(10), 1187, 2002.
- Lunati I., Attinger S. & Kinzelbach W. (2002b): Heuristic extension of Homogenization to pre-asymptotic plumes, In: S.M. Hassanizadeh, R.J. Schotting, W.G. Gray, and G.F. Pinder

- (eds), *Computational Methods in Water Resources*, Vol. 2, 1139-1145, *Developments in water science*, 47, Elsevier, Amsterdam, 2002.
- Lunati I., Kinzelbach W. & Soerensen I. (2003a): Effects of pore volume-transmissivity correlation on transport phenomena, *J. Contam. Hydrol.* 67 (1-4), 195-217.
- Lunati I., Vontobel P., Kinzelbach W. & Lehmann E. (2003c): Visualization of water uptake and transmission in a granite sample by neutron tomography, *PSI Scientific Report Vol. III*, PSI, Villingen, Switzerland, 2003.
- Lunati I., Vontobel P., Kinzelbach W. & Lehmann E. (2003d): Laboratory visualization of two-phase flow in a natural fracture by neutron tomography, *Groundwater in Fractured Rocks*, Prague, Czech Republic, September 15-19, 2003.
- Lunati I. & Kinzelbach W. (2003): Gas tracer tests in an unsaturated fracture: water-soluble gases as partitioning tracers, conference proceeding of TOUGH2 Symposium 2003, Berkeley (CA), USA, March 12-14, 2003.
- Lunati I. (2003): *Conceptual Models of Single and Multiphase Transport in a Fracture*, Eidgenössische Technische Hochschule Zürich, Ph.D. Thesis no. 15082.
- Lunati I. & Kinzelbach W. (2004): Water-soluble gases as partitioning tracers to investigate the pore volume-transmissivity correlation in a fracture. *Journal of Contaminant Hydrology* 75, 31-54.
- Majer E. L., Myer L. R., Peterson J. E., Karasaki K., Long J. C. S., Martel S. J., Blümling P. & Vomvoris S. (1990): Joint seismic, hydrogeological and geomechanical investigations of a fracture zone in the Grimsel rock laboratory, Switzerland. *Nagra Technical Report NTB 90-49*; Nagra, Baden, Switzerland.
- Marschall P., Croisé J., Fischer U., Senger R. & Wyss E. (1998a): Gas flow through water-saturated shear zones: field- and laboratory experiments and their interpretation, *Mat. Res. Soc., Symp. Proc.*, Vol. 506, 741-748.
- Marschall P., Vomvoris S., Jaquet O., Lanyon G. W. & Vinard P. (1998b): The Wellenberg K-Model: A Geostatistical Description of Hydraulic Conductivity Distribution in the Host Rock for Site Characterization and Performance Assessment Purposes. *Mat. Res. Soc., Symp. Proc.* Vol. 506.
- Marschall P., Albert W., Carbonell R., Carrera J., Davies P.B., Kinzelbach W., Mayor J.C. & Niehren S. (1998): GTS/GAM: Investigation programme for the GTS Phase V experiment "Gas migration in shear zones" (1998-2000). *NAGRA Internal Report 98-12*. Wettingen, Switzerland.
- Marschall P. & Croisé J. (1999): Grimsel Test Site - Determination of two-phase flow properties in shear zones. - *Nagra Technical Report NTB 97-06*; Nagra, Wettingen, Switzerland.
- Marschall P. (2006): Grimsel Test Site – List of GAM project documents. *Nagra Aktennotiz*; Nagra, Wettingen, Switzerland.

- Meier P. M., Carrera J. & Sánchez-Vila X. (1998): An evaluation of Jacob's method for interpretation of pumping tests in heterogeneous formations, *Water Resour. Res.*, 34(5), 1011-1025.
- Neuweiler I., Attinger S. & Kinzelbach W. (2001): Macrodispersion in radially diverging flow field with finite Peclet number 1. Perturbation theory approach, *Water Resour. Res.*, 37(3), 481-494.
- Neuweiler I., Sørensen I. & Kinzelbach W. (2004): Experimental and theoretical investigations of drainage in horizontal rough-walled fractures with different correlation structures, *Advances in Water Resources*, 27, 1217-1231.
- Olivella S. & Carrera J. (1987): KRINET (kriging Network). Computer code for optimal design of observation networks through geostatistics. User's guide (draft) E.T.S.I. Caminos Canales y puertos. Universitat Politècnica de Catalunya, Barcelona, Spain
- Olivella S., Gens A., Carrera J. & Alonso E. E. (1996): Numerical formulation for a simulator (CODE_BRIGHT) for the coupled analysis of saline media. *Engineering Computations*. 13(7): 87-112.
- Pickens J. F., Grisak G. E., Avis J. D., Belanger D. W. & Thury M. (1987): Analysis and Interpretation of Borehole Hydraulic Tests in Deep boreholes: Principles, Model Development and Applications. *Water Resources Research*, Vol. 23, No. 7, pp 1341-1375.
- Ramajo H., Jodar J., Carrera J. & Olivella S. (1999). GTS/GAM: UPC – Progress report on modeling of gas migration processes, NAGRA Internal Report, Wettingen, Switzerland
- Ramajo H., Sanchez-Vila X., Carrera J. & Olivella S. (2000): Simulation of gas dipole tests in fractures at the intermediate using a new upscaling method. *Upscaling Downunder*, a Symposium and Workshop on Upscaling Reservoir properties and related issues. Melbourne, February 2000.
- Ramajo H., Jodar J., Carrera J. & Olivella S. (2001): Modelling gas tracer tests within a fracture. *Groundwater quality 2001. Third International Conference on Groundwater Quality*, 18-21 June, 2001, University of Sheffield, pp. 239-240.
- Ramajo H., Olivella S., Carrera J. & Sánchez-Vila X. (2002): Simulation of gas dipole tests in fractures at the intermediate scale using a new upscaling method. *Transport in porous media*, 46 (2-3): pp269-284.
- Schneebeli M., Flühler H., Gimmi T., Wydler H. & Läser H. (1995): Measurements of Water Potential and Water Content in Unsaturated Crystalline Rock. *Water Resources Research*, Vol. 31, No. 8, pp. 1837-1843.
- Senger R., Marschall P. & Lavanchy J.-M. (1998): Gas Threshold Pressure Tests in Deep Boreholes for Determining Two-Phase Flow Properties of the Host Rock at the Proposed L/ILW Repository, Switzerland. *Mat. Res. Soc., Symp. Proc.* Vol. 506, 829-838.
- Sørensen I. (1999): Solute transport and immiscible displacement in single fractures, *Nagra Int. Rep.*, 99-50, Nagra, Wettingen, Switzerland.

- Su H. & Kinzelbach W. (1999): Application of 2-D random generators to the study of solute transport in fractured porous medium. Water 99: Handbook and Proceedings, 627-630, Queensland, Australia.
- Thury M. & Bossart P. eds. (1999): Mont Terri Rock Laboratory: Results of the Hydrogeological, Geochemical, and Geotectonical Experiments performed in 1996 and 1997. Bern, Switzerland, *Landeshydrologie und -geologie, Geologische Berichte* Nr. 23.
- Trick T., Fierz T., Proust E., Meier P. & de Combarieu M. (2000): Gas tracer test series GT2 in the GAM shear zone, Nagra Int. Rep., Nagra, Wettingen, Switzerland, 2000
- Trick T., Piedevanche M., Proust E., Meier P. & de Combarieu M. (2001): Gas tracer test series GT3 in the GAM shear zone, Nagra Int. Rep., Nagra, Wettingen, Switzerland, 2001
- Trick T. (2000): GTS V/GAM: Results of hydraulic tests in GAM 98-004, NAGRA Internal Report, Wettingen, Switzerland
- Trick T. (2001): GTS V/GAM: Results of hydraulic tests in the GAM shear zone (December 2000), NAGRA Internal Report, Wettingen, Switzerland
- Vomvoris S. & Frieg B. (1992): GTS – Overview of Nagra field and modeling activities in the Ventilation Drift. Nagra Technical Report, NTB 91-34; Nagra, Wettingen, Switzerland.
- Walker D. D., & Roberts R. M. (2003): Flow dimensions corresponding to hydrogeologic conditions. WRR Vol 39 (12).
- Wyss E. (1996): GTS-TPF: Site preparation, borehole installation, hydraulic characterization and gas threshold-pressure tests at the Grimsel Test Site, NAGRA Internal Report; Wettingen, Switzerland
- U.S. Department of Energy Carlsbad Area Office (1997): International Research and Development Plan. DOE/CAO 97-1266, Rev. 0, 44 p.

Acknowledgements

The authors would like to acknowledge the contributions of key individuals. Craig Boney (SNL) performed the porosity and permeability tests (cf. Chapter 3) and, throughout the testing programme, showed exemplary diligence and dedication to this work. Dr. Susan Altman (SNL) performed the X-ray imaging work out of intellectual and scientific curiosity (cf. Chapter 3).

Insa Neuweiler, Stefan Niehren and Ivan Sørensen (all ETH) contributed to the project with their experimental studies on solute and gas transport in artificial fractures (Chapter 3), with equipment developments for online particle tracer detection (Chapter 5) and, last but not least, with theoretical studies on the upscaling problem (Chapter 5).

Wilfried Albert (Albert-Donié GeoConsult), Georg Klubertanz and Rainer Schwarz (both Colenco) were responsible for the design, execution and interpretation of the radar measurements (Chapter 7).

Special thanks go to Bill Lanyon for the thorough review of the report. The editors benefited greatly from fruitful discussions and helpful recommendations.